MAYNOOTH UNIVERSITY

A 3D MUSE View of the Th 28 Precessing Stellar Jet

presented by

Aisling Murphy

Submitted for the degree of Doctor of Philosophy

Research Supervisor

Dr. Emma Whelan

Head of Department

Dr.Creidhe O'Sullivan

in the
Faculty of Science and Engineering
Department of Experimental Physics
Maynooth University

June 2022

Declaration of Authorship

I, Aisling Murphy, declare that this thesis titled, 'A MUSE View of the Th 28 Precessing Stellar Jet' and the work presented in it are my own. I confirm that:

- This work was done wholly or mainly while in candidature for a research degree at this University.
- Where any part of this thesis has previously been submitted for a degree or any other qualification at this University or any other institution, this has been clearly stated.
- Where I have consulted the published work of others, this is always clearly attributed.
- Where I have quoted from the work of others, the source is always given. With the exception of such quotations, this thesis is entirely my own work.
- I have acknowledged all main sources of help.
- Where the thesis is based on work done by myself jointly with others, I have made clear exactly what was done by others and what I have contributed myself.

Signed: Aisling Murphy

Date: 27th June 2022

Dedicated to my grandmothers, with love.

"With magic, you can turn a frog into a prince. With science, you can turn a frog into a Ph.D and you still have the frog you started with."

— Terry Pratchett, *The Science of Discworld*

Contents

List of Figures

List of Tables

MAYNOOTH UNIVERSITY

Abstract

Faculty of Science and Engineering
Department of Experimental Physics

Doctor of Philosophy

by Aisling Murphy

Protostellar jets are an important component of star formation, acting as a window into the inner regions of the protoplanetary disk while also impacting on the evolution of the star-disk system and the surrounding molecular cloud. Integral field spectroscopy (IFS) has proven a valuable tool for jet studies, as this allows three-dimensional spatial and spectral information to be collected simultaneously across the extended jet. VLT/MUSE is an exceptionally powerful IFS instrument operating in the optical and near-infrared (NIR) band with large spatial and spectral coverage. In this thesis, we present the analysis of MUSE observations of the jet from the Classical T Tauri Star Th 28 to explore the potential of MUSE for jet studies and to develop Python tools which support the analysis of MUSE data. We are able to characterise the morphology and kinematics of the Th 28 jet in detail, including six newly identified knots. A key result from our analysis of the jet morphology is the detection of a 'wiggling' in the jet which shows a clear point-symmetry between the jet lobes indicating precession. We model the jet trajectory and show that this may be the signature of a brown dwarf companion ($\leq$ 70 M_{Jup}) orbiting within the inner disk region. This work also investigates the physical diagnostics of the jet using optical and NIR emission line ratios, and highlights the asymmetric densities and excitation conditions between the two lobes of the jet, in tandem with their asymmetric morphologies and velocities. The results of this project to date emphasize both the potential for further work investigating the origins of the observed asymmetries and precession in the Th 28 jet, and the incredible power of MUSE to comprehensively investigate protostellar jets.

Acknowledgements

I wish to sincerely thank my supervisor Dr. Emma Whelan, whose sound advice and steady encouragement have seen me through this PhD work. I am constantly grateful for her expertise, her patience, and especially her level-headed sense of perspective whenever I have found myself struggling with the urge to panic.

I gratefully acknowledge the kind help and expertise contributed by our collaborators, especially Catherine Dougados, Deirdre Coffey, Francesca Bacciotti and Andrew Kirwan. I particularly thank Catherine Dougados and Francesca Bacciotti for all their advice, patient explanations and incisive feedback during this project. My sincere thanks also to Staci, Aoife and Grainne for their help in proofreading this thesis.

I also wish to thank the lecturers and staff of the Maynooth Experimental Physics department for making it such a welcoming and enjoyable environment to research and teach in, from helping me with my questions to chatting in the tea room or putting out (metaphorical) fires in the undergraduate labs. I am grateful especially to my fellow postgrads past and present who helped me find my way and provided moral support and practical advice, as well as many hours of great chats and craic.

Special thanks are owed to my family and friends for their unwavering support and encouragement throughout my studies. I am deeply grateful to my parents, without whom I could never have gotten to this point; to my brother and sister for their endless help and good humor; and to my grandmother Breda, whose kindness and constant support made my PhD studies in Maynooth possible. Finally, I would like to sincerely thank the many friends who have put up with my sense of humor and been a source of inspiration, wisdom and sanity over the past few years.

Introduction

This thesis presents an analysis of VLT/MUSE observations of a jet from the Classical T Tauri Star Th 28. The twin goals of this work were to comprehensively investigate the structure and physical conditions of the Th 28 jet by exploiting the 3D dataset provided by MUSE, and to use the Th 28 observations as a starting point to explore the potential of MUSE for jet studies, as well as to develop Python tools which support analysis of MUSE jet observations.

Chapter 1 of this Thesis will therefore begin with an introduction to the background of stellar jets, their origins and significance in the context of star formation. We will see that jets play an important role in the evolution of the star-disk system, and how the MUSE instrument is uniquely suited to help us to understand the processes at work in the inner disk region as well as the connection between the star and the surrounding disk.

Chapter 2 discusses the MUSE observations of Th 28, the data reduction process, and the preparation of the data for analysis. Here we also give a short description of the Python modules written to facilitate the analysis in this project.

Chapter 3 focuses on the morphological and kinematic investigation of the jet, including the many emission lines in which the jet is observed and the overall morphology of both jet lobes. We obtain proper motions and radial velocities for the knots along the jet, including six knots which we identify for the first time.

Chapter 4 gives an in-depth analysis of a precession signature in the jet. We show that the centroids of both jet lobes can be fitted with a precession model and derive inferred parameters for a possible companion object which might cause this, as well as investigating possible uncertainties which might affect this finding.

Chapter 5 focuses on the physical diagnostics of the jet using the optical and NIR emission line ratios made available by the spectral coverage of MUSE, including the jet density and excitation. In this chapter we also estimate the mass accretion onto the star and the mass outflow rate of the jet.

Finally, *Chapter 6* discusses the main conclusions of this project and the potential for future work both with MUSE observations and the Th 28 jet in specific.

Chapter 1

Background

Jets and outflows are a ubiquitous feature of young stars and are thought to be an integral part of the star formation process and the mechanisms that link the protostar with its accretion disk. Observations of jets can offer insight not only into the processes that shape the formation of the star and the inner protoplanetary disk, but also how star formation feeds back into the surrounding molecular cloud and regulates the formation of stellar clusters. Advances in instrumentation such as integral field spectrographs (IFS) allow increasing amounts of information about the structures, kinematics and spectra of these objects to be collected simultaneously, opening the way to a more comprehensive understanding of these dynamic and multi-faceted objects.

This chapter provides an overview of the background concerning star formation and the significance of protostellar jets and T Tauri stars, followed by a discussion of the main models for protostellar accretion and jet launching. We then review some of the notable observable phenomena associated with jets, and how the advancement of IFS instruments offers new opportunities to further our understanding of them. The final parts of this chapter will introduce the Multi-Unit-Spectroscopic Explorer (MUSE), the IFS instrument used in this project, and Th 28, the jet on which this work is focused.

1.1 Young Stars, Jets, and Disks

1.1.1 From Molecular Clouds to Protostars

The large-scale picture of star formation can be broadly conceptualized as a series of hierarchical stages of mass contraction and collapse onto ever-smaller spatial scales, from parsec-scale clouds to circumstellar disks a few hundreds of au across.

At the largest scale, stars form within molecular clouds (MCs): cold, dense, turbulent regions of molecular gas within the interstellar medium (ISM) which may be several 10s of parsecs in diameter. Their total masses range from 100 $M_\odot$ in small MCs to between a few 10^4 $M_\odot$ and 10^7 $M_\odot$ in the case of Giant Molecular Clouds (GMCs) (Dobbs et al., 2014). MCs are well traced by emission from CO molecules, which are excited at very low temperatures, and the first CO maps of these clouds were produced in the 1970s (Lada, 1976; Kutner et al., 1977; Blair et al., 1978). Later work went on to map the molecular gas distribution within the Milky Way Galaxy (Dame et al., 1987, 2001), and since then the structure, kinematics and evolution of MCs have been closely studied.

This project focuses on a star in the Lupus 3 cloud, one of a local complex of nine small molecular clouds at distances of 140-200 pc (Hara et al., 1999; Teixeira et al., 2020). The complex is located in the sky above the galactic plane at the northern extent of the Gould Belt of star-forming regions. The Lupus clouds are shown in extinction in Figure 1.1. Among them, the Lupus 3 cloud shows the most active star formation with both optically revealed accreting young stars and less evolved dense cores and protostars (Schwartz, 1977; Comerón et al., 2003; Nakajima et al., 2003; Teixeira et al., 2005).

Molecular clouds are primarily formed of H_2, but significant amounts of other molecules and dust grains are also present; indeed, the molecularly dominated phase of the ISM comes about not only due to high densities, but is catalyzed by the presence of dust grains (Molinari et al., 2014). The density within the cloud is unevenly distributed but shows a mean value of $n_{H_2} \sim 100$ cm^{-3}. Further, MCs show a complex velocity structure, and observations with higher angular resolution in optically thin tracers reveals equally complex internal structures. Within the cloud, gas and dust form a network of filamentary structures seen in both GMCs (Bally et al., 1987; Kirk et al., 2013) and small MCs like the Lupus clouds (Tachihara et al., 2007; Benedettini et al., 2015).

It is in these filaments that stellar cores will eventually form. These are formations of cold, turbulent gas flows, several parsecs in length and around 0.1 pc in width (André et al., 2010; Arzoumanian et al., 2011), themselves organized into interconnected branches and loops (Schneider et al., 2010; Hill et al., 2011). Filaments are produced where colliding or converging flows form dense, low-velocity sheets behind shock regions. These cool into molecular gas, forming filaments which in turn fragment into clumps. These regions have a mass density > 1 $M_\odot$ pc^{-3}, and their distribution is well correlated with the locations of young stars $<$ 5-10 Myr in age. In older star-forming clusters the gas is eventually cleared from the filament, and the structure becomes less organized.

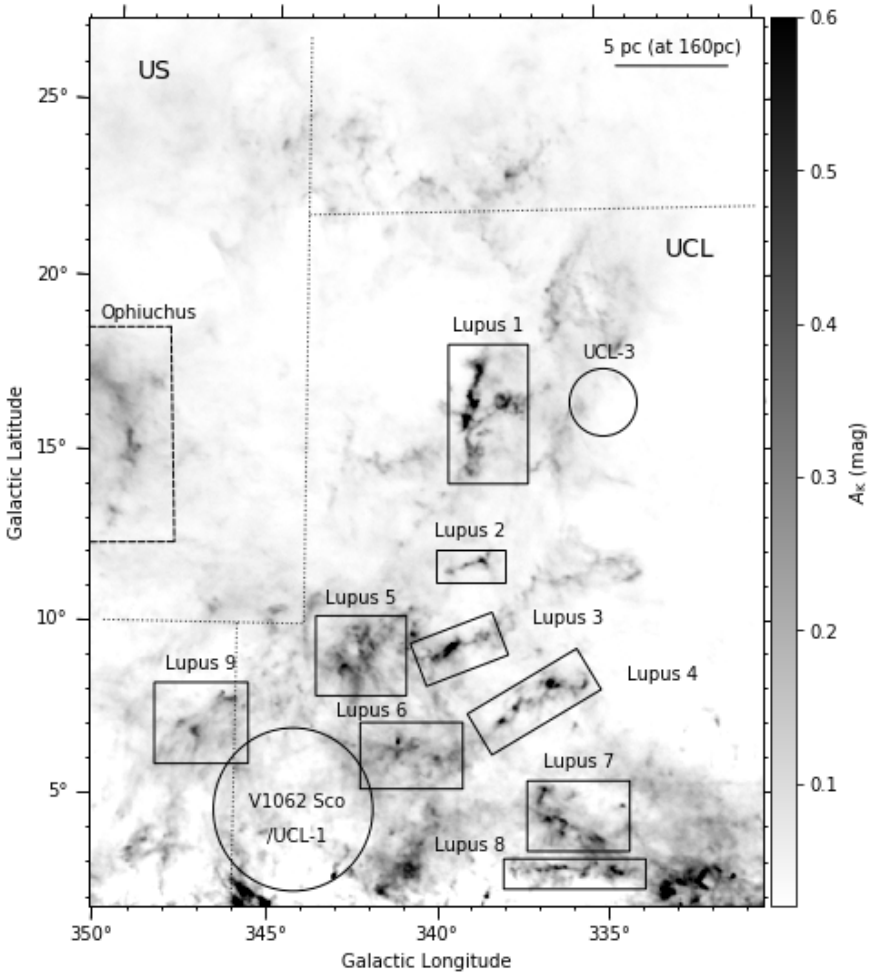

FIGURE 1.1: Planck extinction map (Abergel et al., 2014) showing the Lupus molecular cloud complex as well as the compact groups V1062 Sco/Upper Centaurus-Lupus-1 (UCL-1) and UCL-3, reproduced from Teixeira et al. (2020).

Within the clumps, dense cores form, reaching masses of a few $M_\odot$. The cores are typically clustered together along the filaments, with low velocity distributions. They are deeply embedded in their parent filament, from which they accrete mass until the formation of a protostar within the core heats the surrounding cloud sufficiently to accrete or disperse all the nearby gas, leaving the protostar and accretion disk (Myers, 2009; André et al., 2010). Eventually the formation of stars by accretion, and feedback from sources such as supernovae and protostellar outflows, will disrupt the parent cloud and star formation will decline. Small MCs in particular may be significantly disrupted by the effects of ionizing radiation within a few Myr (Dale et al., 2012). However, this simple picture of star formation on the galactic scale hides many open questions concerning the life cycle of MCs, the physical processes which drive each stage, and the role of feedback from different sources; all of these remain very active areas of debate (Dobbs et al., 2014; Molinari et al., 2014).

1.1.2 Protostellar Evolution

Protostars and pre-main-sequence stars form from collapsing stellar cores, with the gas and dust around them flattening into a circumstellar accretion disk from which the forming star continues to gain mass until it eventually ignites hydrogen burning and contracts onto the main sequence. These young stellar objects (YSOs) have been observed in several different stages of formation. Low-mass YSOs (< 2 $M_\odot$) are typically classified into an evolutionary scheme illustrated in Figure 1.2, with different stages defined by their spectral characteristics and bolometric temperature (Lada & Wilking, 1984; Lada, 1987; **?**; Evans et al., 2009).

Class 0: These are low mass protostars at the earliest stages of formation, with a core mass of ~ 1 $M_\odot$. At this stage they are still deeply embedded in a dense, optically opaque envelope of gas and dust, with the result that they are very low in luminosity, and their observed spectral energy distributions (SEDs) are dominated by thermal emission from the surrounding dust. They can be detected in sub-mm continuum emission as a centrally peaked, extended envelope within the cloud indicating the formation of a compact object (**?**). They can also be identified by the presence of bipolar outflows, which are detectable in SiO emission indicating molecular gas characterised by warm shocks with temperatures of a few 100 K (Podio et al., 2015, 2016; Jhan & Lee, 2021).

Class I: As the protostar accretes and evolves, it heats the surrounding dust further, and the peak of the SED starts to move into the IR range as shown in Figure 1.2. The stellar photosphere is still obscured by the dust envelope, with the slope or the peak of the SED used to define how much of the envelope has been cleared away. The transition to a Class I object is defined either by the proportion of its bolometric luminosity which is emitted in the sub-mm band, or at a bolometric temperature of ~ 70 K (Evans et al., 2009).

Class II: The emission from the envelope around the star diminishes and the peak of its SED moves further, into the optical range. When the star has accreted enough material for its envelope to become optically thin at its peak wavelengths it is considered a Class II object. Objects in this category with less than about 2 $M_\odot$ and an estimated spectral type of G0 or later are the Classical T Tauri Stars (CTTSs), which will be the main focus of our discussion; those with > 2 $M_\odot$ and an earlier spectral type are classified as Herbig Ae/Be stars. Class II objects still show a near- to mid-IR excess from the presence of a circumstellar disk; in fact, they are of particular interest because they are the last point in the star's evolution where a significant disk is present, and hence the signatures of planet formation can be observed (Lada, 1987; Testi et al., 2022).

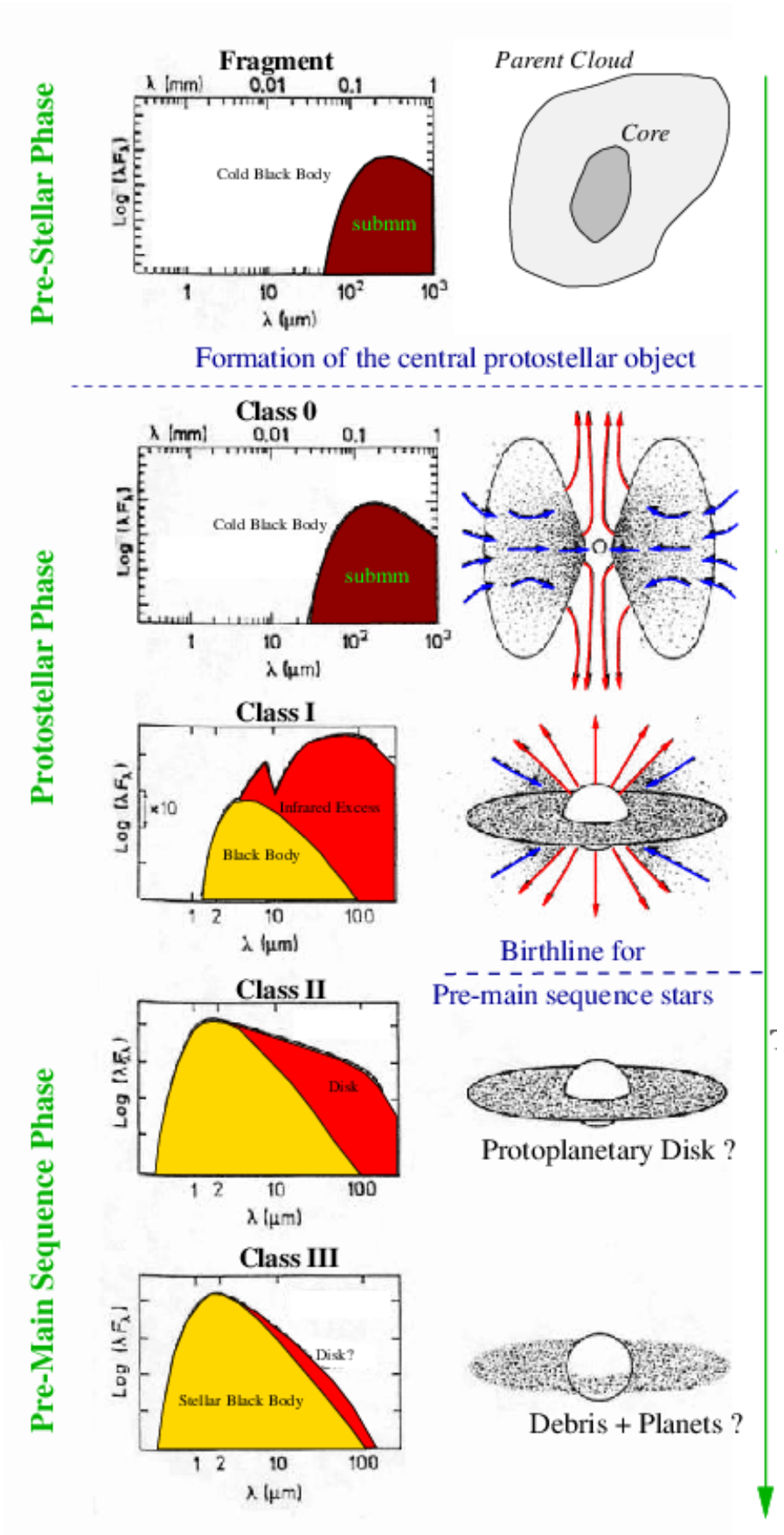

FIGURE 1.2: Diagram of protostellar evolutionary stages, from **?**.

CTTSs have an IR spectral index[1] between -1.6 and -0.3 and show high variability in their optical spectra, with strong lines in emission indicating significant material around the star (Greene et al., 1994). They are distinguished by excess emission in optical spectral lines, particularly the H Balmer lines such as Hα: this is in contrast to main sequence stars which show Hα in absorption, and was one of the first indicators that these lines are linked to accretion onto the young star. The profiles of these lines vary significantly on time-scales from hours to months, along with other optical and UV lines whose strength correlates with the Hα emission. As will be discussed further in Section 1.2.1, these signatures represent high-density gas at 0.5 - 1 $\times 10^4$ K, infalling onto the star at roughly freefall velocities (Edwards et al., 1994).

Class III: Eventually, between about 1-10 Myr, the surrounding disk is depleted by accretion or dispersed, and the strong accretion lines seen in the CTTS sources diminish or disappear (Cieza et al., 2007). At this stage the star has transitioned to a Class III, or a Weak-line T Tauri Star (WTTS). The spectrum only shows an IR excess in the far IR, with a spectral index $<$ -1.6, indicating any remaining disk material is cool and located far from the star (Greene et al., 1994).

CTTS sources, as mentioned, present a valuable cross-section in time where the processes of accretion, outflow launching, and planet formation are still taking place around the star, but the regions close to the star itself are now optically visible. Further, many of them are located in nearby star forming regions ($\sim$ 120-160 pc in distance), making them ideal subjects to study the formation of stars and disks with high angular resolution. For these reasons they are important targets for the study of star formation, and this also gives them the advantage of being relatively well-characterized as a class.

The protostar is now in its final stages of evolution before the main sequence, but still shows many characteristics of a pre-main sequence (PMS) star, including a relatively low effective temperature and bolometric luminosity, as well as strong magnetic activity and X-ray emission. Another key signature is the presence of Li absorption in the spectrum, as Li is quickly destroyed by the high-temperature nuclear reactions within a main-sequence star.

Both categories of TTS are known to have extremely strong magnetic activity (Basri, 2007; Donati et al., 2012; Nicholson et al., 2018; Hill et al., 2019), and CTTS spectra show complex optical accretion and absorption features (see Section 1.2.1). Another important characteristic is that CTTSs have been shown to rotate far below their breakup velocity,

[1]The spectral index is a measure of the dependence of the star's radiative flux density on the wavelength at which it is measured, usually estimated from the ratio of the star's flux at two different wavelengths in the IR range. It can be visualised as a measure of the slope of the SED in the IR region; for stars $< 2M_\odot$, this slope will tend to decrease and then become strongly negative as the star evolves and the flux from the disk diminishes.

contrary to what would be expected due to their accretion of angular momentum from the surrounding disk (Bouvier et al., 1986; Bertout, 1989). This gives rise to what is called the 'angular momentum problem': the question of how angular momentum is removed from the star-disk system during accretion, which will be further discussed later in this chapter.

1.1.3 Circumstellar Disks

Accretion disks form as the core is rotationally flattened during infall and collapse. They are primarily observed in the IR and sub-mm bands, with molecular line emission from OH and H_2O serving as important tracers of the disk kinematics and rotation. The opacity of the disk is dominated by its dust content, absorbing and re-emitting stellar radiation at longer wavelengths. The temperature of the dust depends on its proximity to the protostar, so that different radii can be probed using continuum emission at different wavelengths; the outer, colder disk regions are better traced by mm emission, whereas the warmer inner disk regions can be studied in the near-infrared (NIR) range (Alexander et al., 2014). Over the first few Myr the emission signatures of the disk decline dramatically, from an IR excess fraction of about 100% in sources less than 1 Myr old to less than 10% after 5 Myr. This tracks with the decline of accretion signatures, along with the signs of gas and dust in the outer disk (Andrews & Williams, 2005; Cieza et al., 2008).

Eventually complete dispersal of the gas around the star occurs by the Class III phase. Transitional disks have also been observed, which show only partial clearing of the inner disk, but these are rare, and the scarcity of these objects seems to imply a rapid transition between the CTTS and WTTS stages on a timescale of $\sim 10^5$ yr (Cieza et al., 2008). The dispersal of the disk is thought to be driven by a combination of accretion onto the star and magnetohydrodynamic (MHD) and photo-evaporative winds. MHD winds will be discussed in detail later in this chapter, but are mainly thought to play a role in dispersal from the inner disk during the earlier stages of evolution. Significantly, they are also a mechanism that can exert a torque on the star-disk system, and may dominate the evolution of angular momentum within the disk.

Photo-evaporation of the disk occurs due to high-energy (EUV or X-ray) radiation from the star heating the upper layers of the disk. This provides thermal energy to the gas which may escape if it is sufficiently far above the disk midplane. This results in a pressure-driven, centrifugally launched flow. While all these mechanisms may co-exist, accretion is likely to dominate the disk dispersal in the early stages, while at later times

photo-evaporation becomes dominant and rapidly clears the remaining disk (Alexander et al., 2014).

1.1.4 Jet Features in Young Stellar Objects

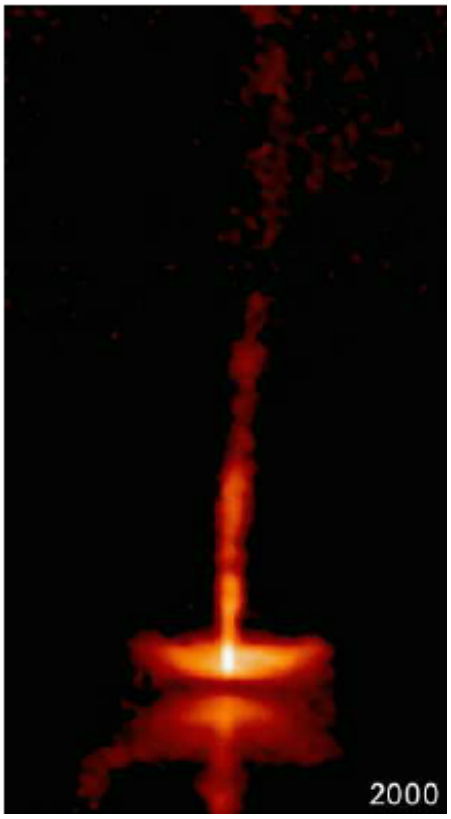

FIGURE 1.3: HST image of the HH 30 jet and disk, highlighting the geometry of the system with the jet launched perpendicular to the disk. Credit: NASA/ESA.

Alongside the signatures of accretion disks are often found bipolar jets and outflows. The connection between accretion and ejection/outflow features will be discussed further later in the chapter, but these collimated jets are ubiquitous features of accreting objects spanning all ranges of masses, from active galactic nuclei (AGN) (Mirabel & Rodríguez, 1999) to objects as small as brown dwarfs (BDs) (Whelan, 2014). Links have been shown between the presence of jets and indicators of accretion mechanisms, indicating a fundamental connection between accretion and ejection, and the occurrence of similar jet phenomena across such a broad range of objects is evidence for common accretion and ejection mechanisms at work.

Indeed, the large-scale signatures of protostellar outflows, in the form of Herbig-Haro (HH) objects, were identified before circumstellar accretion disks were identified (Herbig, 1950, 1951; Haro, 1952, 1953). These were observed as small patches of apparent nebulosity exhibiting continuum and optical line emission suggesting weak ionization

and hence a fast shock. Further observations in the 1970s showed that these knots were connected by optically visible linear structures which originated from young stars. As a more complete picture of the star-disk system emerged, it became clear that HH flows represented bipolar outflows launched perpendicular to the circumstellar disk. Knots and HH objects are signatures of the outflowing jet, formed either at a terminal bow shock where the jet encounters dense ISM material, or by internal shocks (see Section 1.3.3).

The common features of jets launched from all types of object include a bipolar morphology, high collimation along the jet axis, the presence of shocks and indications of episodic variations in velocity or mass outflow rates, which may be the result of variable accretion at the source. The jet is launched along an axis perpendicular to the accretion disk, as illustrated in Figure 1.3. In protostellar sources the primary winds or jets have typical velocities ranging from 10 km s^{-1} to 10^3 km s^{-1}. Individual jets exhibit a wide range of morphologies depending on the properties of their source and the environment into which they propagate, from well-collimated jets to bipolar lobes and wide-angle winds (Reipurth & Bally, 2001).

Protostellar outflows are thought of as having two main components, with a central atomic jet surrounded by a wider, slower molecular outflow. The central jet is narrow and highly collimated with typical opening angles of just a few degrees; this collimation is shown to occur soon after jet launching, with a typical opening angle before 50 au of 20-30°, followed by rapid collimation into a narrow beam. (Mundt et al., 1991; Hartigan & Morse, 2007) The jet is typically composed of atomic material with velocities of a few 100 km s^{-1} measured from radial velocities and proper motions; this component is optically bright, showing emission from atomic forbidden emission lines (FELs) excited by shocks with velocities of a few 10s of km s^{-1} (Raga et al., 1990).

Figure 1.4 illustrates the range of wavelengths from which jet emission can be seen, corresponding to regions with different excitation levels. As well as optical emission, they are detected in near- to far-IR emission tracing shocked gas and neutral atomic components; additionally, X-ray emission sometimes traces fast shocks within these jets (Bally, 2016). Atomic jets marked by chains of HH objects (see for example the HH 212 jet, shown in Figure 1.5) can extend over several parsecs, with angular extents of several degrees (Ogura, 1995; Reipurth et al., 1997; Bally et al., 2012).

In contrast, molecular outflows are less collimated and exhibit lower velocities on the order of 10 km s^{-1}. These may consist of material swept up and entrained by the inner jet, and they carry most of the outflowing mass and momentum. Low-J transitions of CO trace these outflows, with higher-J transitions of SiO, H_2 and H_2O highlighting more accelerated, warmer gas (Frank et al., 2014).

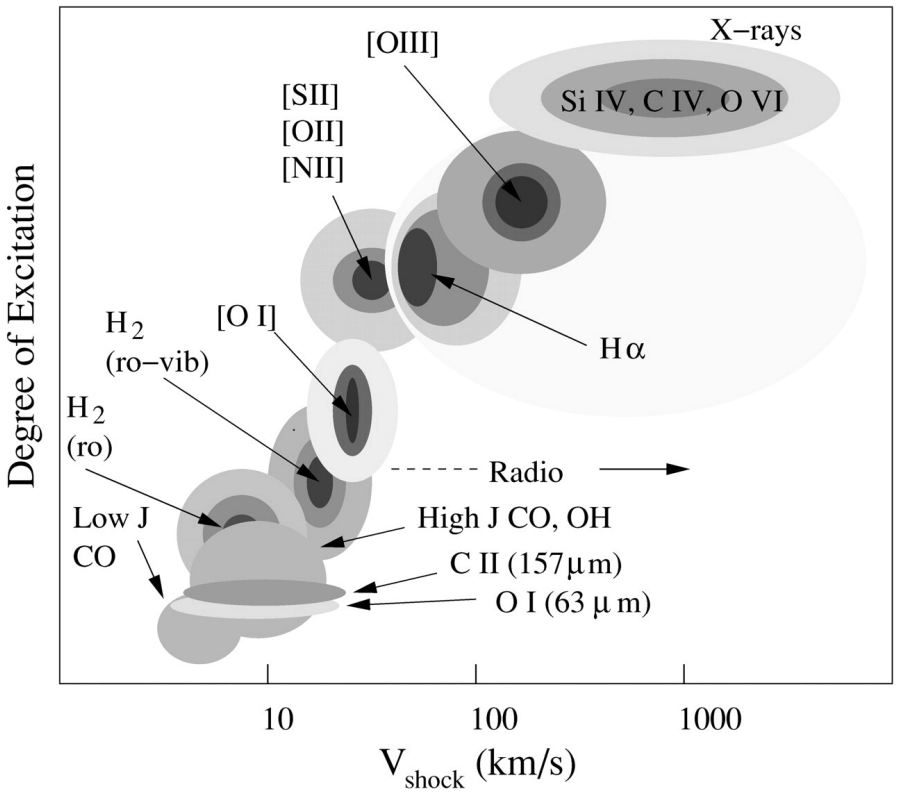

FIGURE 1.4: Chart showing the range of emission wavelengths observed in jets, with the corresponding excitation levels of the regions they trace, from Reipurth & Bally (2001).

High-velocity CO also traces the edges of a wide-angle cavity that forms around the outflow. This is in part formed by the terminal bow shock of the jet and the outer components entraining and sweeping up material from the surrounding cloud; however sideways 'splashing' from internal shocks also transfers momentum to the surrounding gas and causes it to be displaced. Both fast jets and slower, wider winds transfer momentum outward from the star, with emission in sub-mm CO lines probing the mass and radial velocities of entrained gas, allowing estimates of the momentum which is fed back into the surrounding cloud (Arce et al., 2010, 2011, 2013).

While the jets observed across all protostars have many characteristics in common, distinct trends can be identified as the star evolves. Class 0 outflows are primarily molecular flows traced by H_2, CO, and SiO emission, with typical extents of less than 1 pc. However, they are also very dense with $n_{H_2} \sim 10^4$ - 10^7 cm^{-3} and thus have high mass outflow rates. Jets from Class 0 and I sources are generally denser and cooler (temperatures ranging from a few 10 K to 1500 K) than those of CTTS sources, and show substantially lower ionization fractions (Nisini, 2009; Frank et al., 2014; Bally, 2016). At this early stage they already show the collimation and knotty structures characteristic of jets, although only faint HH objects are observed.

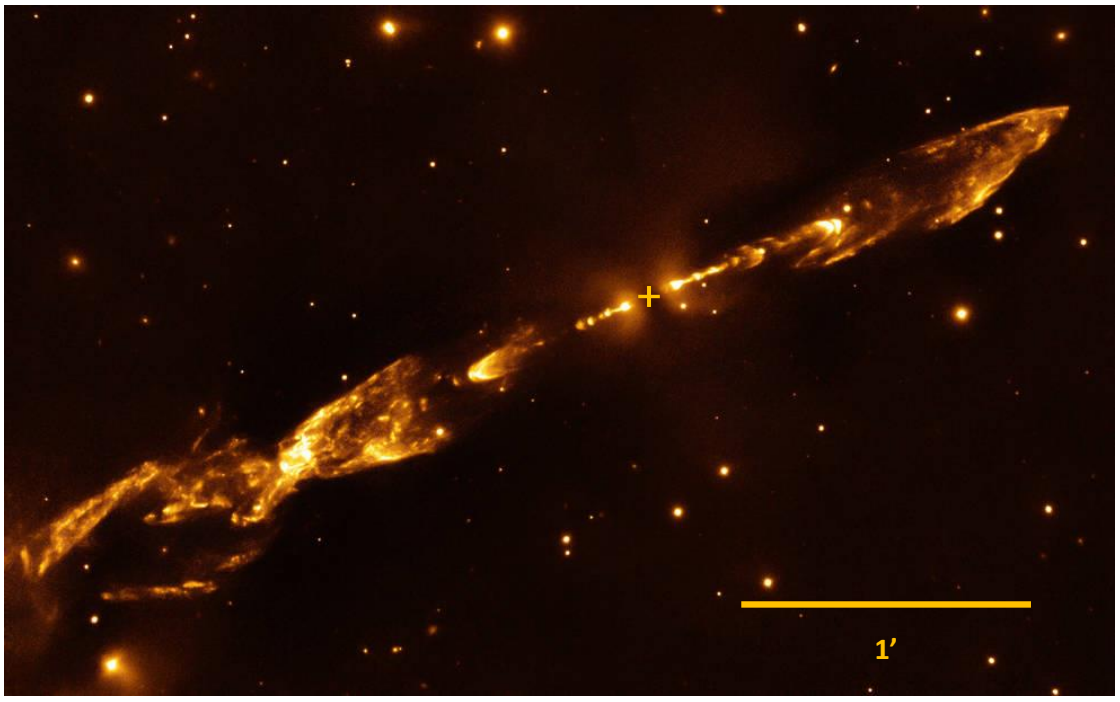

FIGURE 1.5: The Class 0 jet HH 212 observed in narrow-band imaging of the H_2 2.122 μm emission line, showing both jet lobes marked by HH objects. The approximate position of the protostellar source is indicated with a yellow cross within the dark region in the image centre, within the edge-on disk. The jet was imaged with the Infrared Spectrometer and Array Camera (VLT/ISAAC). Credit: ESO/M. McCaughrean.

More evolved Class 0 jets show the typical high-velocity inner jets surrounded with slower, wide-angle molecular lobes, within a low-density cavity containing slow winds and shocked material. As the star transitions to Class I, the outflow power and momentum output through the jet decline, at the same time as the primary winds become faster, more ionised, and primarily atomic. Over time the flows can punch out of the surrounding molecular clump and deposit mass and momentum into the surrounding medium, with prominent HH flows seen emerging from the cloud. The surrounding cavity is inflated by wide winds and the jet bow shocks, and expands outward, potentially forming additional low-velocity shocks along the cavity walls (Arce & Sargent, 2006; Arce et al., 2007; Frank et al., 2014).

Still more evolved Class I and II jets are dominated by the fast atomic component, with emission from H I and FELs from metals with low ionisation potential. They typically show velocities of 100 - 400 km s^{-1}, with lower densities ($n_H \sim 10^2$-10^4 cm^{-3}). As the star evolves further to Class II, the jet becomes fainter, with molecular emission diminishing. The overall mass outflow rate declines throughout the lifetime of the jet: typical mass outflow rates for the primary jets drop from 10^{-6} $M_\odot$ yr^{-1} in Class 0 jets to 10^{-7}-10^{-8} $M_\odot$ yr^{-1} for Class I and CTTS sources, as the star approaches the

end of its accreting phase (Hartigan et al., 1995; Podio et al., 2006; Antoniucci et al., 2008; Podio et al., 2015).

1.2 Accretion and Ejection

This section will primarily be concerned with our current theoretical models for the origins of jets and their connection to the star-disk system. That collimated outflows are connected to the processes of accretion from a disk is well-established, and this seems to hold not only for protostellar outflows but also for much larger scale jets, e.g. those launched by X-ray binary sources and active galactic nuclei (AGN) (Mirabel & Rodríguez, 1999). In YSO jets in particular, not only are jets *only* observed from sources which are actively accreting from a disk, but signatures of accretion luminosity are well correlated with the FEL luminosity observed from the atomic jets. Further, across all mass scales, the typical jet velocities closely track the escape velocity of the jet source, suggesting that most of the traced mass is ejected from the inner regions of the accretion disk (Livio, 2009).

In order to examine how jets are launched, then, this section will first review the process of magnetospheric accretion, before looking at how the major models of jet launching and the main observational results needed to constrain or rule out the different possibilities.

1.2.1 Magnetospheric Accretion

The transfer of mass between the circumstellar disk and the central protostar is understood as a process of magnetospheric accretion, which comes about via the interaction of the magnetic fields of the star and the inner disk (Alencar, 2007; Ardila, 2007). Mass is transported radially inward through the disk (requiring it to lose angular momentum in the process). Accretion occurs at the inner truncation radius of the disk, where the magnetic pressure of these fields overcomes the ram pressure due to accreting material. This results in captured gas being channelled along the magnetic field lines in funnel flows (illustrated in Figure 1.6) which form infalling accretion columns with roughly freefall velocities of a few 100 km s^{-1}, and densities $n_H \sim 10^{12}$ cm^{-3} (Hartmann et al., 1994).

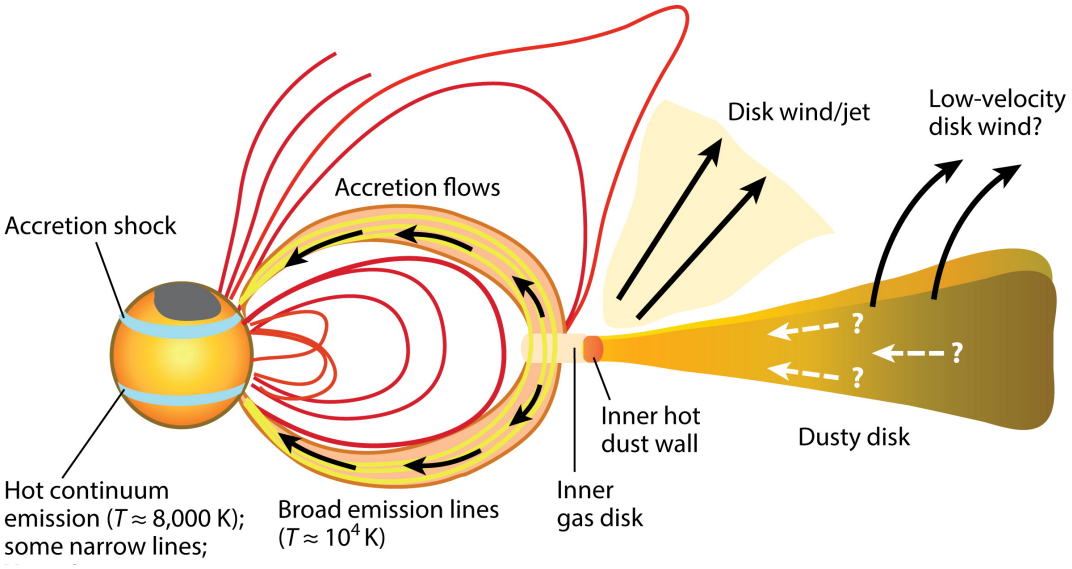

FIGURE 1.6: Overview schematic of accretion and jet launching models, from Hartmann et al. (2016).

When the infalling material reaches the stellar surface, a J-shock[2] occurs, and the conversion of kinetic to thermal energy heats the gas to temperatures as high as 10^6 K. The radiation from the shock directed toward the stellar surface (the radiative preshock) causes photospheric hot spots of 0.5 - 1 $\times$ 10^4 K.

The validity of these models is supported by the strong, predominantly dipolar magnetic fields detected from CTTSs, with sufficient field strengths at the truncation radius (equal to a few stellar radii R_*) to disrupt the disk (Johns-Krull et al., 1999; Symington et al., 2005; Alencar, 2007). The structure of the accretion columns and shocks is inferred from the spectral signatures of the different components. Typical CTTS spectra show optical and IR emission lines with an 'inverse P Cygni' profile, combining strong, broad emission with a red-shifted absorption component, the width of which indicates the bulk motion of material at several 100s of km s^{-1} and is a signature of infall in accretion columns (Edwards et al., 1994). Additionally, the veiling or filling-in of absorption lines from around the star is observed, and can be attributed to excess UV and optical emission from the accretion shock where the infalling material reaches the stellar surface (Calvet & Gullbring, 1998). The Hα line may be used to estimate mass accretion rates, however this emission comes from a complex and dynamic region which also contains, for example, Hα emission from stellar winds. The strong spectral and photometric variability of CTTSs can also be attributed in part to the modulation of accretion signatures by stellar rotation (Giampapa et al., 1993; Johns & Basri, 1995).

[2]A J-type shock or 'J-shock' is characterized by a discontinuity or 'jump' in shock velocity, temperature and density at the shock front due to strong heating by ion-neutral collisions (Draine & McKee, 1993).

These spectral features mean that when trying to measure the accretion rate onto a star, there are a number of possible signatures which can be used including the infrared (IR) excess (due to reprocessing of the accretion radiation in the disk), the ultraviolet excess and the degree of absorption line veiling. Additionally, the accretion rate can be estimated using the observed correlations between these features and the optical emission line intensities, a method which we will examine in more detail in Chapter 5 (Alcalá et al., 2014; Nisini et al., 2018).

Ideally, making an accurate determination of accretion rates requires examining multiple accretion signatures from different wavelength bands, as different signatures probe different accretion regimes. For example, the IR excess is produced by the dissipation of accretion energy by the surrounding disk. However, it includes contributions from other sources such as reprocessed light from the star itself, and the difficulty of isolating these contributions poses difficulties in using this as a measure of accretion rates. The ultraviolet excess is somewhat better in that it results primarily from the accretion shock formed where material infalling along stellar magnetic field lines meets the photosphere at a boundary layer. In practice, considerations such as the geometry of the system (e.g. whether the disk is at an inclination which allows the stellar spectrum to be observed directly) mean that different signatures will be feasible to use when studying individual objects.

1.2.2 MHD Models of Jets

Accretion disks are supported by differential rotation at close to Keplerian velocities at each radius, with the inner edge of the disk coupled to the stellar magnetic field (Bally, 2016). The connection between the star and disk offers a mechanism to regulate the stellar spin and slow down its rotation (Königl, 1991; Zweibel et al., 2006). However, the removed angular momentum then needs to be transported elsewhere, and horizontal transport through the disk has been shown to be too inefficient to account for this. An answer to this problem is provided by MHD centrifugal acceleration models (Blandford & Payne, 1982; Pudritz & Norman, 1983) which suggest the excess angular momentum is transported vertically by particles carried along open magnetic field lines.

This in turn gives rise to MHD models of jet launching, where jets and outflows carry angular momentum away from the star-disk system and exert a braking torque, accounting for the low rotational speeds observed in young stars. The general model is based on the presence of a large-scale open magnetic field, anchored in a rotating object such as a star or accretion disk. This field controls the accretion of ionized material from the inner disk, with a portion of the material accreted along the field lines while the rest

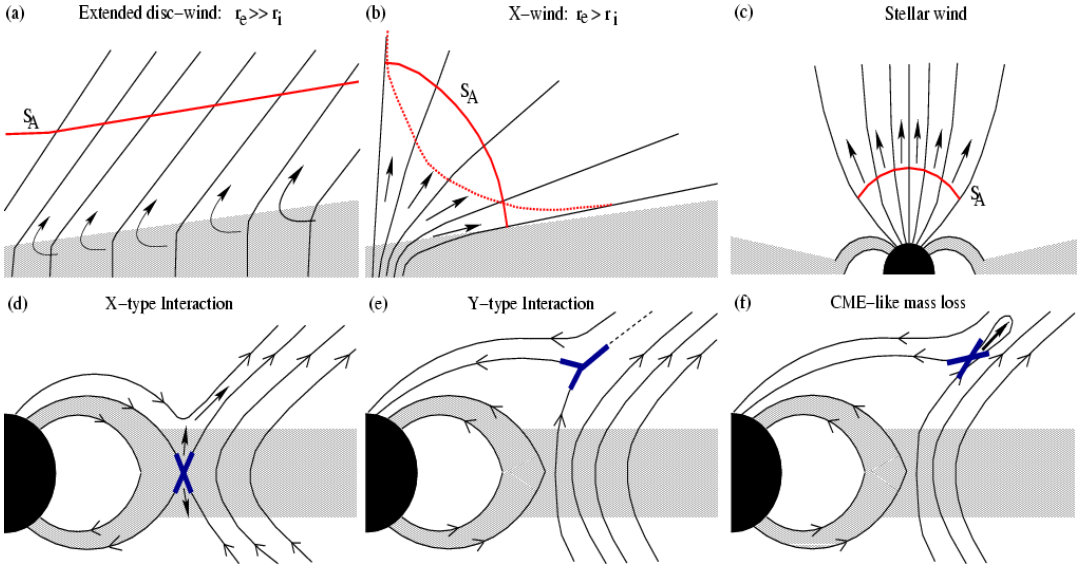

FIGURE 1.7: Models of jet launching from Combet & Ferreira (2008). The upper panels illustrate several proposed models of steady jet launching, while unsteady processes are shown in the lower panels.

is accelerated along the magnetic field lines by a combination of Lorentz and centrifugal forces, eventually becoming super-Alfvénic. The removal of angular momentum is then a 'loss-free' process, in which most of the rotation energy is transferred to wind kinetic energy (Cabrit, 2007).

The common features observed across jets from sources across a wide range of masses and evolutionary stages supports the existence of a common mechanism (or set of mechanisms) for jet launching. The precise nature of these mechanisms is still unclear, however, and a number of possible scenarios have been proposed (Dougados, 2008; Edwards, 2008). The major MHD models for the origins of the jet are distinguished primarily in the source of the outflow mass lost to the jet, i.e., where the jet is launched from, and the exact type of interaction between the star and disk magnetic fields which produces this collimated jet outflow. Figure 1.7 shows sketches of several of these models and will be referred to throughout this discussion.

The primary scenarios to consider are the disk wind and X-wind models. Disk wind (or 'D-wind') models (Ferreira, 1997; Pudritz et al., 2007) place the jet origin in magnetic field lines anchored in a relatively broad range of radii (up to several au) within the disk (see the upper left panel of Figure 1.7). These field lines originate from the parent cloud and become compressed as the stellar core collapses, becoming pinched and twisted by rotation. Convection and shearing within the disk result in a helical magnetic field configuration. Charged particles from the upper layers of the disk are then accelerated outward along the open field lines, forming a jet. Fast components

with velocities $\sim$ 100 km s^{-1} are launched from radii close to the star $\sim$ 1 au, with slower outflow components being launched from greater distances.

Such a model implies a greater degree of interaction with the disk, making it particularly relevant to the question of whether the jet affects disk evolution. It also enables a high ratio of jet to accretion power and allows the wind to extract most of the angular momentum needed from the outflow. This is because the jet mechanical power approximately equals the rate of energy removal between the inner and outer launch radii, and this can easily reach the high efficiencies observed. The final jet velocity depends on the magnetic lever arm parameter λ, the ratio of extracted versus initial specific angular momentum. From Ferreira et al. (2006):

$$\lambda = (\frac{r_A}{r_0})^2 \tag{1.1}$$

where r_0 is the launch radius and r_A is the cylindrical Alfvén radius). (See Section 1.3.1 regarding estimates of λ from jet poloidal and toroidal velocities.) The final jet velocity in this model is then:

$$v_j = \sqrt{\frac{GM_*}{r_0}}\sqrt{2\lambda - 3} \tag{1.2}$$

Observations of low-mass YSOs suggest moderate lever arms $\sim$4-18 (Ferreira et al., 2006). In this model the lever arm parameter is inversely related to the efficiency of mass loading onto field lines ($\xi \simeq 0.1$). This implies a lower limit to the one-sided ejection to accretion mass loss rate of:

$$\frac{2\dot{M_{out}}}{\dot{M}_{acc}} = \xi \ln(\frac{r_{out}}{r_{in}}) \tag{1.3}$$

Here r_{out} is the outer limit of the launching radius and r_{in} approximately the corotation radius ($\sim$ 0.1 au). If $\frac{r_{out}}{r_{in}} \sim 10$ in the region where the optical jet is launched, then this is consistent with observations of a typical ratio $\dot{\mathrm{M}}_{\mathrm{out}}/\dot{\mathrm{M}}_{\mathrm{acc}} \sim$ 0.01 - 0.1 (Cabrit, 2007). The mass loss through the disk wind need only be a few percent of the mass accretion rate, as a small fraction of the outflowing gas can effectively remove most of the disk angular momentum. This model implies extraction from an extended region and hence a large flow footprint. Much effort has been devoted to models of MHD disk wind launching, investigating the conditions required to produce a jet and the interactions with the underlying disk (see Ray & Ferreira (2021) and references therein) with 3D simulations advancing to models of accretion and jet launching in single and binary systems (Sheikhnezami & Fendt, 2015, 2018).

X-wind models (Shu et al., 1994; Camenzind, 1990; Cai et al., 2008) also suggest that the jet originates in open stellar magnetic field lines anchored in the disk. However,

in this case they are field lines from a relatively small region near the inner truncation radius of the disk, around 0.05-0.5 au, (see the centre upper panel in Figure 1.7). Material from this region is centrifugally accelerated as a wide angle wind, with the magnetic torque from the anchor point and the X-wind acting to spin down the star (Shu et al., 2000; Pudritz et al., 2007; Shang et al., 2007). In these models angular momentum is lost only from the inner boundary of the disk, which requires an additional mechanism to transport the material to the truncation radius. What this mechanism might be is unclear. Additionally, compared with the D-wind scenario, these models predict a higher poloidal jet velocity and smaller rotation signatures in outer regions of the jet. Predictions from X-wind calculations have proven inconsistent with star-disk simulations based on MHD turbulence (Ferreira & Casse, 2013), as well as the observed jet velocities, which show a sharp radial decline away from the jet axis (Ray & Ferreira, 2021).

While these are the primary models which are often compared with jet observations, a few other mechanisms for jet launching have also been considered. Stellar wind models also work on the basis of a a steady ejection process (Sauty et al., 1999; Matt & Pudritz, 2005). As the name implies, these place the jet origin in MHD winds flowing along open field lines from the star itself (e.g. upper right panel, Figure 1.7). In more recent Accretion Powered Stellar Wind models, a fraction of infalling material is then deflected and ejected by a combination of thermal pressure and turbulent pressure from Alfvén waves, both produced in the magnetospheric accretion shock. This produces an enhanced stellar wind which removes angular momentum along open magnetic field lines connected to the stellar surface, which contributes to the braking of the star (Matt et al., 2012; Ray & Ferreira, 2021).

However, this type of outflow would require a very high conversion efficiency to kinetic energy in order to match observed jet mass-fluxes (Ferreira et al., 2006). Additionally, large amounts of energy are required to power both this wind and the observed radiation from the accretion shock; this implies a correspondingly higher mass accretion rate and spin-up torque which is difficult to balance with the amount of angular momentum the stellar wind can remove (Ray & Ferreira, 2021). Therefore such stellar winds are generally not expected to account for the majority of the mass outflow observed. A number of models also invoke unsteady ejection scenarios (Ferreira et al., 2000; Zanni & Ferreira, 2013) through magnetospheric field lines (e.g. the reconnection X-wind (ReX wind) and CME-type loss models, shown in the lower panels of Figure 1.7). Although these ejection models are effective at providing a spin-down torque on the star and disk, the ballistic propagation of the ejected plasmoids does not reproduce the observed YSO jets well by itself (Ray & Ferreira, 2021).

At present, the evidence from observations of jets as well as the theoretical considerations favor a D-wind model as the primary origin mechanism of YSO jets. However, it is very likely that more than one of these mechanisms may be at work in jet launching, with more than one ejection site contributing to the observed outflows: for example, a sporadic ReX wind combined with a steady stellar or X-wind, surrounded by a wider disk wind (Ray & Ferreira, 2021). Not only are disk winds by themselves unable to directly spin down the central star, but many jets show multiple components with a fast, highly collimated inner core surrounded by a slower wide-angle component. It may be the case that these reflect origins in separate regions or contributions from multiple launching processes (Frank et al., 2014; Bally, 2016).

1.2.3 Collimation

One of the most consistent features of protostellar jets at all stages is their collimation, as mentioned in Section 1.1.4. High-resolution observations of CTTS jets in optical emission lines show jets to have a typical large opening angle of 10-30° within 30-50 au of the source, before undergoing rapid collimation such that after about 100 au the jet opening angle is narrowed to just a few degrees, with a width of roughly 10-40 au at 50 au from the source (Ray et al., 2006; Frank et al., 2014). The same properties have been shown for Class 0 and I sources traced in molecular and mid- to near-IR emission (see for example Cabrit (2007); Davis et al. (2011). This implies that a universal mechanism is required to collimate jets from the earliest stages.

These observations impose some constraints on models of jet launching. They imply a launching region for the optical jet no more than a few au in diameter, with an initial opening angle consistent with the Mach angle for a supersonic jet, and collimation into a unidirectional flow after 50 au (Cabrit, 2007). The jet beam must align with the disk axis, with observed precession no more than a few degrees on short (< 10 year) timescales. The collimation properties of these jets do not appear to change at different evolutionary stages, and therefore collimation cannot rely on the presence of an infalling envelope.

Such constraints have effectively ruled out non-MHD mechanisms of collimation. Thermal disk pressure in older class II objects is insufficient to focus the jet beam, as gravity is now dominated by the star rather than the disk. Pressure from the ambient medium would require very high densities in order to refocus the shocked wind in less than 50 au, with pressure on the same order as the wind ram pressure. The extinction due to such high densities would be a factor of 600 greater than that observed in jet-bearing YSOs (Cabrit, 2007).

External magnetic pressure has also been considered as a possibility; however, this would require a high percentage (2-20%) of the initial core poloidal flux to be retained in the inner 50 au and this is not possible taking into account losses to the star and field diffusion (Cabrit, 2007). Turbulent magnetic pressure would also require a high energy density with a large-scale magnetically-dominated turbulent region, and there is no clear source that would produce this.

As a result, the most plausible mechanism for focusing the jet is MHD self-collimation. As touched upon above, MHD disk wind models describe a wind launched along a magnetic field anchored in a rotating object, with a non-zero current across the magnetic surfaces. Just above the disk, the magnetic energy of the poloidal field exceeds the kinetic energy of the poloidal outflow, so that the plasma follows the magnetic field and this enforces co-rotation. Past the Alfvén point, the inertia of this wind drags behind and winds up the field lines into a hoop-like structure, producing a strong toroidal component in the magnetic field. From Tsinganos (2007), the poloidal field strength B_p is described by:

$$B_p = \frac{B_0}{R^2} \tag{1.4}$$

where B_0 is the field strength at the jet base and R is the radial distance from the star. Its ratio to the azimuthal field B_φ is described as:

$$\frac{B_\varphi}{B_r} = -\frac{\Omega}{v_0}\bar{\omega} \tag{1.5}$$

where Ω is the angular frequency of the rotating body and $\bar{\omega}$ is the distance from the jet axis.

As a result of this the azimuthal magnetic field strength increases at points farther from the rotation axis, dominating the poloidal field at around the Alfven radius ($r_A = \sqrt{\lambda r_l}$, where r_l is the launching radius). The Lorentz force that results thus points toward the polar axis. As centrifugal forces, thermal and magnetic pressures are negligible, and magnetic tension decreases toward the axis, this results in the poloidal field lines bending toward the central axis and collimating the magnetic surfaces via hoop stress. A cylindrical core is thus formed in a process which depends on the magnetospheric rotation. Models which are based on a disk wind have the advantage that the launching mechanism itself adds a toroidal field to the outflow, substantially reducing the required poloidal field strength for collimation (by two orders of magnitude) (Meliani et al., 2006).

The jet collimation then depends on λ and the field strength B_p at the disk surface. Models of collimation based on truncated MHD disk winds have been able to reproduce

atomic CTTS jet widths with a launching radius of 0.1-1 au (Stute et al., 2012). However, when comparing this model with observations, it should be noted that the optically visible jet may only represent the densest axial regions of the flow. It is possible then that surrounding wider-angle streamlines may be collimated over a larger distance, though this would depend strongly on the mass-loading of the outer winds.

1.3 Observations of Jet Features

In this chapter we have so far examined the context of star formation in which jets arise, and the primary theory around their launching and connection to the star and accretion disk. In this section we review some of the important features of jets which are seen in observations and how these are connected to both the jet origins and their propagation through the surrounding environment.

1.3.1 Jet Rotation

A key prediction of both D-wind and X-wind models for jet launching is rotation of the jet around the outflow axis as it transports angular momentum from the star-disk system. It should therefore be possible to detect signatures of rotation just beyond the region where the jet is accelerated, in the form of systematic shifts in radial velocity across the jet beam. Assuming launching from an axisymmetric, stationary magnetocentrifugal wind, measuring these shifts would further make it possible to estimate the specific angular momentum of the jet rv_ϕ, the launching radius $r_l = rv_\phi/v_p^2$ and the magnetic lever arm $\lambda = rv_\phi v_p$ (Anderson et al., 2003; Ferreira et al., 2006). Determinations of the jet launching radius are naturally of major importance by themselves, since this is the most obvious distinguishing factor between the various models, with stellar wind models predicting distances of a few stellar radii, X-Wind models predicting distances of around 0.05-0.5 au, and radii up to a few au for disk-wind models. Distances this small cover a few tens of milli-arcseconds at most and thus require extremely high spatial resolution for direct observation. Searching for transverse velocity shifts therefore offers a way to constrain several key parameters and serves as an important test of the launching models.

Several studies have sought to detect and measure rotation signatures close to the jet base. Observations investigating such rotation can focus on different wavebands to probe different layers of the flow, with near-ultraviolet (NUV) emission from layers close to the jet axis, optical emission farther out, and NIR emission from outer layers; we would expect then to observe faster rotation close to the jet centre (Woitas et al., 2005).

This is a very technically challenging task, requiring both high spatial and spectral resolution at the limits of currently available instruments. Nevertheless, a number of studies have identified transverse velocity gradients in a growing number of objects (Bacciotti et al., 2002; Woitas et al., 2005; Coffey et al., 2004, 2007). IFS techniques have played a role here as 'pseudo-IFS' observations (discussed further in Section 1.5.2) are used to obtain transverse cuts of the jet to search for these gradients. Typical velocity shifts are on the order of 10-20 km s^{-1}. The derived toroidal and poloidal velocities imply jet footprints between 0.1 au and 3-5 au, with moderate values of $\lambda \leq 10$, consistent with the observed ratio of mass outflow and accretion; further, the inferred toroidal magnetic field dominates over the poloidal field as expected for collimation via hoop stress, so that the results overall support a warm steady disk wind scenario (Bacciotti, 2009). On the other hand, this technique samples only the outer streamlines of the jet, and thus does not fully exclude an inner stellar or X-wind component (Frank et al., 2014).

Some puzzling results have also been found, for example the initally detected counter rotation between the jet and disk observed in RW Aur (Cabrit et al., 2006) and inconsistent later findings (Coffey et al., 2012). It is possible that the toroidal velocity signatures may be expected to temporarily reverse (Sauty et al., 2012), which may present a complicating factor in identifying jet rotation. Additionally, detecting these small velocity shifts falls at the limit of current instrumentation, and the results require careful analysis to disentangle signatures of rotation from other factors that could also cause an asymmetric velocity shift, for example asymmetric shocks, precession, or interaction with a warped disk (Cerqueira et al., 2006; Frank et al., 2014). As instrumentation advances, future high-resolution observations will increase the likelihood of eliminating these alternatives and search for jet rotation within the inner 100 au of the flow.

1.3.2 Low and High Velocity Jet Components

High-resolution spectra of YSO jets in both molecular and FEL emission have revealed multiple velocity components arranged in an 'onion-like' structure, with an apparent core of high-velocity, tightly collimated gas surrounded by a wider-angle low-velocity flow (Bacciotti et al., 2000; Beck et al., 2007; Coffey et al., 2008; Pyo et al., 2009; Whelan et al., 2021). In position-velocity maps (or PV maps) these appear as a drop in velocity toward the edges of the jet (Agra-Amboage et al., 2011).

In spectra of the jet we also observe a double-component velocity structure (first identified by Kwan & Tademaru (1988)), with a high-velocity component (HVC) at > 100 km s^{-1} and a low-velocity component (LVC) at less than 100 km s^{-1}, as

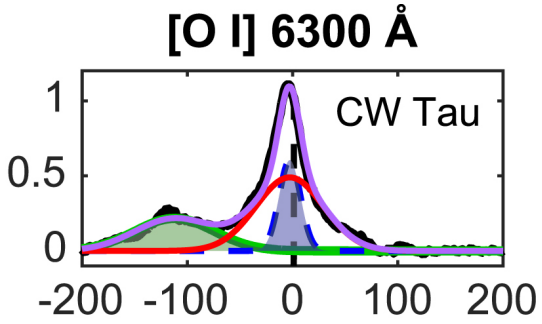

FIGURE 1.8: Example of high-velocity and low-velocity components (HVC and LVC) in the [O I]λ6300 of the CW Tau jet, from Simon et al. (2016). Flux is shown on the y-axis and wavelength in Å on the x-axis. The original spectrum is shown by the black line, with the fit to the HVC in green. The LVC shows two components, a narrow component (shaded blue region) and a broad component (shown by the red line). The purple line marks the total fitted model.

illustrated in Figure 1.8; in many spectra the LVC can be further differentiated into a broad component (FWHM $>$ 40 km s^{-1}) and a narrow component (FWHM $<$ 40 km s^{-1}) (Simon et al., 2016; Fang et al., 2018; Banzatti et al., 2019; Whelan et al., 2021). The LVC is less excited and extends only to about 50-80 AU from the source before disappearing gradually. In contrast, the HVC is associated with the extended jet and shows greater collimation, with velocities of a few 100 km s^{-1}. Spectroastrometric analysis shows that while the HVC initially rises in velocity with distance from the source, consistent with expectations for an accelerating jet, the LVC demonstrates the opposite behaviour, with a drop in velocity at increasing distances corresponding to what would be seen for sampling the streamlines at increasing disk radii (Whelan et al., 2021). Together this evidence suggests that the HVC is launched from a region within 0.05 au of the source while the LVC originates from a broader footprint at 0.1 - 4.5 au.

It is unclear if these two components represent origins in separate disk regions or launching mechanisms. The components appear distinct under long-slit spectroastrometry (Whelan et al., 2021), and there appears to be a smooth transition at the boundary between them with the LVC velocity rising closer to the outflow axis (Bacciotti et al., 2000; Giannini et al., 2019). The limited signatures of shocks and interaction between components argues against an X-wind model (Frank et al., 2014) and the observed drop in velocity near the jet edges is consistent with an MHD disk wind being launched from a range of disk radii. These features may therefore lend support to a two-component model comprising a stellar magnetospheric wind sheathed in a wider MHD disk wind.

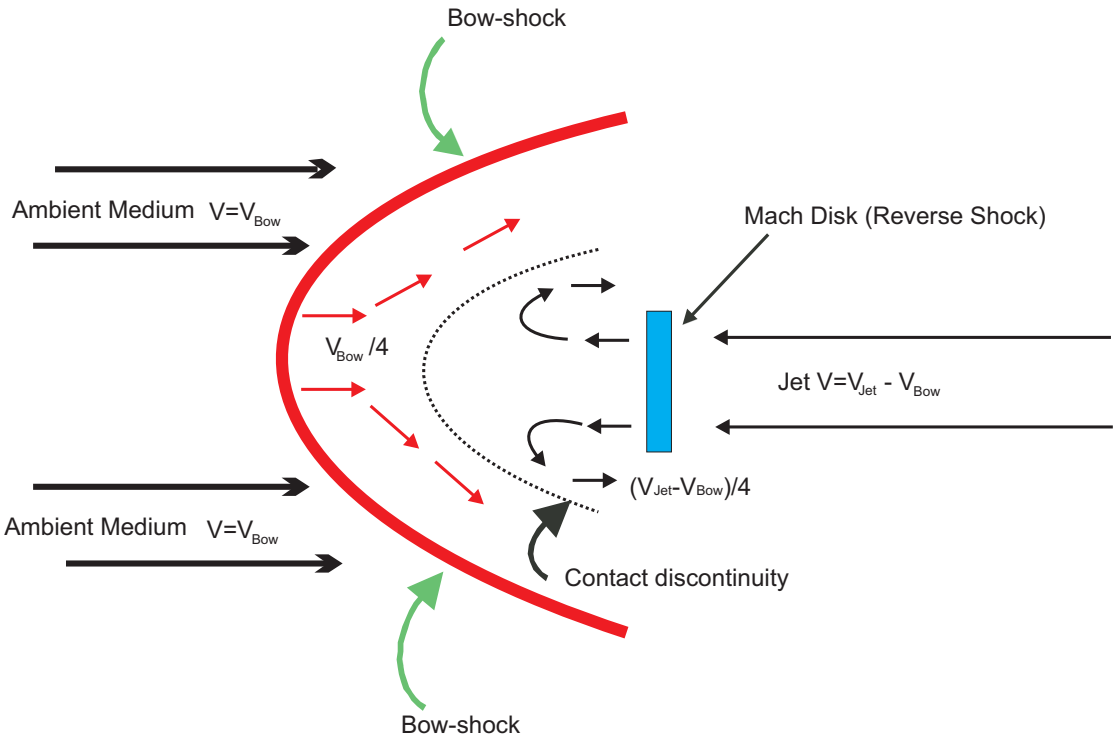

FIGURE 1.9: Diagram illustrating the two-shock model, highlighting the separation between the forward shock where the jet material impacts the ambient medium, and the Mach disk which acts on the jet material behind the shock. Kindly provided by E. Whelan.

1.3.3 Knots and HH Objects

HH flows were the first signatures of jets to be detected (Dopita et al., 1982; Mundt & Fried, 1983). They appear as small (20-30"or less) nebulae with high proper motions, often arranged in pairs or chains which may be curved in trajectory (due to deflection or precession of the outflow axis) (see for example Hartigan et al. (2019)). While some are clearly associated with well-collimated jets and have classical bow-shock morphologies, they can also be found in chaotic arrangements depending on the propagation environment and the ejection properties of the source. The objects described as 'knots' in a jet may be roughly considered as falling into two categories: the high-excitation HH objects formed as the jet interacts with the surrounding environment, and the internal knots found closer to the source, with smaller separations between them; the processes responsible for their formation are unclear, however. We distinguish also between bow shocks where the jet rams into a slower medium, and 'internal working surfaces' formed where faster-moving gas overtakes slower elements of the flow (Raga et al., 1990).

HH objects trace the primary jet or wind, and generally show decreasing velocities (measured via proper motions and radial velocities) with increasing distance from the source (Devine et al., 1997). The gaps between these shocks also increase with distance,

indicating periods on the order of 100s of years between ejections. Combined with their high excitation, indicating high shock velocities, this suggests that they represent large-amplitude variations in ejection velocity and mass outflow rates (Raga et al., 2002) and may be an indicator of episodic accretion. They may also represent changes in the ejection direction or collimation of the jet (Reipurth & Bally, 2001).

The bow shocks which form at the head of the jet can be described using a 'two-shock' model, illustrated in Figure 1.9. This comprises a 'forward shock' where the pre-shock ISM is accelerated, heated and compressed by the oncoming jet, and a 'reverse shock' or 'Mach disk' where the outflow is in turn decelerated, heated, and compressed. The immediate post-shock region is characterised by high temperatures of 10^4 - 10^7 K and collisionally ionised H. Behind the shock is a cooling region where the excited gas radiates and cools, with the cooling time and length (the separation between the shock and radiating region) correlated positively with the shock velocity, and inversely with the gas density (Bally, 2016). As a result, denser gas cools more rapidly, tending to increase any density fluctuations in the post-shock gas which can cause fragmentation into dense clumps.

FEL emission from species such as O, S^+, and N^+ is enhanced in the cooling region as compared with ionised H, they can be collisionally excited many more times before recombination. A stratification can also be seen in high-resolution observations, with emission lines from higher-ionization species such as O^{++} peaking closer to the bow shock than less-ionized species like S^+ (Schwartz et al., 1993; Heathcote et al., 1998; Hester et al., 1998). The shock front itself is traced by recombination lines of H including strong Balmer line emission. If the shock velocity exceeds about 60 km s^{-1} it may form a thin zone radiating only in H recombination lines, which appear as 'Balmer filaments' extending around the shock front. Faster shocks with velocities greater than 100 km s^{-1} will also emit UV radiation ahead of and behind shock, ionising and heating the surrounding gas further, and X-rays may even be produced in very fast shocks $>$ 400 km s^{-1}.

The smaller shocks found closer to the source (often in groups) show much lower shock velocities (significantly lower than the flow velocity). Typically these form compact knots with low-excitation spectra, supporting shock velocities of only a few 10s of km s^{-1}. They are ejected on timescales of a few years, and may represent much smaller amplitude variations in the ejection velocity (i.e. on the order of 30-40 km s^{-1}, corresponding to the observed v_{shock}) (Raga et al., 1990; Raga & Noriega-Crespo, 1998).

On the other hand, it has also been proposed that they may result from hydrodynamic or MHD instabilities in the jet flow, for example shocks caused by Kelvin-Helmholtz instabilities. In each case, different internal structures would be predicted

(Micono et al., 1998), or alternatively the two models make different predictions for the spatial profiles and knot proper motions as they travel outward from the source (Caratti o Garatti & Eislöffel, 2009). However, applying either of these tests requires high-resolution observations (< 1"), and accurately measuring knot proper motions requires multiple observations with baselines of several years.

1.3.4 Asymmetric Jets

Where both lobes of the bipolar jet can be observed, approximately 50% of CTTS jets show marked asymmetries between the red and blue-shifted jets, in parameters such as their velocity, collimation, ionisation, or the number and spacing of any knots observed (Hirth et al., 1994; Woitas et al., 2005; Agra-Amboage et al., 2011; Podio et al., 2011). Similar asymmetries have been observed in jets from Herbig stars (Ellerbroek et al., 2014).

Asymmetric jets are of particular interest since the source properties (e.g. stellar mass, disk truncation radius) are the same for both sides of the jet, meaning that the cause of their differing properties is disentangled from these parameters. These jets can therefore offer insight into the launching process and the parameters which affect it. For example, Woitas et al. (2005) show that the asymmetries in the RW Aur jet lobes imply differing launch footprints on each side, with more tightly-constrained toroidal magnetic fields in the blue-shifted lobe. The asymmetries could be caused by a disk wind launched from a disk with differing magnetic diffusivities or ionization properties on either face (Frank et al., 2014).

Additionally, the influence of the propagation environment must be taken into account, as this may also be asymmetric on either side of the source. Ellerbroek et al. (2014) show that while the HD 163296 jet lobes have asymmetric mass outflow rates, velocities and ionizations, they eject knots on synchronous timescales, and the velocity dispersion scales with the jet velocity in each lobe, suggesting a similar energy input into both. They suggest that environmental asymmetries may dominate in cases where the mass-loss rate is similar in both lobes, but in other cases the asymmetries may be intrinsic to the launching of each lobe.

1.3.5 Jet Precession

The shapes of jets show that their trajectory can change over time, with a wide variety of observations showing jets which bend or 'wiggle' over time, often traced by the extended chains of HH objects. There are several potential causes for this behavior: for example,

'C-shaped' jets may be caused by deflection via a strong side-wind from another star (Estalella et al., 2012). Alternatively, either these or 'S-shaped' jets (which suggest precession of the outflow axis) might be signatures of motion due to the orbit of a companion, with the symmetry of the jet lobes either side of the source indicating whether the dominant effect seen is precession or the orbital motion of the star (Masciadri & Raga, 2002).

Either scenario would predict substantially different companion orbits and masses (Masciadri & Raga, 2002; Anglada et al., 2007); however, identifying directly which model should be applied is often difficult as it is often only possible to observe one jet lobe close to the star (the red-shifted lobe is often obscured, or one lobe is much fainter or less extended than the other). Additionally, for apparent precession occurring over long timescales (hence long length scales) often only part of a cycle is observed and it is difficult to discern whether a periodic precession is at work. We will return to these models and their applications in much more detail in Chapter 4.

1.4 Motivations for Studying Jets

In this chapter we have already seen how models of jet launching are crucial to understanding how young stars are able to accrete mass while maintaining low rotational velocities, and how jets are therefore tied to both the accretion process and the evolution of the disk. Understanding this interaction thus lends insight into otherwise hidden aspects of the star-disk connection and the properties of the disk. By observing jets, we can place constraints on a number of important parameters, which can help to determine which mechanisms contribute to jet launching. The X-wind and disk-wind models both predict mass outflow rates comparable to the mass accretion rate, as well as winds which should rotate around the outflow axis (Bally, 2016). However, they also predict different thermal velocities, launching radii rates at which the jet removes mass and angular momentum from the star and disk.

Perhaps the most important properties to determine are the total jet density and the mass-loss rate through the jet. The current models are highly dependent on these parameters, and estimation of the jet density allows the mass fluxes through the jet to be estimated based on the velocity, radius and density of the jet. The radius, electron density and ionisation fraction can be estimated through imaging and line flux diagnostics as discussed in later chapters. However, determining the mass-loss ratio can be difficult due to challenges in estimating the mass accretion rate (Frank et al., 2014).

Signatures of transverse rotation can be used to determine the launch radius and hence estimate the disk location from which the jet is launched, as well as to estimate the outflow of angular momentum carried by the jet (Anderson et al., 2003; Ferreira et al., 2006; Coffey et al., 2004, 2007). Jet collimation can be constrained with measurements of the jet width (i.e. the full-width half maximum) and how this changes with distance from the source is a key parameter. Observations typically cannot resolve the inner jet within 15 au from the source, however the rapid collimation of the jets rules out purely hydrodynamical models and is consistent with disk wind models of moderate to high efficiency.

In addition, because the jet is linked to the magnetic field and activity of the central star, it can offer a means to probe the behaviour of a source which may be very embedded or otherwise unresolved. The periodicity and size of gaps between HH shocks may trace variations in the ejection velocity and mass outflows, implying episodic accretion (Kirwan et al., in prep.). They thus enable us to reconstruct histories of the stellar accretion and ejection on timescales of 10^4 - 10^5 years, a significant portion of the protostar's lifetime. A precessing or periodically wiggling trajectory in the jet may point to an otherwise undetected companion object and give clues to its mass and orbital properties as will be discussed in Chapter 4 (Masciadri & Raga, 2002; Anglada et al., 2007).

The disk wind model and supporting evidence indicating that the jet is launched from a region covering several au within the inner disk also suggests that the jet may impact the same regions in which terrestrial planets are likely to form (Whelan et al., 2021). Simulations of accretion with and without the presence of stellar jets indicate that the presence of a jet may cause significant changes in the disk density structure and transport processes (Combet & Ferreira, 2008). Efficient angular momentum removal due to an MHD wind could induce fast radial accretion, while X-rays from the jet base may impact chemical processing in the upper disk layers through heating and photo-evaporation. On the other hand, a dusty disk wind could also screen the disk from stellar X-rays and FUV radiation, while the thermal processing and fallback of dust grains from the jet may play a role in forming and redistributing chondrules within the disk (Frank et al., 2014).

On larger scales, jet-driven outflows of material propagate to large distances within the surrounding molecular cloud. The terminal shocks can then act as probes of the surrounding ISM and clump material, in particular regions with minimal CO emission. Analysis of emission from shock-excited material provides a way to study the ionisation, density and composition of the ambient medium.

The outflows themselves may play a significant role in driving the chemical and turbulence rejuvenation of the molecular cloud, as they sweep up gas from their parent

core and inject it back into the inter-clump or interstellar medium (Reipurth & Bally, 2001). Dissociation of molecules in shocks enhances the abundance of atomic and ionic species, while the delivery of momentum into the surrounding cloud may help to support the cloud against collapse. Along with other sources of turbulence (e.g. winds from giant OB stars) they may then help to explain the small star formation efficiencies of 0.01-0.1 typical for molecular clouds (McKee & Ostriker, 2007). Outflows may also help to limit star formation on smaller scales by unbinding gas from their parent cores and driving away material from accreting protostars. As a result, studying jets can help us to understand not only the process of stellar formation on the scale of an individual star, but on a population level within molecular clouds.

1.5 Observing Jets in the Optical and NIR

Although we have seen in the previous sections that jets can be studied at a wide range of wavelengths, the optical-NIR range is of particular interest to us. From a practical standpoint, many atomic jets can be traced by emission lines in this part of the spectrum; additionally, optical-NIR instruments allow for the best spatial resolution, either with ground-based adaptive optics (AO) to decrease the instrument point-spread function (PSF) or with space-based observations. The different kinematic components of jets can vary in velocity from a few 10s to 100s of km s^{-1}; intermediate spectral resolution and sub-arcsecond spatial resolution are also therefore ideal in order to accurately probe the structure and internal processes of the jet. As mentioned, jets from CTTSs are ideal targets for such studies since they are no longer embedded in an envelope and are therefore optically visible.

Bright FELs from species including Fe^+, O, N^+ and S^+ trace the low-density environments within jets, allowing their morphological and kinematic properties to be investigated, as well as properties such as the mass outflow rate. Since the intensity of different emission lines depends on local conditions such as gas density, ionisation and temperature, they can be used to study these conditions in different regions or velocity components of the jet, including the terminal shocks and internal working surfaces, as we will explore in Chapter 5 (Bacciotti & Eislöffel, 1999; Hartigan & Morse, 2007; Coffey et al., 2010).

Forbidden lines of refractory species such as Fe^+ and Ca^+ can tell us about the properties of dust in the jet, and its reprocessing and destruction by shocks. Optical permitted lines, especially the Balmer lines Hα and Hβ, also trace jet structures, and can be used to estimate extinction along the jet; permitted lines measured from the source

position, on the other hand, can be used to estimate the mass accretion rate $\dot{M}_{acc}$, and hence the jet efficiency (the ratio of mass loss to mass accretion).

Some of these properties, such as estimating the jet efficiency or the 'footprint' of its launching region, are key parameters for constraining the developing models of jet launching discussed in Section 1.2.2. Along with other parameters, such as the momentum flux through the jet and the dust composition, they are also relevant to questions of jet-driven feedback into the surrounding molecular cloud, or the interaction of the jet with the protoplanetary disc.

This section will discuss the relative advantages of imaging and spectroscopy in the optical and NIR range, as well as some of the key tools used to visualize and analyze combined spectral-spatial data. This will form a prelude to the next section, which discusses how integral field spectroscopy is able to combine these techniques along with many of their advantages.

1.5.1 Imaging

Imaging studies have the immediate advantage that they can typically cover large fields of view, allowing them to cover large portions of outflows which may extend over several arcminutes on the sky (see for example the CTTS jets imaged by McGroarty & Ray (2004)). They can thus capture large amounts of detail about a jet's morphology, for example knots and bow shock structures, and the jet width along the axis (which can be used to estimate the mass outflow rate), as well as signs of interaction with the surrounding medium or even winds and jets from other nearby protostars. They can also detect 'wiggling' in the jet axis which may be due to precession of the jet, or orbital motion caused by a companion to the jet source.

Observations at multiple epochs can track changes in structure or brightness of the jet knots; they can further measure the proper motions of these objects, giving their velocity in the plane of the sky as well as their direction of travel (which is often important to confirm whether a HH object plausibly belongs to a particular outflow) (Wang & Henning, 2009; Kirwan et al., in prep.). Along with tracking the ejection of new knots, these measurements can be used to form a history of the mass-loss from the jet source over a period of hundreds or thousands of years.

The limitation of imaging by itself is that it can offer large amounts of spatial information about the jet, but limited spectral information. Multiple observations with different wavelength filters may be needed if, for example, we wish to look at the structure of the jet in Hα and [SII], or use emission line ratios to estimate the density or ionization

properties in the jet. (Additional exposures in a continuum emission band are in any case needed to effectively subtract the stellar continuum from the jet emission for analysis.) This requires additional observing time and overheads, and the risk of problems due to changing observation conditions.

1.5.2 Spectroscopy

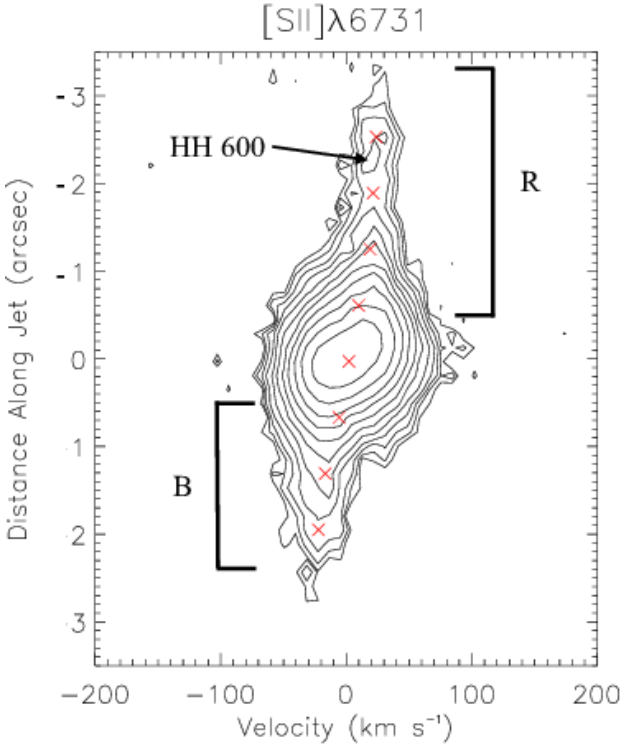

FIGURE 1.10: Example of a PV map for the Par Lup 3-4 jet, from Whelan (2014), obtained from X-Shooter data.

Observations with spectrographs are the converse of imaging studies, in that they offer a great deal of spectral information at the cost of limited spatial information (see for example Whelan (2014); Whelan et al. (2014)). Some spatial information is obtained, however, within the width of the detector slit. We can make use of this by examining the PV map for the jet emission at a given line. An example of a PV map is shown in Figure 1.10; it combines one spatial axis (the slit length) with a velocity axis centred at the rest velocity of the emission line (along the wavelength or dispersion axis of the slit). In this case the slit is aligned along the jet axis, so that the spatial axis corresponds to the distance along the jet; we can therefore examine, for example, how far the different velocity components of a given line extend along the axis, or even detect knots provided they are close enough to the source to be seen within the slit.

However, the slit can equally be placed perpendicularly to the jet axis, resulting in a transverse PV map. This essentially gives a cross-section through the jet beam, allowing the velocity structure around the axis to be studied, to look for asymmetries across the jet beam or to measure the jet width close to the source (Coffey et al., 2008, 2010).

For a given slit position, of course, the spatial information obtained is along only one dimension, and limited typically to a few arcseconds in extent. On the other hand, depending on the spectral coverage and resolution of the instrument, a wealth of information about the line fluxes and physical conditions within that region can be accessed. Because information about the conditions close to the jet base is key to constraining launching models, the spectra are usually sampled close to the source (where most of the bright emission lines are detected in any case). The shape of the line profiles, for example in Hα can be analysed to learn about the different regions from which it is being emitted, giving clues to outflow components such as stellar winds as well as the rate of accretion from infalling material. As mentioned, ratios between the flux intensities of different emission lines allow us to determine physical conditions within the jets and the rate of mass outflow (Coffey et al., 2010; Whelan et al., 2014), but we can also examine how these differ in different components of the jet, for example comparing temperature and density between high and low-velocity layers of the outflow (Nisini et al., 2016; Giannini et al., 2019).

An additional technique that can be used with a long-slit spectrograph is to align the slit with the jet axis and take several exposures, stepping the slit position across jet beam for each observation. The resulting 2D spectra can then be stacked together to create a cube of data that contains both spatial information about along and across the jet. For example, the observations of DG Tau by Bacciotti et al. (2000, 2002) and further analysed in Maurri et al. (2014), show how this technique is used with HST-STIS to obtain detailed spectral information about the transverse jet and illustrate the 'onion layer' kinematic structure, while also allowing a 2D spatial image of the jet to be constructed. This technique may be thought of as a 'pseudo-IFU' format, approximating some of the advantages of the integral field units (IFUs) that will be discussed in the next section. However, this still requires multiple exposures to construct a single datacube, and the spatial field covered is limited both by the slit width (in the longitudinal direction) and the number of exposures (in the transverse direction).

1.6 Integral Field Spectroscopy and MUSE

In observing jets, the challenge is to study a relatively faint jet next to a bright and highly variable young star, with a complex structure containing multiple different components

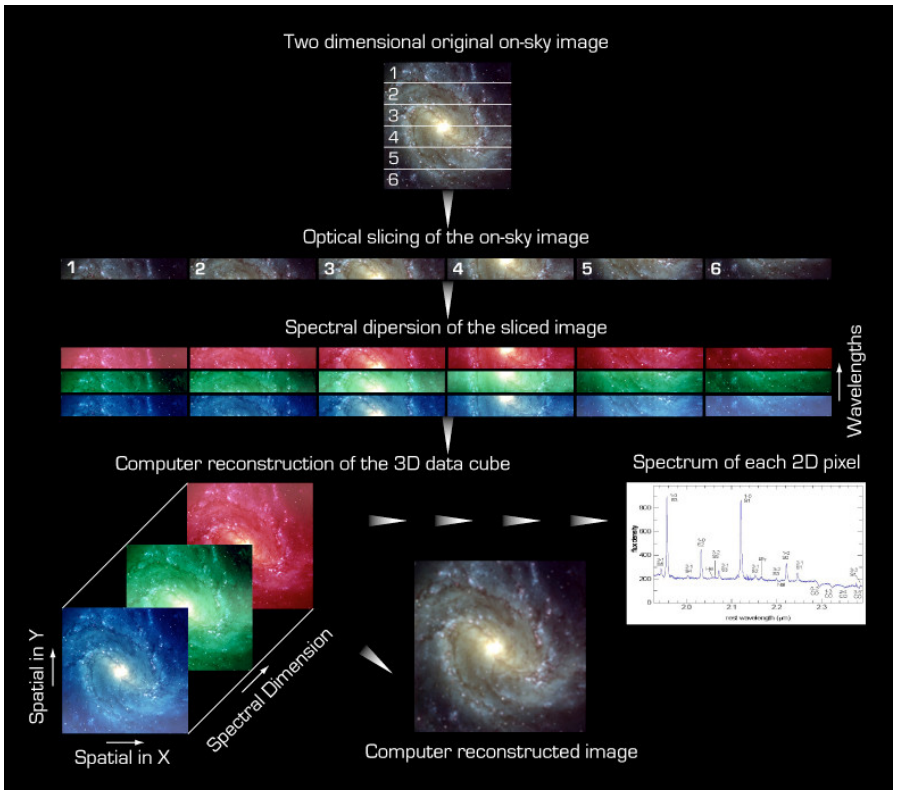

FIGURE 1.11: Illustration of IFS data, showing the structure of the produced datacube. Credit: ESO.

within sub-arsecond scales. To do this we need to be able to efficiently sample and remove both the stellar emission and emission from night-sky emission lines (the latter applicable of course to ground-based observations). We also want to sample as large a region of the extended jet as possible with ≤ 1" spatial resolution, and in as many emission lines as possible. We have seen in the preceding section the advantages offered by both imaging and spectroscopic observations. However, given the variable nature of the jet and source, and the practical need for efficiency in observation time, it would be invaluable to collect similarly detailed spatial and spectral information simultaneously (Dougados, 2008).

This is possible using IFS, a technique which collects simultaneous spectral information across a full 2D field of view. This project will centre on the analysis of jet observations obtained with the Multi-Unit-Spectroscopic Explorer (MUSE), a second-generation IFS instrument on the Very Large Telescope (VLT). This section will discuss the background and context of MUSE, and show that MUSE is a uniquely powerful instrument which offers the capability to study jets across a broad spatial and spectral range in a single observation.

IFS instruments produce a 3D 'datacube' comprising the two spatial dimensions of the field of view, as well as the wavelength axis. As shown in Figure 1.11, we can think

of this datacube as a series of images at each wavelength in the IFU spectral range, or as an image for which every pixel in the field of view (FOV) represents a 1D spectrum. The cube sections corresponding to wavelengths of interest can be extracted from the cube and sliced along any axis required. These can be used to produce either velocity-binned images of the jet in a given emission line (monochromatic images or channel maps integrated over a given wavelength/velocity range).

Alternatively, integrating over one spatial direction creates PV diagrams showing the distribution of emission at different velocities along a given spatial axis, longitudinal or transverse to the jet. The 1D spectra at any region in the FOV can equally be extracted, for example to examine emission line profiles or estimate fluxes. Each datacube therefore represents a tremendous amount of information about a target jet.

This makes it possible to readily isolate the stellar continuum from the jet emission as well as distinguishing regions within the jet which may show different physical conditions. Additionally, the high angular resolution possible enables studies at small scales to effectively examine the launching region, while the improved spatial coverage (compared to long-slit spectral observations) makes it possible to cover a much greater extent of the jet both longitudinally and transversely.

Practically IFS has the advantage of rapid collection of data, making these instruments efficient in time cost. As noted, this includes removing the need to take separate continuum-band exposures for subtraction, since this can be sampled from continuum-only regions of the spectral axis. (Depending on the FOV of the IFS instrument, separate sky exposures may still be required to adequately estimate the night-sky spectrum.) Target acquisition is made easier, as compared with long-slit spectroscopy, precise placement of the target relative to the slit is less crucial. IFS data also suffers significantly less from spurious effects introduced by the use of AO and is thus very compatible with these corrections, enabling enhanced spatial resolution.

The main limitation lies in the need to trade-off between spatial and spectral coverage, with the result that IFS instruments tend to have relatively small fields of view compared with imaging instruments, and poorer spectral resolution and coverage than long-slit spectrographs (Dougados, 2008). IFS is therefore well-suited to observations which need good spatial and spectral resolution, as well as the spatial coverage to observe small to moderate-sized extended objects (Allington-Smith & Content, 1998).

In the rest of this section we review the major types of integral field spectrograph, as well as some examples of IFS applied to observations of protostellar jets. Finally, we introduce MUSE, the integral field spectrograph used in this study, and the key

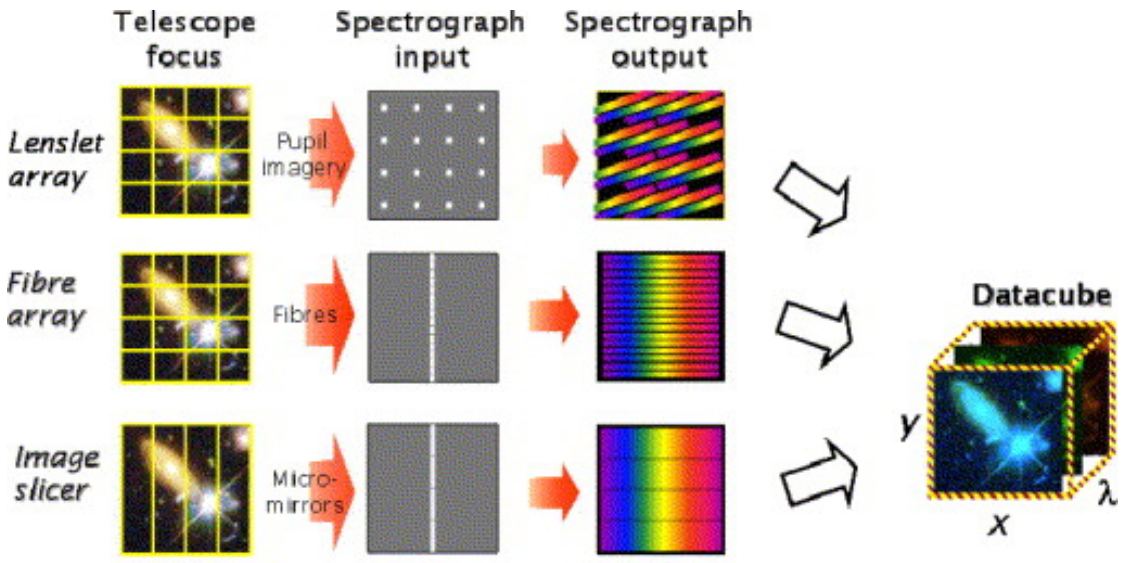

FIGURE 1.12: Illustration of the main types of integral field spectrograph, from Allington-Smith & Content (1998); Allington-Smith (2006).

features which make it a powerful instrument for comprehensively investigating jets in the optical-NIR range.

1.6.1 Types of IFS

Integral field spectrographs fall into one of three or four categories, which are differentiated essentially by how the spatial FOV of the telescope is divided and the sub-images dispersed into spectra and passed to the spectrograph elements. A more detailed discussion of these methods is given in Allington-Smith & Content (1998), but in this section we will give a brief overview.

The first type of IFS uses arrays of lenslets to segment the image formed by the telescope. These then form separate sub-images which are dispersed into discrete spectra. This is illustrated in the top part of Figure 1.12. The dispersion direction is tilted from the FOV axes to avoid overlaps in the spectra; however, a bypass filter is still needed to properly isolate the spectral region of interest and prevent contamination. The maximum spectral range is limited by the ratio between the image size at the telescope pupil and the spacing of the subimages (which is in turn determined by the size of the individual elements). If this ratio is high, a longer spectrum can be observed, but this requires fast lenslet arrays and spectrographs, posing practical and technical challenges in construction. This type of IFS is therefore best-suited to applications which require short wavelength bands or else low-resolution spectra. Some examples of these instruments are OASIS (and its predecessor TIGER) (originally at the Canada-France-Hawaii

Telescope (CFHT) and later transferred permanently to the William Herschel Telescope (WHT)), as well as SAURON at the WHT.

The second category of IFS uses a bundle of close-packed optic fibres at the instrument focus to split the image and reformat it into a pseudoslit; the light from the fibres is then dispersed into a long-slit-spectrograph (Figure 1.12, middle). Examples of these instruments include WHT/INTEGRAL and WHT/HEXAFLEX. In this case the spectrum can be as long as the detector will allow, but the major technical limitation lies in balancing the core to cladding ratio of the optic fibres. The largest core possible is desired to maximize the area used to collect the image at the focus (and minimize dead space), but in practice the cladding must be a minimum thickness to prevent significant light loss to evanescent waves ($> 10\ \lambda$). In optical detectors this means that the practical 'fill factor' of the fibre bundle is no more than 60-75%. Additionally, this type of IFS can suffer focal ratio degradation if the output beam is too fast, introducing complications of design which require large spectrograph optics to compensate.

A variant of this category are IFS instruments which use fibre-lenslets, combining the optic fibres with lenselets at the input (and possibly output). Examples include SMIRFS-IFU at the UK Infrared Telescope (UKIRT), WHT/TEIFU, and GMOS at the Gemini Observatory. This reduces both of the issues encountered with fibre-based IFUs, but at the cost of being difficult to manufacture and requiring careful matching of the lenselets and fibres. These instruments are also typically unsuitable for cryogenic cooling due to the fragility of the bonds between the lenslets and fibres; a notable exception is VLT/SINFONI, an IR IFS designed to have optic fibres manufactured with integrated lenslets.

The last major category of IFS, on the other hand, is well-suited for telescopes with cryogenic cooling, as it relies on reflective optics only. These are the 'slicer' instruments, such as VLT/MUSE, GEMINI/NIFS, and KWCI at the Keck Telescope. In these instruments the telescope image is incident on a mirror composed of narrow slices tilted at slightly different angles to each other. This means that the diverging beam from each mirror (and each 'slice' of the spatial field) is reflected in a different direction, and then again by a mirror offset parallel to the long axis of the slice. The lower part of Figure 1.12 shows how the field can then be rearranged into a long thin field of all the slices end-to-end, which is passed to the spectrograph slit. These instruments have several advantages, one of which is that the full spatial information of the field is maintained along the slit, with the design maximizing the number of spatial and spectral resolution elements as well as the size of the FOV, without requiring very large spectrograph optics.

Instrument	Telescope	Type	R	Spectral range	Spatial FOV	Operational
TIGER	CFHT	Lenslet	540-1300	0.35-1 μm	7”$\times$ 7”- 10”$\times$ 10”	1987-1996
OASIS	CFHT/WHT[a]	Lenslet	1000-4300	4000-9000 Å	1.”6 $\times$ 1.”2 - 15”$\times$ 12”	1997-
GMOS	Gemini	Fibre-lenslet	210-8800	3600-10300 Å	7”$\times$ 5.”5 - 3.”5 $\times$ 5”	2001-
SINFONI	VLT	Fibre-lenslet	2000-4000	1.1-2.45 μm	3”$\times$ 3”- 8”$\times$ 8”	2004-2019
NIFS	Gemini	Slicer	5000	0.95-2.4 μm	3”$\times$ 3”	2006
MUSE	VLT	Slicer	1800-3600	4000-9000 Å	1’$\times$ 1’	2014
					7.”5 $\times$ 7.”5	
KWCI	Keck	Slicer	1000-20000	3500-10500 Å	8.”25 - 33”$\times$ 20”	2017

Table 1.1: Table summarizing major IFS instruments used in jet observations. a), Originally installed at the CFHT and later moved to the WHT.

1.6.2 Using IFS to Study Jets

In this section we will review several examples of studies which investigate jets with IFS instruments. This is by no means an exhaustive review, but will serve to highlight the value of this technique to jet observations, as well as some of the early limitations. The characteristics of the major instruments used in these studies are summarised in Table 1.1 along with those of MUSE and the newer IFS instrument Keck/KWCI for comparison.

We look first at studies in the NIR band, as most earlier IFS instruments were designed to observe in this range, in large part to ensure compatibility with early AO systems and take advantage of the enhanced spatial resolution these offered. For example, SINFONI observations of the DG Tau jet were obtained by Agra-Amboage et al. (2011) with AO correction enabling an effective resolution of 0."15 over an 8" × 8" field of view. SINFONI covers a total wavelength range of 1.1-2.45 μm in separate H and K bands with intermediate spectral resolution, allowing the structure and kinematics of the jet to be examined in NIR [Fe II] emission lines, as well as estimating the density and mass-flux through the jet.

Similarly, Erkal et al. (2021) recently made use of H-band observations obtained with Gemini/NIFS to study both jet lobes of DO Tau, with 0."15-0."175 spatial resolution over a 3" × 3" FOV. Combined with the intermediate velocity resolution of the instrument, this allowed them to place upper limits on the transverse jet rotation velocity, as well as measure velocity asymmetries in the micro-jets; furthermore, the simultaneous imaging of both jet lobes allowed them to detect and model a small-scale wiggling in the jet trajectories, showing the likelihood that this is induced by the orbital motion of an undetected companion object.

Increasingly, IFS instruments have also been constructed for the optical band. An earlier example is CFHT/TIGER which was commissioned in 1987 and operated until 1996, to be succeeded by OASIS in 1997. Both instruments enabled AO-corrected observations of jets in the optical band (Lavalley et al., 1997; Lavalley-Fouquet et al., 2000; Agra-Amboage et al., 2009). We draw brief attention to one study by Lavalley-Fouquet et al. (2000), who used the OASIS IFS instrument to observe DG Tau in order to investigate the physical conditions and heating mechanisms in the jet. OASIS offers a number of observing modes and filters, and this observation used the 6200-6550 Å) and 6500-6850 Å) optical bands. While limited, this spectral coverage was sufficient to cover the key emission lines used in the diagnostic analysis with R $\sim$ 3000-4000. In this mode the available field of view was $5'' \times 6.''2$. It should be noted that although wider field

modes are available, they are accompanied by a corresponding drop in spatial resolution which make them less useful for jet observations.

We can also compare jet observations by Beck et al. (2007) and Cerqueira et al. (2015) using Gemini/GMOS to observe HH 34 and HH 111, respectively. Beck et al. (2007) made use of the instrument's two-slit mode to obtain a relatively broad wavelength range of 6220-6840 Å). The FOV for the observations was 7" × 5"; in order to obtain data for a range of positions along the jet, the observations had to be repeated for three separate pointings over four nights. Likewise, to study the excitation and knots along the length of the HH 111 jet, Cerqueira et al. (2015) needed 8 fields of 3."5 × 5", spread over two nights in 2007 and 2010 (three in total, as technical issues on one of the original 2007 observing nights required an additional night in 2010).

These examples highlight some key advantages that MUSE contributes to IFS observations of jets. As mentioned, the early focus on using this technique for NIR instruments means it is only relatively recently that AO-corrected IFS observations have become available in the optical band. Second, although NIR instruments afford good spectral coverage, optical IFS instruments are typically limited to a few hundred Å per observation, and neither type of instrument can typically cover a large band simultaneously. For example, SINFONI observes the H and K bands separately, introducing difficulties due to changes in observational and source conditions between exposures. In the case of Beck et al. (2007), the overlap between the two slits needed to enable the spectral coverage of their OASIS observations resulted in contamination of the key [O I]λ6300 emission line, so that although estimates of the electron density were obtained, the study was unable to carry out the full set of intended diagnostics.

Finally, most IFS instruments have quite limited fields of view, of perhaps substantially less than < 10" squared. When observing an extended object such as a jet, this means that only a small region can be observed at one time; observing a wider range of positions along the jet therefore requires multiple observations, which is both time-consuming and also introduces greater risks of changes in observing conditions and data quality. In the next section we will fully introduce the MUSE instrument, and we will see that it is ideally suited to fill these gaps in IFS capability.

1.6.3 The MUSE Instrument

MUSE was commissioned on Unit Telescope 4 (UT4) of the of the VLT in 2014, with AO-corrected observations in the Wide Field Mode (WFM) offered in 2017, and an additional Narrow Field Mode (NFM) available since 2018. Shown in Figure 1.13, MUSE is a slicer IFS which operates in the optical-NIR range between 4900-9000 Å in its nominal mode,

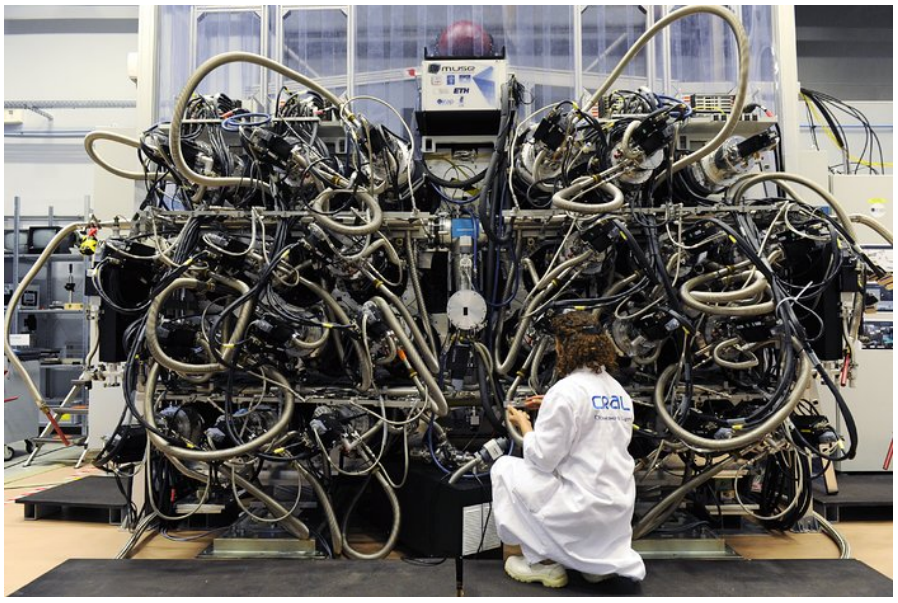

FIGURE 1.13: The MUSE instrument. Credit: ESO

with a resolution R $\sim$ 1600-3500 (a mean value of 3000) across this range (Bacon et al., 2010). An extended spectral range (4650-9000 Å) is also available, although this is vulnerable to second-order contamination at the red end of the spectrum.

In the WFM, MUSE covers an exceptionally large 1' $\times$ 1' field of view. This is sampled by 24 individual Integral Field Units (IFUs); as discussed in Section 1.6.1, the image within each IFU is sliced into subfields which are then rearranged end-to-end and fed to the unit spectrograph and CCD (Charge Coupled Device). This allows MUSE to cover a large contiguous field of view with 0."2 pixel sampling.

The spatial resolution is further enhanced by the Ground Atmospheric Layer Adaptive Corrector for Spectroscopic Imaging (GALACSI) system for AO corrections. This makes use of 4 Na laser guide stars attached to the UT4 telescope as well as a deformable secondary mirror. In AO-corrected modes, a notch filter is applied excluding the 5800-6000 Å range, to prevent contamination from the resulting Na emission lines. Additionally, the NFM facilitates even higher-resolution observations, with 0."025 pixel sampling over a 7."5 $\times$ 7."5 field of view.

This powerful combination of features means that MUSE is capable both of emulating the high spatial resolutions over a small FOV seen in other IFS instruments (along with intermediate spectral resolution), while providing unique capabilities of large *simultaneous* spatial and spectral coverage. This allows us, for example, to sample a wide range of optical-NIR emission lines such as H I, [S II], [N II], [O I], [O III], and [Fe II] transitions, allowing us to compare diagnostic line ratios from knots and HH objects

which are highly time-variable. We can further study large extents of a given jet, or both lobes at the same time, and compare the structures and physical conditions in both.

Further, this is possible in an extremely time-efficient way, minimizing the need for many exposures of a single target; the large field of view in WFM also means that in the case of jets, the night-sky spectrum will most likely be obtained from the sky regions of the science FOV, without needing to take separate sky exposures. MUSE observations therefore enable us to comprehensively study the morphology, conditions and kinematics of the extended jet at the same time.

1.7 Th 28

The focus of this study is the CTTS ThA 15-28 (hereafter Th 28, also called Sz 102, or Krautter's Star) which is located in the Lupus 3 cloud at a distance of approximately 160 pc. This is thought to be a young G-K type dwarf with an estimated mass of 1-2 $M_{\odot}$ and age < 3.5 Myr (Louvet et al., 2016). Th 28 possesses a bipolar jet (HH 228) oriented close to the east-west direction that has been well-resolved in previous optical and IR studies. Observations with low-resolution optical spectroscopy show the stellar region and the jet to emit in a number of FELs, with a spectrum similar to that of a Herbig-Haro object superimposed on a weak red continuum.

It is significantly under-luminous (0.03 $L_{\odot}$) (Liu et al., 2014), suggesting an edge-on view of the accretion disc which matches the low inclination angles ($< 10°$) estimated for the jets and associated HH objects. This makes Th 28 a valuable target for study by enabling a wider extent of both red and blue jets to be observed. The extended jet is shown in Figure 1.14. Narrow-band imaging and spectrocopy have catalogued a number of Herbig-Haro objects as well as a western Herbig-Haro object (HHW) associated with the red-shifted jet (Krautter, 1986; Graham & Heyer, 1988; Comerón & Fernández, 2004). These knots are between 95 and 1040 years old, and show a regular distribution with estimated timescales on the order of a century between ejection. This suggests some episodic ejection activity, and though it has been suggested this could be due to a binary companion in a close eccentric orbit, no evidence for such a companion has yet been observed. In total these objects trace the full length of the jet to a distance of 0.32 pc from the central star.

Notably, there are signatures of marked asymmetry between the two jets, with the western red-shifted component appearing to be more extended in optical, slower, significantly more collimated, and less ionised. The blue-shifted jet is fainter and less collimated, but more ionised and faster by a factor of 2-3. A more detailed overview

of previous diagnostic results for these jets will be given in Chapter 5; however, the blue-shifted jet is overall estimated to be hotter, denser, and more ionized.

The Th 28 jet is also significant for being one of the jets in which strong signatures of rotation have been identified close to the jet base using optical data with 0."1 spatial resolution across the jet (Coffey et al., 2004). However, the velocity gradients observed showed both jet lobes rotating in the opposite sense to the disk, contrary to expectations from launching models, and further attempts to measure the jet rotation using NUV data at higher resolution found inconclusive results, making it unclear if the detected velocity gradients are due to rotation of the jet (Coffey et al., 2007).

Th 28 therefore presents a promising object for observation and analysis using MUSE, with its edge-on disk allowing the jet to be studied within 1-2" of the source, extended micro-jets spanning a length of roughly 20" either side of the source, as well as a number of nearby HH objects. The extended morphology and bright emission spectra allow MUSE's large spatial and spectral range to be used to full advantage, and in the following chapters we will see that MUSE allows many aspects of the jet to be examined in comprehensive detail.

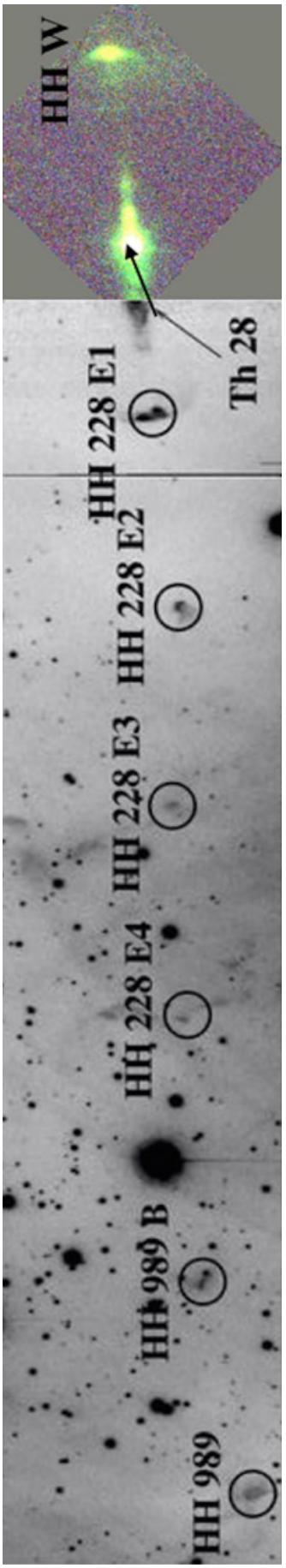

FIGURE 1.14: Composite image of the TH 28 jet, produced by combining a Hα image of the 2014 MUSE FOV (right portion) and an image of the knots in the extended HH 228 flow as in (Comerón & Fernández, 2011). Kindly provided by E. Whelan.

Chapter 2

Data Reduction and Analysis Tools

In this section, we discuss the MUSE observations of Th 28, the data reduction process, as well as the set of Python tools we have written for the analysis of the MUSE datacubes, which form the basis of the work described in this thesis. We will also discuss the main procedures carried out with these Python routines to prepare the data, including subtraction of the stellar continuum and rotation of the datacubes to align the jet axis with the horizontal image axis.

2.1 Observations

The MUSE observations were made on 23rd June 2014, during the instrument's science verification phase. The average seeing was 0."9 during the observations and the pixel scale was 0."2. The observations were taken in Wide-Field Mode (WFM) and rotated by 48° so that the diagonal axis was aligned with the jet PA and thus the FOV encompassed the maximum possible extent of the red-shifted (western) jet. As the WFM FOV is 1'x 1', this allowed the observations to capture approximately 80" along the jet axis. Figure 2.1 shows the resulting view of the Th 28 jets and western bow shock in Hα emission, including several background stars. The wavelength range of the observations was 4570 Å to 9350 Å with an average velocity resolution of approximately 100 km s^{-1} in the 6300-6700 Å range.

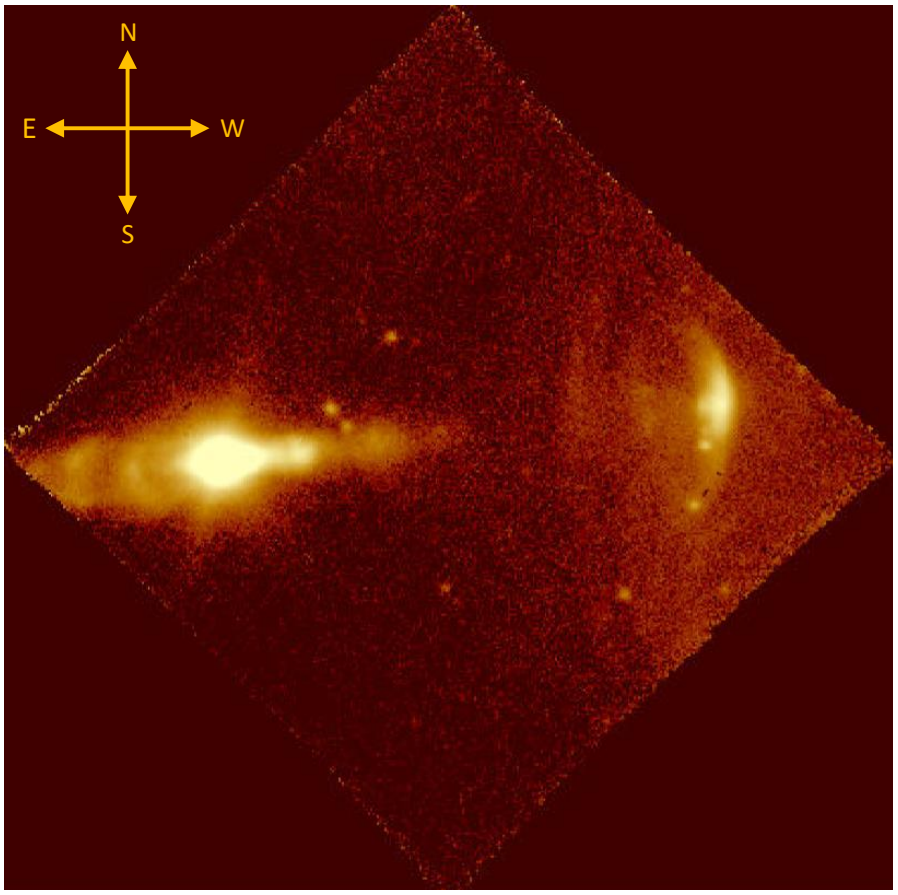

FIGURE 2.1: The MUSE view of Th 28 showing the full field of view in the combined Hα emission across all velocities before continuum subtraction. A number of background stars are visible in the field, as well as the western Herbig Haro object associated with the red-shifted jet.

2.2 Data Reduction

The MUSE FOV is divided into 24 subfields, each of which is fed into an integral field unit (IFU) containing a 4k × 4k pixel CCD. Each CCD field is in turn separated into 48 slices, covering a wavelength range of 4800-9000 Å. Figure 2.2 shows a simplified diagram of the main steps in the pipeline, which can be divided into two parts. Broadly speaking, the first stage can be said to comprise the reduction of the data from each individual IFU (and each individual exposure) on its own, including the target observations, astrometric data, standard star exposures, and sky exposures. The second stage is post-processing, where the data from individual IFUs is combined, final calibrations carried out, and finally the separate exposures combined.

The key steps in the reduction are discussed during the rest of this section. This work made use of two versions of the reduced data. The original data reduction was carried out using version 1.0.4 of the pipeline, and produced a single datacube covering the 4800-9000 Å range. The second reduction process was carried out using version

2.0.1 of the pipeline, to take advantage of updated pipeline processes and calibrations. However, due to the high computational demands of the MUSE reduction pipeline, this data was sliced into individual 500 Å bands in separate datacubes ('the re-reduced cubes'). This had the additional effect of truncating the overall wavelength range to 5000-8500 Å. Because it makes use of a more up-to-date pipeline, the latter dataset is the primary basis of this work; however, for sections which rely on accessing emission lines outside the reduced wavelength range (e.g. the Hβ line at 4861 Å) we make use of the older dataset.

2.2.1 Bias and Dark Subtraction

The first stage of the reduction, as mentioned, must be carried out for all object, standard star, sky and astrometric exposures as well as for individual IFUs. The first step is the removal of the bias of each CCD. This refers to a constant offset voltage applied to the CCD to prevent negative counts being misrepresented by analog-to-digital conversion. In the case of MUSE, each CCD is read out in four quadrants, so there are four different bias values in addition to any spatial gradients across the detector.

To correct for this, a set of bias frames are taken with 0s exposure time, so that there are no counts due to photons, only the bias voltage. At least three bias frames are required (11 daily frames are produced for MUSE). The pipeline can then trim these frames and combine them into a 'master bias' using a 3-σ clipped average; this minimises the effects of readout noise on an individual frame. The master bias is then subtracted from all other exposures. Additionally, the bias level can vary over time, so the overscan values for each frame are used to offset the bias value: the overscan values are obtained from continuing to read the CCD where there are no physically available pixels; in the case of MUSE the overscan regions are located in a cross at the centre of the frame.

Similarly, the 'dark current' is an instrumental effect consisting of excess counts caused when electrons are excited to the CCD conduction band by thermal excitation rather then by photons. This can be corrected for by using 'dark frames', long exposures (on the order of a typical science exposure) taken with the telescope shutters closed, so that they contain no photo-electrons but only the bias and dark current. For MUSE, this is a monthly sequence of five 30-minute frames. The master bias is then subtracted from the dark frames; the MUSE pipeline recipe converts the darks from analog-digital units to photon counts, and then combines them into a 'master dark'. (This is again done via sigma clipping, which should exclude any cosmic rays from the final frame.) The master dark is normalized to 1 hour of exposure time, with units of e^- hr^{-1} px^{-1}.

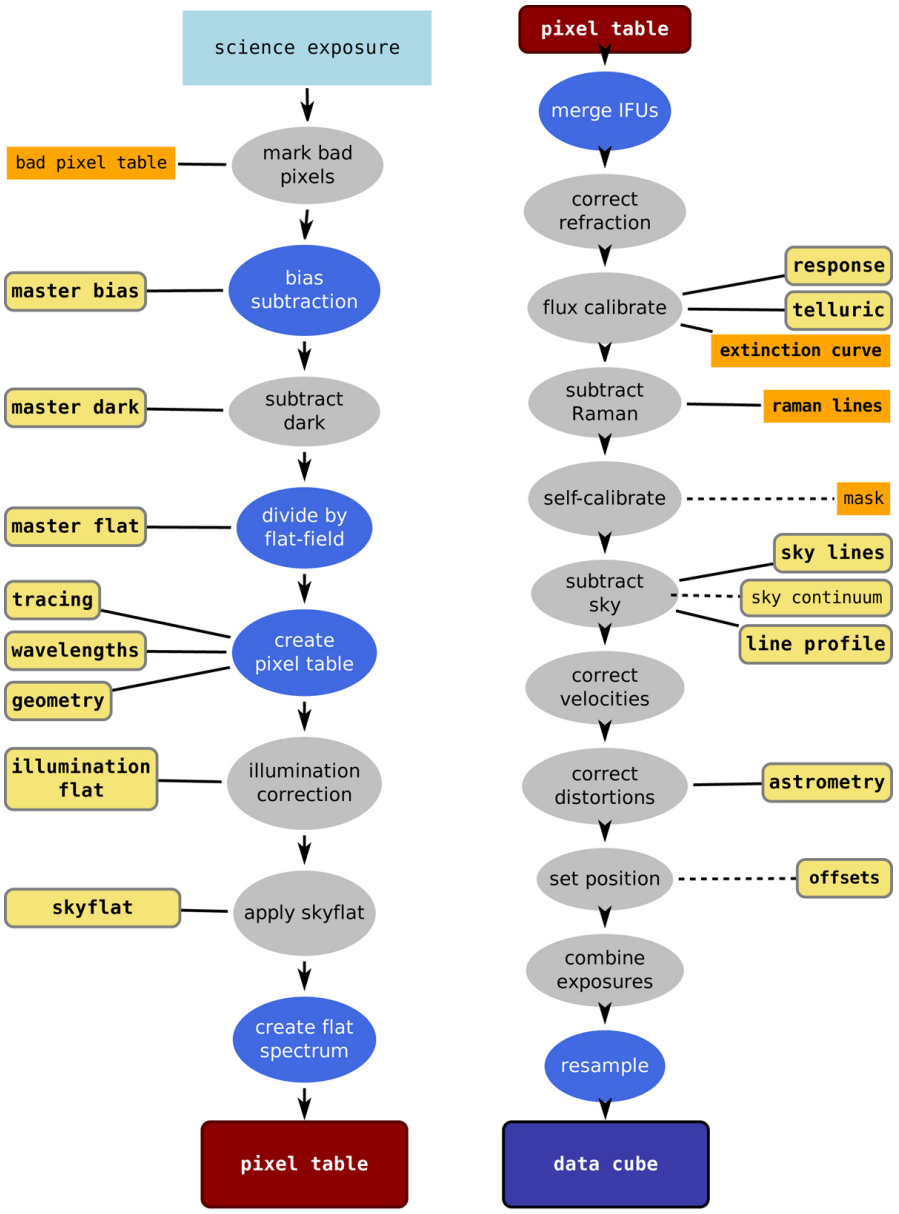

FIGURE 2.2: Overview of the MUSE data reduction pipeline (Weilbacher et al., 2020). The left part of the diagram shows the initial reduction steps carried out for all individual exposures from each IFU; the right-hand side shows the post-processing steps which carry out final calibrations, sky subtraction, and combination of the exposures into a single dataset.

As with many modern instruments, MUSE is well cooled and the typical values of dark current in this frame are ~ 1 e$^-$ hr^{-1} px^{-1}, so the effect of dark current is small and correcting for it is considered optional in the pipeline. However, if selected, the master dark is subtracted from all the remaining frames.

2.2.2 Flat fields and Twilight Frames

The flat field frames (or 'flats') and the twilight or 'skyflat' frames can be grouped together as both being a means to correct for the effects of varying illumination across the detector, pixel sensitivity (including the detection of dark pixels) and defects such as dust affecting the detector.

Flat fields are the primary illumination correction and are frames taken under illumination by a uniform light source. After bias and dark subtraction, they are scaled to match the exposure time of the frame to be corrected, and combined into a 'master flat'. The target frames (after bias and dark subtraction) are then divided by the normalised flat field. In the MUSE pipeline, this stage also serves the important function of checking the slice positions on the CCD and providing trace information which is needed to recombine the slices to their correct spatial positions in a later step.

The twilight frames serve as an additional illumination correction and are used as a separate step of the reduction in the MUSE pipeline. These are bright sky background exposures typically taken during twilight hours; at least 3 exposures are needed, which must themselves be reduced using bias and dark subtraction, wavelength calibration, and using the tracing solution from the flat fields as well as information about the instrument geometry to assign co-ordinates to each pixel. The advantage of the twilight corrections is that it combines illumination information from all the IFUs to correct for differences in their relative efficiencies.

2.2.3 Wavelength Calibration and Line Spread Function

The wavelength calibration for MUSE is carried out using a combination of three arc lamps in air (HgCd, Xe, and Ne) to ensure that a smooth wavelength solution is obtained across the full spectral range of the instrument. Typically five exposures ('arc frames') are required for each lamp to maximize the signal-to-noise ratio (S/N) of weaker lines without saturating the detector at the brightest lines. The exposures are bias-subtracted and combined for each individual lamp separately, to reduce line blending and facilitate identification.

The *muse_wavecal* recipe is then used to detect and identify the lines for each lamp. The emission lines are detected first at the centre of each detector slice using Gaussian fitting, with a pattern-matching algorithm used to identify each from an input catalogue, and traced to the edges of the slice. The recipe then fits a wavelength solution to each slice, which consists of a 2D polynomial describing both the spatial curvature of the arc lines and their dispersion with wavelength. This produces a wavelength calibration table

which will be used to determine the spectral pixel co-ordinates for the final IFU pixel table, by evaluating the polynomial at each particular CCD position.

Because the arc exposures may be taken several hours apart from the science exposures, an additional correction is implemented in the final pixel tables to account for any shifts in calibration that may occur due to changes in the ambient temperature. This is done by reconstructing a high S/N spectrum of the sky background in the science exposures around the bright [O I] skylines at 5577.339 Å and 6300.304 Å, which serve as points of reference. Any detected shift from the central wavelength of these lines is then subtracted from the wavelength column of the pixel table.

The wavelength calibration table, along with the arc lamp exposures, is also used to characterize the line spread function (LSF) of each slice of the IFU. Analogous to the point-spread function for a spatial point source, the LSF characterizes how light from a monochromatic source is distributed on the focal plane, and is primarily determined by the finite resolution of the instrument. The LSF estimate is a key component in estimating and subtracting the sky spectrum, and so the *muse_lsf* recipe is used to obtain a good representation of this function for each IFU. Ideally at least 10 exposures per lamp are used to obtain good S/N in the wings of the arc lines. The recipe then uses the brightest and most isolated arc lines from the catalogue to fit a 2D polynomial which determines how the LSF varies with both spatial position (i.e. across each slice) and wavelength. During the sky subtraction this LSF solution will be combined with the estimated sky line fluxes to model the spectrum to be removed.

2.2.4 The *muse_scibasic* Recipe

This recipe converts the raw science frames for an individual IFU (and individual exposure into a pixel table ready for the post-processing stage of the reduction, and is carried out both for the science frames and for the standard star, sky and astrometry frames. For each CCD it removes the instrumental signature using the products of the steps already discussed, including bias and dark subtraction, conversion from adu to photon count, flat-fielding, and propagation of the twilight efficiencies.

Spatial and spectral co-ordinates are assigned to each pixel in the corresponding dimensions, using the trace tables and input instrument geometry table for the former, and wavelength calibration table for the latter. At this stage the wavelength range may also be cropped for convenience or to save computational resources, as was the case for the re-reduced data in this study. The pixel tables are then ready for the post-processing stage.

2.2.5 Flux Calibration and Astrometric Corrections

The flux calibration is a critical step to convert the measured photon counts at each position into an estimate of the absolute flux which is comparable with other observations. To do this the *muse_standard* recipe uses exposures of a spectrophotometric standard star to account for the sensitivity of the instrument at different wavelengths, as well as normalized telluric absorption. The standard star exposures undergo the same basic reduction as the science frames to this point, as well as correction for differential atmospheric refraction (DAR) at different wavelengths. A datacube of the field in these exposures is then reconstructed, and high S/N spectra extracted for every detected star, followed by a smoothed elliptical Moffat fit to extract the stellar fluxes.

The pipeline then selects either the brightest star or the one closest to the centre to use as the reference. Its measured fluxes (as observed by MUSE) are compared to a reference table of fluxes for the standard field, taking into account the measured airmass and a provided atmospheric extinction curve. This allows the recipe to determine the instrumental sensitivity function over the full wavelength range; it also identifies wavelengths affected by telluric absorption and derives a telluric correction spectrum. The response function is linearly extrapolated to the full MUSE wavelength range and smoothed, producing a final response curve which is used to calibrate the science frames.

Similarly, astrometric fields are used by the *muse_astrometry* module to calibrate the pixel scale and overall distortion of the MUSE observations across the FOV. Reference catalogues are based on existing HST imaging of Milky Way Globular Clusters, with fields located toward the outer edges of the clusters used to calibrate WFM data. These astrometric frames are also reduced using the basic reduction to create bias- and flat-field corrected pixel tables, as well as correction for DAR.

A cube of the stellar field is then reconstructed with a large wavelength sampling (50 Å px^{-1}) to improve S/N and the central three wavelength channels median-averaged. The reference stars in the exposure are detected using thresholding and Moffat fitting before pattern-matching is used to identify them against the sky positions given in a reference catalogue. The full set of matched objects is then used to obtain an astrometric solution comprising a six-parameter world coordinate representation.

2.2.6 Sky Subtraction and Post-processing

The final calibration of the science frames for each exposure is carried out using the *muse_scipost* recipe. This first involves merging the pixel tables from individual IFUs, taking into account the relative efficiencies determined by the twilight exposures and

dividing by an averaged (large-scale) flat-field spectrum. This is followed by DAR correction and application of the flux calibration and telluric absorption solutions.

The sky subtraction can also be carried out as part of this step provided that the target is not large enough to cover a very large portion of the FOV (otherwise separate sky exposures must be obtained and a night sky model created using a separate pipeline recipe). In the *muse_scipost* routine, the darkest fraction of the the field (10-20%) is taken as the sky region. The spectrum sampled from these positions is used as a guide to fit the sky lines, combining their measured fluxes with the modelled LSF at each wavelength and spatial position to obtain a full sky spectrum which can be subtracted from the full science table. The sky continuum emission is then also fitted and subtracted.

The recipe further corrects for the radial velocity of the observer (for our data the default barycentric correction was used), and the astrometric solution is applied. Finally, the exposures can then be combined (either as part of this step or separately using the *muse_exp_align* recipe) and the pixel tables resampled into a fully reduced datacube.

2.3 Wavelength Calibration

Some IFU instruments, particularly in the NIR band, have been shown to have substantial wavelength shifts in the final reduced datacubes, corresponding to large systematic velocity shifts. For example, checks against the OH sky lines show a shift of as much as 30-40 km s^{-1} in SINFONI observations (Lopez et al., 2013; Whelan et al., 2018) which must be identified and corrected for. We therefore wished to investigate whether we could also check the final MUSE datacubes for any systematic shifts in the final wavelength calibration.

However, the MUSE pipeline is computationally very expensive (requiring very large amounts of available memory), and as discussed in Section 2.2.4, the sky modelling and subtraction is carried out entirely within one of the final reduction steps. Consequently we do not have access to a wavelength-calibrated cube with the sky spectrum still included. Therefore spectra were sampled from the sky regions in the final datacubes for both the re-reduced and original datasets, and the median spectra obtained to check if there were sufficient residual sky lines against which to check the calibration. In particular we chose the [O I]λ5577 and [O I]λ6300 sky lines which are very bright and well-separated from other emission lines, and in the wavelength range of 5000-6500 Å which is of most interest for our study. (From Section 2.2.3, these are also the primary lines used in the pipeline to check the calibration solution, for much the same reasons.)

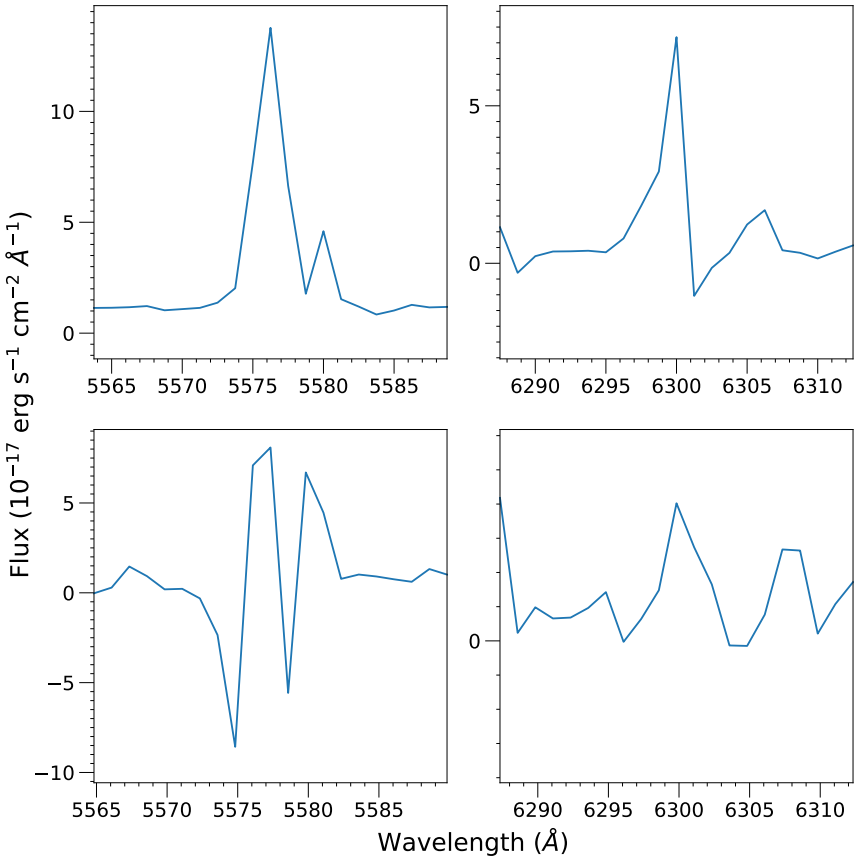

FIGURE 2.3: Sampled sky lines from the original reduced MUSE cube (top) and re-reduced cubes (bottom panels). Left panels show the [O I]λ5575 line and right panels show the [O I]λ6300 line.

In practice, the small residual spectra remaining proved to be unsuitable for this purpose. As shown in Figure 2.3, the line profiles show very small spikes around a region of slight oversubtraction, corresponding to the remaining wings of the line after the peak has been subtracted. We therefore find that we cannot use the residual sky lines to check the calibration of the central wavelengths. However, as will be discussed further in Chapter 3, the radial velocities measured for the Th 28 jets are entirely consistent with our expectations based on previous literature, and there is no evidence for any significant systematic shift in wavelength across the MUSE spectra.

2.4 Python Tools for MUSE Data Analysis

As part of the work for this project, a set of Python modules was written to interact with the MUSE datacubes. The primary motivations for this were to provide utility and easy handling and analysis of the data with functions specific to examining and fitting the

jet morphology, kinematics and diagnostic emission lines, as well as to interface between the datacubes and the FORTRAN-based Bacciotti-Eislöffel diagnostic code (and future updates of the same). The current modules primarily make use of the *astropy*[1], *numpy*, *matplotlib* and *lmfit* packages which are publicly available.

In this section we will briefly discuss the overall structure of the modules, and the main object classes and their functions which are used in this work. The primary module is *museclasses*, which contains the primary data object classes and their associated functions; additionally there is the *mcgen* module which contains general utility functions (fitting, sorting header information etc.) and the *mcplot* module which provides classes and functions related to easy visualization of the output from museclasses (e.g. comparing multiple slices through a jet, outputting fit reports from numerous cross-sections). Here we will primarily discuss the *museclasses* module and its utility for this study.

The general structure of the module classes is shown in Figure 2.4, with the main object classes arranged in order of reducing dimensionality: i.e. we move from 3D cube objects, MCube and LineCube, to the 2D slices LineSlice and PVMap, to the 1D WavSpec. All of these classes share several generic functions, e.g., to generate copies of the object, to save it as a FITS file which can be examined in an appropriate viewer (e.g. SAOimage DS9 or QFitsView), and a load function which retrieves the data from a FITS file and populates the appropriate object information from the FITS header. As appropriate, they also have functions to set the centre (or target pixel co-ordinates) of the image field, or to extract subset of spatial and/or spectral information from within the object.

2.4.1 Cube Classes

The object classes which represent 3D datacubes are MCube and LineCube. MCube represents the full original MUSE datacube with all extensions and header information included, allowing this this to be easily accessed and interacted with, and can be loaded directly from the reduced datacube file. We note that the basic structure of these classes is compatible with other ESO-format datacubes, and a variant of the MCube class (SCube) was created to interact with SINFONI data in exactly the same way. The main difference is simply in the assumed instrument parameters (e.g. the size of spatial and wavelength pixels) and a future modification will be to merge these into an overarching datacube class which automatically reads and sets the parameters for a specific instrument from the file header.

[1](Astropy Collaboration et al., 2013, 2018)

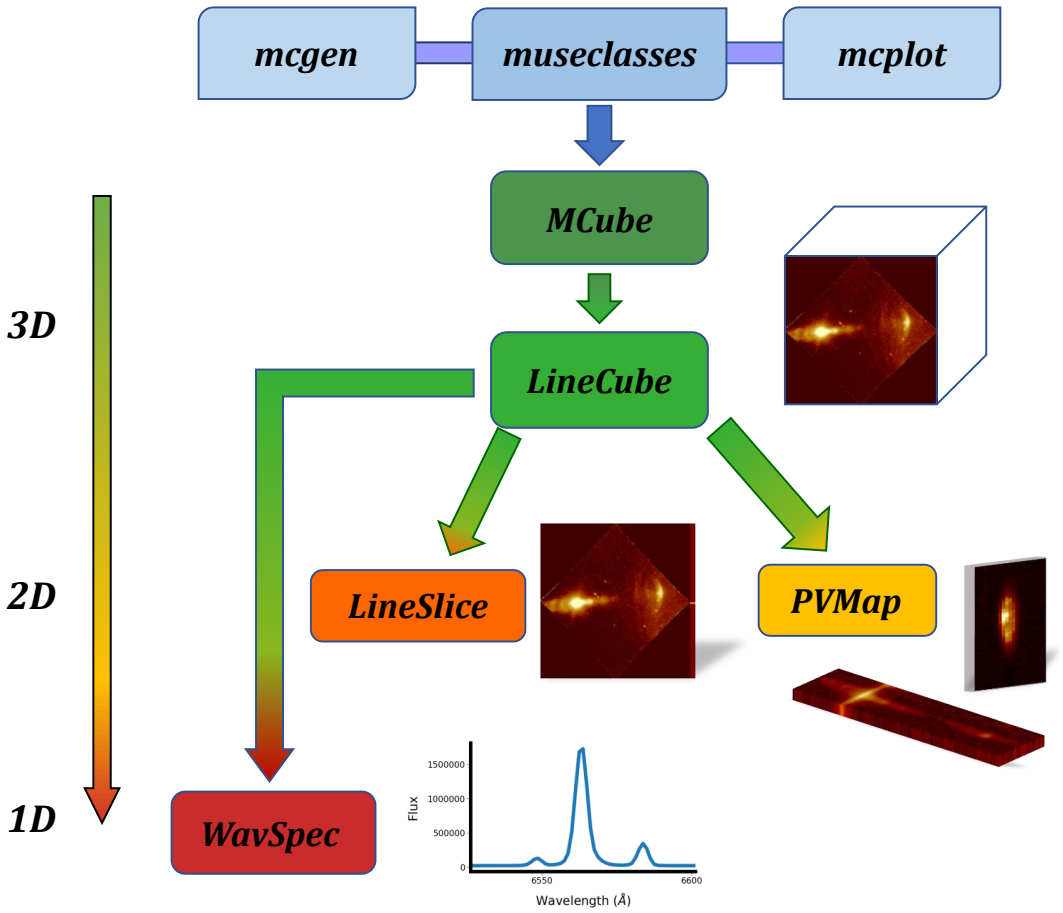

FIGURE 2.4: Diagram showing the hierarchy of the main object classes used in the Python code written to analyse the MUSE datacube, with illustrations of the corresponding data types, i.e. 3D datacubes, 2D slices and 1D spectra.

Both MCube and LineCube have the *getline()* and *getspec()* functions, which have parallel purposes. The *getline()* function extracts a LineCube centred at the given wavelength, given a specified radius in spectral pixels. If the cube is too short on one or both sides for the specified radius (e.g. specifying a radius of 20 Å around an emission line at 5007 Å, from a cube that starts at 5000 Å), then a warning is printed and the selected radius is truncated as necessary. The wavelength scale information is then updated (and a 'targline' attribute added to the header and the object, recording the target wavelength) before the LineCube is returned.

The spatial counterpart to *getline()* is the *zoomify()* function. Given a spatial region defined either with x-y pixel co-ordinates, or specified in a region file created in SAOImage DS9, this method extracts the corresponding data and returns it as a LineCube with the header parameters updated accordingly, including the target position (based on the parent cube; if one selects a spatial region far away from the target object, the 'centre' may be a pixel outside the field of the new cube). The main function specific to the

MCube class is *masslines()*, which automatically invokes the *getline()* function for a list of wavelengths to facilitate quick and easy catalogue extraction.

The *getspec()* function, meanwhile, returns a WavSpec object containing the 1D spectrum along the wavelength axis at the x, y co-ordinates specified, with a given radius around the centre and a user-specified method of combining the spectra from each pixel (the default is 'sum'). In the MCube class this allows for quick inspection of the spectrum at a given spatial region.

The primary class used for interacting with data pertaining to a given emission line is LineCube, which represents a (typically much smaller) subset of the MUSE data cube centred on a specific emission line. This stores the header information from the MCube, and by default covers the full original FOV, but allows the user to work with a smaller data file containing only the spectral region of interest.

The LineCube class has several associated functions used in this work. A general utility function is the *cubeslice()* method, which returns an array of the individual wavelength channels in a cube, with appropriate velocity bins assigned based on the calculated wavelength interval and rest wavelength. (A counterpart function, *slicemerge()*, can be used to concatenate slices back into a datacube if needed.) The *binchannels()* method invokes this to separate velocity channels within the cube and allow the used to quickly select those to combine. This returns an array of LineSlice objects containing the resulting spectro-images. By default the selected channels are summed, but the user can also select mean or median-averaging.

Conversely, the *getpvmap()* method retrieves slices along the wavelength axis, i.e. in position-wavelength or position-velocity space. Given a spatial region in the cube FOV, this method extracts the corresponding block of data from the array and sums or averages them along one axis (with the method again user-defined) to create a 2D map. By default the data is collapsed along the image x-axis (corresponding to a longitudinal PV map along the outflow axis of a horizontal jet), but this can be switched using the axis keyword, either to match a jet aligned closer to the y-axis of the image or to produce a transverse PV image (the jet cross-section). The method updates the spatial information in the header as well as adding information about the velocity range and resolution of the image, and returns a PVMap object as described in the next subsection.

Finally, the *basesub()* and *specsub()* methods are desgined for subtraction of the source continuum, and will be discussed in Section 2.5.

2.4.2 The 2D Slice Classes

2D 'slices' of the MUSE datacube are represented using the LineSlice class in the x-y plane (essentially a spectro-image of the FOV) and its specialized subclass PVMap, which serves the same purpose for a slice in the x-z or y-z planes, with the appropriate header changes.

LineSlice and PVMap objects have a version of the *zoomify()* method which allows subregions to be easily extracted. Both of these also interact with the JetPlot and SubPlot classes in the *mcplot* module, which use the LineSlice information to facilitate creating visual plots (e.g., allowing automatic centering on the target position, sampling a specified background region and automatically subtracting the mean, calculating the 1-σ level of the background noise).

As will be discussed in the following chapters, it is of interest to obtain the properties of the jet beam along the outflow axis. The *beamfit()* function takes a selected region within a LineSlice field containing a jet axis (assumed to be approximately horizontally aligned in the present version), and bins these into cross-section segments with a specified pixel radius (e.g. corresponding to 1" bins along the axis). It then fits a profile model to the cross section at each point and returns a set of LineFit objects as well as arrays corresponding to the fitted centroids and FWHMs measured for each segment.

The *beamplot()* function in turn makes use of this to quickly plot the FWHM and centroids along the jet for a given region within a LineCube, with the addition that the user can choose the velocity channels to be binned together before the jet is fitted (for example, if wanting to compare the jet width in different velocity components). This function also allows the user to specify the target position and several other positions to sample along the jet axis. By default, the fitted FWHM at the source position is automatically subtracted in quadrature from the widths at the other positions to obtain the intrinsic width, and a linear fit applied to the remaining points to estimate the full opening angle of the jet. A planned update by the author will allow a user-provided estimate of the source width (e.g. the expected resolution at the source position) to be used instead.

Additionally, the *jetrotate()* function uses *beamfit()* to allow a set of LineCubes to be rotated spatially so as to align the jet axis with the horizontal (or vertical) axis of the datacube. This will be discussed further in Section 2.6

2.4.3 1D Profiles

The WavSpec class represents 1D spectra class, and is used in many of the profile-fitting functions, as well as allowing an easy means to examine, interact with and save spectra from a cube. Two important functions are the *specplot()* function, which produces and optionally saves a plot of the spectrum flux against either pixel position or wavelength scales[2], and *basefind()*, which given one or more continuum pixel ranges (ideally one on each side of the emission line of interest) fits and returns the estimated continuum baseline as a WavSpec; this optionally also plots the spectrum with the fit overlaid for inspection.

Additionally, there are the *linefit()* and *multiline()* profile fitting functions, which use *lmfit* models to obtain line (or spatial cross-section) fits. The primary version is *linefit()*, which assumes only one peak to be fitted. This allows the user to specify guesses for the peak centre, amplitude and standard deviation, then fits a profile as well as optionally showing a plot of the fit. The default model fitted is a Gaussian, but Lorentzian or Moffat profiles can also be specified as a keyword. If no user guesses for the peak shape are specified, the fit will by default guess a centre equal to the target wavelength of the spectrum, with $\sigma = 1.0$ and an amplitude equal to the maximum value in the spectrum. The function then returns a LineFit object containing all the fit information, and will optionally output a plot of the fit overlaid on the spectrum for inspection. The *multiline()* function is a variant of *linefit()* which allows up to four component peaks to be combined, for example in separating two lines with blended wings; however, at present this is only reliable for fitting two components. Future updates planned by the author will attempt to improve the reliability of this function when fitting three or four-component models.

2.5 Continuum Subtraction

A key goal of this project is to examine the inner regions of the Th 28 jet, close to the stellar position. Given this, it was important to determine the most effective method for removing as much of the stellar continuum emission and spectral features as possible, as well as the background stars visible in the field of view (as seen in Figure 2.1). A secondary goal was to see if effective removal of the stellar spectrum would allow a low-velocity component of the [O I]λ6300 emission to be resolved as has been seen in other jets.

[2] An additional option to plot flux against velocity units relative to the rest velocity of a chosen emission line will be added in a future update to the code by the author.

As a rudimentary method for background subtraction, spectra and position-velocity diagrams of a given emission line were used to identify a region of nearby wavelengths with continuum-only emission. This region was then sampled and a median-averaged image taken as the continuum estimate. This continuum image was then subtracted from each wavelength of the extracted line. This technique was sufficient to remove the background stars and reduce the continuum image, but was flawed in a number of ways. Since it sampled the continuum only on one side of the emission line, it did not account for any potential slope in the stellar continuum, and would not remove any stellar spectrum features such as absorption lines. As a result this method was of limited use as a general tool.

To improve the continuum subtraction of Th 28 and to produce more general tools for datacube analysis, linear baseline and stellar spectrum subtraction methods were investigated. As illustrated in the upper panel of Figure 2.5, linear baseline subtraction involves sampling a relatively flat continuum region on either side of the emission line; a linear fit is then made to the continuum and subtracted from the line spectrum. This method removes any slope from the continuum but will be most effective only if the stellar spectrum is relatively flat, without features such as absorption lines.

In stellar spectrum subtraction, a region of the stellar emission away from the jet position is chosen and the spectrum sampled. Ideally this then gives the stellar spectrum including any absorption or emission lines from the star itself. This spectrum is then scaled to match the continuum level at a given spatial position and subtracted from the spectrum (illustrated in the lower panels of Figure 2.5). This method accounts for both absorption lines and any continuum slope, and may be more effective in separating the line emission from around the star from the low-velocity [O I] component. Both of these methods have the advantage of being easily automated and applied to every spatial pixel of a given region, or over the whole image.

The [O I]λ6300 line is a key emission line for the diagnostics to be carried out in this project, as well as being of interest due to tracing the low-velocity component (LVC) close to the star (see Chapter 1). As isolating the LVC requires careful removal of the stellar emission, this line was chosen as the focus in determining the best continuum subtraction method for the observations of Th 28. The spectrum of this line was extracted from the central star position in order to identify whether it contained any significant absorption features. An example is shown in Figure 2.6. As can be seen, the continuum spectrum of Th 28 is very flat around the emission lines; this is likely to be due to the very embedded nature of the source. If the spectrum of an embedded star is dominated by light scattering from the surrounding disk, this can result in 'veiling' or filling-in of any absorption lines.

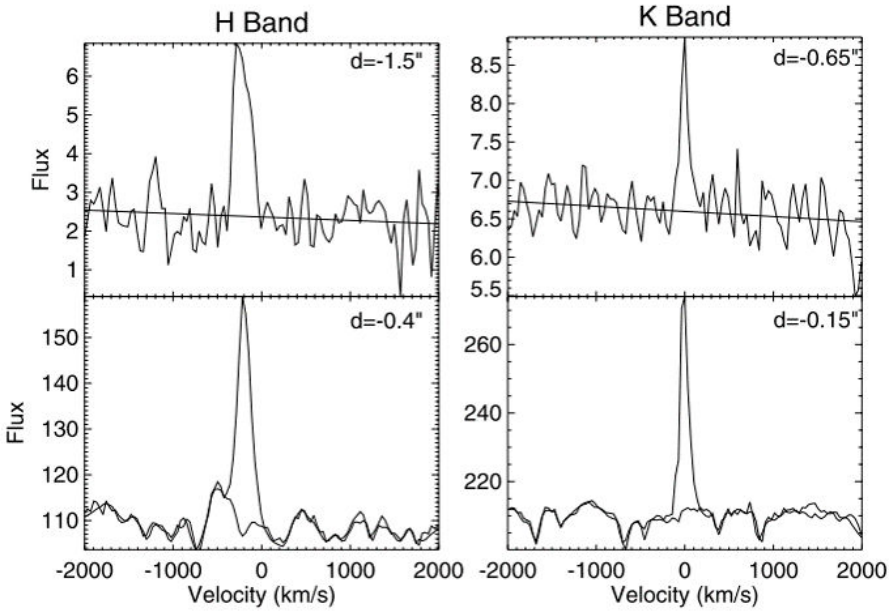

FIGURE 2.5: Top: Linear baseline fitting applied to two spectra. The fitted baselines are then subtracted to remove the estimated continuum. Bottom: Stellar Spectrum subtraction. The stellar spectrum has been sampled and scaled to match the continuum level; it can be seen as the overlaid spectrum below the main emission line. This is then subtracted to remove stellar spectral features, for example the blue-shifted component in the H-band image. Figure from Agra-Amboage et al. (2011)

To verify whether this was the case for Th 28, the ratio of the emission line peak to the mean continuum flux was mapped across the field of view (see Figure 2.7). Across the stellar region, this ratio is nearly constant, indicating that scattered light is predominantly responsible for the continuum emission. A linear baseline subtraction was therefore considered appropriate for this source. A Python function (*basesub()*) was written to extract the [O I] spectrum at each pixel position, fit a linear baseline to continuum regions, and subtract this baseline. Continuum regions were selected by visual inspection of the spectrum, and the root-mean-squared of this continuum plotted against the standard deviation for the spatial field of view around the star and inner jet. The values showed the relationship expected if these were continuum regions (i.e. the variation is governed by random noise).

Both to make a complete comparison of these methods, and as a general-purpose tool for future data analysis, a second function, *specsub()* was also written to apply stellar spectrum subtraction across a selected field of view. Given a reference spectrum sampled from the stellar emission and continuum regions to sample for scaling, the function could then scale the stellar spectrum appropriately and subtract it at each spatial position. However, this method would primarily be of use in the region around Th 28; for example, the background stars visible behind the western HH object would

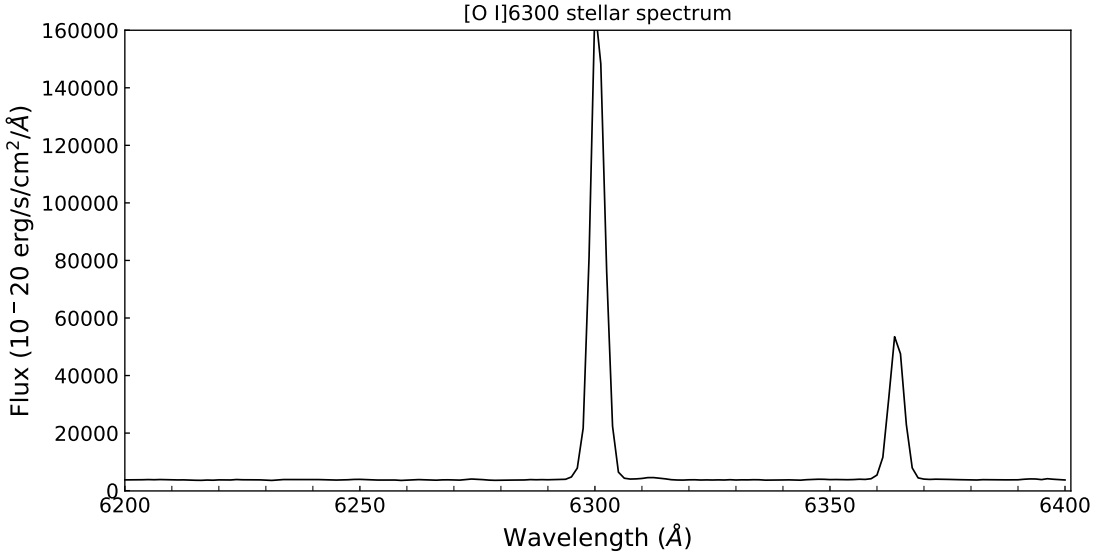

FIGURE 2.6: [O I]λ6300 spectrum sampled from the central stellar position. It can be seen that the stellar spectrum is flat around the emission line with no visible absorption features.

have high continuum levels but not the emission spectrum of Th 28, which would result in oversubtraction of [O I] emission from the bow shock.

Each of the Python routines for continuum subtraction iterates over the pixels in a given spatial region, and retrieves the continuum level from z-pixel (wavelength) ranges selected by the user. In the *basesub()* method, a linear baseline is then fitted to this level and subtracted from the spectrum of each pixel; for *specsub()* this is compared with the continuum level of a stellar reference spectrum at a position chosen by the user. The *specsub()* method then scales the reference spectrum to the measured baseline average and subtracts it. Both methods return a continuum-subtracted emission line cube, as well as a cube containing the subtracted spectrum/continuum for inspection.

Figure 2.8 shows the results of applying both methods to the [O I]λ6300 line, with a plot of the 2D spectrum before subtraction shown in the upper panel. The lower panels show the spectrum after linear baseline subtraction (left) and scaled spectrum subtraction (right). While the spectrum subtraction removes a portion of the continuum, this is primarily in the region around the base of the red-shifted jet, where significant oversubtraction occurs creating strongly negative values. In fact, inspection of spectra sampled from the source region (above or below the jets) shows significant contamination by scattered [O I] emission from the red-shifted jet. As a result a 'clean' stellar spectrum cannot be sampled, and this subtraction method removes much of the jet emission rather than only the continuum. In addition, this technique resulted in oversubtracted regions visible in the channel maps, which would also make the data unsuitable for deconvolution

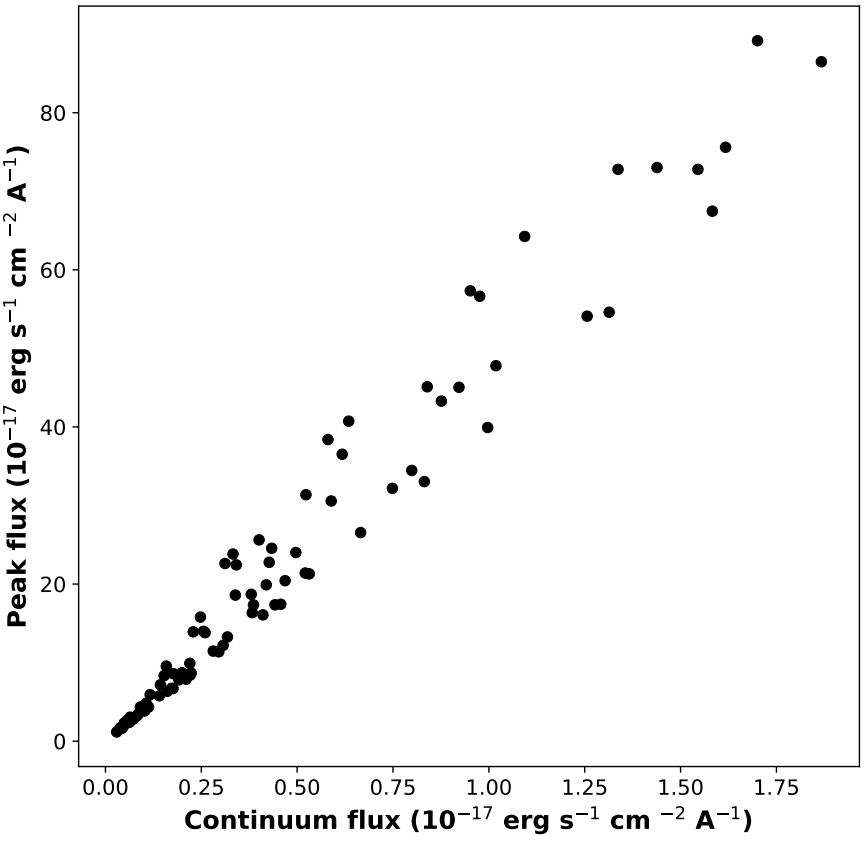

FIGURE 2.7: Peak versus continuum flux across the unsubtracted stellar region in [O I]λ6300 emission. The slope and hence ratio is approximately constant. All fluxes are given in units of 10^{-17} erg s^{-1} cm^{-2} $\mathring{A}^{-1}$.

procedures as discussed in Chapter 3, since negative regions produce severe artefacts during deconvolution. In contrast, while the baseline subtraction cannot remove the line emission from around the star, we see that it removes most of the continuum emission without also removing the jet close to the star or causing significant oversubtraction.

Neither subtraction technique allowed the isolation of an LVC in [O I], which may be due to a combination of the jet orientation and the velocity resolution of the MUSE instrument. Since the Th 28 jet is oriented almost parallel to the plane of the sky, it exhibits relatively small spectral dispersion between velocity components, and the LVC is expected to have a velocity of approximately 30 km s^{-1}. As the spectral resolution expected for MUSE in [O I]λ6300 is 100 km s^{-1}, this precludes isolating such a small velocity shift.

Given the issues described for scaled spectrum subtraction, a linear baseline subtraction method was chosen for all further analysis of the Th 28 observations. Figure 2.9 shows a comparison spectro-image of the jet in Hα before and after the subtraction. The continuum emission from the star is reduced in the second image, although the strong

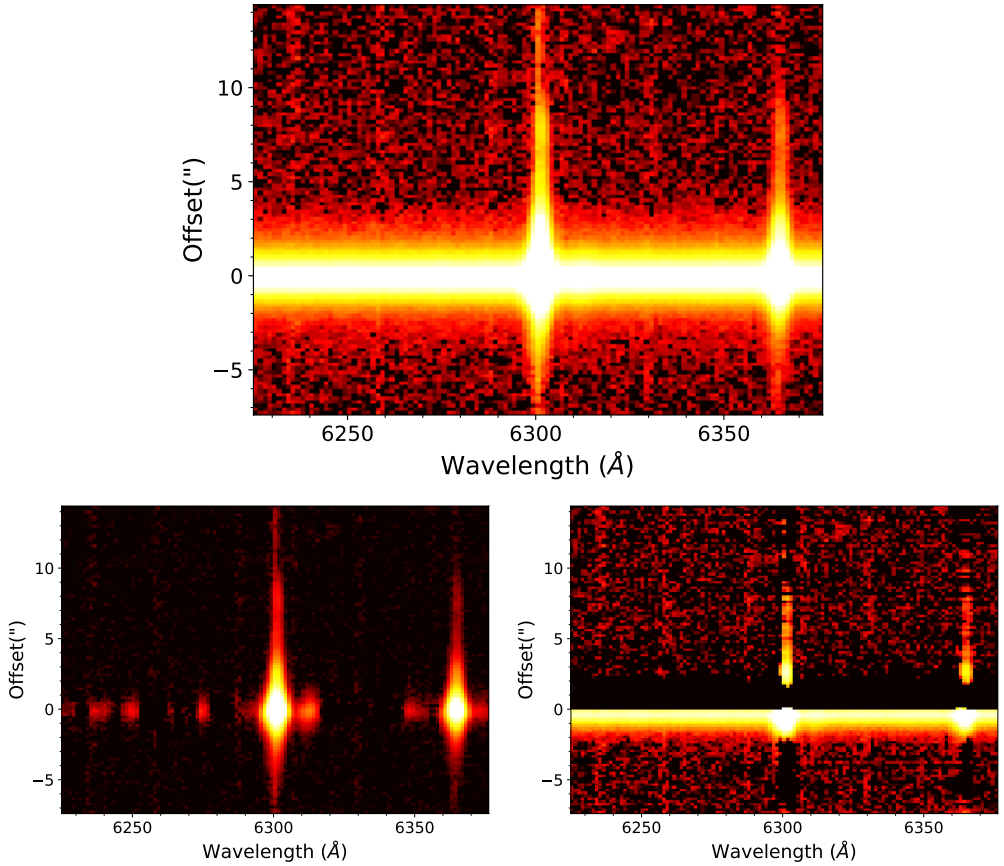

FIGURE 2.8: Top: Position-wavelength map of the [O I]λ6300 line along the jet axis. The stellar continuum is visible as the bright horizontal band. Bottom: The same map sampled after linear baseline subtraction (left) and after scaled spectrum subtraction (right).

line emission from the star and jet means that this is not obvious in the spectro-image. On the other hand we can see that the background stars have been successfully removed from the field, and the western Herbig-Haro object is still preserved for study. Of note in the lower left panel of Figure 2.8 is the thin vertical line close to 6300 Å; this represents residual sky emission. Of the emission lines which are important for this study, the bright [O I]λ6300 line is the only one with a significant residual sky contribution. This was removed by binning regions of sky emission in the [O I]λ6300 datacube to obtain an estimate of the average residual sky line; a Gaussian fit was made to this, which was then subtracted from the datacube at all positions.

2.6 Rotation Procedure

As the jet axis was at a slight angle to the perpendicular axis, a rotation procedure was implemented using the bright Hα emission from the more collimated red-shifted jet

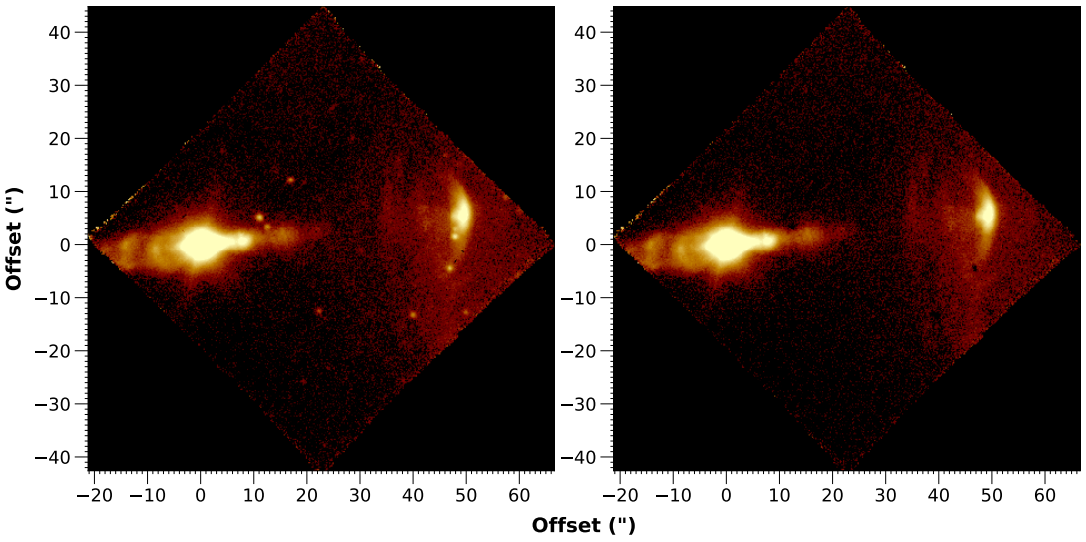

FIGURE 2.9: Image of the Th 28 MUSE field in Hα before (left) and after (right) continuum subtraction. Several background stars which can be observed in the left image are removed after subtraction. In the right panel a small oversubtracted region can also be observed in the faint lower wing of the bow shock HHW due to a bright star at this position causing the flux for removal to be overestimated.

lobe as a guide. The three central velocity bins of the Ha emission line were summed to create a combined image. A Python function *jetrotate()* was then implemented which uses one input LineCube as a reference cube (ideally containing the brightest emission line tracing the axis). The cube is binned over the velocity channels specified by the user to generate a LineSlice, and *beamfit()* is called to estimate the centroid positions along the jet axis. A linear fit through these then estimates the slope and the angle to the chosen image axis. For both the reference cube and any additional cubes included, a numpy interpolation routine *np.rotate()* is then used to rotate each of the wavelength slices through the specified angle, and a set of rotated cubes returned. (Alternatively, a user-defined angle can be preset rather than estimating it automatically.)

Using this routine, the image section containing the red-shifted jetlobe was sampled and binned in 2-pixel segments along the x-axis and the angle of the jet axis estimated to be 5.2° from the horizontal; the datacubes for each emission line of interest were then rotated to align them with the x-axis. The fitting procedure was repeated to confirm that the rotated jet axis was close to horizontal, with an estimated residual angle of 0.2°.

2.7 Summary

- In this chapter we have reviewed the main components of the data acquisition and reduction for the MUSE observation of Th 28, including the main steps in the data reduction pipeline used to produce the final calibrated datacubes.
- We also give an overview of the Python modules written to handle the data which form the primary tools used in the data analysis for this work. These are modules geared towards MUSE and other IFU datacubes from ESO instruments, with functions specialized to facilitate quick and easy analysis of jet observations.
- Two methods of continuum subtraction were considered to remove the stellar contribution from the spectra, however, a baseline subtraction method was chosen due to the heavy veiling of the Th 28 spectrum and the difficulty in sampling the stellar spectrum without scattered jet emission. The datacubes were also rotated to align the jet axis with the horizontal (x) axis of the image field of view.

Chapter 3

Morphology and Kinematics of the Th 28 Micro-jets

This section of the study focuses on the morphological features and kinematics of the micro-jets within approximately +/- 20" of the source, with the bow shock HHW to be examined in more detail in a later section. The top panel of Figure 3.1 shows the full Th 28 jet observed by the MUSE observations, illustrating the main features of interest.

Analysis of the full MUSE cube reveals a wealth of FELs as well as Hα and Hβ, tracing the inner jets. Following the data reduction and calibration outlined in the previous chapter, a full list of emission lines detected in the jet was compiled (see Table 3.1) and used to make a continuum-subtracted atlas of spectro-images (see Appendix A.1). To investigate the micro-jet structure in more detail, we use a deconvolution procedure to reduce the effect of seeing and increase the spatial resolution close to the source. This procedure and the results are described, as well as the identification of several new knots within the micro-jets, the kinematic information extracted, and the measurement of the jet width and centroid position along the axis of the micro-jets.

3.1 Morphology

3.1.1 Velocity Channel Maps

The majority of the jet emission can be binned into three velocity channels: a high-velocity blue-shifted bin from -200 to -90 km s^{-1}, a central low-velocity channel at +/- 90 km s^{-1}, and a high-velocity red-shifted channel from +90 to +200 km s^{-1}. Figure 3.1 shows these channel maps of the jet in Hα as well as the most important FELs from

λ_{air} (Å)	Line	Blue	Red	HHW
4861.3	Hβ	Y	Y	Y
4958.9	[O III]	Y	N	Y
5006.8	[O III]	Y	N	Y
5158.8	[Fe II]	N	Y	Y
5197.9	[N I]	N	Y	Y
5261.6	[Fe II]	N	Y	Y
5577.34	[O I]	Y	Y	N
5754.6	[N II]	N	Y	N
5875.9	He I	N	Y	N
6300.3	[O I]	Y	Y	Y
6363.7	[O I]	Y	Y	Y
6548.9	[N II]	Y	Y	Y
6562.8	Hα	Y	Y	Y
6583.5	[N II]	Y	Y	Y
6678.2	He I	N	Y	N
6716.4	[S II]	Y	Y	Y
6730.8	[S II]	Y	Y	Y
7065.2	He I	N	Y	N
7135.8	[Ar III]	Y	Y	N
7155.2	[Fe II]	N	Y	N
7172	[Fe II]	N	Y	N
7291.5	[Ca II]	N	Y	Y
7319	[O II]	Y	Y	Y

Continued on next page.

TABLE 3.1: All the emission lines in which the jet is detected.

Table 3.1 – Continued from previous page

λ_{air} (Å)	Line	Blue	Red	HHW
7323.8	[Ca II]	N	Y	Y
7330.2	[O II]	Y	Y	Y
7377.8	[Ni II]	N	Y	Y
7452.5	[Fe II]	N	Y	N
7636.2	[Fe II]	N	Y	N
8127.1	[Cr II]	N	Y	N
8498	Ca II	N	Y	Y
8542.09	Ca II	Y	Y	N
8617	[Fe II]	N	Y	Y
8891.9	[Fe II]	N	Y	Y
9051.9	[Fe II]	N	Y	N
9226.6	[Fe II]	N	Y	N
9267.6	[Fe II]	N	Y	N

Table 3.1 relevant to future diagnostic studies. Due to the small inclination of the Th 28 jet of $< 10°$ to the plane of the sky (discussed further in Section 3.1.4) the red- and blue-shifted jet lobes exhibit relatively small peak radial velocities, hence both jets can be observed in the central velocity channel. Emission from both can also be seen in the HV channels due to the FWHM of the jets (150 km s^{-1} and 260 km s^{-1} in the red- and blue-shifted jets respectively, measured in Hα at +/- 2-3" from the source). All velocities are quoted with respect to the systemic velocity of Th 28, measured by Graham & Heyer (1988) to be +5 km s^{-1}.

Although continuum emission has been subtracted, significant line emission is seen from around the star, which may be due to scattering of jet emission from a flared disk surface (see Burrows et al., 1996). Scattered emission from accretion flows close to the star may also contribute significantly to this. As it was not possible to obtain an uncontaminated stellar spectrum, any photospheric contribution cannot be readily removed. However, many features of the micro-jets can still be examined.

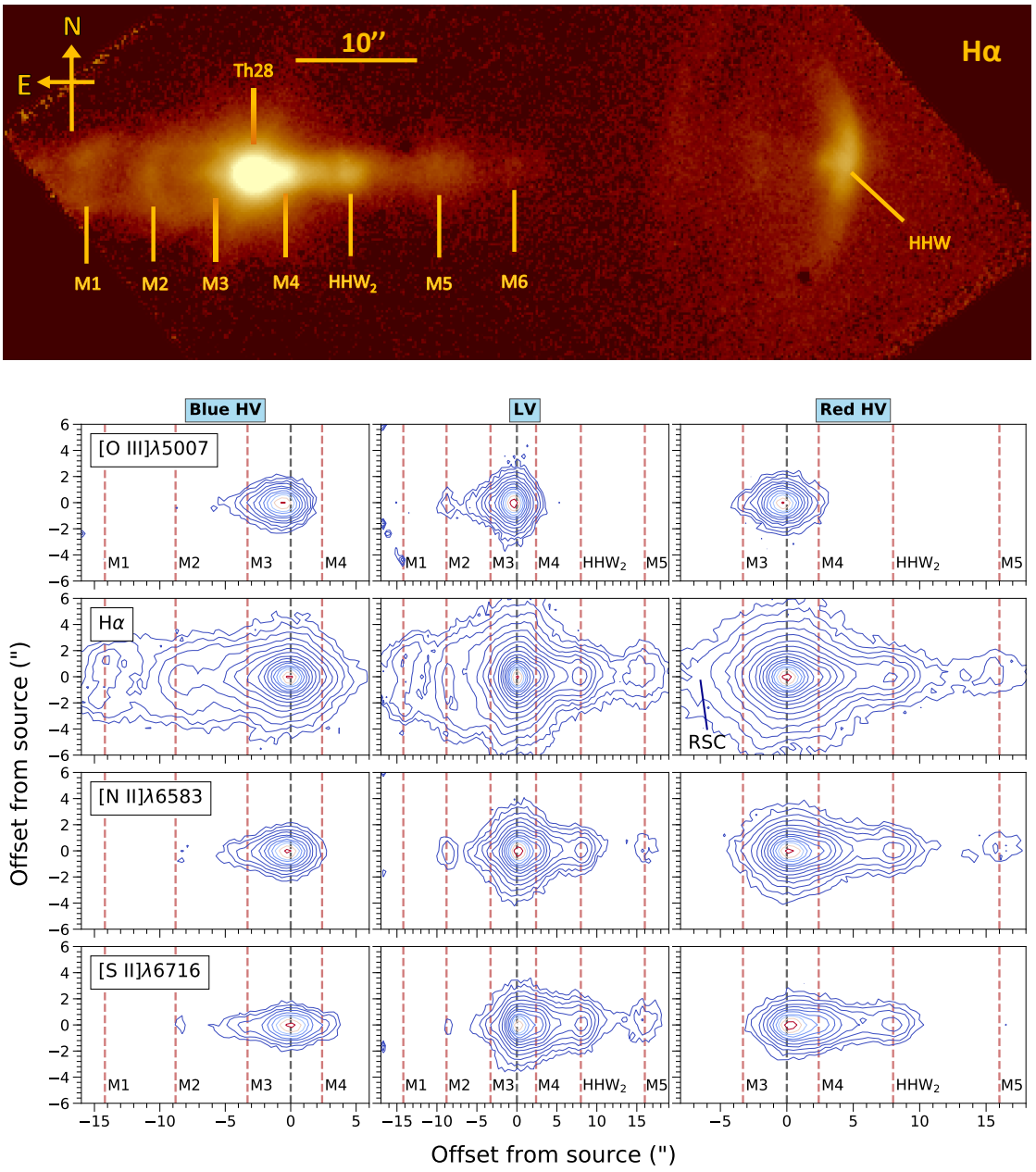

FIGURE 3.1: Top: The full MUSE view of the Th 28 jets, showing the combined Hα emission across all velocities before continuum subtraction. Below: Spectro-images showing the Th 28 jet emission from the primary optical FELs of interest. The positions of the star and all knots discussed in this paper are indicated with the vertical black (star position) and red (knots) lines. Contours begin at the 3-σ level, with adjacent contours increasing as a factor of $\sqrt{3}$. Left, the blue-shifted emission (-200 to -90 km s^{-1}). Centre: the central velocity bin (-90 to +90 km s^{-1}). Right: the red-shifted emission (+90 to +200 km s^{-1}). Note the presence of significant Hα emission in the red-shifted high velocity channel (labelled RSC).

The blue-shifted eastern jet is generally fainter in emission. It appears much wider and more diffuse in Hα emission, with two bow or bubble-shaped knot features visible at -8."8 and -14."2 from the driving source (labelled here M2 and M1). These knots

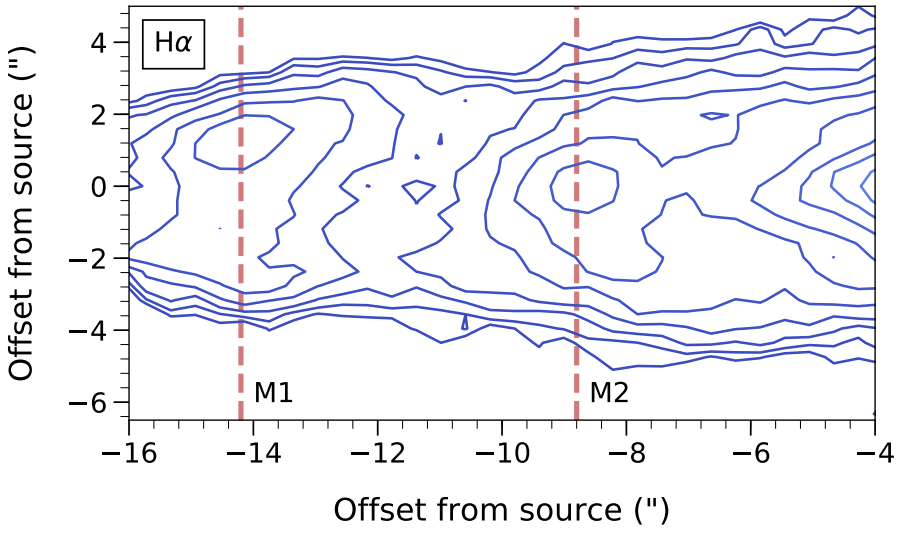

FIGURE 3.2: Bow-shaped knots in the eastern jet of Th 28, shown in blue-shifted Hα emission. Contours begin at the 4-σ level. The outer knot (left) is detected only in this emission line. Knot positions are marked with red lines.

have not been described in previous observations of TH 28 and are shown in more detail in Figure 3.2. Of the two, the inner knot M2 appears to be more cohesive, with a central prominent peak; by contrast M1 appears fainter and possibly fragmented, with the strongest peak not in the centre but offset approximately 1" north of the jet axis.

In contrast to the wide Hα flow, the FEL channel maps show the blue-shifted jet as a much more collimated flow extending to about 5" from the source, as well as emission from the peak of M2. The M1 knot is not visible in any lines other than Hα. Within 5" the blue-shifted lobe of the micro-jet is also visible in the *red-shifted* channels of Hα and [O III]λ5007 emission (see right panels of Figure 3.1) with $v_{rad} > +100$ km s^{-1}, which may be due to scattered emission from the red-shifted jet. The very base of the blue-shifted jet also appears to be detected in Hβ, [O I], [He I] and [Ca II].

The red-shifted western jet is brighter and detected in many more FELs than the blue-shifted jet (refer to Table 3.1 and atlas of channel maps), appearing as a collimated flow extending to a prominent knot at 7."8 from the source (HHW_2). Within the innermost region (< 5" from the source) the jet also appears in [Fe II], [He I], [N II] and [N I] lines. Visible in Hα, [N II] and [S II] are additional large knots at 16" and 21."6 (labelled M5 and M6 here). These are discussed further later in the chapter. Finally the large bow shock HHW is also visible in numerous emission lines as shown in Figure 3.3.

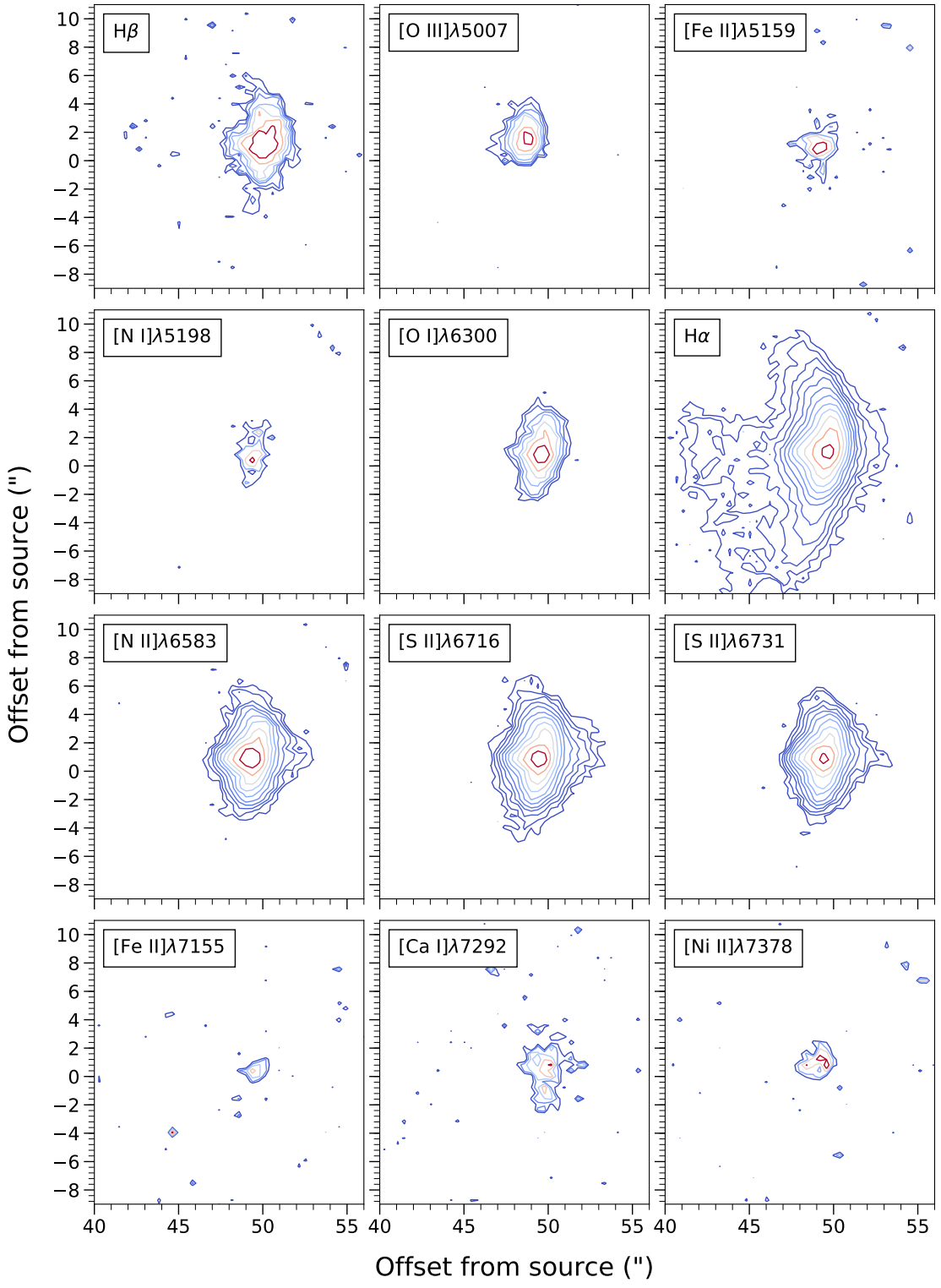

FIGURE 3.3: The western bow shock HHW shown in red-shifted emission. Contours begin at 4-σ of the background noise for the Hα channel and 2-σ for the fainter refractory lines ([Fe II], [Ca II] and [Ni II]); all other contours begin at the 3-σ level, and contours increase as factors of $\sqrt{2}$.

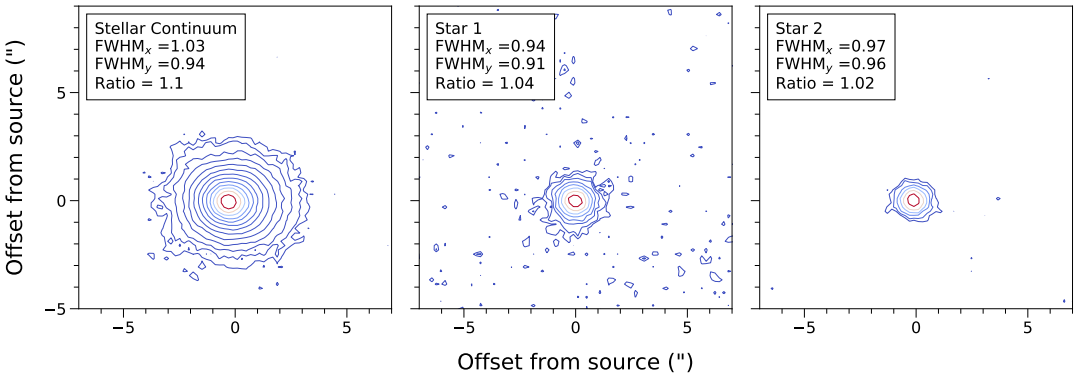

FIGURE 3.4: Spectro-images showing samples of the PSF estimated from continuum images of Th 28 (left) and two background stars (center, right) in the Hα wavelength band, with contours starting at 4-σ of the background noise and increasing as factors of $\sqrt{3}$. Measured FWHM values are given in the y and x directions (perpendicular to and parallel with the jet direction, respectively).

3.1.1.1 [O III] Emission and Refractory Species

As well as key FELs of O, N and S which are relevant for physical diagnostics of the jet conditions (discussed in depth in Chapter 5), we note the detection of the micro-jets in several other emission lines of interest, in particular the presence of [O III]λ5007 emission from the blue-shifted jet, shown in Figure 3.1. This line was previously reported by Comerón & Fernández (2010) and associated with the stellar wind; however, in this data the [O III] emission is clearly seen from the micro-jet and the centre of the first bow shock M2. That this is seen in the blue- and not the the red-shifted lobe is consistent with previous estimates indicating the blue-shifted jet is more strongly ionised (Liu et al., 2014). However, it is especially interesting as an indicator of shock velocities >100 km s^{-1}.

The jet is furthermore detected in several refractory species, including several lines of [Fe II] extending along the red-shifted micro-jet. Liu et al. (2021) reported the detection of permitted lines of Ca II in the red-shifted jet to a distance of 0.”5. We also see a possible extension of Ca II emission extending to approximately 2” in this jet, as well as forbidden [Ca I] and [Ca II] lines which trace the red-shifted flow as far as the bright knot HHW$_2$. These are of interest as emission lines such as [Fe II] and [Ca II] provide flux ratios useful for diagnostics of the conditions within the jet as well as allowing the abundance of dust and the shock structures within the jet to be investigated (Nisini, 2009; Podio et al., 2009; Giannini et al., 2013).

3.1.2 Deconvolution

To enhance detail in the jet regions closest to the star, a Richardson-Lucy deconvolution algorithm was applied to the continuum-subtracted data. Background regions of the continuum-subtracted image were sampled to estimate the residual background flux. This offset was subtracted from the image and included as a parameter in the deconvolution task.

To obtain an estimate of the PSF, we sampled continuum images of Th 28 and the two brightest background stars in the FOV. In each case, the images were found as an average of the continuum emission on both sides of the emission line of interest. Figure 3.4 shows examples for the PSF in the Hα region, while the full set of measurements are tabulated in Table 3.2. To evaluate the PSF shape, we fitted each sample with a Gaussian function along cross-sections in the x and y directions (parallel to and across the jet axis direction). We find that the PSF consistently shows a small elongation in the x direction; however, this is slightly more pronounced in the continuum image of Th 28, reflecting a probable contribution from scattered light along the jet axis.

We therefore attempted to carry out deconvolution using as the PSF an image of a 2D Gaussian function with the FWHM values fitted from the brightest background star; this would avoid artefacts introduced by masking additional nearby background stars. However, the resulting deconvolved images suffered from heavy artefacting close to the star and the inner part of the micro-jets. We were instead able to use the bright continuum image of Th 28 as the PSF, which prevented this artefacting despite the slightly elongated PSF shape. The average FWHM$_y$ was 0.”94, with average FWHM$_x$ 1.”03 along and across the jet axis respectively, making the PSF slightly wider than the average estimated seeing of 0.”9. The PSF shape appears to have no significant impact on the results obtained from the deconvolved images which are discussed in the rest of this chapter.

The spectro-image of the inner jet at each wavelength was then deconvolved with the estimated PSF for 20 iterations using the IRAF *lucy* task. The instrument gain was taken to be 1.1 and the readout noise to be 2.6 (from the MUSE User Manual). This produced a recompiled data cube of the deconvolved line emission at each wavelength. The average PSF FWHM estimated from the continuum emission at the source position was reduced from 1.”0 before deconvolution to 0.”44 after deconvolution. Figures 3.5 and 3.6 show spectro-images of the inner region of the jet before and after deconvolution using the IRAF Lucy-Richardson routine. The scattered [O I]λ6300 emission seen on the blue-shifted side of the star is absent in the deconvolved images, and more structure

can be seen in both jets. This is especially visible in the more diffuse blue-shifted jet, where the knot M3 can now be seen at -3."3.

Examination of the deconvolved spectro-images shows multiple knots which are consistent with those in the images before deconvolution, and a couple which were not previously visible. In most of these lines, the deconvolved central and red-shifted images show up to three knots visible in the inner red-shifted jet, at positions of 2."5, 5."4, and 7."8 from the central source. In the blue-shifted jet the large knot at 8."8 is clearly seen in the deconvolved images, as well as a series of smaller possible knots at -3."3, -5" and -6" from the source. The fitted positions of these knots do not appear to change after the deconvolution; only the peaks of the knots closest to the source (+2."5 and -3."3) become more distinct and thus can be fitted more accurately.

3.1.3 Knot Identification

In total, we detect six new knots (labelled M1 to M6) not previously identified in the Th 28 jet. M1, M2, M5, and M6 are visible before deconvolution while M3, and M4 are only clearly detected after deconvolution. To further examine the new knots detected in the deconvolved image, profiles of the flux along the jet axis in Hα and [S II] emission, both before and after deconvolution, were analysed. Examples are shown in Figure 3.7. In general, these show peaks corresponding well to the knots seen in the channel maps. Although the deconvolved profiles are limited to the inner 10" of the micro-jets, they clearly show bumps representing possible knots in the inner jet which are not obvious beforehand. Error bars shown at the position of peaks representing potential knots are estimated as 1-σ of the background before deconvolution. Each of these new knots, as well as the previously reported HHW_2 and HHW, are discussed individually below.

Beginning with the blue-shifted jet, the two knots M1 and M2, at projected distances of -14."2 and -8."8 respectively, are well detected in both spectro-images and in the flux profiles, though the former is only visible in Hα emission as described above and is outside the region of deconvolution. Their bow-shaped morphology is dissimilar from the shape of the other knots which are far enough from the star to observe a distinct shape. Further in, the knot M3 at -3."3 appears faintly visible as a 'shoulder' in the flux before deconvolution, but becomes a distinct peak in the deconvolved images and flux profiles. To further investigate the veracity of both this and the knot M4, discussed below, we examined PV maps from X-Shooter[1] observations of the jet taken in 2015 (shown in Figure 3.8). These show a knot visible in the [O II] emission of the blue-shifted jet at -3."77. This further implies a proper motion of 0."47 yr^{-1} for M3.

[1]X-Shooter is an intermediate-resolution spectrograph also at the VLT and covering the 3000-25000 $\AA$ range, with separate UV, optical and IR arms. See Vernet et al. (2011).

	Th 28			Star 1			Star 2		
Line	FWHM$_y$ (")	FWHM$_x$ (")	Ratio	FWHM$_y$ (")	FWHM$_x$ (")	Ratio	FWHM$_y$ (")	FWHM$_x$ (")	Ratio
Hα	1.03	0.94	1.1	0.94	0.91	1.04	0.97	0.96	1.02
[N II]λ 6583	1.03	0.94	1.1	0.95	0.91	1.04	0.98	0.96	1.02
[O I] λ6300	1.05	0.95	1.1	0.99	0.94	1.06	1.04	1.04	1.0
[S II]$\lambda\lambda$6716/31	1.02	0.93	1.1	0.94	0.91	1.04	0.94	0.94	1.0

TABLE 3.2: Table of FWHM values estimated for the sampled PSFs (shown in Figure A.6).

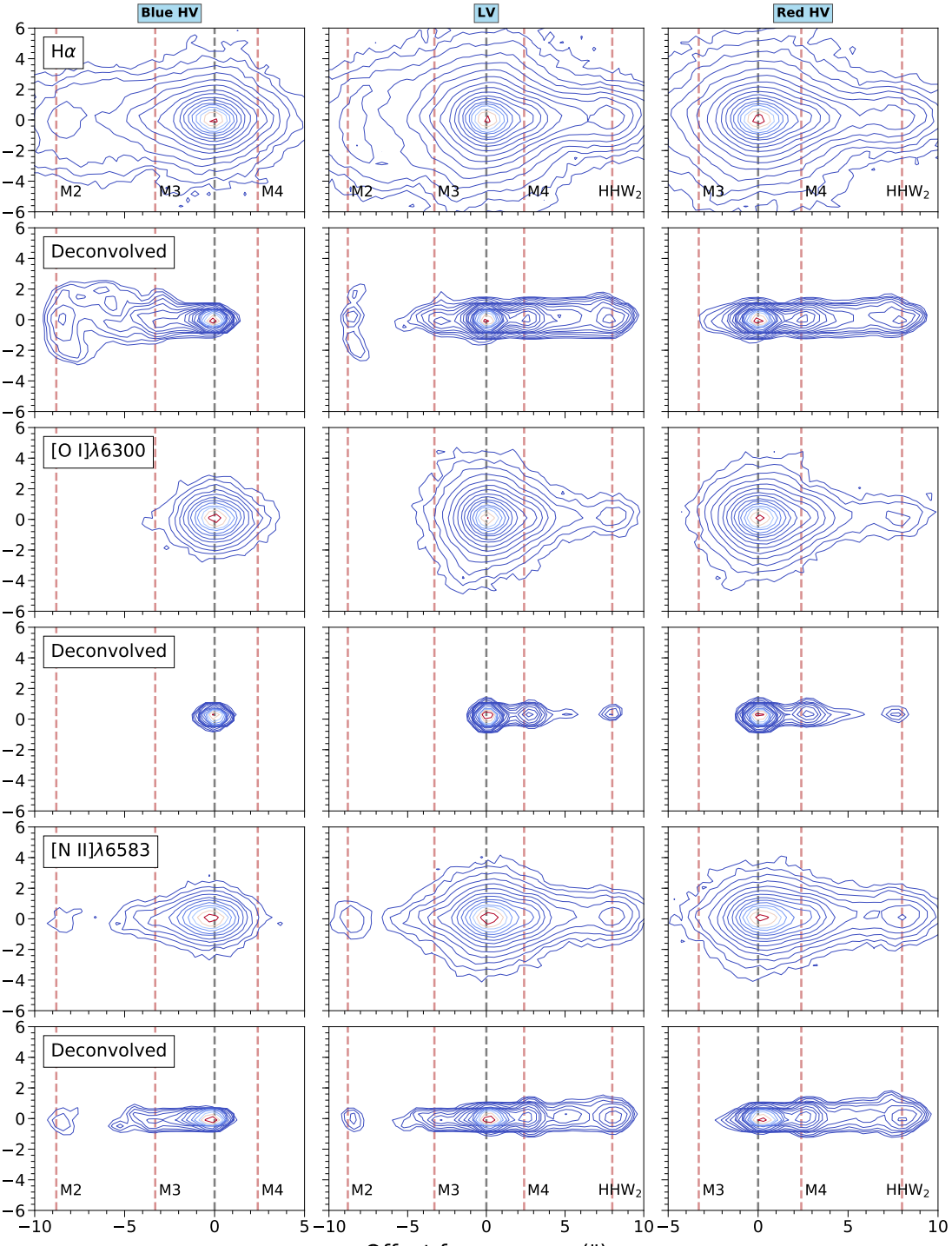

FIGURE 3.5: Spectro-images showing the primary emission lines before and after Lucy-Richardson deconvolution (20 iterations), shown in three channels: the blue-shifted HVC (-150 to - 90 km s^{-1}); centre, the low-velocity channel (+/- 90 km s^{-1}); and the red-shifted HVC (+90 to -150 km s^{-1}). The inner jet region in each emission line is shown first with the same region after deconvolution shown below it. Contours begin at the 3-σ level. Star and knot position markers as in Figure 3.1.

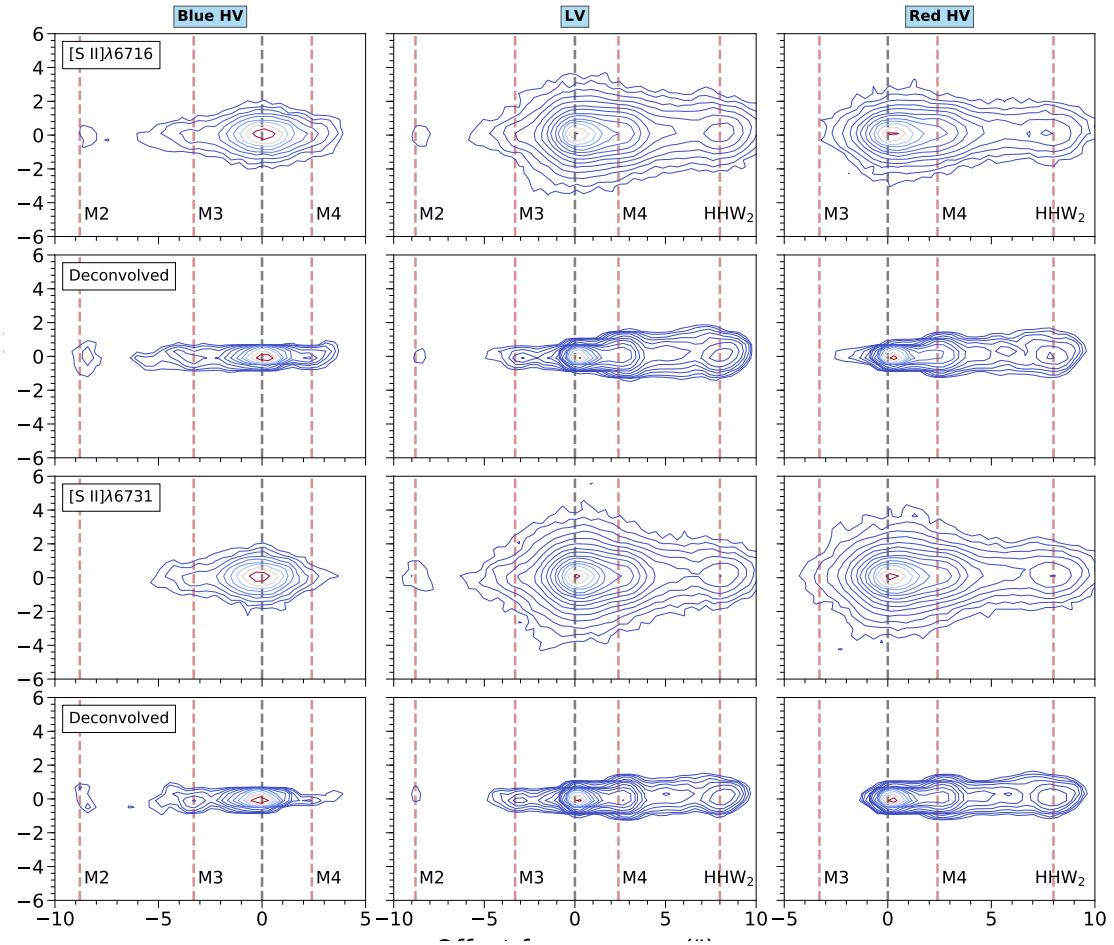

FIGURE 3.6: Continuation of Figure 3.5, showing the second [S II] line before and after deconvolution.

In the flux profile of the red-shifted jet, similarly, a distinct shoulder can be seen at about +2."5 to 3" which becomes a distinct knot (M4) in the deconvolved flux profiles and channel maps. This knot is also seen in channel maps and PV diagrams of the [Fe II]λ7453 line before deconvolution. The peak is fitted to +2."5 from the source and can also be seen in the X-Shooter data at + 2."85 from the source.

Comerón & Fernández (2010) previously identified another knot within this region of the red-shifted jet, designated HHW_2 and estimate its proper motion at 0."34 yr^{-1}. Based on the position of this knot at 4."5 in 2004, with a proper motion of 0."34 yr^{-1}, its position in 2014 would correspond almost exactly to the bright red-shifted knot centred at 7."8. We therefore identify this as HHW_2, the only knot within our region of interest to have been previously reported. Additionally, the two weaker knots at 16" and 21."6 are visible in the flux profiles of Hα; as with the eastern knots, only the inner and brighter of these two is visible in [S II] as well.

Finally, although the large red-shifted bow shock HHW is nominally outside the micro-jet region which is the focus of this chapter, it is included here for a complete

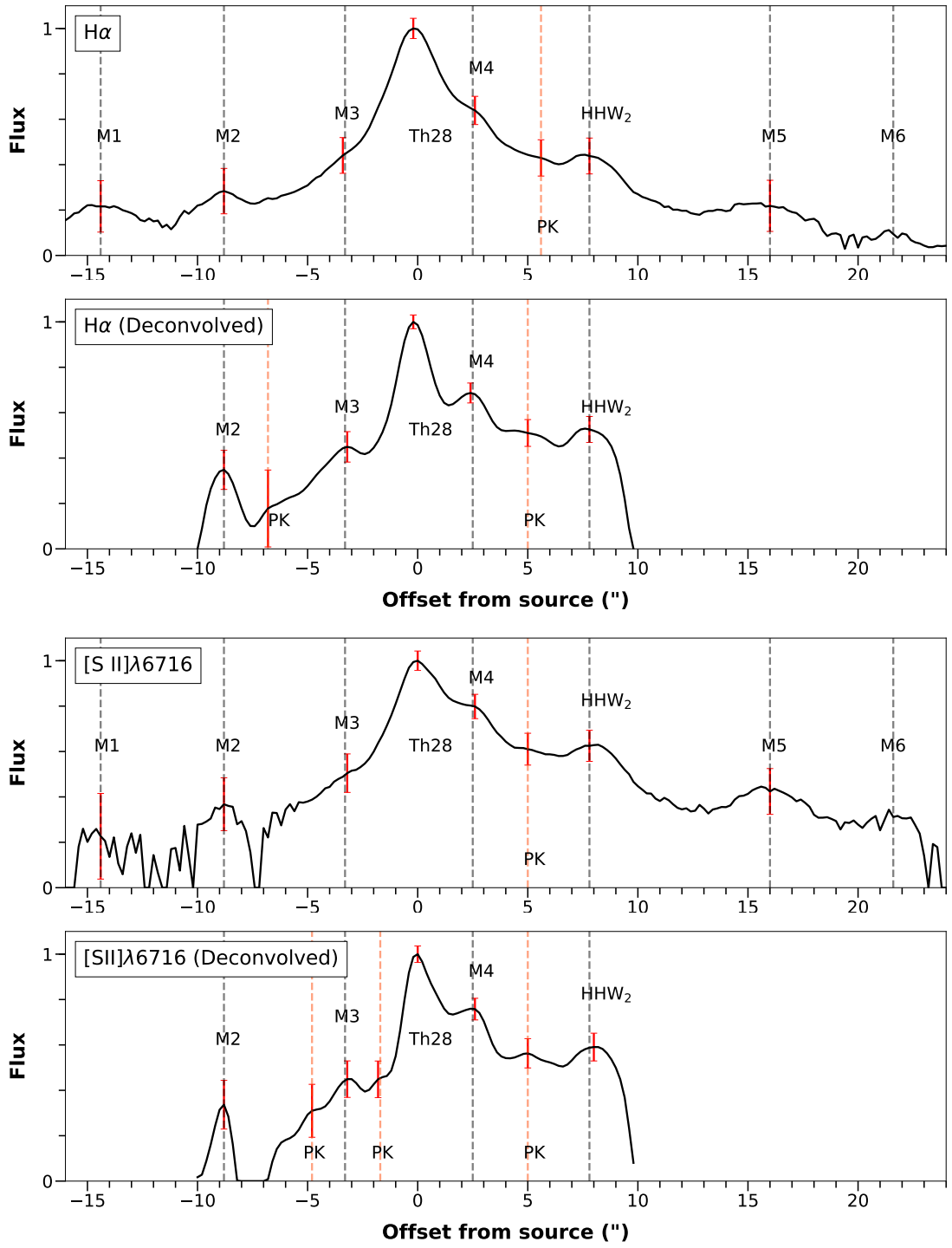

FIGURE 3.7: Hα and [S II]λ6716 flux along the axis of the jet, taken from a horizontal slice through the jet centre after rotating the velocity-binned image by -5.2°. Profiles are shown taken before and after deconvolution, with deconvolved profiles truncated at ± 10". The flux axis is plotted on a log scale to prevent the plot being dominated by extremely high flux around the star and normalised to better compare the profiles in both lines. Possible knots are marked as PK.

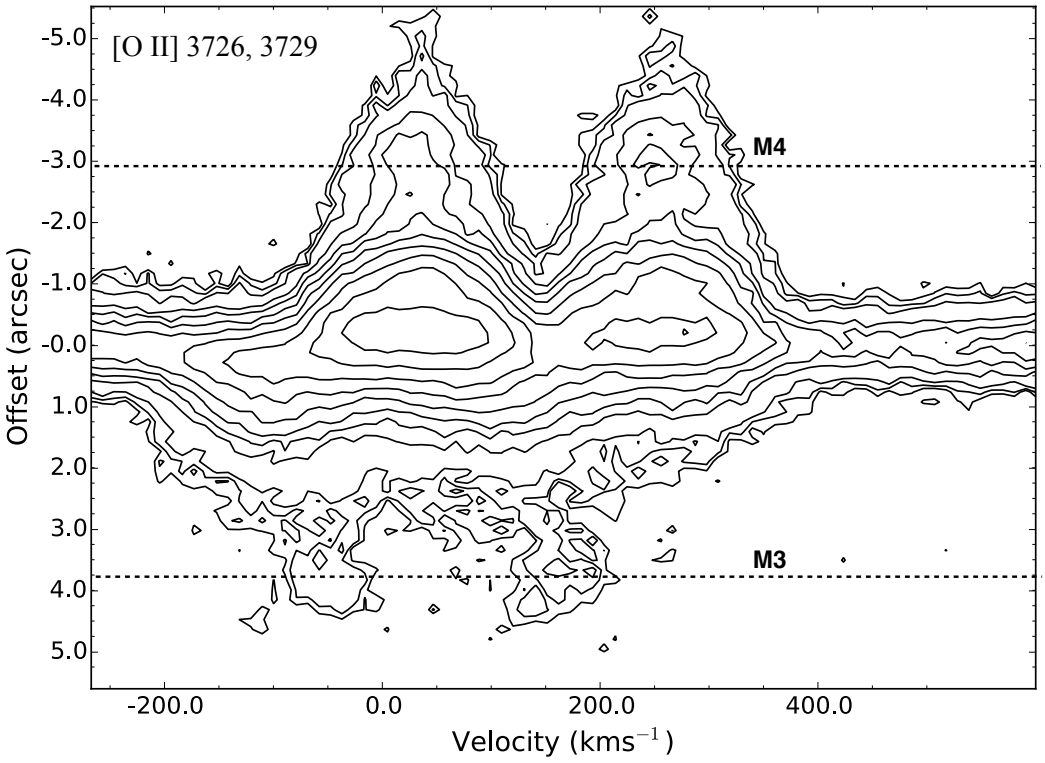

FIGURE 3.8: PV map of the Th 28 jet showing the [O II]$\lambda\lambda$3726, 3729 doublet in the inner jet region, with the spatial axis centred at the source position. The data is obtained from X-Shooter observations in 2015, and the positions of the knots M3 and M4 are marked.

picture of the knots in the jet. HHW has been identified in numerous observations of the Th 28 jet; its central position was measured at 45."2 from the source in 2004 (Wang & Henning, 2009) and its tangential velocity estimated to be 0."4 yr^{-1}, (Comerón & Fernández, 2010). We measured its position to be 49."6 from the source in 2014, giving a slightly higher proper motion estimate of 0."44 yr^{-1}.

Figure 3.9 shows a comparison plot of all knot positions within the MUSE FOV during the 2014 observations, including the new knots we have identified. We mark both the actual and predicted positions (red crosses) of HHW and HHW$_2$. The predicted positions are almost perfectly aligned with their observed positions in 2014, supporting the proper motion estimates previously made.

The peaks marked as possible knots in the flux profiles and in deconvolved channel maps at -6."6 and 5" - 6" may be discussed together since they have several features in common: they appear in similar positions either side of the source, they are both visible as weak bumps in the flux profiles, and it is unclear whether they constitute one or possibly more knots. While their appearance is consistent across lines and velocity bins, the number of bumps in each region varies, and the channel maps do not resolve distinct

knots in these regions before deconvolution. Perhaps notably, both of these bumpy jet regions lie just behind the large knots at M2 and HHW_2. Given this inconsistency, and that neither the PV diagrams nor the spectro-images before deconvolution show knots at these positions, we consider these to be artefacts of the deconvolution rather than true knot structures.

3.1.3.1 Knot Proper Motions and Ages

Proper motions can be obtained both for those knots previously reported, and for the new knots M3 and M4 by comparing their knot positions in the MUSE and X-Shooter observations. This allows us to constrain the proper motions close to the driving source. In the red-shifted micro-jet, we detect M4 at +2."5 in 2014, and at +2."85 in 2015. This gives us an estimated proper motion of 0."35 yr^{-1}. This is consistent with the estimate of 0."34 yr^{-1} for HHW_2 (Comerón & Fernández, 2010).

For the blue-shifted lobe, the knot M3 found at $\sim$ -3."3 in 2014 is found at -3."77 in 2015, giving an estimated proper motion of 0."47 yr^{-1}. This is the same as the proper motion of the closest blue-shifted HH object HHE_1 as estimated by Wang & Henning (2009), and a little higher than the 0."43 yr^{-1} found by Comerón & Fernández (2011).

The knot proper motions in the red-shifted jet are generally well-constrained. With an uncertainty of 0."1 on the estimated knot positions, an uncertainty of 0."14 yr^{-1} for M3 and M4 is obtained by error propagation. For HHW_2 and HHW which have broader peaks in the flux profiles, we allow an uncertainty of 0."2 in their positions in the MUSE data, and find proper motion uncertainties of 0."05 yr^{-1} (note that the proper motion uncertainty is reduced due to the longer baseline between observations used to measure these proper motions). The uncertainty of the knot ages is then estimated by combining these in quadrature with the estimated uncertainty on the knot positions as given in Table 3.3. The remaining micro-jet knots, M1, M2, M5 and M6 were not within the spatial range of the X-Shooter data; we therefore take their proper motions as those of M3 and HHW_2 for the blue- and red-shifted knots respectively.

The profiles of the jets are generally striking in their spatial symmetry, as can be seen in the figures. Both have knots at about 15 ", 8 ", and 3 " from the source. We therefore estimate the ages of the knots (shown in Table 3.3) and find that several knots appear to be paired with counterparts in the opposite jet. The innermost pair (M3 and M4) at +2"-3" were both ejected in 2007 ($\pm$ 2 yrs), while HHW_2 appears to have been ejected in 1992 $\pm$ 7 yrs, close to the first blue-shifted bowshock at -8."8 in 1995 $\pm$ 8 yrs. The blue-shifted bowshock M1, at -14."2, may be the counterpart of the red-shifted knot M5 at +16", however their estimated ages and corresponding ejection times (1984 and

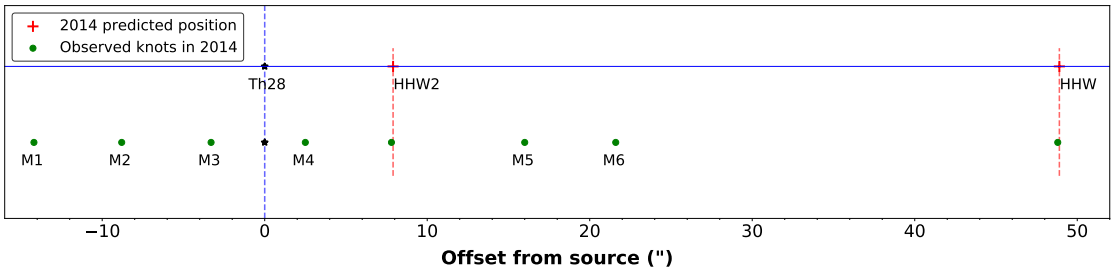

FIGURE 3.9: Knot positions along the jet axis within the FOV of our MUSE data. Also plotted are the predicted positions of HHW and HHW2 based on previous velocity and position measurements; these correspond almost perfectly with their positions in our observations.

1968) are significantly different, even given the large uncertainty of 13 years associated with each. This may be due to the blue-shifted knot being slowed by interaction with the surrounding medium, although individual proper motion estimates would be needed to check if M1 is moving more slowly than estimated.

For HHW, with a proper motion of 0."4 yr^{-1} (Comerón & Fernández, 2010), we infer it to have been ejected around 1890 ± 15 years. We can compare this with HHE_1, which was observed at -39" from the source by Wang & Henning (2009) in their 2004 observations and for which Comerón & Fernández (2010) gives the ejection year to be 1915 (± 7 years, taking the estimated uncertainty of 0."03 yr^{-1} on the proper motion). If this knot represents a counterpart to HHW, it then seems likely that the proper motions of one or both knots have changed significantly over time. Previous work estimating the ages of the knots in the extended blue-shifted jet indicated intervals as short as 50 years between ejections, and noted that the decreasing intervals between knots closer to the source might suggest an increase in the frequency of knot ejection. However, as this work shows, Th 28 appears to be forming knots on much shorter timescales of ∼10-15 years, making it more probable that intervening knots have simply become too faint to be detected; indeed, this can be clearly seen with the red-shifted knots from 8-22", which are progressively fainter with the M6 knot falling below the 3-σ detection level.

3.1.3.2 Knot Radial Velocities

For each of the identified knots, the radial velocity in Hα and [S II] was measured using a spectrum summed over a 1" × 1" region around the knot centre. This was carried out for both the unconvolved and deconvolved data cubes; the former are discussed here, while the effects of deconvolution are discussed in a later section. As an example, the fits to the unconvolved Hα cube are shown in Figure 3.10; the full set of radial velocity fits is contained in Appendix A.3.

Jet	Knot	Offset (")	PM (" yr^{-1})	v_{tan} (km s^{-1})	v_{rad} (km s^{-1})	FWHM (km s^{-1})	i_{knot} (°)	Age (yr)
Blue	M1	-14.2 ± 0.1		-357	-85	160± 5	13.4± 3.5	30.2 ± 13
	M2	-8.8 ± 0.1		-357	-80	175± 5	12.6± 3.5	18.7 ± 8
	M3	-3.3 ± 0.1	0.47± 0.1	-357	-60	210± 6	9.5± 3.0	7.0 ± 2
Red	M4	+2.5 ± 0.1	0.35± 0.05	266	+20	140± 4	4.4± 2.5	7.1 ± 2
	HHW_2	+7.8 ± 0.1	0.34± 0.05	258	+30	120± 4	6.6± 2.5	22.3 ± 7
	M5	+16 ± 0.1		266	+30	120± 4	6.4± 2.5	45.7 ± 13
	M6	+21.6 ± 0.1		266	+25	120± 4	6.4± 2.5	61.7 ± 18
	HHW	+49.6 ± 0.1	0.4± 0.05	304	+35	120± 4	6.6± 2.5	124 ± 31

TABLE 3.3: Table of knots detected in the MUSE observations. The first column specifies in which jet (blue- or red-shifted) each knot is observed. Distances are projected; radial velocities and FWHMs are measured from the [S II] lines except for M1 which is measured only in Hα.

		Radial Velocity (km s^{-1})				FWHM (km s^{-1})			
Knot	Offset (")	Hα	[N II] 6583	[S II] 6716	6731	Hα	[N II] 6583	[S II] 6716	6731
M1	-14.2	-85				160			
M2	-8.8	-77	-79	-74	-85.5	200	160	190	150
M3	-3.3	-37	-61	-54	-65	260	205	210	200
Th 28	0.0	+14	+9	+10	+4	214	155	150	185
M4	2.5	+22	+20	+21	+19	150	140	140	140
HHW$_2$	7.8	+27	+31	+31	+27	130	120	120	120
M5	16.0	+30	+26	+32	+30	130	120	120	120
M6	21.6	+28	+25			115	120		100
HHW	49.6	+35	+33	+36	+33	125	120	115	115

TABLE 3.4: Table of radial velocities and FWHM values estimated for the knots in the Th 28 jet. Note that the values for v_{rad} have an approximate uncertainty of 10%, while the FWHM values have uncertainty of 3-5%.

Table 3.4 shows the full set of radial velocity and FWHM measurements for the identified knots in Hα, [S II] and [N II]. All velocities are given in the barycentric frame and have been corrected for the systemic velocity of +5 km s^{-1}. The knots in the blue-shifted jet show consistent velocities of -60 km s^{-1} to -80 km s^{-1}, a factor of 2-3 larger than the +20 km s^{-1} to +35 km s^{-1} radial velocities found in the red-shifted knots this is consistent with previous estimates for the velocities of the HH objects associated with either jet (Comerón & Fernández, 2010, 2011). Uncertainties on the FWHM of the lines were estimated using both the estimated uncertainty on the Gaussian fit and the equation given by Porter et al. (2004) as $\delta\sigma = \frac{\sigma}{\sqrt{2}S/N}$. As the latter equation gave estimated uncertainties of $< 1\%$, we adopt the more conservative error of 3-5% from the fitting routine.

Of note, the innermost knots M3 and M2 both show slightly lower radial velocities (-60 km s^{-1} and +20 km s^{-1}) than the other knots in their respective jets. This may indicate that the jet at these positions contains a contribution of scattered light from the opposite lobe, 'pulling' the overall spectrum back towards 0 km s^{-1}. The bright red-shifted lobe might then be less affected by scattered emission from the blue-shifted lobe, and indeed the discrepancy ($\sim$20 km s^{-1}) is greater between M3 and the other blue-shifted knots than it is for M4 versus the other red-shifted knots ($\sim$5-10 km s^{-1}).

In particular, the velocity of M3 measured in Hα is found to be -37 km s^{-1}, roughly half that measured in FEL emission; this is likely a symptom of the Hα emission being affected by reflected emission from near the star and inner disk; we note also that in the blue-shifted jet and near the source position, the Hα emission seems to trace a broader component, approximately 230 au in width compared with values of 150-200 au for the FELs. This may suggest that the Hα emission traces a slower, wider flow in the jet. As a result, we take the radial velocity measured in [S II] to be a more accurate measure for the knot. The radial velocities given in Table 3.3 are taken from the [S II] measurements.

3.1.4 Jet Inclination Angle and Velocity

The estimated proper motions of the blue-shifted and red-shifted knots are 0."47 yr^{-1} (from M3) and 0."35 yr^{-1} (from M4, HHW$_2$), respectively. Assuming a distance of 160 pc, and taking the overall radial velocities of the two jets to be -80 km s^{-1} and +30 km s^{-1}, the velocities of the red and blue-shifted jets are estimated at 270 km s^{-1} $\pm$ 30 km s^{-1} and 365 km s^{-1} $\pm$ 60 km s^{-1}, respectively, with corresponding inclination angles of +6.5° and -13.0° to the plane of the sky. This estimate excludes the innermost knots M3 and M4 since their radial velocities are likely to be underestimated as discussed above. Uncertainties on the radial velocities are taken to be 10% of the velocity resolution, approximately 10 km s^{-1}. The full set of inclination angles based on the measurements for individual knots is given in Table 3.3.

The knots within each of the jets give a consistent, if somewhat puzzling, picture. The red-shifted knots generally agree with an inclination angle of 6-7.5°, whereas the blue-shifted knots show an inclination angle that is twice as large, at 10-13° towards the observer. These findings are in line with previous estimates based on the proper motions and radial velocities of the outer HH objects (see Chapter 1); however, we note that this implies a substantial difference in inclination angle of 5-6° between the two jets. Some stellar jets are known to possess lobes with deflected or misaligned axes, and while we detect no difference in the PA of the Th 28 micro-jets (discussed in Chapter 4), it is possible that there is a small deflection in PA $\leq$ 1°.

3.2 Jet Beam Width and Centroids

3.2.1 Jet Width and Opening Angles

The jet width (FWHM) is measured by Gaussian fitting of the jet cross-section, using the deconvolved data cubes to remove the effect of the seeing. Each cross-section has

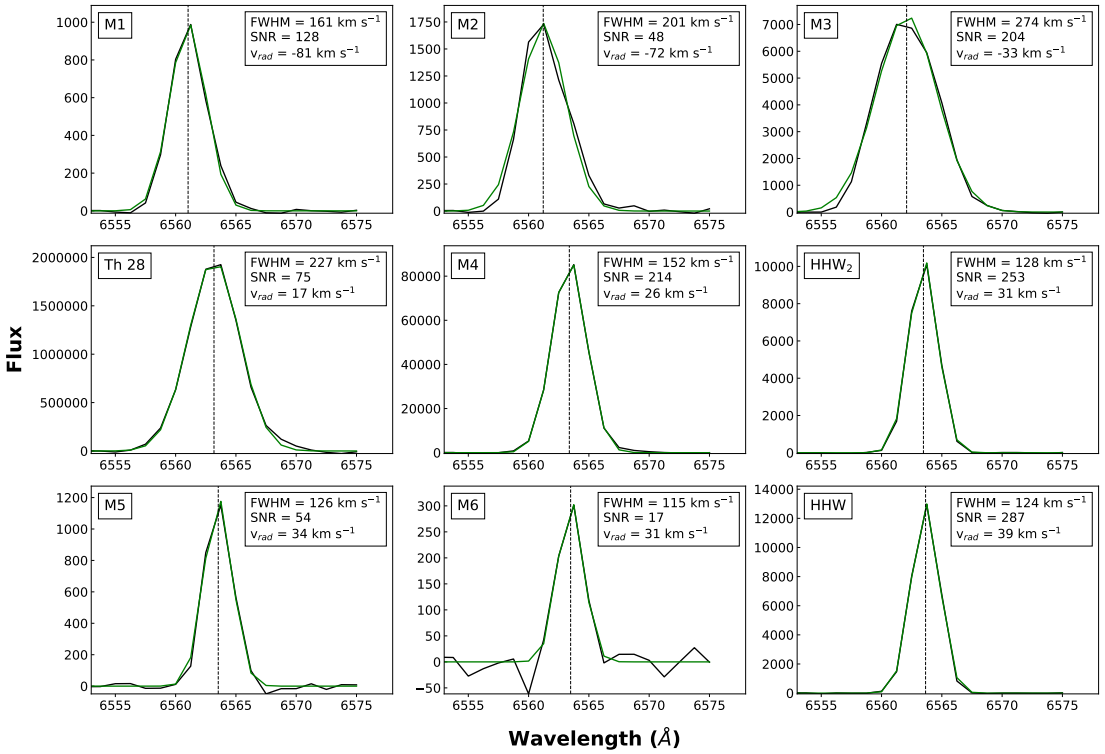

FIGURE 3.10: Fits to the peak radial velocities of the knots detected in the Hα micro-jets and source position. Line profiles are binned from a 1" x 1" region centred at the knot position.

spatial binning of 1" along the jet axis; measurements are taken from the centres of the detected knots (avoiding the wings of the spatial PSF in the x-direction) to obtain accurate estimates of the jet width (Raga et al., 1991; Mundt et al., 1991). The jet width at the source position is subtracted in quadrature from the fitted width along the jet axis to recover the intrinsic width. FWHM uncertainties are estimated as in Section 3.1.3.2.

Examples of the resulting fits for both micro-jets are shown in Figures 3.11 and 3.12 (for the full catalogue of fits see Appendix A.4). Measurements below the FWHM of the source PSF (∼0."4 in the deconvolved images) were excluded. To estimate the full jet opening angle α we combine these with the HST-STIS measurements from Coffey et al. (2007). In the red-shifted jet this adds optical-line jet width estimates of 0."27 and 0."41 at +0."3 from the source (43-66 au width at a distance of +48 au). In the blue-shifted jet only NUV measurements are available, which gives an upper estimate of 0."2 at -0."3 from the source (32 au width at -48 au distance). The opening angle in each case is calculated using the deprojected knot positions (with $i_{red} = 6.5°$, $i_{blue} = -13°$) and we quote the positions below accordingly.

Table 3.5 shows the estimated opening angles for both jets based on several velocity bins of the Hα and [S II]$\lambda\lambda$6716, 6731 emission. In the red-shifted jet we measure an

Jet	Line	$>v_{rad}$ (km s^{-1})	$<v_{rad}$ (km s^{-1})	FWHM (au)			α (°)
				M3	M4	HHW_2	
Red-shifted	Hα	-30	+30	-	110	160	4.8
		+30	+90	-	114	168	5.2
		+90	+150	-	107	150	4.4
		-30	+150	-	112	163	4.9
	[S II]λ6716	-30	+30	-	149	202	6.7
		+30	+80	-	155	190	6.2
		+80	+140	-	155	178	5.5
		-30	+140	-	154	192	6.2
	[S II]λ6731	-30	+30	-	114	154	4.5
		+30	+80	-	128	162	4.9
		+80	+140	-	133	160	4.8
		-30	+140	-	126	160	4.8
Blue-shifted	Hα	- 30	- 140	165	-	-	15.6
	[S II]λ6716	- 30	- 140	115	-	-	9.9
	[S II]λ6731	- 30	- 140	93	-	-	7.3

TABLE 3.5: Table of fitted opening angles for both micro-jets based on deconvolved Hα and [S II] emission.

average width of 130 au at knot M4 (+2.6"), with a slow increase to 170 au at the position of HHW_2 (+7."8). In both knots the [S II]λ6716 line shows a somewhat larger width than in Hα or [S II]λ6731; For the red-shifted jet we find full opening angles of 4.5-6°, with no clear trend between velocity channels. These results are in line with opening angles of 2° - 4° measured in a number of other jets (Burrows et al., 1996; Dougados et al., 2000).

In the case of the blue-shifted jet, the more distant knot M2 has a laterally extended bow-shock morphology which is not representative of the true jet width. In this lobe the width is therefore measured only at the knot M3 (-3."3). As described above, this jet is relatively faint, and larger velocity bins were required to obtain a good fit. In this lobe a significant difference is seen in the results between emission lines. In Hα, M3 has a width of 165 au (α = 15.6°) whereas in both [S II] lines it is only 90-100 au (α = 7-10°). This suggests that the Hα emission traces a wider component of the flow; such a large discrepancy may further indicate that M3 is an unresolved bow shock, with Hα emission tracing the shock wings and [S II] emission limited to the central peak.

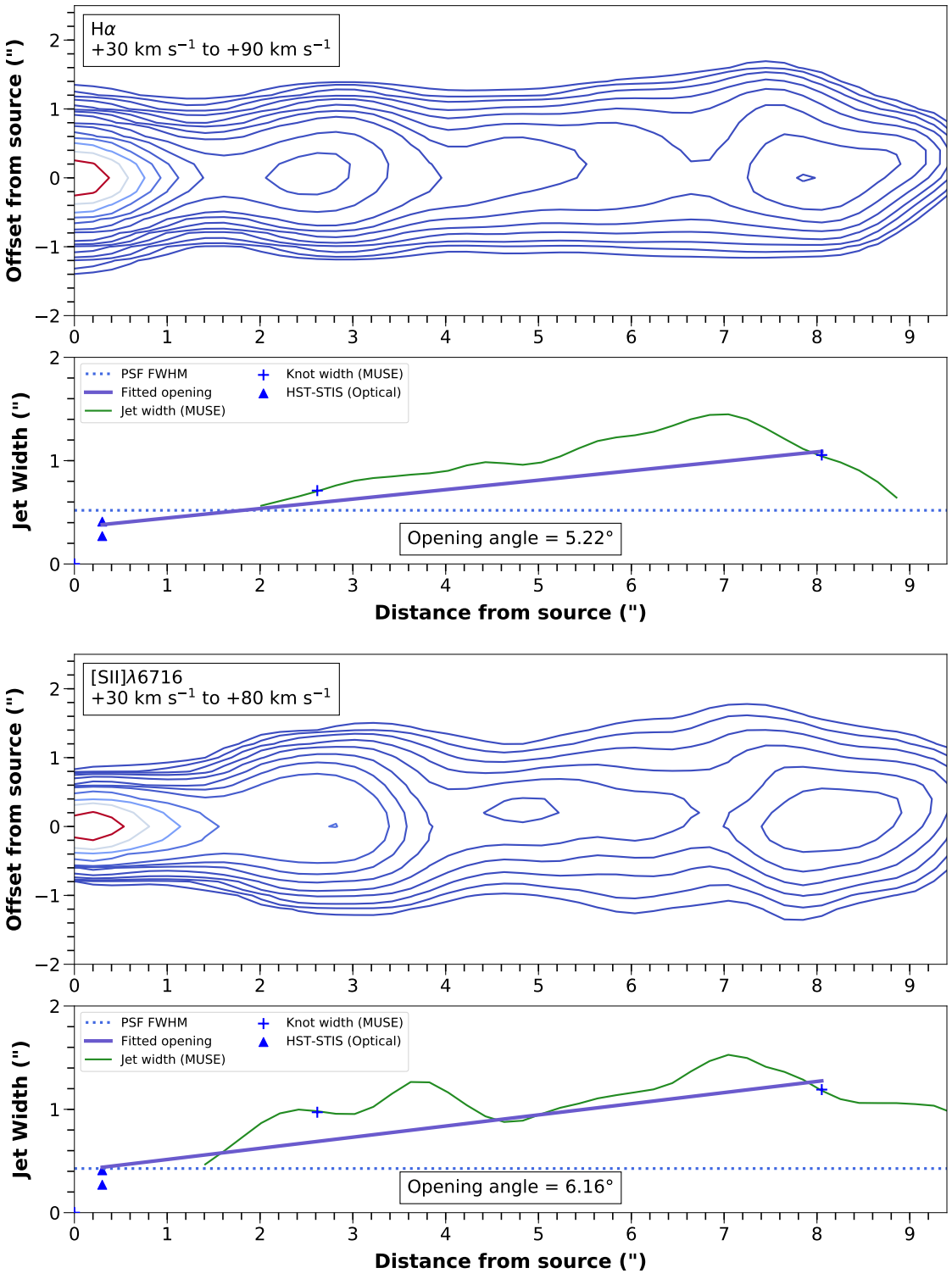

FIGURE 3.11: Jet width measured along the red-shifted micro-jet, with the source position at the origin of each plot. The opening angle in each case is estimated by a fit to the lower bounds of the FWHM measurements, corresponding approximately to observed knot positions.

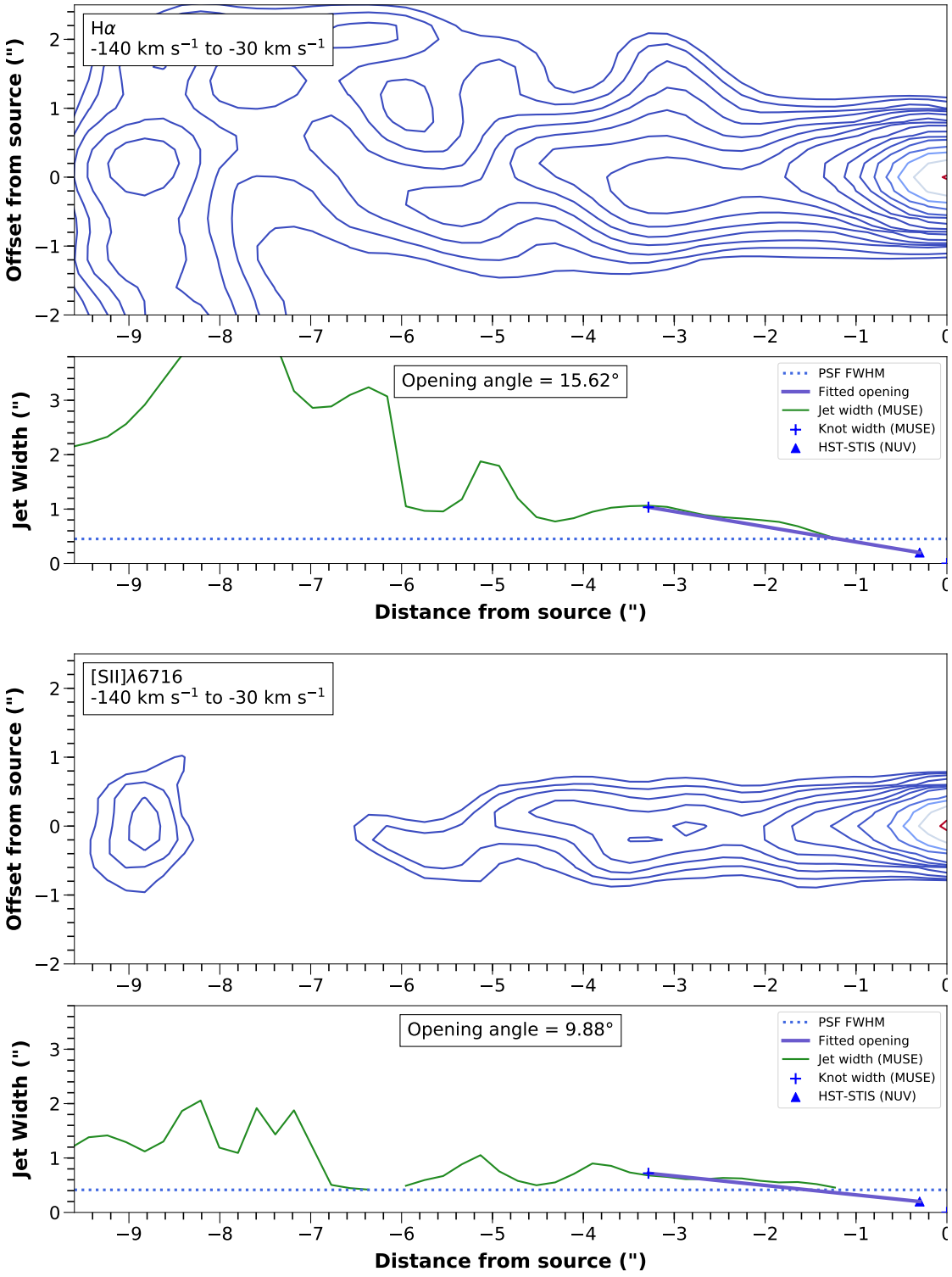

FIGURE 3.12: Jet width measured along the blue-shifted micro-jet, with the source position at the origin of each plot. The opening angle in each case is estimated by a fit to the lower bounds of the FWHM measured for the main peak at the observed knot positions. Note that the plot in green corresponds to the overall width measured by fitting a single Gaussian across the jet and is therefore substantially wider where a bow shock is present in Hα.

3.2.2 Jet Centroids

As well as using Gaussian fitting to study the jet width, the position of the jet axis (jet centroid) was also investigated as a function of distance from the driving source. The fitting procedure as described above was adopted. Additionally, as a small angular offset remained after rotating the datacubes to the horizontal axis (see the procedure described in Chapter 2.6), the centroid positions are corrected by subtracting a linear fit to these points. Both jets show indications of displacement around the jet axis. However, as mentioned, the faintness and complexity of the blue-shifted jet make investigating its structure a more challenging task. We therefore restricted our initial centroid position measurements to the red-shifted micro-jet.

The centroid positions of this jet show a small wiggling which is approximately periodic on a length scale of 2-3", visible before and after deconvolution. Figure 3.13 compares the estimated jet centroid positions for several velocity bins in Hα emission, before deconvolution. Error bars on the centroids are estimated as $\frac{0.4FWHM}{SNR}$ of the fitted Gaussian at each position (Porter et al., 2004). Within the micro-jet, the pattern of wiggles is relatively consistent across all velocity bins. While the jet is fitted best within the low-velocity red-shifted bins (-30 kms^{-1} to +90 kms^{-1}), the same wiggles can be seen in the low-velocity blue-shifted emission as well (see subsection 3.3 concerning blue-shifted emission from this jet).

The wiggles appear to have a maximum amplitude of 0."1 - 0."2 from the jet axis, which corresponds to about half a pixel in the field of view. Figure 3.14 concentrates on the -30 kms^{-1} to +90 kms^{-1} channel and presents a comparison between the Hα centroids and the main jet-tracing FELs. The same pattern of wiggling can be observed across all of these lines, although the [O I]λ6300 emission is less accurately fitted due to the emission being relatively faint further from the source. From Figure 3.15 we can see that the centroids in all lines also correspond well to the spectro-image contours before and after deconvolution. This agreement suggests that the wiggle observed is a real feature of the data. Investigating this in depth forms the basis of Chapter 4.

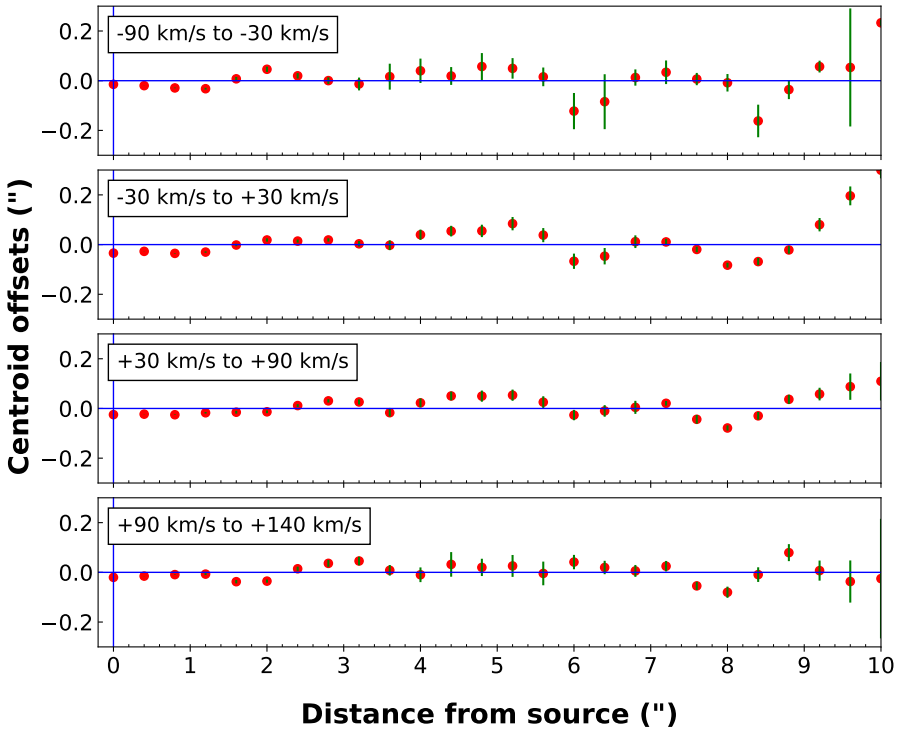

FIGURE 3.13: Centroid positions fitted to the Hα emission from several velocity channels of the western jet.

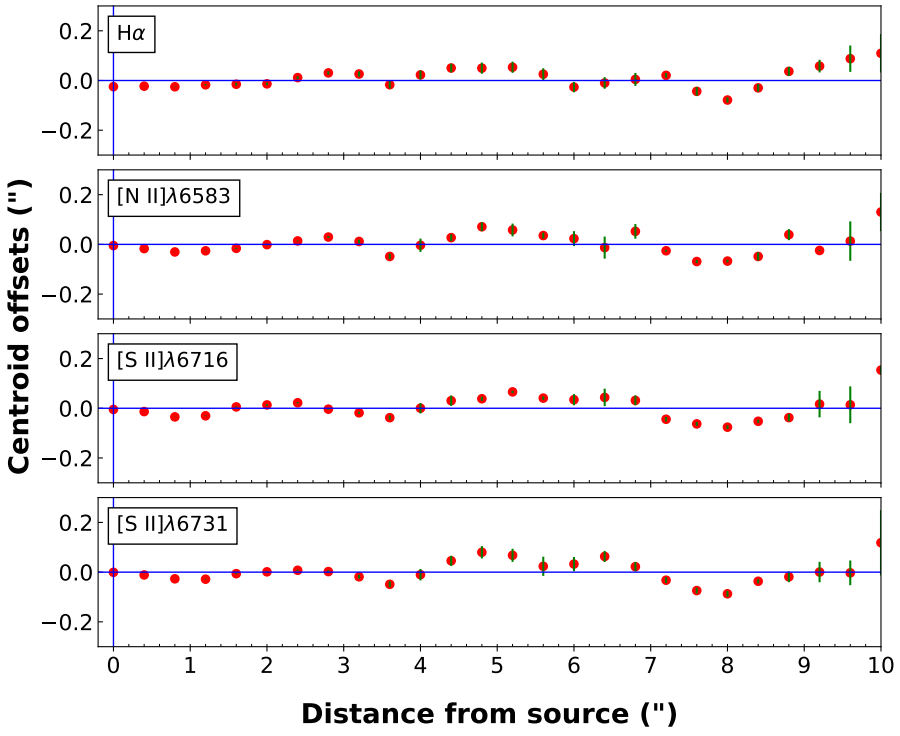

FIGURE 3.14: Centroid positions fitted to the peak velocity channel in several key FELs.

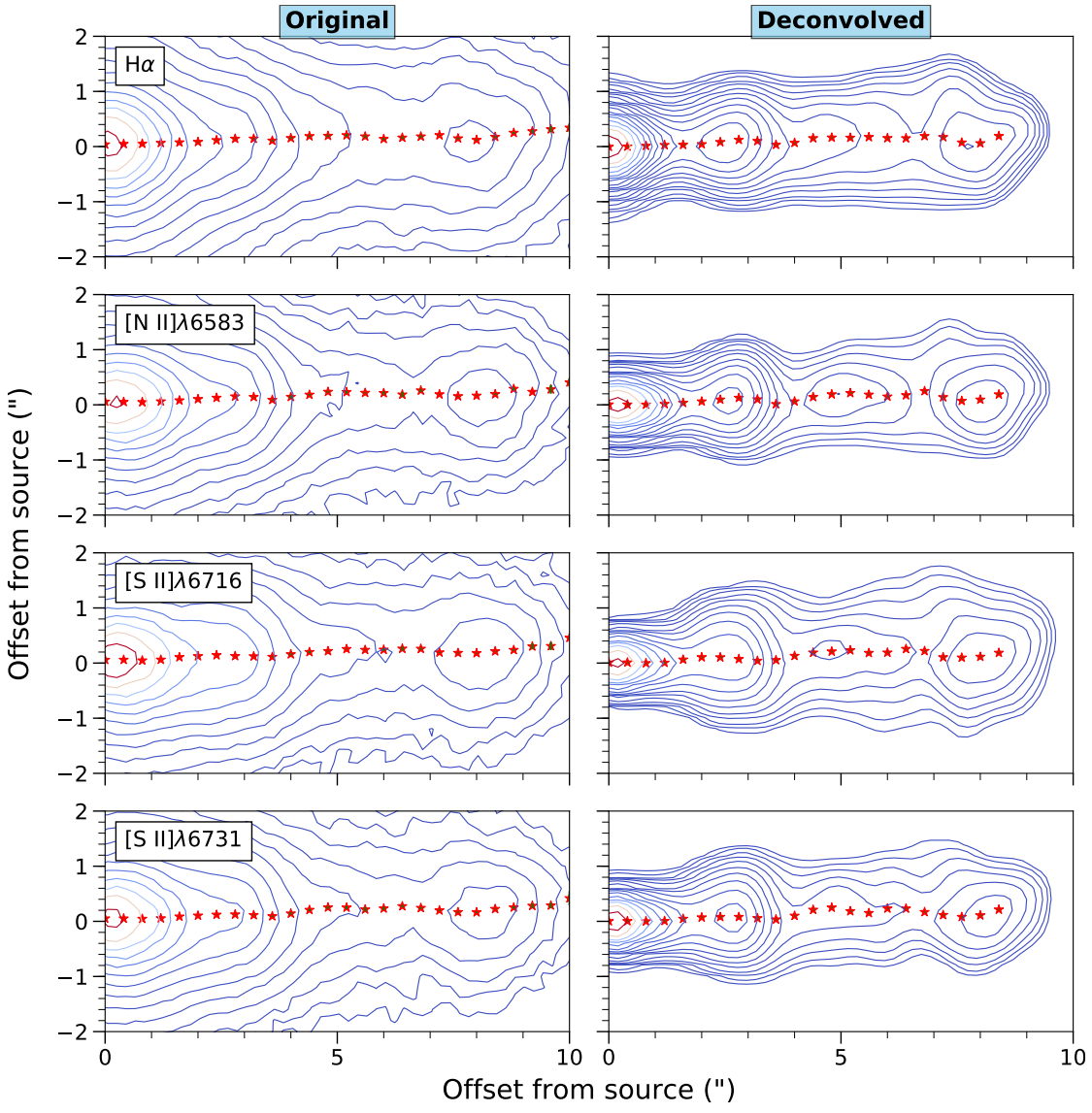

FIGURE 3.15: Centroid positions fitted to key FELs in the red-shifted jet, before and after deconvolution. The corresponding spectro-image contours are overlaid.

3.3 Kinematics

3.3.1 Position-Velocity Diagrams

The rotated, continuum-subtracted data cubes of each jet emission line were used to produce PV maps along the axis of the micro-jets. A full atlas of these maps is given in Appendix A.5. As shown by the spectro-images, the majority of lines are seen in the red-shifted jet, particularly within the first ∼3" of the source. The full red-shifted micro-jet (to 8") is seen in the permitted H and forbidden O, S and N lines, as well as [Fe II]λ7155 and [Ca I]λ7292. [Fe II]λ7453 clearly shows the knot M4 at approximately+2."5-3" in the red-shifted jet. Conversely, the blue-shifted jet is visible in fewer lines, with the majority extending to < 3-4" from the source.

Figure 3.16 shows PV maps of the rotated micro-jets in the main emission lines of interest, before (top) and after deconvolution (bottom). The velocity centroids over-plotted are Gaussian fitted from the spectra binned at 1" intervals along the jet axis. The standard uncertainties taken from the SNR of the velocity profile give uncertainties of ≤ 2 km s^{-1} and we therefore take a more conservative uncertainty as 10% of the velocity resolution (≈ 10 km s^{-1}). The low shift in mean velocities due to the micro-jets' orientation is clearly illustrated here, with emission from the red-shifted jet nonetheless extending into low-velocity blue-shifted channels. The asymmetry in radial velocities between the jets is also pronounced, with the blue-shifted jet centred at a roughly constant velocity of -80 km s^{-1}, greater by a factor of 2-3 than the red-shifted jet at +30 km s^{-1}. The blue-shifted bow shocks M1 and M2 are clearly seen, as well as the red-shifted knots HHW$_2$ and M5.

The fitted velocity centroids also reveal multiple components in the blue-shifted jet, including red-shifted emission. Before deconvolution, a low-velocity red-shifted component (30-50 km s^{-1}) can be detected to a distance of 9", the position of the first prominent bow shock M2; this emission is most prominent in the Hα and [S II]λ6731, and shows a constant velocity. Coffey et al. (2007) also found a double-peaked profile in PV maps of the Hα emission in this jet (taken at 0."5 from the source), with a low-velocity red-shifted component centred at 30 km s^{-1}. They attribute this component to reflected light from the red-shifted lobe, as the line profile closely matches that of the red-shifted micro-jet.

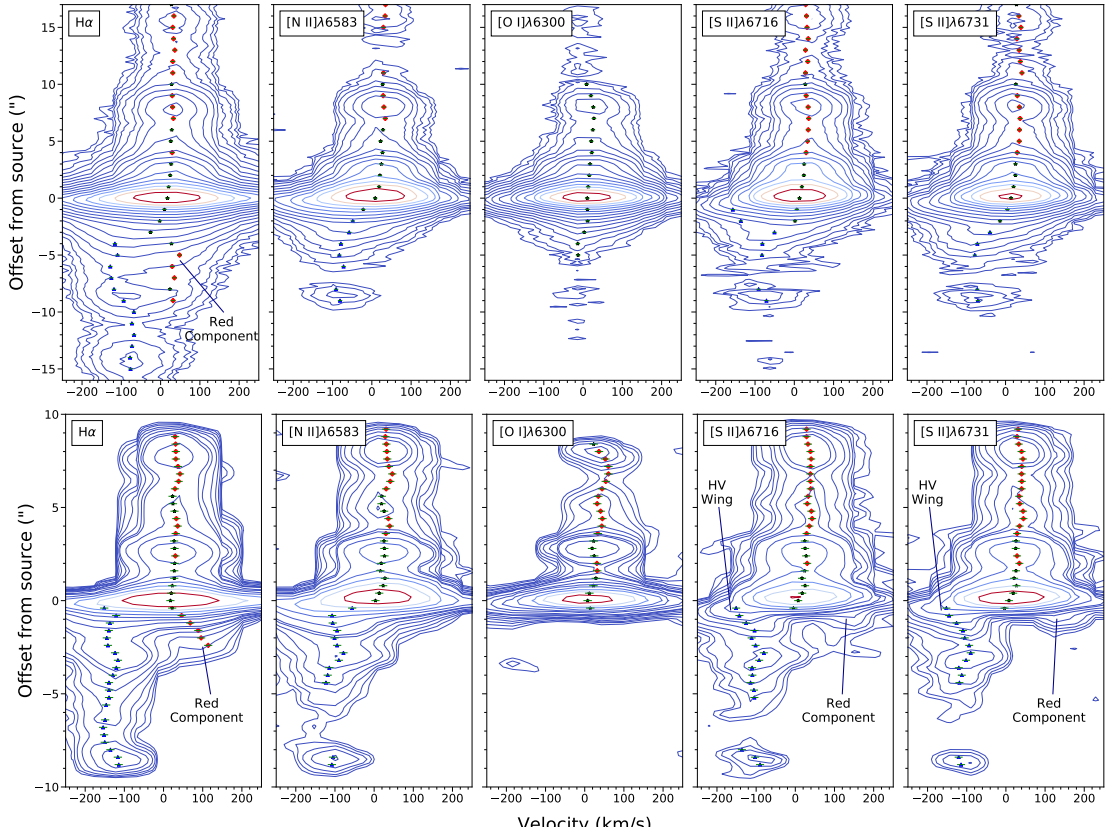

FIGURE 3.16: Position-velocity maps of the primary jet emission lines with overplotted velocity centroids. Blue and red points indicate blue and red-shifted velocities respectively, while black points indicate centroids within the central velocity channel (approximately ± 30 km s^{-1}). Error bars are 10% of the velocity resolution. Top: the jet before deconvolution; bottom: the jet following deconvolution. Note that the latter cover a shorter range along the jet axis.

3.3.1.1 Effect of Deconvolution

The PV maps of the jet after deconvolution are also shown in Figure 3.16 (bottom), allowing the effect of deconvolution to be examined. Overall, deconvolution increases the velocity separation of components within the same jet; while the red-shifted jet appears centred at +30 km s^{-1} as before, the blue-shifted jet is now centred at approximately -90-100 km s^{-1}. The only red-shifted component observed is fitted in Hα emission within 2" of the source, and shows a steady increase in velocity moving outward along the jet axis, from +30 to +100 km s^{-1}. The knots M3 and M4 are visible in the deconvolved maps at -3."3 and +2."5. Additionally, the possible knot at +5" is now seen more clearly, and though weak appears centred consistently in the same position.

Finally, an additional high-velocity wing can be seen in the blue-shifted jet within 1" of the source, although it is somewhat faint. This wing extends as far as -300 to -350 km s^{-1} in the Hα profile, suggesting it may correspond to the high-velocity blue wing reported by Comerón & Fernández (2010) in the spectrum of Th 28.

3.3.1.2 Hα and [S II] Maps across the Jet

One way of investigating the source of the double velocity components observed in the blue-shifted jet is to look at how the distribution of the velocity components change across the jet; i.e. whether a cavity can be detected in the central portions of the jet, with a smooth transition to a single intermediate velocity component at the upper and lower edges

To examine this, we binned the jet in the unconvolved Hα datacube into three levels of 5 pixels in width (1"), corresponding to upper, centre and lower slices. We thus obtain three PV maps along the jet axis. Additionally, we can carry out the same procedure for the deconvolved jet. The longitudinal slices along the jet are illustrated in Figure 3.17, with the regions in the deconvolved jet placed more closely together due to the reduced width of the jet. We then fit the velocity centroids along the jets at each vertical level to determine if there is any change in the fitted components. The resulting PV maps are shown in Figures 3.18. In both sets of slices, the blue-shifted jet shows two components (blue and low-velocity red-shifted) which appear generally the same in the centre and lower slices. They do not move closer together towards the upper or lower edges of the jet, and do not open outwards along the jet axis in a way that suggests a cavity, and in the upper slices only the blue-shifted component remains.

Instead, it appears that the red-shifted emission is a result of reflected light from the red-shifted jet or other emission close to the star. It is also possible there is some contribution from strong bow shocks in the inner portion of the jet, as the red-shifted emission appears in these regions and matches up well to the most red-shifted portions of the knots. At 14" where the outer knot is faint, only blue-shifted emission is seen similar to that in the slices taken at the spatial edges of the jet. Overall, no real difference is seen in the kinematics across the jet, and no signature of a cavity is detected.

3.3.2 Transverse Maps

In addition to the PV maps taken parallel to the jet axis, we examined maps of transverse cuts across the jet, taken at knot positions across both micro-jets. The velocity centroids of these maps were also fitted to determine if any trend or velocity shift across the jet axis existed which might suggest a rotation about the axis. No such trend was observed in either micro-jet, as shown in Figures 3.19 and 3.20. This is in contrast to the findings of Coffey et al. (2007) who observed a velocity shift of 10-20 km s^{-1} across the red-shifted jet (in the southwest-northeast direction), suggesting rotation around the axis.

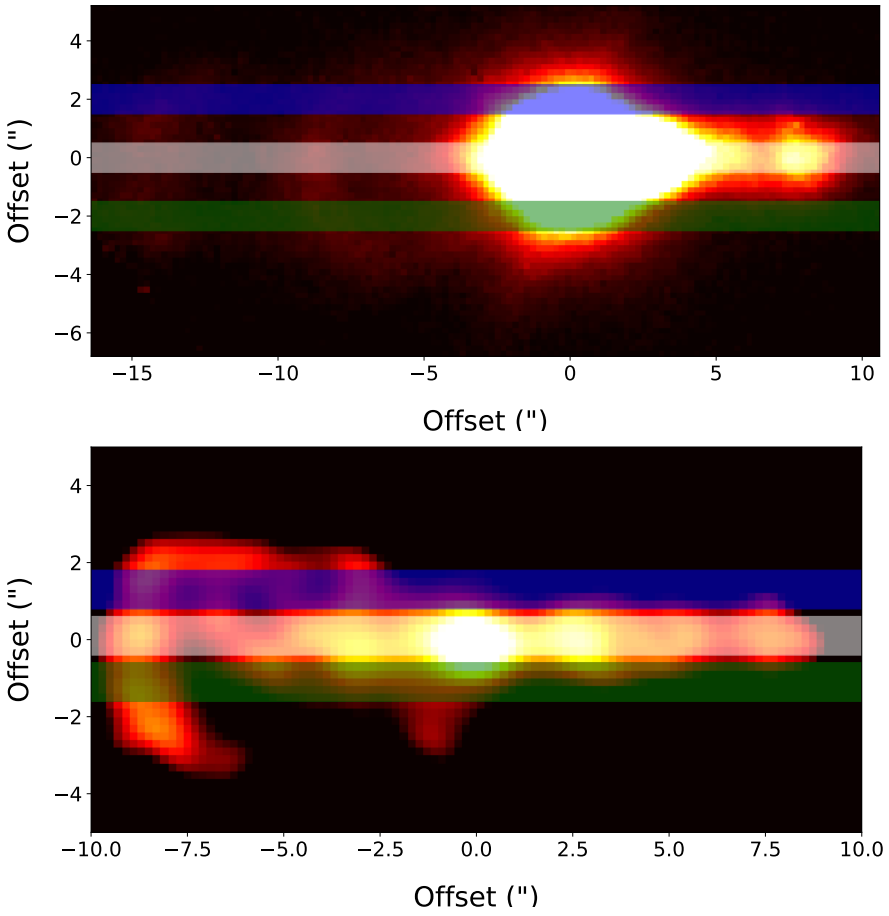

FIGURE 3.17: Regions chosen for the PV map slices shown in Figure 3.18, overlaid on the corresponding Hα spectro-images; top is the unconvolved jet and bottom is the deconvolved jet. The upper slices are shown in blue, centre slices in white and lower slices in green. In the unconvolved PV slices these correspond to vertical offsets of +1."5 - +2."5, ±0."5 and -1."5 - -2."5 from the source, respectively. In the deconvolved jet they correspond to the regions +0."8 - +1."8, -0."4 - +0."6 and -0."6 - -1."6.

However, this is unsurprising, both due to the significantly lower velocity resolution of MUSE and the difference in spatial resolution. Detecting such rotation requires resolving the jet width close to the base, before this signature is lost due to other kinematic features (note that Coffey et al. (2007) observed both jets at +/- 0."3 or 48 au from the source). In these seeing-limited observations, the jet is not resolved until approximately 4" from the source, at which distance we clearly detect signatures of kinematic features such as shocks and wiggling, which have a high likelihood of contaminating any rotation signatures. In principle, future MUSE observations with adaptive optics corrections would have the potential to detect jet rotation signatures in the jets closer to the star. However, this would still be very challenging, given that rotational velocity shifts are expected to be a few 10s of km s^{-1} at most and hence much smaller than the velocity resolution of MUSE (approximately 100 km s^{-1} for the relevant optical lines).

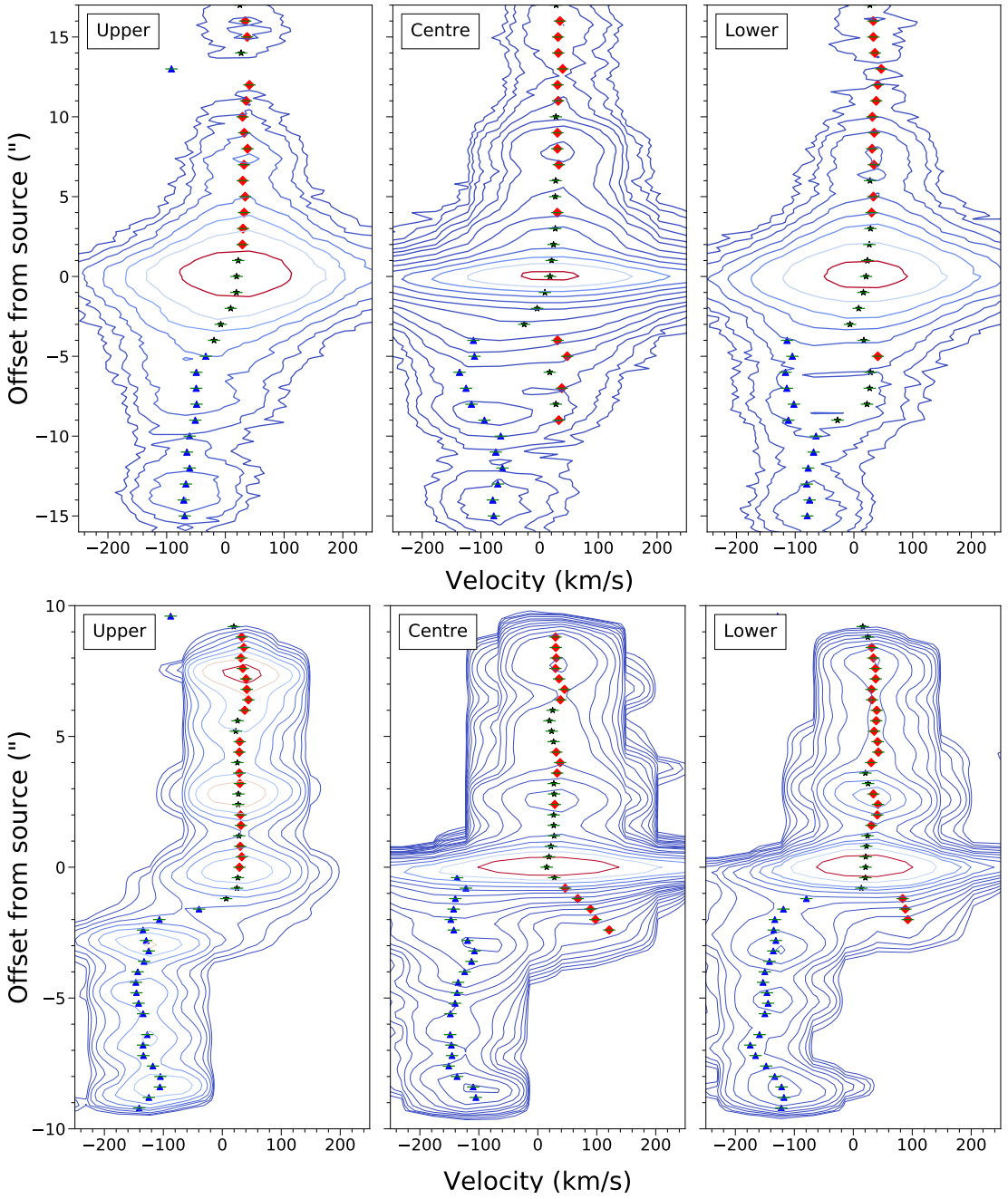

FIGURE 3.18: Position-velocity maps along the jet axis of the Hα jets before (top) and after (bottom) deconvolution, showing slices along the jet at different positions across the axis, from north to south (left to right). The velocity centroids are overplotted as in Figure 3.16; contours begin at 3-σ of the background level in the unconvolved maps and increase as multiples of $\sqrt{3}$.

Nevertheless, the transverse maps of the bow shocks in the blue-shifted jet (shown in Figure 3.19) illustrate the apparent red-shifted component associated with the central region of the bow shock (upper plots), which is lost in deconvolution (lower plots).

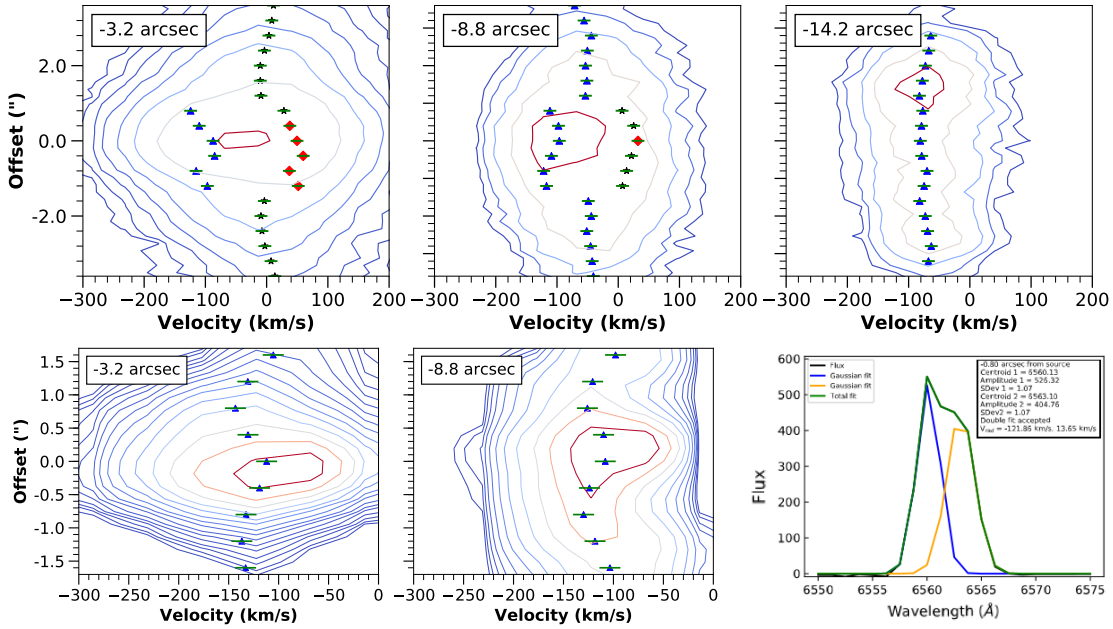

FIGURE 3.19: Position-velocity maps showing transverse cuts of the blue-shifted jet at the identified knot positions, shown in Hα. Top: transverse cuts taken before deconvolution, showing double velocity components associated with the centre of the bow shocks in the two brighter knots closer to the source. Bottom: tranverse cuts following deconvolution; here the weaker red-shifted emission has been lost. The outer knot at -14."2 lies outside the deconvolved region. The error bars are taken to be 10% of the velocity resolution, approximately 10 km s^{-1}. Bottom right: a sample fit of a cut across the central portion of the unconvolved knot at -8."8.

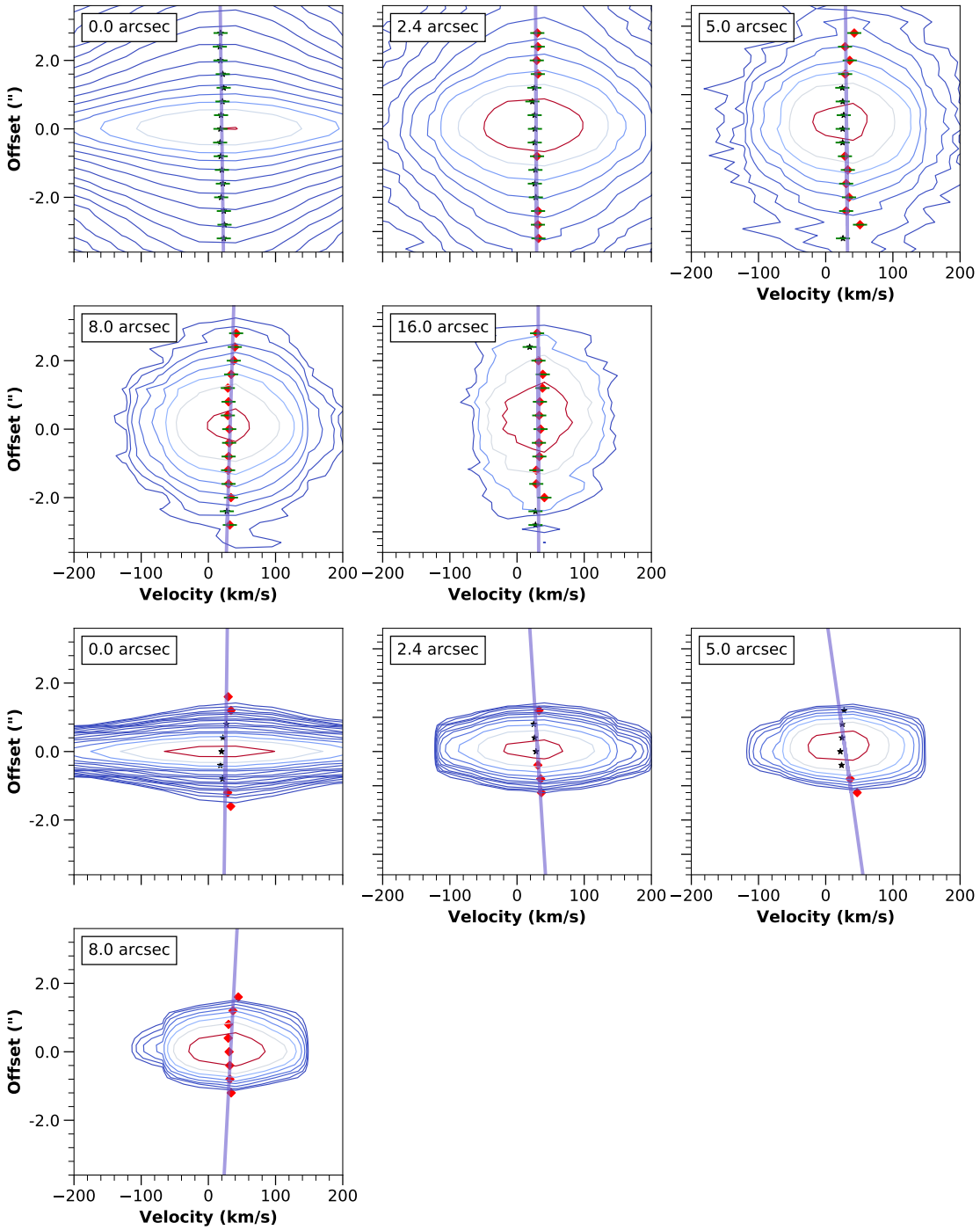

FIGURE 3.20: Position-velocity maps showing transverse cuts of the red-shifted jet at the identified knot positions, shown in Hα. Top: the knots before deconvolution. Bottom: the knots from the deconvolved cube. The knot at 16" is outside the deconvolved region. Overplotted in each case is the linear fit to the velocity centroids (running from top to bottom of each figure). While some skew is detectable mainly in the cuts from the deconvolved cube, these are mainly influenced by points at the edges of the jet where the fits are overall weaker.

3.4 Summary

- The 2014 MUSE observations of Th 28 allow us to map the inner jets of this star in a wide array of optical emission lines, including FELs of [O I], [N II] and [S II] which are key for physical diagnostics of conditions in the jet. The blue-shifted jet is also clearly detected in [O III] emission, indicating the presence of fast shocks ($v_{shock} > 90$ km s^{-1}) and higher ionization in this lobe relative to the red-shifted jet. Several lines of refractory elements (primarily [Fe II] and [Ca II]) are also detected in the red-shifted lobe.

- From this data we identify six new knots in the Th 28 jets: M1, M2 and M3 in the blue-shifted jet and M4, M5 and M6 in the red-shifted jet. In this lobe we also identify the position of the previously reported knot HHW_2 as well as an additional possible knot at +5". The proper motions of the innermost knots M3 and M4 are measured by comparison with 2015 X-Shooter observations and are found to be consistent with estimates for the other knots within each jet. The ages of all the identified knots indicate that knot formation is occurring on a timescale of $\sim$ 10-15 years. We also find that the knots on either side of the source form approximate pairs, suggesting symmetry in the timing of new knot formation across the jet.

- Estimates of the jet velocity obtained via combining the proper motions and radial velocities yield jet velocities of $v_{jet} = 270$ km s^{-1} in the red-shifted lobe and 365 km s^{-1} in the blue-shifted lobe. Similar to previous measurements of the more distant HH objects, we find a significant difference in inferred inclination angle with i_{blue} = -13° and i_{red} =+6.5°.

- The observations highlight the asymmetric nature of the two jets in both velocity and overall morphology. The blue-shifted jet is fainter, less collimated (α_{blue} = 7-15°) and characterized by the presence of large, fast bow-shock structures, whereas its red-shifted counterpart is brighter, more collimated (α_{red} = 4-6°) and characterised by compact knots. The blue-shifted jet is 2-3 times faster in radial velocity than the red-shifted jet ($\sim$ -80 km s^{-1} versus +30 km s^{-1} in our observations).

- In addition, the centroid positions of the red-shifted jet are found to wiggle about the jet axis in a consistent pattern which is investigated further in Chapter 4.

Chapter 4

Jet Precession in Th 28

This chapter investigates the wiggling in the Th 28 jet lobes as described in the previous chapter, which can be interpreted as the signature of precession caused by a companion object. We first review models of jet wiggling and how the jet shape can be related to the mass and orbit of a companion, as well as some previous cases where this has been studied.

We then carry out an investigation of the best fits to the Th 28 jet precession in both lobes and derive the parameters of a possible companion. We also briefly consider the case in which this wiggling could be fitted by an orbital motion of the jet source. The final part of this chapter discusses the implications and uncertainties associated with these results, as well as comparing the fitted precession to the positions of the knots in the extended HH jet.

4.1 Background: Wiggling Jets

The models used to fit the wiggling observed in the jet are based upon those used in Masciadri & Raga (2002). This assumes a jet with effectively ballistic motion, in which the density of the jet flow is significantly higher than the surrounding medium. On this basis, there are two possible ways in which a companion object to the jet source may cause a jet to wiggle.

The first is orbital motion, due to the orbiting companion pulling the jet source back and forth in the orbital plane (parallel to the disk, perpendicular to the direction of the jet axis). The second is precession, where the companion's orbit is at an angle relative to the accretion disk; this leads to tidal effects which cause the outflow direction

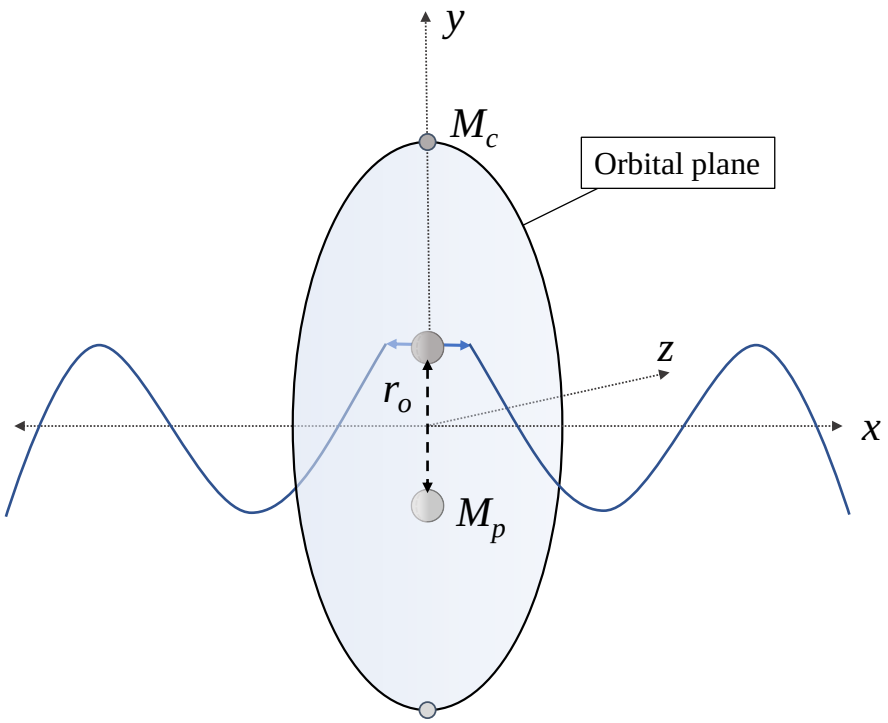

FIGURE 4.1: Diagram showing jet wiggling due to orbital motion caused by a companion.

to precess. Though both types of motion cause the jet to wiggle around a central outflow axis, they are distinct in the resulting jet morphology as shown below.

4.1.1 Orbital Motion

Wiggling in the case of orbital motion is illustrated in Figure 4.1, where the orbital plane of the companion is assumed to be in the same plane (y-z) as the disk (this is not necessarily the case, and if there is a misalignment between the two then we may also see an additional wiggling component due to precession as discussed later in the chapter). The orbit is assumed to be circular, and the jet is launched along the x-axis with velocity v_j. The shape of the jet in the x-y plane (wiggling around the axis) is then given by:

$$y = \kappa * x * \sin(\kappa \frac{x}{r_o} - \psi) + r_o * \cos(\kappa \frac{x}{r_o} - \psi) \tag{4.1}$$

where $\kappa = \frac{v_o}{v_j}$, the ratio of the orbital velocity to the jet velocity and r_o is the orbital radius. The phase angle, ψ, varies from 0 to 2π over one orbital cycle. Since

$$v_o = \frac{2\pi r_o}{\tau_o}, \tag{4.2}$$

with τ_o being the orbital period, the radius and period of the orbit can be obtained directly.

Figure 4.2 below shows the effect of varying each of the parameters r_o, κ and ψ. The wiggle produced by orbital motion is characteristically plane symmetric on either side of the orbital plane. The figure also shows that while v_o and v_j (hence κ) determine the opening angle of the jet shape, both these and r_o affect the length scale of the wiggle. This can lead to significant uncertainty when trying to fit these parameters simultaneously, and it is therefore useful to constrain κ as much as possible beforehand based on the wiggle opening angle.

4.1.2 Precession

In the case of precession, a companion orbiting on a plane inclined to the accretion disk causes the jet axis to precess. This is shown in Figure 4.3 with the jet launching axis precessing around the x axis; the jet trajectory will then be seen to vary in the x-y plane between the two grey dashed lines (which therefore mark the half-opening angle of the precession on either side of the x axis). The orbit of the companion is again assumed to be circular. From (Masciadri & Raga, 2002), the shape of the jet due to precession is given by:

$$y = x \tan\beta \cos\left[\frac{2\pi}{\tau_p}\left(t - \frac{x}{v_j \cos\beta}\right)\right], \tag{4.3}$$

where β is the half-opening angle of the precession cone and τ_p is the precession period. For a given jet, the orbit of the companion may result in wiggling due to a combination of these two components. Based on the equations of motion, the precession period τ_p is expected to be significantly longer than τ_o by an approximate factor of 10 (Terquem et al., 1999). Figure 4.4 below shows the effect of varying each of the factors in this equation, including the precession frequency $\nu = \frac{2\pi}{\tau_p}$. These plots also show the point-symmetry of the jet around the source due to precession. The jet velocity v_j can be estimated from previous observations to constrain the fit.

Inspecting the figures demonstrating the effect of these parameters, we can observe that if we constrain the jet velocity, the three main parameters of both models are analogous to each other. That is, in the orbital motion model, the radius r_o has the same effect on the shape of the wiggle as the frequency ν in the precession model: both vary the peak-to-peak length of the wiggle along the jet axis ('how often the jet wiggles'). Likewise, κ and $\tan(\beta)$ affect both the length of the wiggles and their width or amplitude

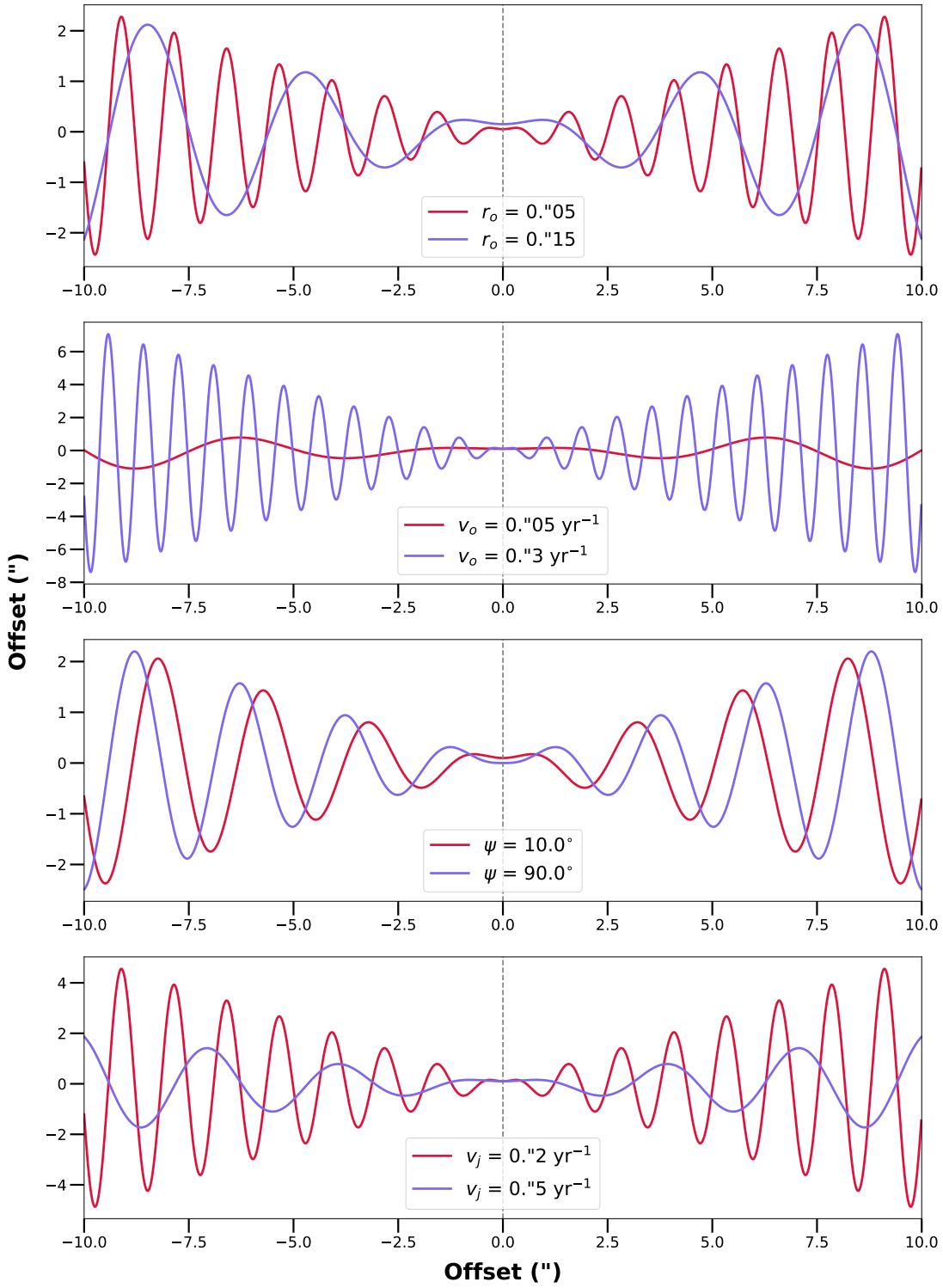

FIGURE 4.2: Comparison of theoretical wiggles based on the model for orbital motion, showing the effect of varying the main parameters of the jet. The source position is at the centre. Top, the effect of different values of orbital radius r_o; second panel, for different values of orbital velocity v_o; third panel, varying the phase, and bottom panel, varying the jet velocity.

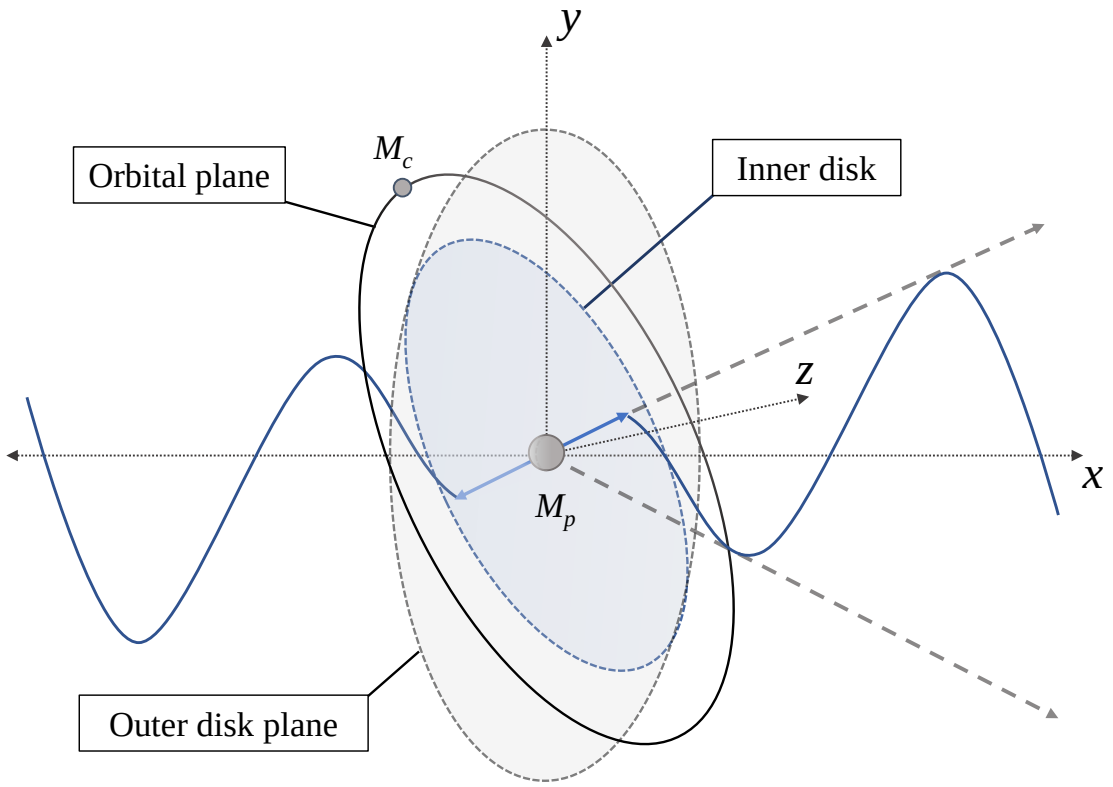

FIGURE 4.3: Diagram showing jet wiggling due to precession caused by an orbiting companion. The orbital plane of the companion (unshaded) is misaligned with the outer disk plane (shaded grey). The inner disk (shaded blue) is shown approximately aligned with the orbital plane to highlight the effect of the companion on this region. The launching axis of the jet precesses around the x-axis with this inner disk region.

(i.e. the maximum offset from the jet axis at a given distance from the source; 'how quickly the jet spreads out'). Finally, both ψ and t control the phase of the wiggle and vary with time. One notable distinction we can observe is the differing effect of v_j in the two models: in the orbital motion model, this is inversely related to the wiggle opening angle, i.e. a faster jet implies a smaller opening angle (smaller κ). In the precession model, however, v_j affects only the length scale of the wiggle (λ) and not the opening angle.

This gives rise to the equivalent precessing jet model as described in Masciadri & Raga (2002). This is the precession model which produces a similar jet trajectory to a given orbital motion model, obtained by choosing $\tan(\beta) = \kappa$ and a precession frequency ν equal to the orbital frequency ω. As will be discussed below, this can be used to investigate whether a wiggle fitted with with an orbital motion model could be explained by precession, by taking the equivalent model and deriving the parameters of the implied binary system.

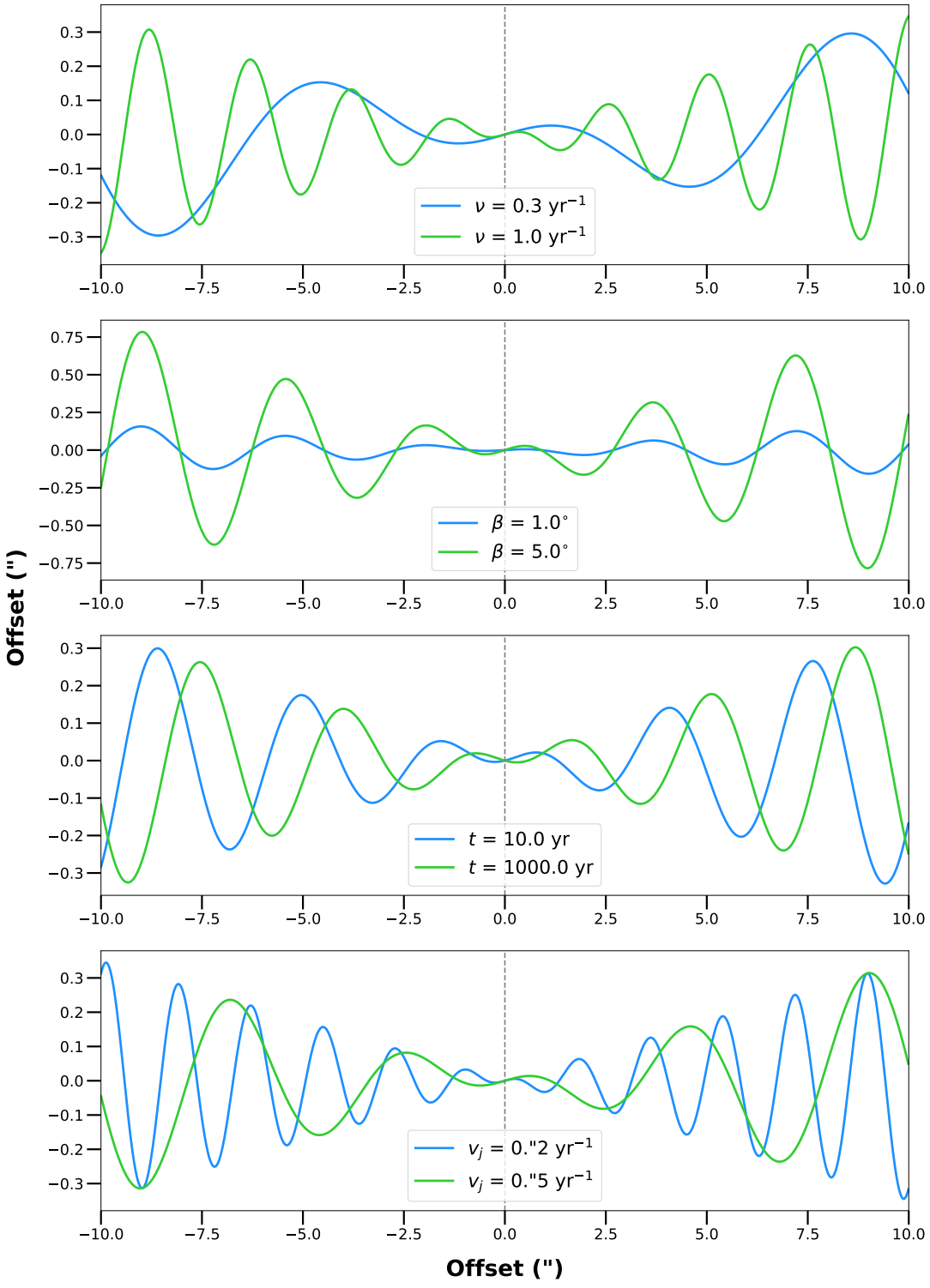

FIGURE 4.4: Comparison of theoretical wiggles based on the model for precession, showing the effect of varying the main parameters of the jet. Top, the effect of different values of precession frequency ν; second panel, for different values of β; third panel, varying the time since launch; bottom panel, varying the jet velocity.

4.1.2.1 Relating Precession and Orbital Parameters

Considering a binary system where M_p is the primary mass (jet source) and M_c is the secondary companion, we can assume that the orbit is circular and Keplerian. We take the ratio of the companion's mass to the total system mass M_{tot} to be μ such that

$$M_c = \mu M_{tot},\ M_p = (1-\mu)M_{tot} \tag{4.4}$$

And the orbital radius of the jet source (r_o) is related to the binary separation a such that

$$r_o = \mu a,\ a = \frac{r_o}{\mu} \tag{4.5}$$

If an orbital model can be fitted to the data, we can estimate the total mass of the binary system from Kepler's Third Law, with

$$\frac{M}{M_\odot} = \mu^{-3}(\frac{r_o}{au})^3(\frac{\tau_o}{yr})^{-2} = (\frac{a}{au})^3(\frac{\tau_o}{yr})^{-2} \tag{4.6}$$

How can this be related to the parameters of an observed or theoretical precession wiggle that co-exists with the orbital motion? From the equations of motion for two masses in a circular orbit, we have:

$$\omega_o = \sqrt{\frac{GM_{tot}}{a^3}} \tag{4.7}$$

where ω_o is the orbital frequency and β is the angle of inclination between the orbital plane of the companion object and the plane of the circumstellar disc (around the jet source). From Terquem et al. (1999), the precession frequency of a circumstellar disc (radius R) with uniform surface density and Keplerian rotation is given approximately by

$$\nu_p = \frac{15}{32}\frac{M_s}{M_p}\frac{R}{a}^3 cos(\beta)\sqrt{\frac{GM_p}{R^3}} \tag{4.8}$$

Then:

$$\frac{\tau_o}{\tau_p} = \frac{\frac{2\pi}{\omega_o}}{\frac{2\pi}{\nu_p}} = \frac{\nu_p}{\omega_o} = \frac{\frac{15}{32}\frac{M_s}{M_p}(\frac{R}{a})^3 cos(\beta)\sqrt{\frac{GM_p}{R^3}}}{\sqrt{\frac{GM_{tot}}{r_o^3}}}$$

$$= \frac{15}{32}(\frac{M_s}{M_p})cos(\beta)(\frac{R}{a})^3(\frac{a}{R})^{3/2}\sqrt{M_p}(\frac{1}{\sqrt{M_{tot}}})$$

$$= \frac{15}{32}(\frac{M_s}{M_p})cos(\beta)(\frac{R}{a})^{3/2}\sqrt{M_p}(\frac{1}{\sqrt{M_{tot}}})$$

Substituting for M_p and M_c, and taking $\sigma = \frac{R}{a}$, the ratio of the accretion disc radius to the binary separation, then

$$\frac{\tau_o}{\tau_p} = \frac{15}{32}(\frac{\mu M_{tot}}{(1-\mu)M_{tot}})\sigma^{3/2}cos\beta\sqrt{(1-\mu)M_{tot}}(\frac{1}{\sqrt{M_{tot}}})$$

$$\frac{\tau_o}{\tau_p} = \frac{15}{32}(\frac{\mu}{\sqrt{1-\mu}})\sigma^{3/2}cos\beta\sqrt{M_{tot}}(\frac{1}{\sqrt{M_{tot}}})$$

And we have the relationship given by Anglada et al. (2007):

$$\frac{\tau_o}{\tau_p} = \frac{15}{32}(\frac{\mu}{\sqrt{1-\mu}})\sigma^{3/2}cos\beta \tag{4.9}$$

We can use these relations either to constrain the precession corresponding to an orbital motion wiggle, or vice versa to constrain the orbital parameters based on a measured precession. Although the shape of the jet caused by precession cannot be used to directly derive the properties of such a companion (aside from the inclination angle of the orbital plane), we can use it to constrain the possible mass and orbit of the companion. For this we need to measure the precession half-opening angle β and period τ_p.

First, τ_o is estimated from the ratio given above. The κ value of the orbital precession must be less than $\tan\beta$, so that the upper bound of the orbital velocity is given by

$$v_o \leq v_j \tan\beta \tag{4.10}$$

$$v_o = \frac{2\pi r_o}{\tau_o} \tag{4.11}$$

If we can estimate or assume values for μ and σ, we can therefore find $\tau_{o,max}$ (from Equation 4.9) and $v_{o,max}$, and use these to estimate the orbital radius r_o and hence

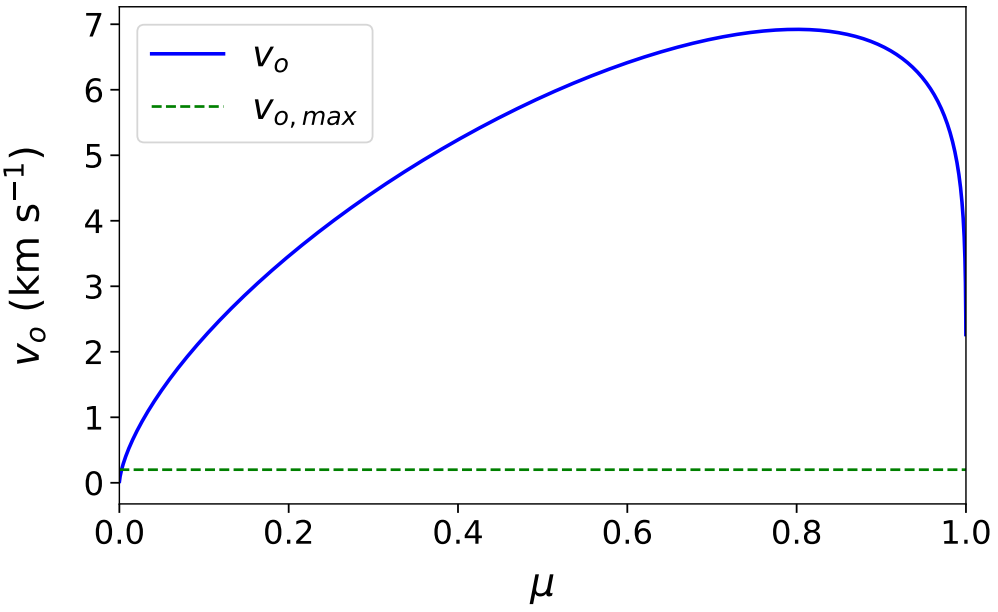

FIGURE 4.5: Orbital velocity v_o as a function of the relative companion mass, μ, showing the two solutions at $v_{o,max}$. The right-hand solution implies $M_c \approx M_{sys}$ and is therefore unphysical.

disk radius R as well as the masses of the two objects. We can assume a value for σ based on theoretical considerations. Where an estimate for μ is already known, this can be used to estimate the masses of the two objects; otherwise, since the jet source can be expected to be more massive than its companion, $\mu = 0.5$ is sometimes taken to estimate the upper limit of the companion's mass. However, a better estimate for the maximum value of μ can instead be obtained using the relations discussed so far. We can rearrange and combine Equations 4.6, 4.4 and 4.2 to obtain the orbital velocity and binary separation as functions of μ, with

$$v_o = 2\pi(\frac{M_{sys}}{\tau_o})^{1/3}\mu \tag{4.12}$$

$$a = (M_{sys}\tau_o^2)^{1/3} \tag{4.13}$$

Equation 4.9 provides the orbital period as a function of μ for given values of β and period τ_p. If we plot v_o against possible values of μ, and apply the condition given by Equation 4.10, we can illustrate that there are two solutions for μ, as shown in Figure 4.5. One solution is close to a value of $\mu = 1$, implying that the companion is much more massive than the jet source; this is unphysical as the driving source is expected to be significantly more massive than a companion which does not drive a jet. This gives us a remaining solution which provides the maximum value for μ. We can therefore

estimate the maximum orbital period, separation and mass of the companion. Similarly, we can constrain μ and derive these parameters if the orbital velocity and period have been measured directly from an orbital motion wiggle.

4.1.3 Values of Sigma and the Broken Disk Scenario

One of the key parameters in relating the wiggle parameters to the orbit of a companion is the ratio σ between the inner circumprimary disk radius and the separation of the companion from the jet source. This poses a major source of uncertainty where (as in the case of Th 28) both are not measured directly. Observations of circumstellar disks in binary systems show a correlation between separation and disk radius with $\sigma < 1$, suggesting that the expansion of the disk via outward transport of angular momentum is truncated by tidal forces due to the presence of a companion (Papaloizou, J. C. B. & Pringle, 1977; Paczynski, 1977; Jensen et al., 1996).

From theory (Artymowicz & Lubow, 1994), the disk is truncated to a point where the viscous torque is balanced by torques caused by tidal and resonant interactions with the companion. Tidal (non-resonant) interactions cause distortions which lag behind the orbit of the companion, generating a viscosity-dependent torque. Resonant interactions (i.e. Lindblad and co-rotational resonances) excite density waves which clear material from the disk. In particular, they clear the disk beyond the radius of the strong 1:2 resonance. In the case of a giant planetary companion rather than a stellar-mass object, the circumprimary disk might extend as far as the orbital radius, otherwise the ratio is expected to be much smaller. Simulations by Artymowicz & Lubow (1994) show that in a binary system with circumbinary and circumstellar disks, the circumprimary disk is truncated between the 1:3 and 1:4 resonances, depending on the eccentricity of the orbit. Therefore in most cases, it is expected that $\frac{1}{4} \leq \sigma \leq \frac{1}{2}$ (Terquem et al., 1999).

However, in the case of a giant planetary companion forming within the circumstellar disk, we can consider an alternative 'broken' disk scenario (Zhu, 2019). Here the presence of a large companion orbiting on an inclined plane to the accretion disk can produce a small broken inner disk that precesses at a separate rate to the outer disk region. The occurrence of this depends both on the mass of the companion and the degree of misalignment. A strongly inclined orbital plane will produce a shallower gap and cause a warp in the disk, whereas a low inclination will produce a deeper gap. For a sufficiently massive companion at a low inclination a complete break can occur; this is also dependent on the viscosity of the disk itself.

This gives a condition for the planetary mass required to break the disk for a given inclination and disk parameters. It also shows that the inclination will be damped over

time, so that for a weakly misaligned (low i) orbit, a massive planet ($\mu > 0.01$) is required to produce significant misalignment of the inner disk before the orbit becomes coplanar (unless the disk itself is quite low-mass). Assuming this is the case and that the inner edge of the resulting disk gap is close to the orbital radius of the companion (σ roughly 1) then the precession ratio is given by:

$$\frac{\tau_o}{\tau_p} = \frac{3}{8}\left(\frac{\mu}{\sqrt{1-\mu}}\right)\sigma^{3/2} cos(i_p) \tag{4.14}$$

where $i_p = 2\beta$ is the angle between the orbital angular momentum vector of the companion and the rotation axis of the jet. We can therefore use this equation to estimate the orbital period where a small close-orbiting companion is inferred.

4.1.4 Feasibility of Observing Precession in the Th 28 Microjet

It is worth considering the implications of these models for the likelihood of detecting either precession and orbital motion in our observations of Th 28. Where a companion orbits on an inclined plane, both of these effects are expected to co-exist as two separate components to the wiggling of the jet shape. However, observing both is not easy, as τ_p is typically expected to be greater than τ_o by a factor of at least ten; consequently the wiggling due to precession will be observed on much longer length scales than that caused by orbital motion.

This can be illustrated using the relationships between both periods given by equations 4.9 and 4.14. Figure 4.6 (top panels) shows these relationships for a system similar to Th 28, with proper motions taken to be 0."35 yr^{-1} (as in the red-shifted jet) and assuming precession over a small half-opening angle $\beta \simeq 1°$. Given a length scale for the wiggling of approximately 2."5, we have a period of 7 years. For several values of σ (with $\sigma = 1$ calculated using the broken disk equation), the figure shows the corresponding period ratios and precession length scale ($\lambda_{precess}$) over a range of μ values.

Without a broken disk, we find that $\tau_o/\tau_p < 10$ only where $\mu \geq 0.5$, implying that the companion object is equal or greater mass to the jet source (i.e. a binary stellar system). In the broken disk scenario, this ratio occurs at lower masses ($\mu \geq 0.25$) but this still implies a low stellar mass companion. For these large companions, $\lambda_{precess}$ lies between 10-100" (less than 10" only for $\mu > 0.5$). In general, then, we would not expect to see precession on small scales of a few arcseconds; first because the jet source is reasonably expected to be larger than the companion and so $\mu > 0.5$ is unphysical, and second because even a low stellar mass companion is more likely to be detected through other methods such as direct imaging or observations of the disk.

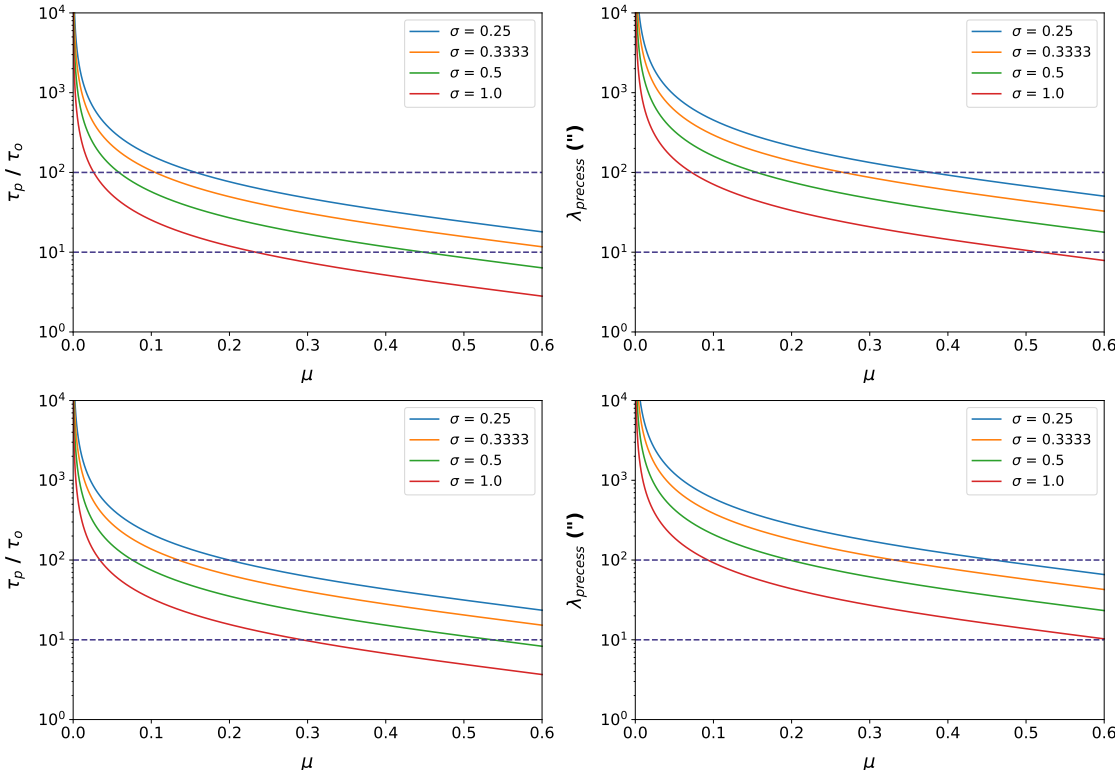

FIGURE 4.6: Precession characteristics estimated using orbital motion parameters similar to the wiggling in the Th 28 jet. Left panels show the expected precession period relative to the orbital period; right panels show the corresponding length scale of the precession. Top: parameters estimated assuming a small precession angle ($\beta = 1°$); bottom: estimates assuming a large precession angle ($\beta = 40°$). All y-axes are on a logarithmic scale.

On what scales might we observe precession from a small companion, then? For $\mu < 0.1$, we see that in all cases, $\lambda_{precess} > 100$". We can also show that these results are not significantly changed for a much larger precession angle 40°, shown in the lower panels of Figure 4.6; indeed, larger precession angles *increase* the precession length scales and make them harder to observe. Note also that these relationships depend on the *ratio* between the masses of jet source and companion, not on the actual total mass of the system.

In the case of Th 28, where we can clearly trace only about 10" in the red-shifted micro-jet, we are unlikely to see a corresponding precession signature if the wiggling observed is due to orbital motion. Conversely, if the Th 28 jet shape is caused by precession, we would expect a much smaller wiggling due to orbital motion, implying a smaller orbital separation and companion. It is therefore a reasonable first assumption that the jet shape is due to orbital motion.

4.1.5 Wiggles in Other Jets

Wiggles are detected in stellar jets on both large (arcmin or parsec) scales with wiggle periods of several kyr (RNO15-FIR, HH 315/PV Cep, V1131 Cyg) and small scales of a few arcseconds with periods of a few years to a few hundred years. Additionally, there are also some less clear cases in which precession may explain the shape of a strongly inclined bipolar jet. This wiggling may be detected in both optical and molecular jets. We note that in some sources, observed wiggles in jets may generally be referred to as 'precession' without observation of a point symmetry or other establishment of the wiggle's origin. For this discussion, we refer to precession only in cases where this model is specifically proposed, especially where an S-shaped jet is detected.

In cases where wiggling jets are detected at longer range (> 1' from the source) or in the form of knots, this can make the jet trajectory more difficult to trace due to the effect of shocks or deflections especially if a wiggling is small in opening angle. Masciadri & Raga (2002) show that the jet shape can be altered relatively quickly (within a few cycles from the source) due to the effects of drag from the surrounding medium. When tracing the wiggle through knots, large sections may also be missing as intermediate knots fade or are lost due to interactions with each other. This also introduces the complication of variable knot velocities and trajectories, which can lead to segments within the wiggle pattern with apparently different precession properties (e.g. HH 47, Reipurth et al. (2000)).

In most cases, it is difficult to trace a jet symmetry close to the source, especially where only one jet is visible or exhibits a recognizable wiggling. Below we examine a few examples of jets with wiggling in only one lobe (for a full catalogue of identified wiggling jets, see Appendix B). Note that where the properties of a binary system/companion object are inferred from the jet shape, the methods used may vary from the procedure outlined above.

Looking first at cases where a wiggle is clearly detected only in one lobe, a classic example is HH 30, a well-known jet driven by an optically invisible star. The outflow extends up to 7' from the source (López et al., 1995, 1996), and the main flow and knots trace a wiggling with $\lambda = 15$" to at least 50". Anglada et al. (2007) note that the whole morphology moves together along the jet axis without changes in the directions of the knot proper motions, as would be expected if the wiggling was due to their being deflected. They conclude this wiggling is compatible with either orbital motion around a large companion (0.25-1.0 $M_{\odot}$), or precession due to a massive planet or brown dwarf companion with a separation of ≤ 1 au from the jet source.

Two more complex cases are HH 47 and IRAS 20126-4104. The HH 47 jet is launched by a known binary source and shows a helical morphology which can be divided into four distinct sections of differing lengths (Reipurth et al., 2000). Masciadri & Raga (2002) examine the sections separately and find that for an orbital motion model these imply periods of 160-280 yr and an orbital radius of 60-100 au. While this is consistent with the observed separation of the binary components, the varying lengths of the jet sections indicates there are most likely other factors affecting the jet shape.

IRAS 20126-4104 is a high-mass (7 $M_{\odot}$), very young stellar object with a poorly collimated molecular outflow. The H_2 flow extends for 1 pc (Ayala et al., 1998) and has an S shaped morphology indicating precession over an angle of 37° (a much larger angle than most of the other examples) with a period of 12×10^4 years (Shepherd et al., 2000; Cesaroni et al., 2005; Su et al., 2007). However, Caratti o Garatti et al. (2008) also find a shorter wiggling in H_2 with an opening angle of 16-21°, $\lambda = 11$", and period = 1100 years. They note that if these distinct wiggle patterns represented a combination of orbital and precession components, then this would require the orbital radius of the companion to intersect the accretion disk; it is possible that instead the wiggling is caused by tidal interactions of multiple stellar companions.

Lastly in this category we place the recent detection of wiggling in DO Tau, an example with several similarities to Th 28. This is also a CTTS driving an optical asymmetric jet, with several HH objects associated with the red-shifted (north-eastern) jet. Erkal et al. (2021) show both lobes of the micro-jets exhibit wiggling within about 1.5" with projected $\lambda \sim 0."6$ (90 au) and half-opening angle $\sim 1.3°$. They compare the jet shape with both orbital and precession models. However, the larger wiggle opening angle in the faster red-shifted jet strongly indicates against the orbital model, in which the wiggle opening angle scales inversely with jet velocity (see Section 4.1.2). A precession model is therefore fitted to the jet with $\beta = 0.5°$ and precession period 9.5 years. In order to obtain a good match to the red-shifted jet, the model required a phase shift and a precession angle approximately twice that in the blue jet be introduced to this lobe. Erkal et al. (2021) suggest this asymmetry in the wiggle properties may be caused if the two jet lobes originate from separate annuli within a warped disk. They further show that the blue-shifted jet precession may be caused by a massive planetary companion (≤ 12 $M_{\rm Jup}$) within a separation of 0.1-0.15 au.

As mentioned, detecting a clear symmetry across the jet source is often not possible, especially close to the source. Typically one micro-jet (usually the receding jet) is significantly fainter or obscured from view by the circumstellar disk or envelope. Where both are detected, one jet may be less regular in morphology (for example, disrupted by strong shocks or deflections) or much fainter than the other. To clearly detect the

symmetry of the wiggle, it is ideal to observe the pattern in both lobes of a jet with low inclination from the plane of the sky, examining the jet shape close to the source.

However, there are several cases where a potential wiggle symmetry can be determined. Where the driving source is identified, these are all examples of PMS Class 0 or I outflows, and the majority of these wiggles are detected as an S-shaped precession symmetry in the jet knots at separations of > 100" from the source. Consequently most are also on relatively long spatial scales ($\lambda > 1$') and with periods of several hundred or thousand years. These long length scales relative to the observed jets mean that typically only one cycle or even a partial cycle of the wiggle pattern is observed, for example G35.20-074N (Beltrán et al., 2016).

However, there are two examples to date in which jet symmetry can be traced close to the source. HH 211 is a class 0 source driving a close to edge-on jet (i = 5° ± 3°) which a has been observed to 3" resolution in SiO, SO, and CO (Lee et al., 2009, 2010). The SiO and CO observations show a reflection-symmetric wiggling in both jet lobes which is observed out to ∼15" from the source. About 3 wiggle cycles are detected with $\lambda = 5.''46$, a half opening angle 0.55°, and a period of 43 ± 23 years. Lee et al. (2009, 2010) finds this points to a very low mass binary where the companion and jet source are both approximately 30 M_{Jup}, with a separation of 4.6 au.

Additionally, HH 111 is a highly collimated jet with lobes extending to 3.5 pc from the source, driven by a possible Class I binary with separation of 15 au (Rodríguez et al., 2008). Interestingly, this jet appears to show two distinct wiggle components in different regions of the jet. The outer parts show a point-symmetric deviation from the inner jet of 4° indicating precession on a period of about 23000 years (Reipurth et al., 1997). Within 2' of the source, however, the jet knots exhibit a mirror symmetric wiggle with $\lambda = 216$", half-opening angle = 0.7° and a period of 1800 years (Noriega-Crespo et al., 2011). This is consistent with a binary containing two solar-mass stars at a separation of 186 au. This may mean that HH 111 is an exceptional case where both the orbital motion and precession components due to a binary companion can be observed, and Noriega-Crespo et al. (2011) note that the ratio $\tau_p/\tau_o = 13$ is consistent with the theoretical predictions discussed in Section 4.1.4.

These examples help to illustrate several points about interpreting jet wiggles. First, a signifcant challenge may be posed by the unique features of a particular system or jet, for example asymmetric or variable jet velocities, or multiple companions/jets, which must be considered carefully in understanding the causes of the jet morphology. Second, the processes which impact the jet shape as it moves outwards must be considered, to distinguish between a wiggling in the jet axis and an apparent wiggling caused by the deflection of HH objects as they travel outwards. Relatedly, it should be noted that

where a wiggle is traced primarily in the knots of a jet, we observe the knots falling at different points in the wiggle cycle (i.e. not only on the peaks).

Finally, we note that in cases where a close companion could cause a wiggling of the jet, our ability to detect this is limited primarily by the relative dynamical time (and hence length) scales of the observable jet and the wiggle cycle caused by the companion. In other words, there is a limited window of companion parameters which can be detected by observing the shape of a given jet, which will be discussed further at the end of this chapter.

4.1.6 Alternative Causes of Jet Precession

The precession of the jet-launching disc is assumed to be due to some tilt or warp in the inner disc. However, several mechanisms will normally act to damp this tilt and return the disc to the orbital plane, e.g. differential rotation at different disc annuli and internal stresses/dissipation (Lubow & Ogilvie, 2000). Therefore a driving mechanism is required to maintain this precession over a long period of time (i.e. several precession cycles). So far we have only considered the case where this is caused by the effect of an orbiting companion. However, we should also consider other mechanisms which have been proposed to create warps within discs; for example, wind-induced Kelvin-Helmholtz instabilities are theorized to generate warps in energetic outflows (Quillen, 2001). Some of these mechanisms are applicable only to very energetic X-ray binaries, however, and so we focus here on those most relevant to a young stellar disc-jet system.

Two main models are proposed by Lai (1999, 2003). First, the stellar magnetic field can exert a magnetic torque on the disc, either due to the interaction of the disc surface current or the twisting of vertical magnetic field lines threading the disc. This in turn can lead to disc warping and precession (Lai, 1999). Alternatively, a circumstellar disk threaded by a large-scale magnetic field can experience perturbations due to interaction with an external magnetic field (provided either by a central magnetic star or other currents in the system (Lai, 2003)). This produces a magnetically-driven warping instability leading to a disc annulus with a net torque and a tilt relative to the disc plane. The result is a region of the disk that undergoes magnetically driven precession retrograde to the disc rotation. In this scenario we would expect the precession period to be on the order of the disk infall time $R/|V_R|$ (with V_R the radial velocity). So far, there is little work confirming that these mechanisms can drive jet precession in YSOs; however, it is important to consider them as an alternative to companion-driven precession.

4.2 Th 28 Precession Model Fitting

The initial investigation of the Th 28 jet centroids shown in Section 3.2.2 focused only on the red-shifted lobe. However, when we examine the centroid positions of the blue-shifted lobe, we find that there is a counterpart wiggling on this side of the jet. The two sides of the jet show a clear point-symmetry around the star, indicating a precession of the outflow axis in contrast to expectation. This is most clearly defined in the [N II]λ6583 centroids, but can also be seen in Hα and [S II] emission when the lowest velocity channel (+/- 30 km s^{-1}) is excluded (see comparison in Figure 4.7). Note that significant [O I]λ6300 emission is not seen from the blue-shifted jet and we therefore do not consider it. The fact that the wiggle is obscured when the low-velocity channel is included indicates that these lines suffer from contamination by low-velocity emission from outer layers of the jet, while the [N II] emission traces the flow closest to the jet axis.

Figure 4.8 illustrates the precession observed across different emission lines. The precession signature is observed to be clearest within ± 6" of the source. To map the centroids, we adopt the same rotation and fitting procedure as described above for the red-shifted jet. In the central velocity channel of [N II] (± 90 km s^{-1}) the jet can be fitted in both lobes from the same image, whereas for the ± 30-140 km s^{-1} channels in each line, the two jets are observed in different wavelength channels. Therefore a different linear correction is estimated in aligning the jet lobes with the horizontal axis (since the collimated red-shifted jet cannot be used as a guide for the blue-shifted image). When fitting a combined precession model therefore separate linear components are included to account for residual rotation from the horizontal axis.

4.2.1 Precession Fitting - Individual Lobes

The initial fitting procedure allowed the model to fit the two jet lobes with precession parameters independently, allowing the model components to fit the data as closely as possible (with some variation between the parameters on each side. Based on the measured proper motions and inclination angles discussed in Chapter 3 we take jet velocities in each lobe of $v_{blue} = 365$ km s^{-1} and $v_{red} = 270$ km s^{-1}. We observe from Section 4.3.1 that the wiggle pattern is most consistent within a limited range close to the source (< 8"), and as discussed the collimated portion of the blue-shifted jet is in any case relatively short and faint. Therefore we limit the fitted portion of the data to a region within ±6" of the source, with the included data points limited to those with smaller error bars. Using initial estimates, β in both jets was constrained to $\sim 1^\circ$ with $\tau_p \sim 8$ years. The phase t was allowed to vary freely.

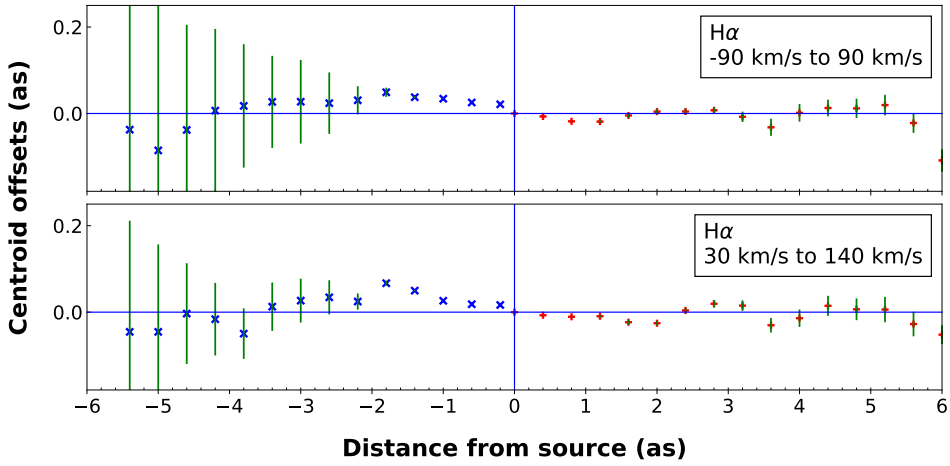

FIGURE 4.7: Centroid positions fitted to the Hα emission in channels including (top) and excluding (bottom) the central velocity channel. Exclusion of the lowest-velocity emission enables a precession signature to be better observed in the blue-shifted jet lobe (left).

We then fitted the [N II] centroids along the deprojected jet axes using these assumptions, carrying out separate fits for the red and blue jet lobes in each case. Initial weighting by the centroid error bars did not significantly improve the fit and in some cases resulted in poorer fits, therefore these results reflect unweighted fits. The results are shown in Table 4.1.

In the red-shifted jet we find consistently that $\beta = 0.5$-$0.6°$, with the best-fit values of τ_p more variable, at an average of 7.3 $\pm$ 1.6 years. The phase t is found to be 6.6 $\pm$ 1 years. In the blue-shifted jet we find somewhat larger values of β at $0.9° \pm 0.2°$; likewise τ_p is consistently fitted at 9 years consistently, while t is very variable at 6.6 $\pm$ 2.4 years. We find an averaged estimate for the length scales of 2.”5 and 4.”2 in the red- and blue-shifted jets respectively. We note that part of the disparity between the lobes is likely because the longer length scale of the wiggle in the faster blue jet means that a full cycle cannot be readily traced, as it is longer than the region of this jet which can be fitted. We also note that the fit in Hα is typically somewhat different to the results in other emission lines, likely due to tracing wider/outer layers of the jet flow.

Using the estimated values of β and v_{jet} in each lobe we also estimate upper limits on the orbital velocity of the jet source due to the companion, finding $v_o = 2.6 \pm 0.5$ km s^{-1} from the red-shifted jet and 5.6 $\pm$ 1.4 km s^{-1} from the blue-shifted jet. The higher estimate in the latter is primarily due to the higher values of β for this jet, an effect most likely due to the poorer S/N as well as the higher degree of interaction with the surrounding medium. As we will see, a larger estimate of v_o corresponds to a larger maximum companion; however, we expect the brighter and more extended red-shifted jet to be a better indicator of the true precession parameters, and in any case the actual

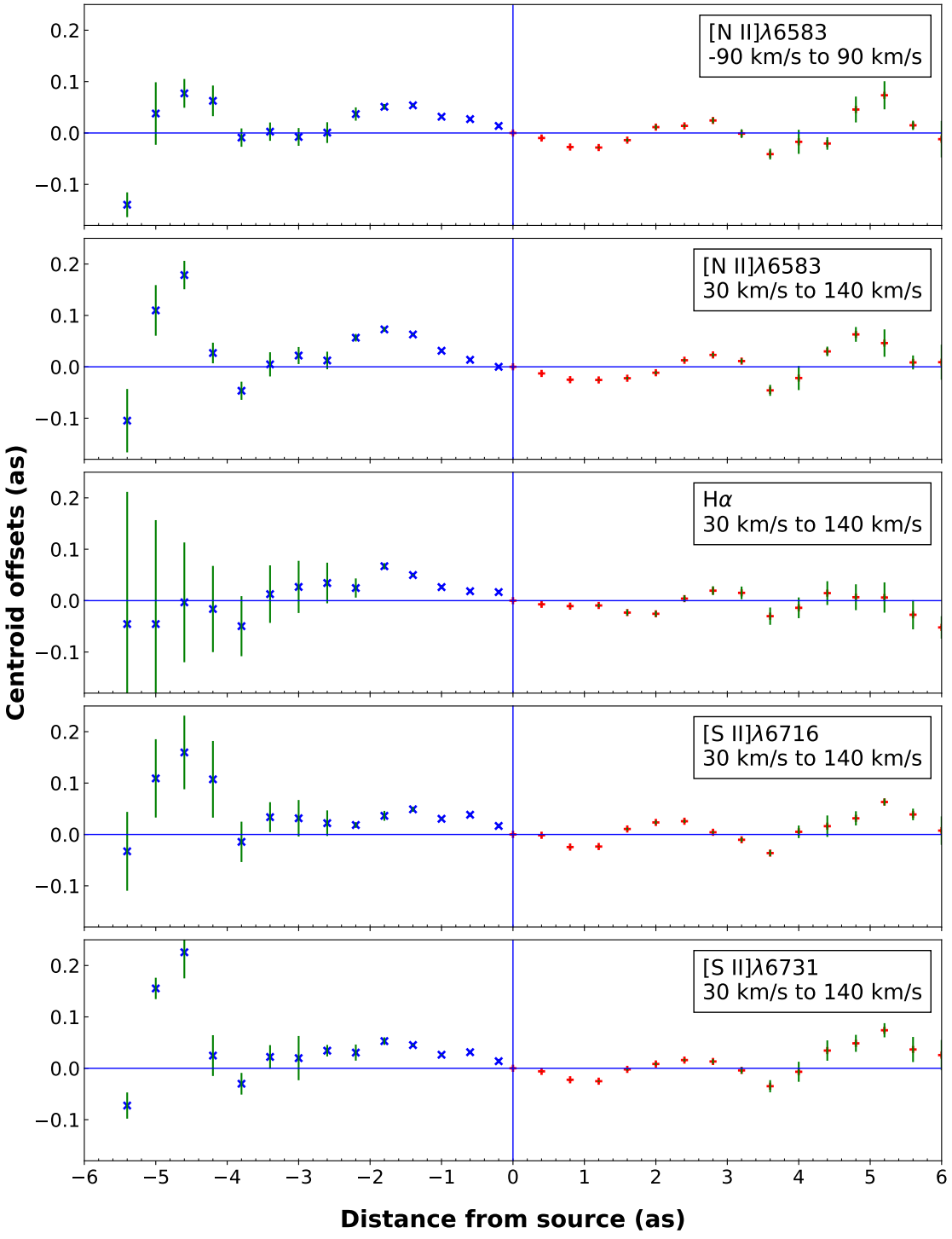

FIGURE 4.8: Centroid positions fitted to the lobes of the Th 28 jet in several emission lines. A consistent wiggling pattern is seen with point symmetry across the source position (origin). Blue-shifted (left side) and red-shifted (right) jet centroids are shown in blue and red, respectively.

orbital velocity (and hence companion mass) is expected to be well below these upper limits.

4.2.2 Precession Fitting - High-inclination Case

We also considered the possibility that the jet velocities and inclinations derived from proper motions do not accurately represent the jet flow, due to the 4-5° inclination disparity between the two jet lobes. Since these estimates are measured from the jet knots this raises the possibility that this is a relatively stationary shock. We therefore examined an alternate scenario based on the inferred jet axis inclination perpendicular to the disk orientation estimated by Louvet et al. (2016). This gives an approximate jet inclination to the plane of the sky of 17°. Combining this with the radial velocities given in Section 3.1.3.2 we obtain $v_{blue} = 260$ km s^{-1} and $v_{red} = 100$ km s^{-1}. Note that this implies significantly lower jet velocities overall; in particular, the asymmetry between the jet lobes is more pronounced in proportion with the radial velocities measured in each. (As noted in Chapter 3, the Th 28 jets are significantly more asymmetric in radial velocity than in proper motions.)

Taking this assumption, we can again fit the precession in both jet lobes, with the results shown in Table 4.2. We find in this case that the red-shifted jet is fitted with $\beta = 0.5° \pm 0.1°$ and $\tau_p = 18 \pm 3$ years, while in the blue-shifted jet $\beta = 1.0° \pm 0.3°$, $\tau_p = 13 \pm 2.5$ years. Due primarily to the lower jet velocities, the inferred orbital velocities are also lower with the red-shifted jet giving $v_{o,max} = 1$ km s^{-1} and the blue-shifted jet giving $v_{o,max} = 4$-5 km s^{-1}.

However, we see that this assumption forces a substantial disparity between the inferred precession period and phase between the jet lobes (with phase $t = 1$ yr in the red-shifted jet, 10 yr in the blue-shifted jet) with substantial variability between phase estimated in different emission lines. We would expect rather that the precession period and phase should be the same at the source, with some small variation in the values measured from our observations of the two jet lobes. Additionally, the high proper motions measured for the inner jet knots imply pattern motions substantially higher than the implied jet velocity in this scenario, with the ratio of pattern to jet velocity $\zeta_{blue} = 1.3$-1.7 and $\zeta_{red} = 2.5$-4.0. In fact these knots are expected to show pattern motions lower than the jet velocity (Eislöffel & Mundt, 1992). This is in fact the case for the jet velocities and inclination angles obtained in Chapter 3.1.4, with $\zeta \sim 0.8$ in both jets. These estimates and the derived precession fits are therefore the most reasonable scenario and are the main focus of this chapter.

Line	Velocity bin (km s^{-1})	Red-shifted lobe β (°)	τ_p (yr)	t (yr)	$v_{o,max}$ (km s^{-1})	λ (")	Blue-shifted lobe β (°)	τ_p (yr)	t (yr)	$v_{o,max}$ (km s^{-1})	λ (")
[N II]λ6583	$\pm$ 90 km s^{-1}	0.6	7.5	7.6	3.0	2.6	1.0	9.0	6.4	6.2	4.2
	$\pm$(30-140 km s^{-1})	0.6	6.9	7.2	3.0	2.4	1.1	9.0	7.6	7.2	4.2
Hα	$\pm$(30-140 km s^{-1})	0.5	5.7	5.7	2.1	2.0	0.8	9.0	8.3	5.3	4.2
[S II]λ6716	$\pm$(30-140 km s^{-1})	0.5	8.4	6.1	2.4	2.9	0.7	9.0	4.2	4.8	4.2
[S II]λ6731	$\pm$(30-140 km s^{-1})	0.6	7.9	6.5	2.7	2.8	0.7	9.0	4.2	4.8	4.2

TABLE 4.1: Table of fitted precession parameters for the red and blue-shifted lobes of the Th 28 micro-jets, using the jet velocities and inclination angles derived from proper motions and radial velocity estimates (Section 4.2.1).

Line	Velocity bin (km s^{-1})	Red-shifted lobe β (°)	τ_p (yr)	t (yr)	$v_{o,max}$ (km s^{-1})	λ (")	Blue-shifted lobe β (°)	τ_p (yr)	t (yr)	$v_{o,max}$ (km s^{-1})	λ (")
[N II]λ6583	$\pm$ 90 km s^{-1}	0.6	20.4	0.1	1.1	2.9	1.0	12.4	8.8	4.6	4.5
	$\pm$(30-140 km s^{-1})	0.6	18.6	1.0	1.1	2.6	1.1	11.9	10.0	5.5	4.3
Hα	$\pm$(30-140 km s^{-1})	0.4	15.7	5.6	1.1	2.2	0.8	14.0	16.0	3.8	5.0
[S II]λ6716	$\pm$(30-140 km s^{-1})	0.4	17.9	0.0	0.8	2.5	1.1	15.9	7.1	5.3	5.7
[S II]λ6731	$\pm$(30-140 km s^{-1})	0.5	19.4	0.0	0.8	2.7	0.7	12.9	10.0	3.4	4.6

TABLE 4.2: Table of fitted precession parameters for the red and blue-shifted lobes of the Th 28 micro-jets, assuming an inclination of 17° from the plane of the sky in both lobes (Section 4.2.2).

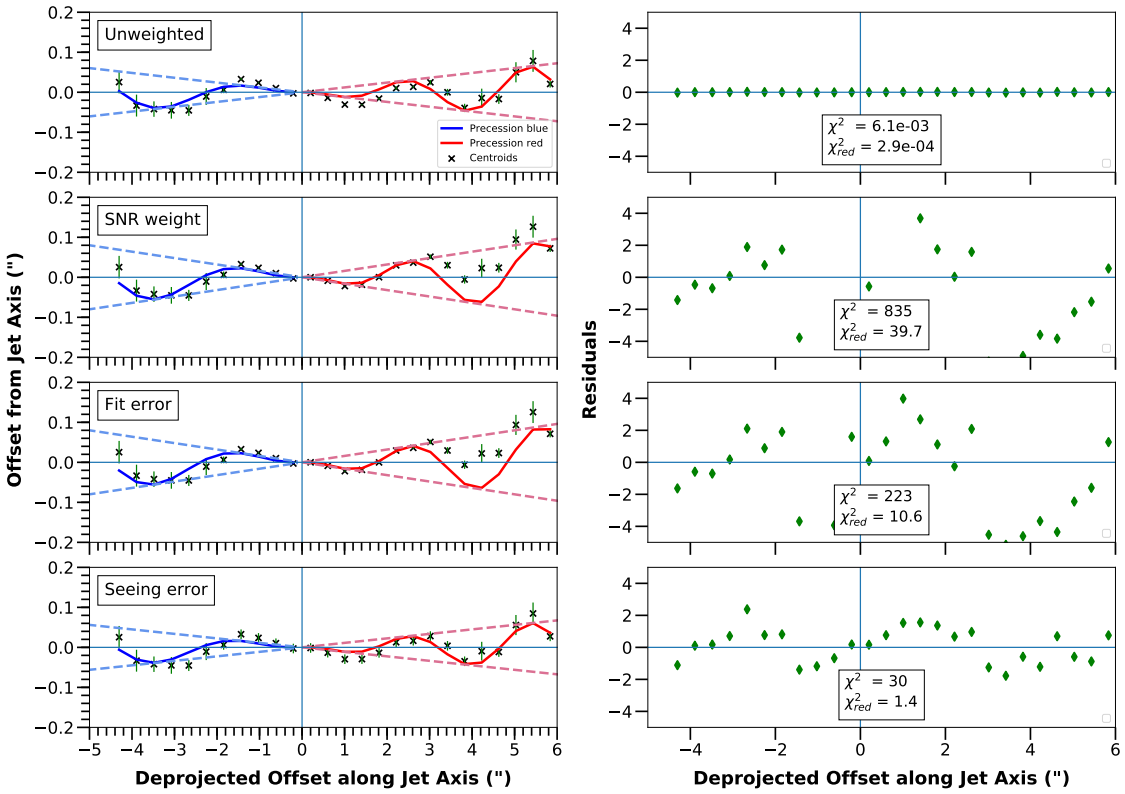

FIGURE 4.9: Comparison of fits to the jet centroids in [N II]λ6583 for different weightings of the fit. Left column shows the weighted fit to the centroids; right, the fit residuals and associated χ^2 estimates.

4.2.3 Weighting the Fits

When carrying out the preceding fits, the data points were not weighted, as weighting by the initial uncertainty on the centroids (estimated by $\frac{0.4FWHM}{S/N}$ (Porter et al., 2004) of the Gaussian fits to the cross-section) did not significantly improve the match to the data points. When carrying out an unweighted fit, we note that *lmfit* estimates the resulting χ^2 statistic from the measured centroids, y and the expected positions from the model, e, by:

$$\chi^2 = \sum_{i=0}^{i} \left(\frac{y^i - e^i}{e^i} \right)^2 \tag{4.15}$$

As shown in the top panels of Figure 4.9, this fit gives a good match to the centroids of the inner jet, with χ^2 values $<< 1$. However, to try and obtain a better fit as well as quantify the goodness of the fit, we wish to determine the best method of weighting the fit. We first consider weighting the data points by the original uncertainty given above.

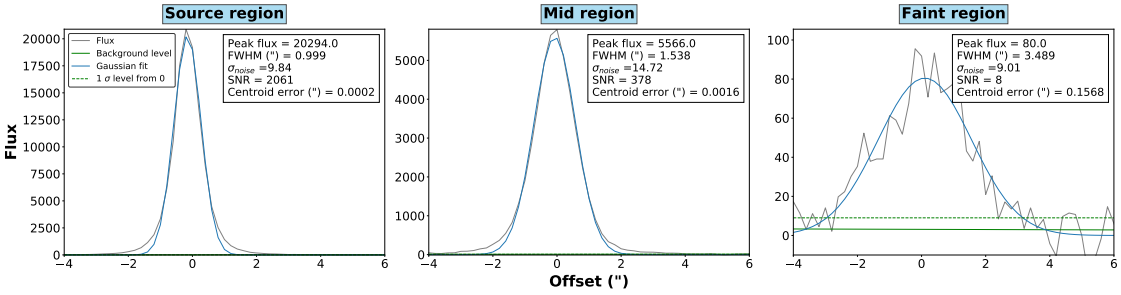

FIGURE 4.10: Sampled fits to different regions of the red-shifted inner jet with associated S/N estimates. Left to right shows fits taken progressively further from the source.

When weights are included, χ^2 is calculated using the uncertainty σ at each centroid, with:

$$\chi^2 = \sum_{i=0}^{i} \left(\frac{y^i - e^i}{\sigma^i} \right)^2 \tag{4.16}$$

Given the number of data points N and degrees of freedom m, we then obtain the reduced χ^2 statistic:

$$\chi^2_{red} = \frac{\chi^2}{N - m} \tag{4.17}$$

We find that this gives very large χ^2 of several hundred or more, while also skewing the fits and giving a poorer match to the data points. This is illustrated in the second row of Figure 4.9 which shows how the weighted fit overly favors the points closest to the source position and causes a substantially poorer match at separations > 2". This is mainly due to the very high peak fluxes from line emission near the source, resulting in S/N values > 1000 as illustrated in Figure 4.10. Such high S/N values result in uncertainties on the centroids of < 0.5 mas close to the source, leading both to very high χ^2 values and a strong over-emphasis on these points in the fitting routine.

We find that these high S/N values and unrealistically small uncertainties are not substantially altered by sampling a wider range of background pixels for the noise estimate, nor the spatial binning of the jet cross-section used. However, given that the high line fluxes observed are most likely caused by reflected emission rather than a true measure of the jet flux, we should consider the uncertainties derived from these S/N values to be an underestimate. We therefore required an alternative method to estimate a more appropriate uncertainty for centroids in these regions.

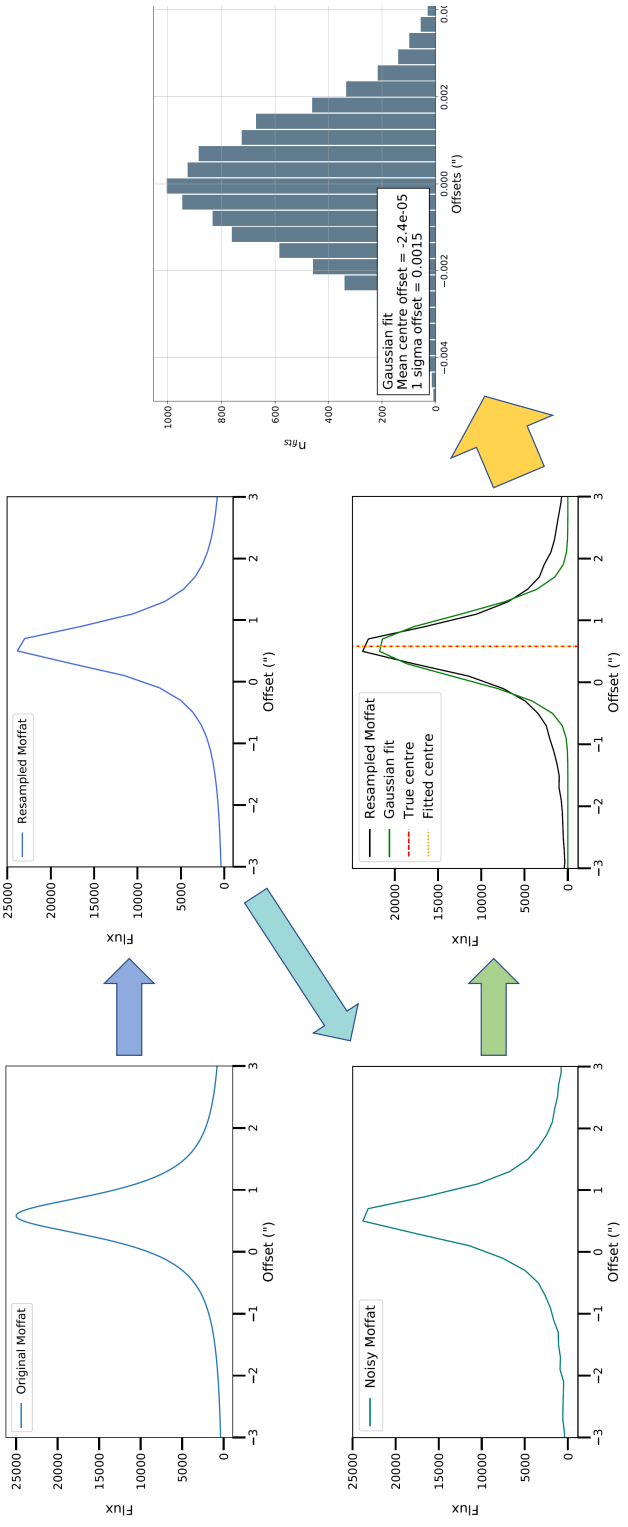

FIGURE 4.11: The procedure used to explore the uncertainties in the *lmfit* fitting routine, using a simulated jet profile with parameters chosen to match the cross-section of the jet within 1" of the source.

We therefore explored the error in the fitting procedure using simulated jet cross-sections. The procedure is illustrated in Figure 4.11. First, we generate a Moffat profile (the closest approximation to the true MUSE PSF) with a FWHM of 1" and a peak of 2.5×10^4, similar to the [N II]λ6583 cross-section at +1" from the source. Initially the profile is generated at a spatial resolution of 0."01, with the centre position randomized within ± 0."8 (4 pixels). The profile is then resampled to a resolution of 0."2 to match the MUSE WFM spatial sampling, and randomly generated Gaussian noise with $\sigma = 100$ is added. Finally, we fit the simulated cross-section with a Gaussian profile initialized to take the centre at 0.0, and find the offset between the true and the fitted centre positions. This is carried out for 10 000 generated profiles to obtain a distribution of the resulting offsets.

As shown in Figure 4.12, the resulting distribution gives $\sigma = 1.5$ mas, and this does not significantly change if a Moffat or Lorentzian profile is used in the fitting routine (although these give a better fit to the core of the cross-section profile). We can take 1.5 mas as the minimum uncertainty on the centroids due to the fitting routine, and an example of the resulting fits is shown in the third row of Figure 4.9. We can see that although the χ^2 value is somewhat improved, it is still quite large with $\chi^2_{red} > 10.0$, and there is no improvement of the fit between the model and the data points. If we take simulated cross-section profiles with a peak flux of $\sim 7 - 8 \times 10^4$ similar to those closer to the source position, we find an even lower uncertainty of 0.5 mas and using this as a minimum error threshold in the centroids produces even poorer precession fits.

The main source of uncertainty in the fitted centroids is due to the effect of the observational seeing. We therefore attempt instead to estimate this uncertainty by comparing centroids measured at the same position in different emission lines. The centroid fitting routine was adjusted to sample the centroids at the same points along the inner jet ± 4", with spatial binning over 0."4 intervals. We measure the standard deviation of the fitted centroid values at each spatial position and take an average across this jet region. The scatter thus estimated is 12 mas (both when averaged across the whole ± 4" region and within ± 1" of the source).

Taking $\sigma = 12$ mas as the minimum uncertainty on the centroids, we obtain a good weighted fit as shown in the bottom row of Figure 4.9, with χ^2_{red} values close to 1. We therefore take this as the most appropriate estimate of the uncertainty.

4.2.4 Precession Fitting: Combined Model

To obtain the final estimate of the precession parameters in the Th 28 jet, we fit a combined model with individual precession components for the red- and blue-shifted

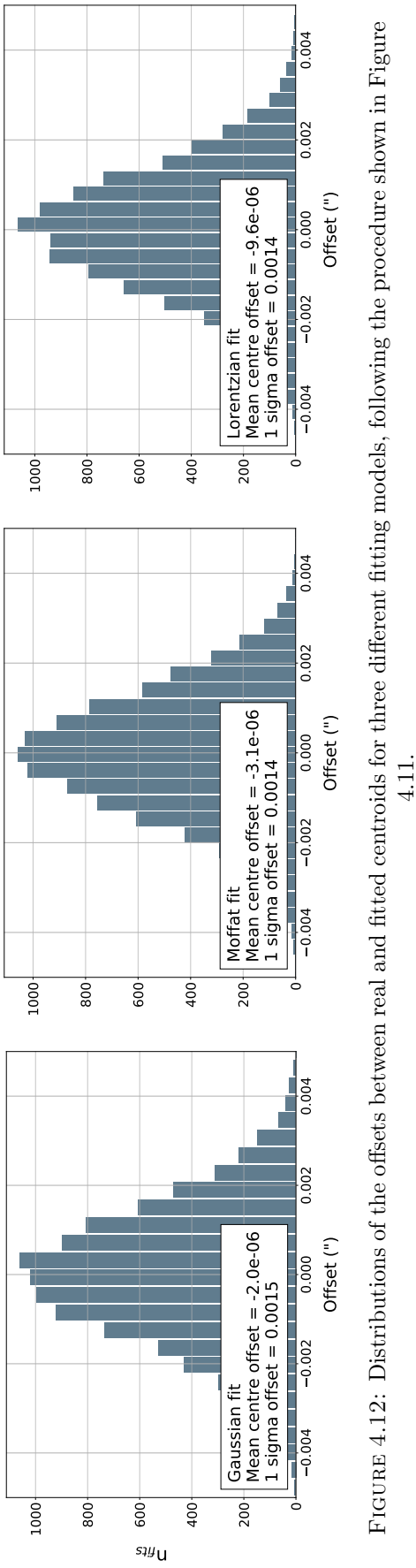

FIGURE 4.12: Distributions of the offsets between real and fitted centroids for three different fitting models, following the procedure shown in Figure 4.11.

Line	Velocity bin (km s^{-1})	χ^2_{red}	β (°)	τ_p (yr)	t (yr)	λ_{red} (")	λ_{blue} (")
[N II]λ6583	± 90	1.4	0.6	8.2	7.1	2.9	3.9
	± 30-140	1.8	0.8	7.4	6.9	2.6	3.5
Hα	± 30-140	1.0	0.5	7.4	7.8	2.6	3.5
[S II]λ6716	± 30-140	0.9	0.6	8.6	6.0	3.0	4.0
[S II]λ6731	± 30-140	0.6	0.6	7.8	6.6	2.7	3.7
Average		1.2	0.6	7.9	7.0	2.8	3.7

TABLE 4.3: Table of fitted precession parameters for the red and blue-shifted lobes of the Th 28 micro-jets.

lobes, allowing the jet velocities to be set individually while constraining β, τ_p and t to be the same on both sides. The fits are weighted as described in the preceding section, with a minimum uncertainty of 12 mas on the centroids, and the jet velocities are taken to be $v_{blue} = 365$ km s^{-1} and $v_{red} = 270$ km s^{-1}. The fit is made over a region within ± 6" in each wavelength channel, with the exact range of centroids included adjusted slightly for each emission line to exclude very faint regions from the end of the blue-shifted lobe.

As mentioned in Section 4.2, we correct for a small residual slope by also fitting a linear component in the model which is then subtracted from the data. No significant difference is found in the PA of the red and blue-shifted jets or the overall correction required. This residual angular offset was found to be $\approx 1.5°$ and combined with the estimated angle in Chapter 2 it gives a total estimated PA of -83.3° and +96.7° for the red and blue micro-jets respectively. This is compatible with the PA estimated by Graham & Heyer (1988) as well as the PA of 97.3° found for the disk rotation axis by Louvet et al. (2016).

The resulting fits are shown in Figure 4.13 with the fitted parameters given in Table 4.3. The close fit to the data points is highlighted by the low χ^2_{red} values for the fits, which vary betweeen 0.6-1.8. The half-opening angle β is estimated between 0.5-0.8° with an average value of 0.6°, while τ_p is fitted between 7.4-8.6 years with an average of 7.9 years. The time t functions as a phase parameter and is fitted between 6-7.8 years, with an average value of 7.0 years. The significant variation of this parameter in the fits is likely to reflect in part the added spatial uncertainty along the jet due to the seeing and the subsequent variation in the estimated length scale of the wiggling, λ. This is particularly the case as the combined model must attempt to fit both jet lobes, which may themselves vary in the apparent precession length scale they show.

Correspondingly, we can see from Figure 4.13 that the blue-shifted lobe is generally slightly less well matched to the fits. This is due to the relative faintness of the blue-shifted jet (reflected in the higher uncertainties of the spatial centroids), combined with the longer length scale of the wiggling in this lobe. In the precessing jet model, it is expected that the length scale λ of the jet wiggles will scale with the jet velocity. In the case of Th 28 we then expect this will be larger by a factor of 1.3 in the blue-shifted jet. With λ_{red} ∼2.8" this then gives λ_{blue} ∼3."5. As this lobe is only resolved to ∼4", it is likely that we are less able to accurately fit the precession parameters in this jet.

4.3 Orbital Motion Model Fitting

The initial investigation of the jet wiggling focused on the red-shifted jet, as it is bright, well-collimated, and can be traced up to 10" without major signs of interaction with the surrounding medium (e.g., the large bow shocks seen in the blue-shifted jet). This suggests the red-shifted lobe is more likely to follow a ballistic trajectory, as well as tracing multiple cycles of the wiggle. Because the blue-shifted jet was not initially included, the jet symmetry was not initially observed. We therefore considered first the case that jet wiggling in the red-shifted lobe was best represented by an orbital motion model, and include the results for completeness.

The fits were confined to the inner micro-jet region (< 10" from the source) where the centroids were fitted with good S/N. The centroid positions along the jet were then fitted for the brightest velocity bins of the Hα and [S II] emission lines. Hα is the brightest emission line and therefore is most likely to give accurate centroid positions; [S II] lines are less bright, but may trace the inner core of the outflow (including any wiggling) more closely. These are also the emission lines used to identify knots and HH objects tracing the Th 28 jet in previous observations.

Initial values for an orbital motion fit can be estimated from the jet shape. For example, the approximate half-opening angle of the redshifted jet wiggle was 1.1°, giving a κ_{init} value of 0.02. We can use these models to construct theoretical orbital and precession trajectories which allow us to constrain the initial parameters further. Figure 4.14 shows two theoretical models chosen to approximate the shape of the Th 28 jet. Both models include an orbital motion and a precession component. The orbital motion wiggle is the same in both cases, with $\tau_o \sim 8$ years, $\kappa = 0.02$, and $r_o = 1.6$ au. The precession component has a small precession angle $\beta = 1°$, making it not much larger than the orbital motion component, with jet velocity of 270 km s^{-1}. The upper panel shows a model with short precession period $\tau_p = 10\tau_o$; the lower panel model has a

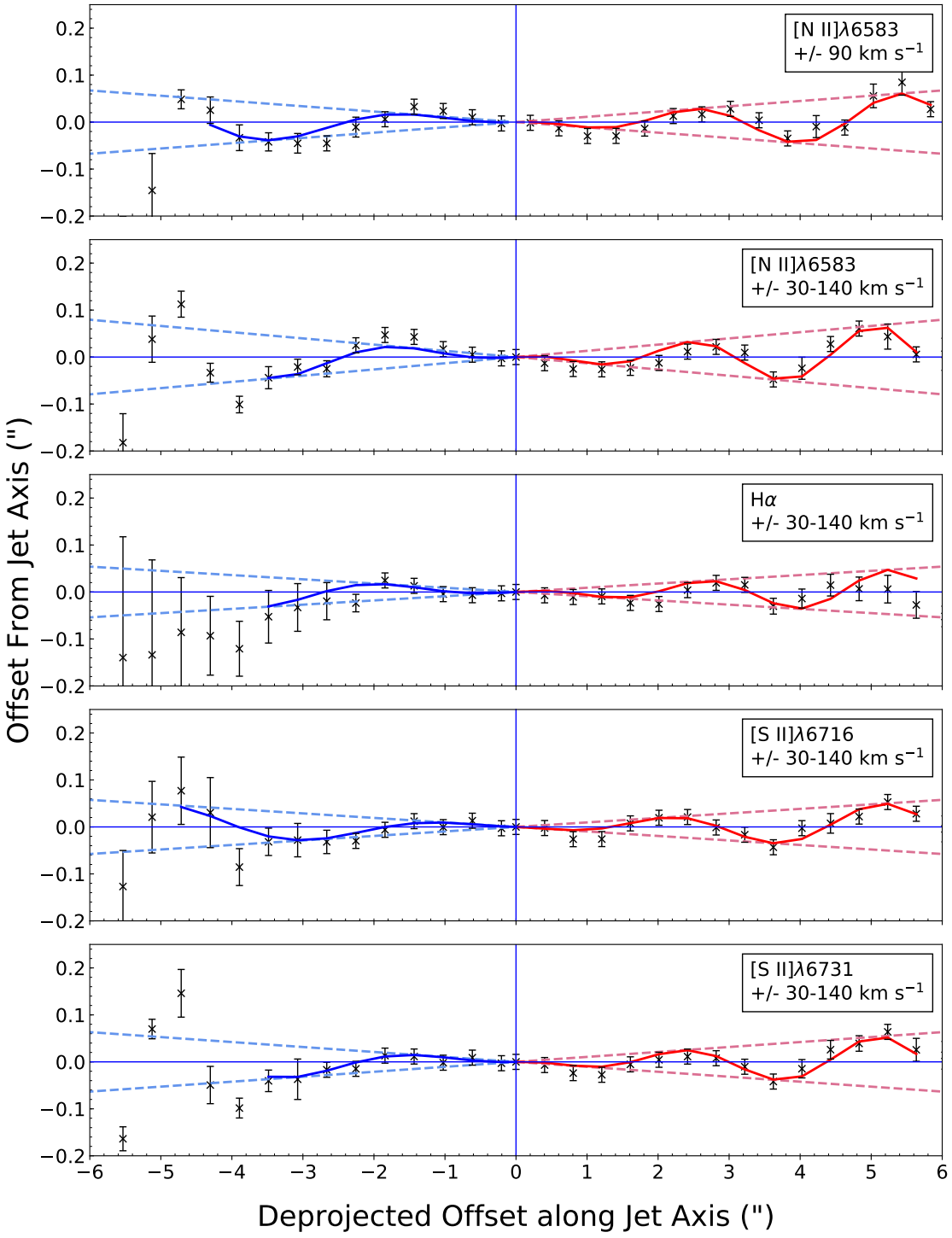

FIGURE 4.13: Combined precession models fitted to several emission lines of the jet, with 0 at the source position. The models and centroids are shown after subtraction of the linear correction; dashed lines mark the half-opening angle on either side of the jet axis.

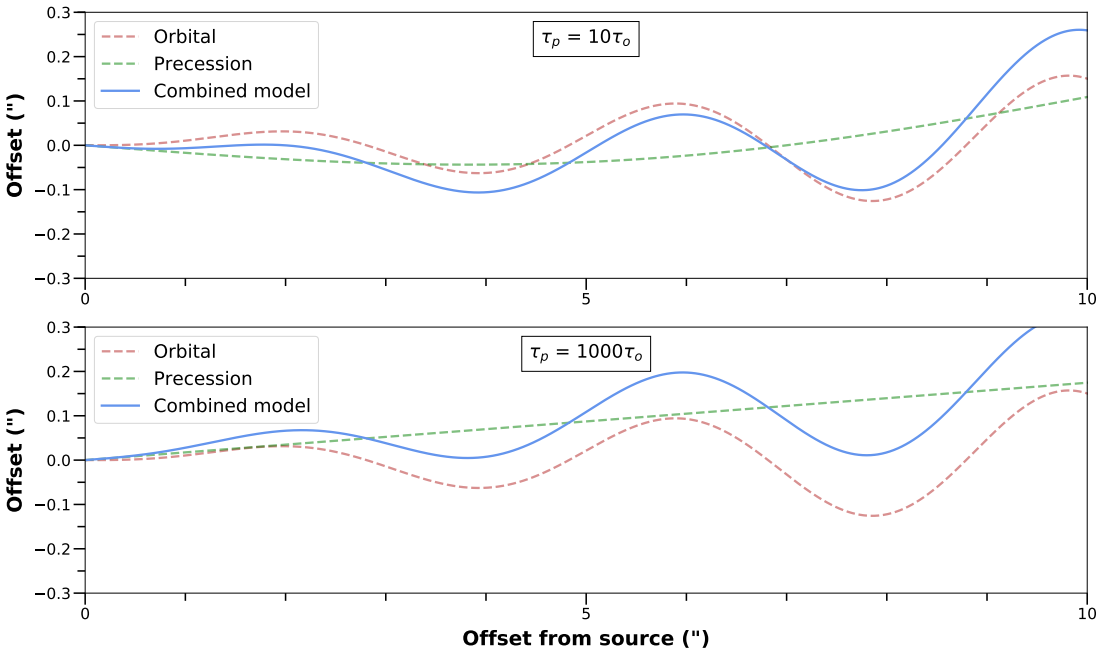

FIGURE 4.14: Theoretical wiggles with combined orbital motion and precession components, based on the estimated parameters for Th 28. Top: the estimate assuming $\tau_p = 10\tau_o$; bottom, the estimate with $\tau_p = 5\tau_o$.

longer period $\tau_p = 1000\tau_o$. As shown in Section 4.1.4, the latter case is expected to be more probable.

These theoretical models allow us to make several inferences. First, the orbital radius of Th 28 must be small, < 2 au, to produce a wiggle with this approximate length scale and opening angle (i.e. given this value of κ). Second, a long-period precession will appear as a slope in the overall trajectory of the jet, approximately linear on small scales. If we are to detect a noticeable large-scale curve in the inner jet, this is only possible for small ratios τ_p/τ_p, ≤ 10. As discussed above this corresponds to an unrealistically large companion, reinforcing that we are unlikely to observe both an orbital motion and precession component in the jet.

4.3.1 Orbital Motion Model

The *lmfit* package was used to define and fit an orbital motion model to the jet centroids, including a small linear component to correct for residual jet PA. The fit was confined to the inner 10" of the brightest $\pm$ 90 km s^{-1} channel of the red-shifted jet. Due to the difficulty presented by r_o and κ both influencing the length scale (λ) of the jet wiggle, the fitting was carried out for three fixed values of r_o, and a grid of κ values between 0.01 to 0.05. The phase factor ψ was allowed to vary freely to obtain the best match to the wiggle shape, and the resulting parameters taken from the best fitting values of κ

r_o (au)	Cube	χ^2 (avg.)	κ	v_o (km s^{-1})	τ_o (yr)	λ (")	μ	M_c ($M_\odot$)	a (au)
0.8	Undec	0.09	0.014	3.8	6.3	2.2	0.2	0.3	4.0
	Decon	0.11	0.014	3.8	6.3	2.2	0.2	0.3	4.0
1.6	Undec	0.23	0.025	6.8	7.1	2.5	0.37	0.6	4.3
	Decon	0.25	0.026	7.0	6.8	2.4	0.38	0.6	4.2
2.4	Undec	0.47	0.040	10.8	6.6	2.3	0.58	0.9	4.1
	Decon	0.47	0.035	9.5	7.6	2.6	0.52	0.9	4.5

TABLE 4.4: Table of parameters fitted to the red-shifted jet using the orbital motion model.

at each assumed orbital radius. The best fits are shown in Figures 4.15 and 4.16 for the centroids measured before and after deconvolution of the Hα and [S II] datacubes.

Table 4.4 shows a summary of the fitted parameters at each orbital radius. The corresponding v_o was calculated from κ and the assumed $v_j = 270$ km s^{-1} while τ_o, μ, and a are calculated from Equations 4.11 - 4.13. We see that the smallest r_o value (0.8 au) gives the lowest χ^2 values and the best fits. For r_o = 1.6-2.4 au, larger values of κ are required to compensate and maintain similar lambda values (i.e. τ_o = 6-7.5 yr) to match the periodicity of the jet; however larger κ values correspond to a larger wiggle amplitude/opening angle such that the predicted centroid offsets quickly become larger than those observed. No substantial difference is observed between the fits before and after deconvolution.

Taking the fits at $r_o = 0.8$ au to be the most plausible, then, we find $\kappa = 0.014$ and $v_o = 3.8$ km s^{-1}. This gives us an orbital period of 6 years, with $\mu = 0.2$ implying a 0.3 $M_\odot$ companion at a separation of 4 au (0."025 at 160 pc). This then implies a disk radius of 1-2 au (assuming σ = 0.25-0.5). This corresponds to approximately the disk region where the jet is thought to be launched, and is therefore not unfeasible. However, this would nonetheless be a very close orbit for a stellar-mass companion, allowing little space for the accretion disk, and it is unclear how this might impact the launching of the jet that is observed.

4.3.2 Uncertainties on Orbital Motion Model

Estimates of the orbital parameters from this model depend on our assumptions concerning several parameters. We take the distance of Th 28 to be 160 pc, with a red-shifted

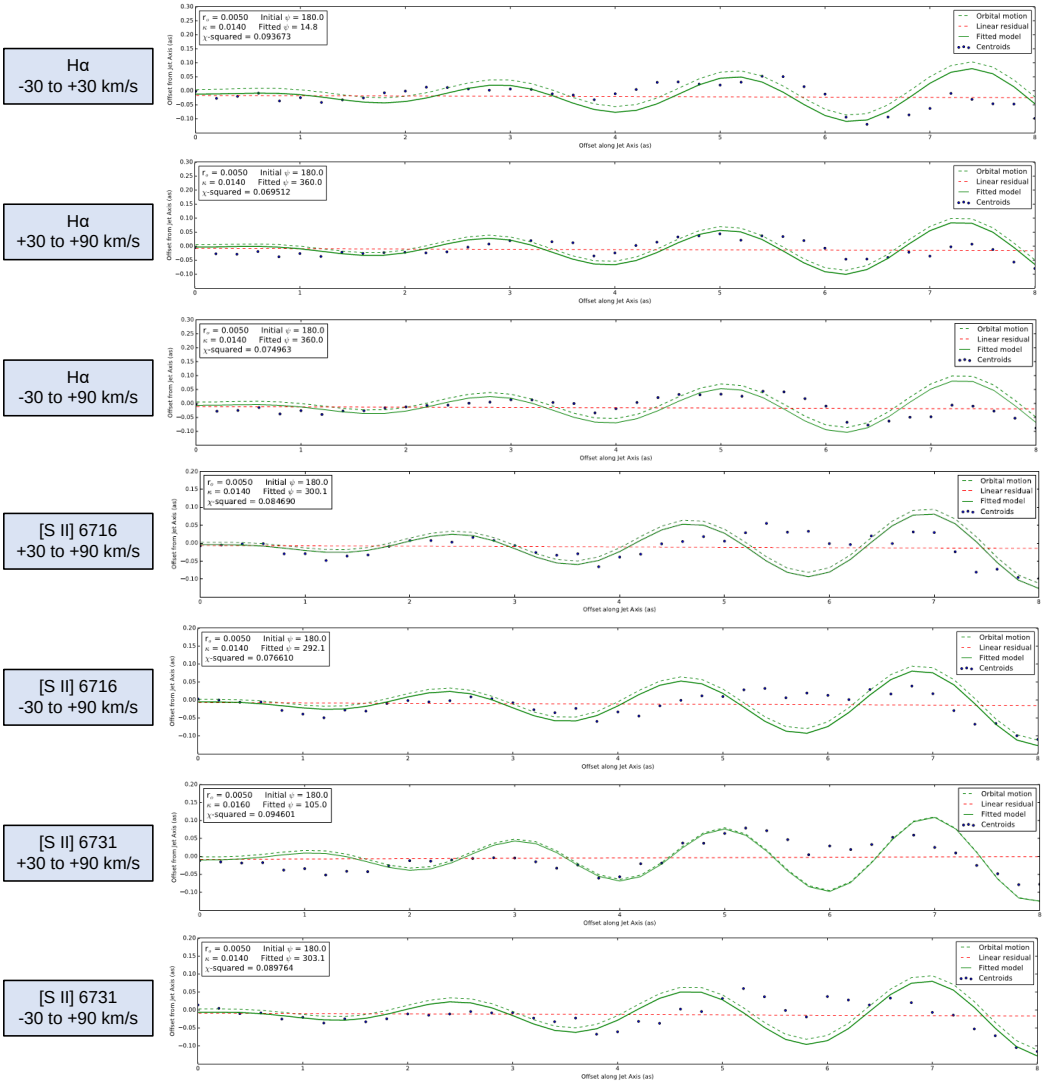

FIGURE 4.15: A selection of fits to different lines and velocity bins of the non-deconvolved data cubes, using the combined orbital motion model. r_o is assumed to be 0."005 (0.8 au at 160 pc).

jet velocity of 270 km s^{-1}. The distance chosen moderately impacts the estimate of the orbital radius (from 1-3 to 0.8-2.4 au) (hence the binary separation and disk size) but also the estimated period of the wiggling. The jet velocity depends primarily on our measurement of the proper motions in the jet, and impacts both the orbital period and velocity estimated from the jet shape. Finally, the assumed mass of the system affects the estimated orbital separation and companion mass.

Here we consider each of these parameters in turn. Taking a 10% uncertainty on the distance of Th 28, this gives us bounds of 145-175 pc. At 145 pc, an assumed orbital radius of 0."005 corresponds to 0.725 au, resulting in a slightly smaller orbital velocity and a small decrease in μ to 0.18; this gives M_c = 0.29 M$_\odot$. Conversely, at 175 pc r_o = 0.875 au, we find slightly increased values of v_o and μ such that M_c = 0.35 M$_\odot$. In

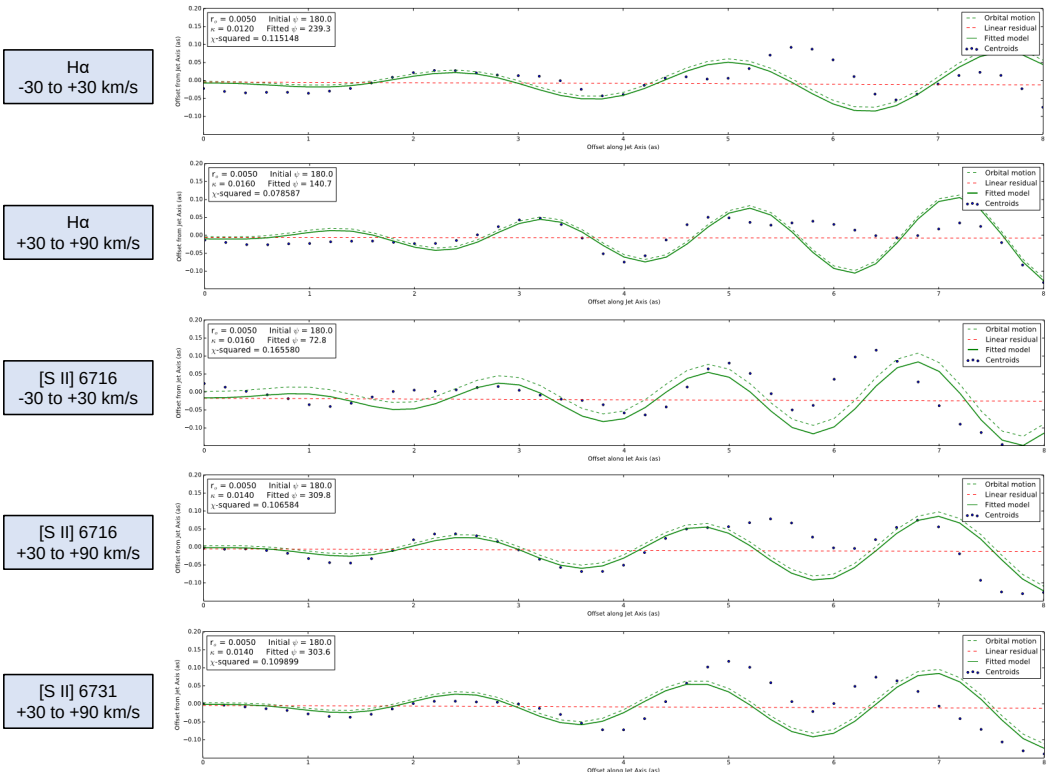

FIGURE 4.16: A selection of fits to different lines and velocity bins of the deconvolved data cubes, using the combined orbital motion model. r_o is assumed to be 0."005 (0.8 au at 160 pc).

both cases a remains 4 au. Similarly, we take uncertainty on the proper motion of the red-shifted jet to be $\pm$ 0."05 yr^{-1}, corresponding to uncertainty on the jet velocity of $\pm$ 30 km s^{-1} at 160 pc. This has a very similar effect to varying the assumed distance: at $v_j = 230$ km s^{-1}, τ_o increases slightly to 7.4 years, while μ slightly decreases to give $M_c = 0.29$ M$_\odot$ at 4.44 au. At the upper bound, $v_j = 300$ km s^{-1}, and $\tau_o = 5.7$ years with a 0.34 M$_\odot$ companion at 2.7 au.

Lastly, the mass of Th 28 has previously been estimated between approximately 1-2 M$_\odot$. At the lower bound, μ increases to 0.23 giving a 0.23 M$_\odot$ companion at 3.4 au separation; at the upper mass bound, $\mu = 0.186$, giving a companion of 0.37 M$_\odot$ at 4.3 au. We can see that in all of these cases, varying our assumed parameters within reasonable bounds of uncertainty has no significant effect on the conclusions drawn from the jet shape.

Line	Velocity bin (km s^{-1})	$v_{o,max}$ (km s^{-1})	μ	M_c (M_{Jup})	τ_o (days)	a (au)
[N II]λ6583	$\pm$ 90	3.0	0.045	75	52	0.32
	$\pm$ 30-140	3.5	0.054	90	56	0.33
Hα	$\pm$ 30-140	2.4	0.03	51	31	0.23
[S II]λ6716	$\pm$ 30-140	2.6	0.035	58	42	0.28
[S II]λ6731	$\pm$ 30-140	2.8	0.039	66	43	0.28
Average		3.0	0.041	68	45	0.29

TABLE 4.5: Table of orbital parameters derived from the precession parameters given in Table 4.3.

4.4 Discussion

4.4.1 Orbital Parameters of a Possible Companion

Returning to the precession model, we then examine whether the precession signature could correspond to an orbiting companion around Th 28. A stellar-mass or brown dwarf companion at distances greater than 20 au is ruled out by recent L-band observations of the disk with NAOS-CONICA (NACO) (F. Comerón, personal comm., 2020), and additionally the small $\sim$ 2.5" scale of the precession wiggle would suggest a companion object within 1 au of the source. Based on the very small angle of precession ($\leq 1^{\circ}$) this inner disk region would have a correspondingly small inclination to the outer disk. We therefore focus on the scenario of close companion and broken disk as described in Section 4.1.3. Although mass estimates for Th 28 vary from approximately 0.9-2.0 $M_{\odot}$ (as discussed in Chapter 1), we take the total mass of the system (jet source and putative companion) to be 1.6 $M_{\odot}$ (Louvet et al., 2016).

Following the procedure outlined in Section 4.1.2.1, we can then use the measured parameters of the jet shape to infer an upper limit on the companion mass and separation. From Equation 4.10, the mean precession parameters from the red-shifted jet give $v_{o,max} = 3.0$ km s^{-1} and hence $\mu_{max} = 0.041$. We thus find $M_c = 70\ M_{Jup}$ with an orbital period of 45 days and a binary separation of 0.3 au. The full set of orbital parameters calculated from the wiggle in each emission line is given in Table 4.5. This shows that while $v_{o,max}$ varies somewhat from 2.4-3.5 km s^{-1} and consequently M_c from 50-90 M_{Jup}, the separation is very consistent at around 0.3 au.

These are not unreasonable orbital parameters for a sub-stellar companion (Almeida et al., 2017; Garufi et al., 2019) but only $\sim$0.1 % of solar-type stars are thought to possess a brown dwarf (BD) companion within 3 au (the 'brown dwarf desert', Luhman et al.

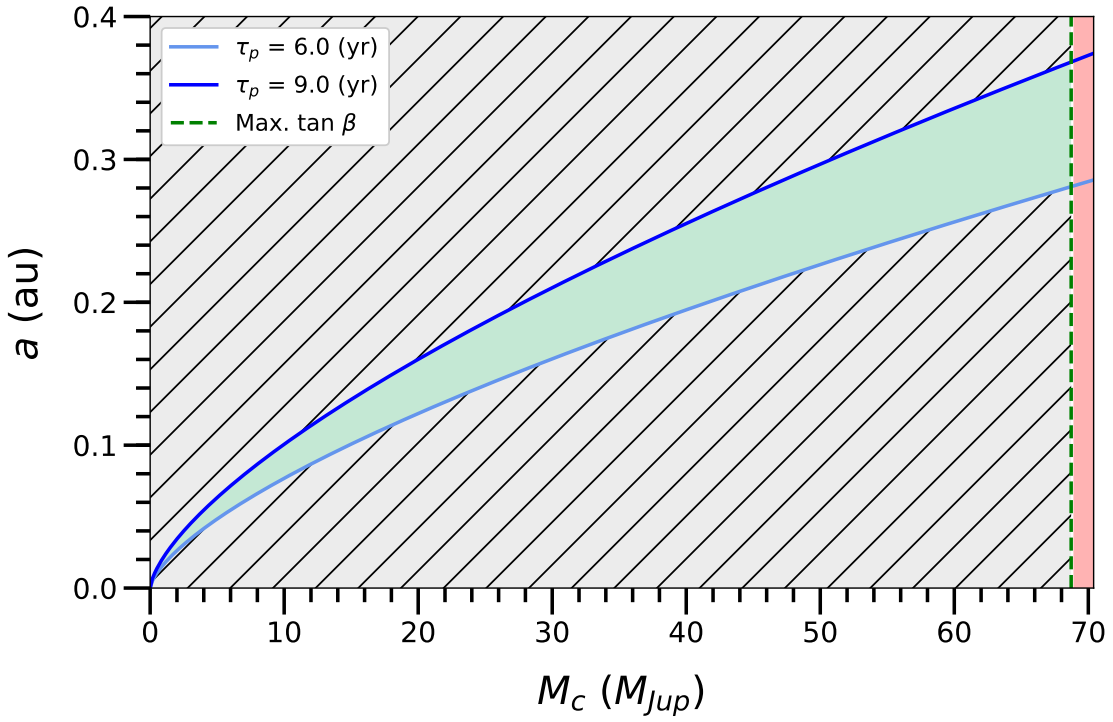

FIGURE 4.17: Parameter limits for the companion inferred from the precession model fits. The green-shaded region between the upper and lower bounds for precession period gives the range of possible separation and companion mass values, with an upper limit set by $v_{o,max}$ (i.e. $\tan\beta$).

(2007)) and therefore such a close BD companion to Th 28 would appear to be very unusual. Recent high-resolution observations of DO Tau also show a similarly small-scale wiggle which may be the signature of a planetary-mass companion in a very close (< 1 au) orbit (Erkal et al., 2021). It should also be noted that our estimated parameters are upper limits on both the mass and binary separation, based on our upper bounds for v_o. The true orbital velocity (and hence values of M_c and a) is expected to be significantly smaller.

We can illustrate this with the plot shown in Figure 4.17. The curves shown in blue give a as a function of the companion mass ($= \mu M_{tot}$, see Equation 4.13 above) for reasonable upper and lower bounds of our estimated precession period. The cut-off point above the maximum companion mass is shaded red. The possible companion parameters are then shown by the region in green. For example, a 12 M_{Jup} companion is expected to have a separation of approximately 0.1 au.

4.4.2 Uncertainties on the Orbital Parameters

Several factors may come into play when assessing the results derived from our model fits. As we have seen, the jet velocity is a crucial parameter for both the fitted model and derived orbital parameters. We derive the velocity in each lobe using the proper motions of their knots, which for the red-shifted jet is well-constrained by multiple measurements to 0."34 - 0."35. However, in the blue-shifted jet we have only one proper motion measurement with uncertainty 0."1 yr^{-1}, making this the greatest source of uncertainty in the jet velocities.

How will our results be affected if the velocity of the blue-shifted jet is varied? To explore this we vary v_j by $\pm$ 0."05-0."1, corresponding to $\pm$ 30-60 km s^{-1}. (corresponding approximately to $v_{o,max} \pm$ 0.1-0.2 km s^{-1}). The results are illustrated in Appendix B.2. We find that a slightly lower velocity ($v_{j,blue} = 330$ km s^{-1}) gives similar or slightly better fits to the jet shape, while in all other cases there is a poorer fit (with average χ^2_{red} increasing from $\leq$ 1.1 to 1.3-1.6). However overall there is little impact on our fitted parameters. At all velocities we find $\beta = 0.6°$, with τ_p= 7.7-8.1 years and $v_{o,max}$ = 2.8-3.0 km s^{-1} giving consistent companion masses of 65-75 M_{Jup} and a = 0.28-0.3 au. In no case does this change the overall findings of the models.

We also consider the impact of our assumed distance of 160 pc for Th 28, previously discussed in Chapter 3. We can take a 10% uncertainty on this value, and therefore examine the results at assumed distances of 144-176 pc. This has no impact on the fitted half-opening angles or precession period, however it corresponds to a small variation in orbital velocity. At D = 144 pc, $v_{o,max} = 2.7$ km s^{-1} with a companion mass of 63 M_{Jup} and $a = 0.27$ au; conversely at D = 176 pc, $v_{o,max} = 3.3$ km s^{-1} with companion mass 85 M_{Jup} and $a = 0.34$ au. Again this has a minimal impact on the overall findings.

An additional concern is whether the variation of the off-axis position of the jet can be determined more accurately. While the S/N ratios of the inner portion of the red-shifted micro-jet are very high as discussed in Section 4.2.3, we have also the added uncertainty at these positions due to contributions from other sources of flux than the jet. Additionally, the fitted offsets are very small relative to the seeing during the observations (0."9). The off-axis distance of the jet (and hence the half-opening angle β) may therefore be underestimated. Ideally further imaging of the micro-jets with adaptive-optics corrections would allow a more accurate estimate of the wiggle parameters, as well as helping to elucidate the kinematics of the jet.

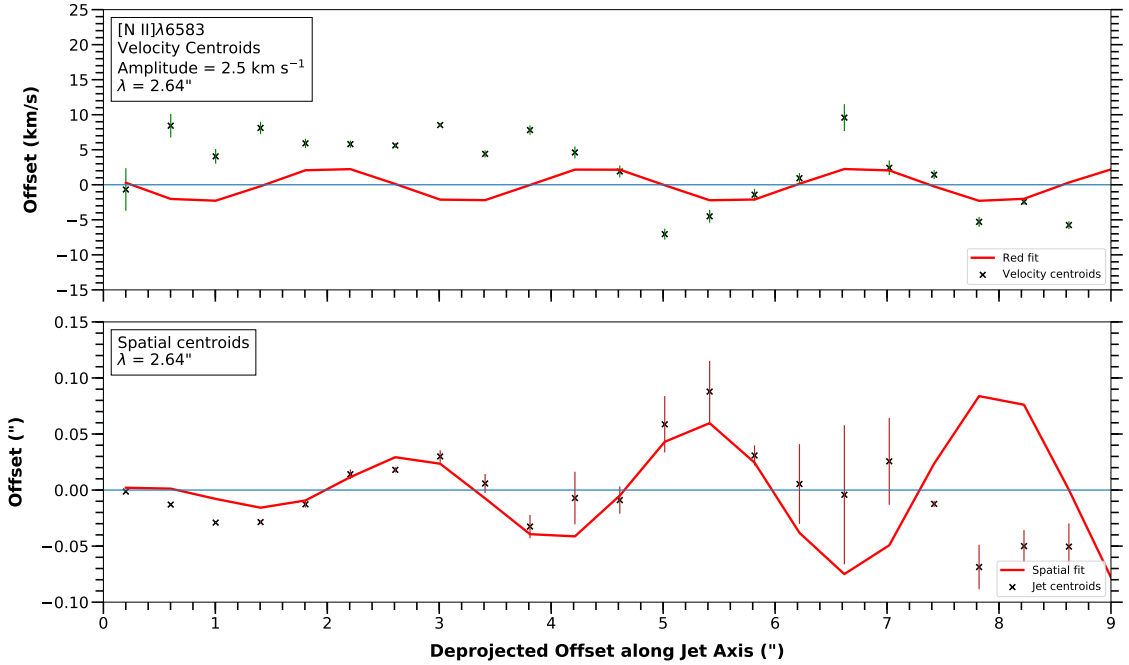

FIGURE 4.18: Comparison of the measured radial velocity shift (top panel) and precession wiggle along the red-shifted jet axis (bottom) with the radial velocity shift model given in Equation 4.18.

4.4.3 Radial Velocity Shifts Due to Precession

A feature of the precessing jet model is that it predicts a similar periodic shift in the radial velocity of the jet. The shift should follow a a sinusoidal pattern with amplitude given by

$$v_{rad} = 2v_j \sin\beta \cos\phi \tag{4.18}$$

The phase should be such that v_{rad} is maximum where the spatial offset from the jet axis is 0. Taking the fitted parameters for the red-shifted jet (β =0.6°) this gives an amplitude of < 3 km s^{-1} using the red-shifted jet velocity of 270 km s^{-1} ($\phi = 6.5°$).

We therefore compared the radial velocity and spatial centroids in [N II], Hα and [S II] in the red-shifted jet and attempted to fit a radial velocity wiggle with the form and phase described. The results are illustrated in Figure 4.18. Although the radial velocities in the 0"-6" range of the red-shifted micro-jet show variations on a scale of +/- 1-5 km s^{-1}, the model was a poor fit to the data with $\chi^2 \geq 7.0$.

This is not surprising as such a velocity shift is significantly smaller than the velocity resolution of MUSE, and is therefore unlikely to be detected in these observations.

Although difficult, it may be possible for future observations mapping the radial velocity along the bright red-shifted jet to detect the small variation predicted from the precession.

4.4.4 Evolution of Precession along the Jet Axis

A question of interest concerns how the precession pattern seen in the jet may evolve as it moves outwards. As mentioned, Masciadri & Raga (2002) have shown that the effects of drag from the interstellar medium can cause the jet to deviate quickly from its initial wiggling trajectory. Bow shocks may similarly cause a deflection from the initial shape. On the other hand, we can observe cases such as HH 111 (and see Appendix B.1 for other examples) where a precession in the jet appears to be traced at large distances from the source.

We first consider the fitted wiggle when compared with the full micro-jets and the more distant knots in the MUSE FOV, that is M1, M2, HHW_2, M6 and HHW. Figure 4.19 shows this comparison for the Hα and [N II] images; the precession model overlaid is taken from the averaged parameters rather than those fitted in these specific emission lines. HHW is shown in the right-hand panels. The model matches well with the position of these more distant knots, although the predicted offsets from the jet axis are in any case small. It should be noted as well that M1, seen on the left-most side of the Hα plot, has a more complicated bow shock structure with two peaks as discussed in Chapter 3.1.1.

As well as the knots observed within the MUSE FOV, the Th 28 jet has a well-documented string of Herbig-Haro objects associated with the blue-shifted jet (Graham & Heyer, 1988; Wang & Henning, 2009; Comerón & Fernández, 2011). Further, examining the FORS1 images of these knots, they appear on first inspection to form a large-scale wiggling pattern. We therefore want to compare the precession model we have fitted with the positions of these extended knots.

To do this, RA and Dec co-ordinates for the source and closest three HH objects (HHW, HHE_1, HHE_2) were obtained from Wang & Henning (2009), observed in 2004. Co-ordinates for the remaining HH objects, taken in 2010, are given by Comerón & Fernández (2011). Although proper motions along the jet axis are estimated for all of the HH objects, to try and obtain the most accurate spatial relationship, we use the proper motions provided by Comerón & Fernández (2011) which give separate components for the $\delta\mu_\alpha \cos\delta$ and $\delta\mu_\delta$ components. As these are provided only for the outer knots in 2011, we use these to estimate the knot positions in 2004 so that they can be plotted alongside the objects detailed by Wang & Henning (2009), and rotate the knot positions

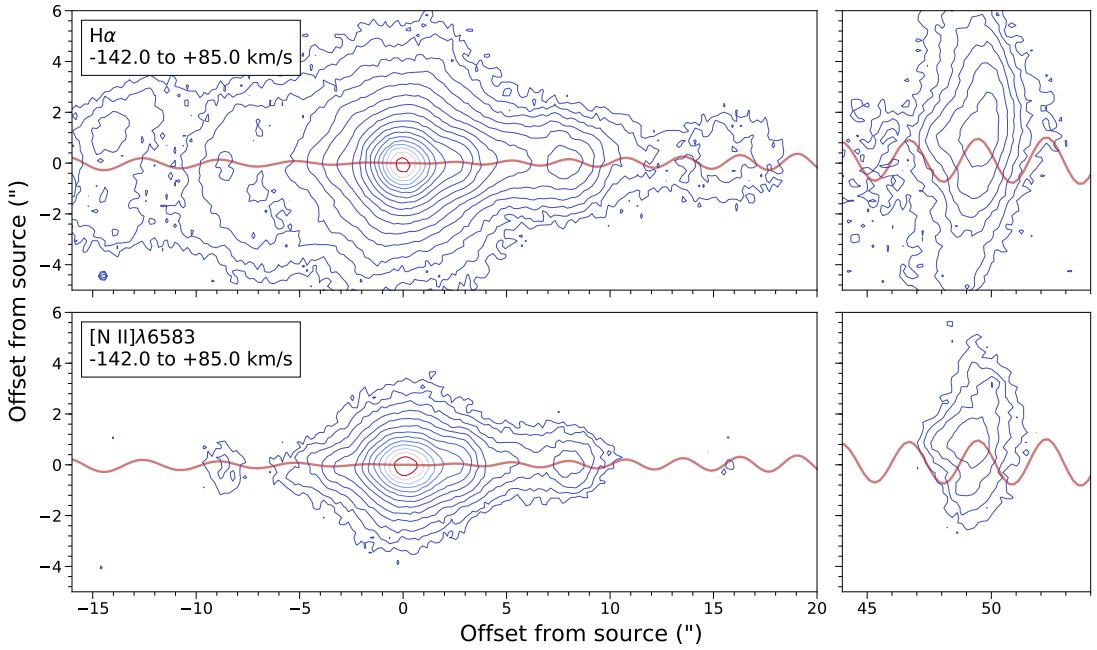

FIGURE 4.19: Contour plots for the inner jet region (left panels) and the bow shock HHW (right panels) with the precession model overlaid (red curve).

by 6.5° to show the jet axis horizontally. Finally, we adjust the estimated t in our precession model accordingly, from t = 7.0 yr in 2014 to t = -3.0 yr in 2004.

The resulting comparison is shown in the first two panels of Figure 4.20, with the middle panel showing a closer view of the HH objects closest to the source. We can see that the model can account well for the positions of the knots HHW, HHE_2 and HHE_3. Although HHE_1 lies outside the range of the model shown, it is still fairly close and could be compatible with a slightly larger value of β, or a small deflection from a position closer to the wiggle trajectory. The farthest knots, HHE_4, HH 989 and HH 989B, however, are clearly outside of the range of positions predicted by the small precession angle. This is what we might expect to find given that the larger the distance from the source, the greater the impact of deflections due to drag and the shocks which are typical in this jet lobe.

As mentioned, however, the extended knot positions appear to trace a wiggling trajectory of their own. We may also therefore consider what precession parameters would be required to match these positions. The bottom panel of Fig. 4.20 shows a precession model constructed to approximate the positions of the blue-shifted HH objects. We find that this requires τ_p of roughly 1000 years and β ~4°. This is very different to the properties of the precession observed close to the source.

This then presents two possibilities: first, that this apparent large-scale precession is a coincidental impression due to the deflection of these HH objects far from the source;

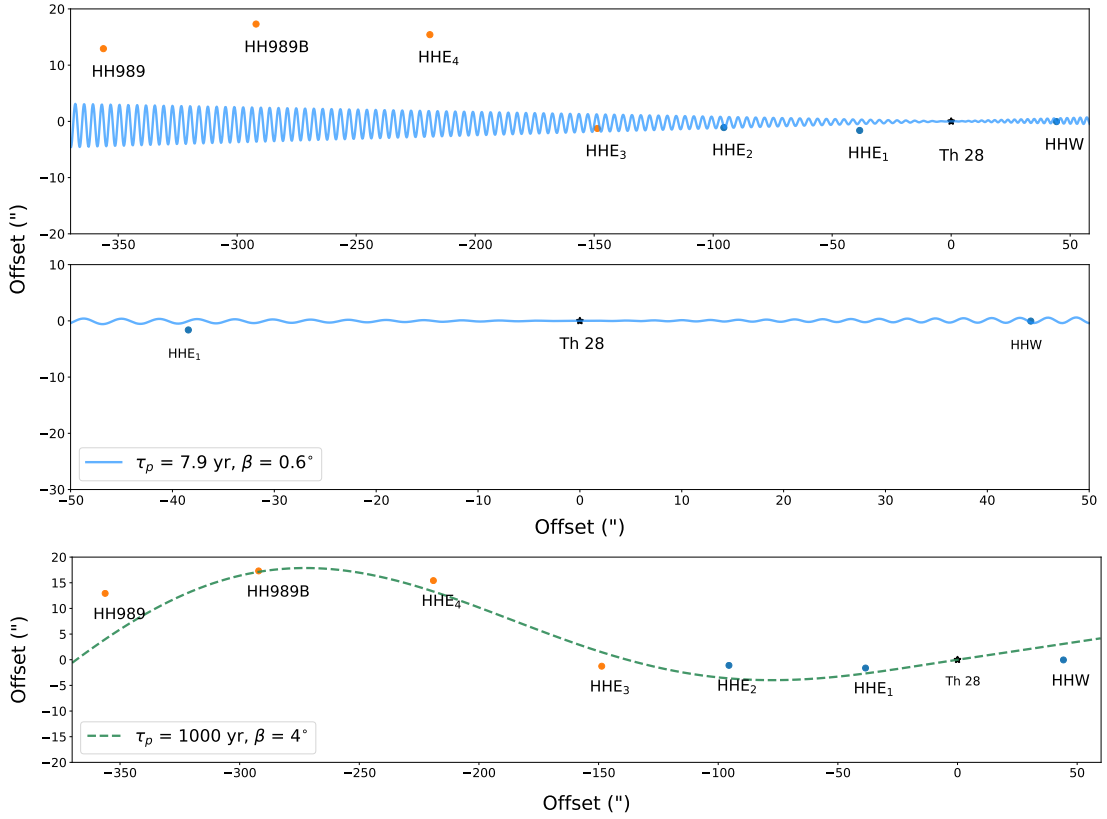

FIGURE 4.20: A comparison of precession models with the HH objects in the extended jet. All knots are shown in their calculated positions for 2004. Points marked in blue are taken from the co-ordinates of Wang & Henning (2009); points in orange are from Comerón & Fernández (2011). Top panel: the full jet compared with the average precession model found in Section 4.2.4. Middle panel: close-up of the same figure showing the two closest knots to the source. Bottom panel: comparison of the knot positions with a hypothetical precession model chosen to approximate their positions.

or second, that there is another long-period wiggling component in the jet, as may be the case in IRAS 20126-4104 (Caratti o Garatti et al., 2008). Unlike the small-scale wiggling, we do not have observations showing an extended HH jet on the red-shifted side beyond HHW, which might show a counterpart wiggling that would be more strongly indicative. One possibility might be to investigate the relative motions of the HH objects and determine whether they move together in a way consistent with their tracing a true wiggle morphology (see Anglada et al. (2007) re HH 30).

We should also consider some caveats regarding particular knots in this supposed pattern. In particular Comerón & Fernández (2011) note that HHE$_3$ is moving away from the jet axis (not directly away from Th 28) in a way that suggests it may originate from an oblique shock produced by the interaction of two knots within the jet. This is also the case for another knot associated with this jet, HH 989C (out of frame in the figures) and lends weight to the possibility that such interactions dominate the jet

morphology in these outer regions. Further, HH 989B is noted to be very faint, with small proper motions, and it is unclear if this is a real HH object.

With these factors in mind, it seems most probable that the apparent wiggling in the extended HH jet is due to the original jet shape becoming distorted by bow shocks and interactions between knots. Given the large spacings between these outer HH objects ($\simeq$50"), we would not expect to clearly trace the observed 2-4" precession wiggle in their positions. As discussed in Chapter 3, Th 28 is seen to eject knots more frequently than these outer jet regions would indicate, and it is likely that most of the intervening knots have faded from view over time, further obscuring the original jet shape.

4.5 Summary

- A wiggling morphology is observed in a number of jets with a wide range of inferred periods and length scales. This may be an indicator of either precession or orbital motion due to a companion object. In a small number of cases it is possible to distinguish between these scenarios via observing the symmetry of the wiggle on either side of the driving source.

- Th 28 is a rare case where the wiggling can be traced close to the source in both lobes of the inner jet, with the symmetry indicating a precession of the jet axis. We are able to fit a model to both lobes which gives a best estimate of $\tau_p = 7.9$ years and half-opening angle 0.6°.

- We use these results to infer upper limits for a potential companion, with $v_{o,max}$ = 3.0 km s^{-1}, $M_{c,max} = 70$ M$_{\rm Jup}$, $\tau_o = 45$ days, and binary separation ≤ 0.3 au. This implies a brown dwarf or massive planetary companion orbiting very close to the jet source. We show that varying our input parameters by reasonable margins of error does not substantially alter this finding.

- An alternative cause for this precession might be a warp in the inner disc due to the disc magnetic fields; however, little is so far known about how these modelled effects correlate to observed star-jet-disc systems.

- Finally, we compare our fitted model with the knot positions of the extended HH jet. We show that the model is compatible with these knots to approximately the position of HHE$_3$ (150") but that beyond this distance, the positions of the HH objects are more likely to be determined by the effects of drag and shocks or knot interactions.

Chapter 5

Diagnostics of the Th 28 Jet

This chapter will investigate the physical conditions within the Th 28 jet, including the electron density, hydrogen density, temperature and ionisation, as well as mass outflow rates through the jet and how they compare with measures of mass accretion onto the driving star.

The first part of this investigation makes use of the Bacciotti-Eislöffel technique (hereafter 'the BE method') for optical line-based diagnostics of the jet physical conditions (Bacciotti & Eislöffel, 1999), applying this along the jet axis to obtain a 1D profile of the jet conditions. We begin with this approach for several reasons: first, the BE diagnostic method gives direct estimates of the jet density, temperature and ionisation, which can be readily compared with previous values obtained for the Th 28 jet using the same technique; second, this allows us to check the application of the new diagnostic code used to carry out the analysis (to be discussed in Section 5.3.1) while minimizing the computational requirements; and finally, given the seeing-limited resolution (0."9 or 4.5 pixels) compared with the ∼1" width of the jet, the diagnostics from spectra obtained at similar binning are likely to provide a good first estimate of the results along the jet axis. A future extension will then be to take advantage of the 3D information available in the MUSE datacube, by applying the BE diagnostic code across 2D slices to create diagnostic spatial and PV maps.

With this goal in mind, the second part of our diagnostic study concerns estimating the extinction along the Th 28 jet and obtaining ratio maps of various emission line ratios, which trace regions of different electron densities, temperatures and ionization fractions along the jet (and across it, in velocity space). While this only traces the relative values of these parameters within the jet, in this way we can make greater use of the broad range of diagnostic line ratios which are available to us in the MUSE data. Future work will bring these strands of the investigation together with the BE diagnostic

code to obtain maps with numerical (rather than relative) estimates of these parameters. Similarly we obtain the first look at maps of line ratios tracing the relative depletion of refractory species within the jet, with a future goal being to derive depletion estimates for these species.

The final part of this chapter focuses on estimating the mass accretion and outflow rates for the Th 28 jet in both the red- and blue-shifted lobes, and comparing the inferred jet efficiencies with previous results.

5.1 Forbidden Emission Lines

To determine the physical conditions within the jet, we will make use of a range of diagnostic tools, but the most important of these depend on making use of the FELs from different species within the jet. We therefore begin with a brief discussion of FELs and how they can be used in jet diagnostics.

Radiative transitions of atoms can be broadly categorised depending on how well they satisfy the selection rules for electron transitions. Permitted lines (such as the Balmer lines of H I) are electric dipole transitions which satisfy all the selection rules; consequently they have relatively large transition probabilities and are typically strong in emission. In comparison, 'forbidden' transitions fail to fulfill electric dipole selection rules, and are produced by the electric quadrupole or magnetic dipole moments of an atom. They are distinguished by their low transition probabilities, with Einstein-A coefficients for the transitions at optical wavelengths approximately a factor $10^5 - 10^8$ smaller than those of permitted lines. FELs are thus relatively weak, and under high density conditions their upper levels are completely depopulated by collisional de-excitation.

However, in low-density regions typical of jets, FELs become significant, and dominate cooling processes at typical nebular temperatures of $\sim 10^4$ K (1 eV). These emission lines trace the outflows in regions where the electron density remains below their critical densities, defined for a given transition ij as

$$n_{cr} = \frac{\Sigma A_{ij}}{\Sigma q_{ij}} \tag{5.1}$$

where A_{ij} is the radiative transition coefficient and q_{ij} the collisional de-excitation rate. For n_e less than the critical density, collisional de-excitation is only partial, while if $n_e > n_{cr}$, collisional de-excitation becomes important. This occurs in regions close to the jet source, where higher densities result in a weakening of FELs. This presents limits

on the regions these lines can probe, as the core of the driving jet engine lies within a few au of the disk.

In the jet regions, however, FELs are crucial outflow tracers, in particular lines derived from low-excitation levels of oxygen, nitrogen and sulphur ions. These are significant in emission despite their low abundance compared to hydrogen or helium due to their significantly lower excitation energies. Different FELs trace different components of the outflow, with [N II] lines tracing high excitation and typically high-velocity components, while [S II] lines trace lower excitation (and typically lower velocity) components, and [O I] lines show emission in both high and low velocity components of the jet. As the next sections will discuss, they are also crucial to investigating the physical conditions within the jet.

5.1.1 Using Line Ratios to Measure Physical Properties

To estimate the electron density n_e in the jet, one can make use of two emission lines from the same species whose excited levels are close in excitation energy (minimizing the effect of temperature on their relative level populations) but which have different critical densities. As an example we take the [S II]λ6716/6731 doublet ratio, which is an important measure of n_e. The energy levels of the [S II] doublet are very closely spaced, leading to lines very close in wavelength at 6716 Å and 6731 Å. This means that in the lower limit of electron density n_e, where each collision produces a photon, the ratio of the two line intensities (I_{31}, I_{21}) is approximately the same as the ratio of the collisional rate coefficients (C_{13}, C_{12}):

$$\frac{I_{31}}{I_{21}} \sim \frac{C_{13}}{C_{12}} =\sim 1.4$$

Below this limit, where $n_e << n_{cr}$, collisional de-excitation is negligible and the emissivity of the lines is proportional to ${n_H}^2$. In the high density limit, in contrast, collisional de-excitation dominates, and this becomes:

$$\frac{I_{31}}{I_{21}} \sim \frac{C_{13}}{C_{12}} \times A_{31}/A_{21} =\sim 0.4$$

where A_{31} and A_{21} are the Einstein-A coefficients for the two line transitions. The line intensities are no longer dependent on n_e and instead their emissivity is proportional to the total density n_H. In between these two limits the number of collisions with free electrons determines the level population, and so the ratio of the line intensities is strongly dependent on n_e. This therefore defines a regime where the line ratio can be

Reference	Obs. year	Instrument	Band	Velocity resolution (km s^{-1})	Spatial resolution (")
(1) Krautter (1986)	1985	VLT/B & C Spectrograph	Optical	90	1.0
(2) Bacciotti & Eislöffel (1999)	1987	VLT/B & C Spectrograph	Optical	75	1.8
(3) Coffey et al. (2008)	2002	HST/STIS	Optical	25	0.1
(4) Coffey et al. (2010)	2006	VLT/ISAAC	IR	30	0.7
(5) Liu et al. (2014)	2003	VLT/UVES	Optical	10	
(6) Liu et al. (2021)	2016	HST/STIS	NUV	45	0.1

TABLE 5.1: Summary of diagnostic studies of the Th 28 jets.

used to measure the ambient n_e; the intensity ratio varies between these two values as a function of n_e, with the transition to high-density regimes occurring at about the critical density 2.5×10^4 cm^{-3}. A similar case applies for the [Fe II]λ7155/8617 ratio, however these lines have much higher critical densities and hence this ratio is sensitive between densities of 1×10^5 - 1×10^7 cm^{-3}.

To estimate the jet electron temperature T_e we instead need to use emission lines of transitions with upper levels that have significantly different excitation energies. In the low-density regime, their relative emissivities will then be proportional to $\exp \Delta E/kT$. The ionisation fraction, x_e, is also important to determine excitation conditions in the jet, and combined with estimates of n_e it is used to estimate the total (H) density $n_H = (n_e/x_e)$. This is possible because in practice the number of free electrons produced by H ionisation dominates with regard to the conditions of all other species, and therefore estimates of n_e and x_e are direct estimates of the conditions for H. The total density in turn allows the investigation of important properties of the outflow such as the mass and momentum fluxes, which are important properties to examine the jet launching and propagation, and to study its feedback into the surrounding environment.

Ref.	Red-shifted Jet		Source position		Blue-shifted Jet	
	n_e (10^4 cm^{-3})	Offset (")	n_e (10^4 cm^{-3})	Offset (")	n_e (10^4 cm^{-3})	Offset (")
(1)	0.1	-2.8	1	-0.9	0.5	+0.9
(2)	-	-	-	-	0.25	+2
(3)	-	-	-	-	0.5	+0.3
(4)	1.4 ± 0.4	-0.5	-	-	2 ± 0.1	+0.5
(5)	6.7 ± 2.2	-0.5	-	-	4.6 ± 2.4	± 1
(6)	1	-	-	-	≥10	-

TABLE 5.2: Estimates of n_e for the jet lobes from previous studies. Note that Krautter (1986) reports an estimate placed at -0."9 of the assumed source center for the n_e at the source position.

Reference	Red-shifted Jet		Blue-shifted Jet	
	n_e (10^4 cm^{-3})	Offset (")	n_e (10^4 cm^{-3})	Offset (")
(2)	-	-	2.5	< 0.1-0.5
(3)	-	-	∼ 2 ± 1	∼ 0.3-0.5
(5)	1.7 ± 0.6	-	1.5 ± 0.5	-

TABLE 5.3: Estimates of ionisation fraction and electron temperature for both jet lobes from previous studies.

5.2 Previous Diagnostics of Th 28

In this section we review the main studies focusing on the optical diagnostics of the Th 28 jet to date. A summary of the sources reviewed including the spatial and spectral resolutions of the data used is given in Table 5.1. Of these, the paper by Bacciotti & Eislöffel (1999) is the only one which includes diagnostics for the bow shock HHW, and along with Krautter (1986) is one of only two which report diagnostics for the extended red-shifted jet (>2" from the source). This study and the optical line diagnostic technique used (the BE method) will be discussed in more detail in the next section. Similarly, Krautter (1986) reports n_e values derived from the [S II]λ6716/6731 ratio which are plotted in Figure 5.1. Here we will discuss the results obtained close to the jet base.

A summary of the estimates for electron density in both jet lobes is shown in Table 5.2. Overall results obtained from the [S II]λ6716/[S II]λ6731 ratio show values of 0.5-1 $\times$ 10^4 cm^{-3} close to the source, dropping to 2000-2500 cm^{-3} at 2" from the source in

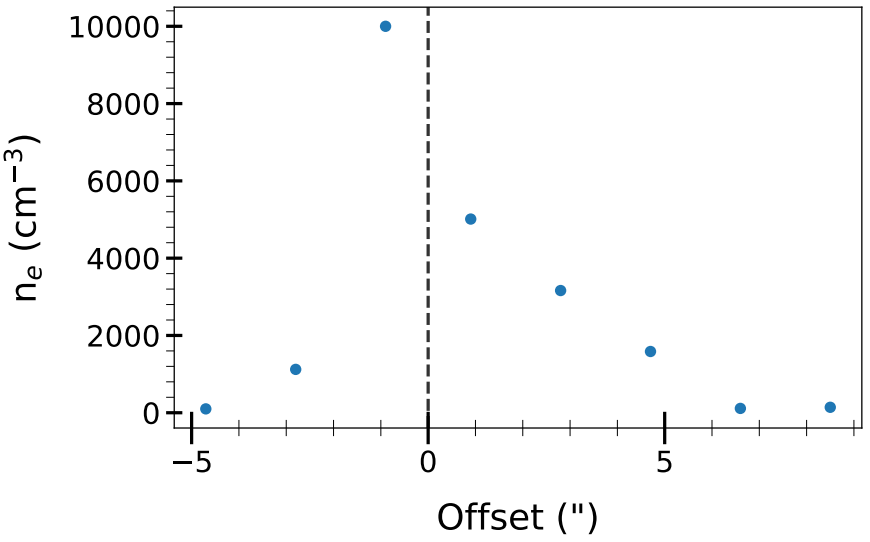

FIGURE 5.1: Estimates of n_e along the Th 28 jet as reported by Krautter (1986), derived from [S II]λ6716/6731 flux ratios assuming $T_e = 1 \times 10^4$ K.

the red-shifted lobe. Transverse n_e maps (Coffey et al., 2008) also suggest a spatial asymmetry, with the [S II] ratio saturating on one side of the jet (indicating a lower n_e limit of 2.5×10^4 cm^{-3}) while it falls close to the low density limit elsewhere ($n_e \sim 50$ cm^{-3}). No velocity trend is observed in these maps. When combined with ionisation fraction estimates (where available), these studies give values for the total density n_H of $\sim 3 \times 10^4$ cm^{-3} (and a lower limit of 1.4×10^5 cm^{-3} in the high-density region found by Coffey et al. (2008)).

Comparing results from the two jet lobes, an asymmetry in n_e is typically observed with higher values ($6.7 \pm 2.2 \times 10^4$ cm^{-3} to $\geq 1 \times 10^5$ cm^{-3}) in the blue-shifted jet compared to those found in the red-shifted jet (1×10^4 cm^{-3} to $4.6 \pm 2.4 \times 10^4$ cm^{-3}) (Liu et al., 2014, 2021). In contrast, measurements by Coffey et al. (2010) using [Fe II] lines show $n_e = 2 \pm 0.1 \times 10^4$ cm^{-3} and $1.4 \pm 0.4 \times 10^4$ cm^{-3} in the red- and blue-shifted jets, respectively; on the other hand, given the significant uncertainties it is unclear how much of an asymmetry these values represent. Additionally the blue-shifted jet has a higher ionisation fraction, so that the total density estimated by Liu et al. (2014) is actually a factor 1.4-2 higher in the red-shifted jet.

Within ∼1-2" of the source, very high densities are consistently indicated, as is expected. As well as the [S II] ratio, [Fe II] lines saturate close to the jet base indicating $n_e > 6 \times 10^4$ cm^{-3}, and this picture is borne out by the detection of permitted lines with high critical densities ($> 10^6$ cm^{-3}) close to the source, including extended emission from Paβ and Brγ up to 150 au from the star. The overall picture is that of a very high density region close to the source, as expected, and asymmetric jet lobes with significantly higher

n_e but overall lower density in the blue-shifted jet, compared to a less ionised but more dense red-shifted jet.

Measurements of ionisation and temperature for Th 28 are somewhat more limited, and are summarised in Table 5.3. At 2" from the source, Bacciotti & Eislöffel (1999) find $x_e < 0.1$ while $T_e \sim 2.5 \times 10^4$ K, while an estimate using the [N II] ratio (as discussed in Section 5.5.2.1) gives $T_e = 1.7 \pm 0.6 \times 10^4$ K in the blue-shifted jet and $1.5 \pm 0.5 \times 10^4$ in the red-shifted jet, suggesting a temperature 13% higher in the blue lobe (Liu et al., 2014). Optical line ratios also suggest an ionisation fraction that is higher by a factor of 2-3 in the blue-shifted jet.

Transverse cross-sections of the jet temperature and ionisation (Coffey et al., 2008) show a temperature peak of 3×10^4 K in a thin region at the peak of the red-shifted velocities, as well as a spine of 2×10^4 K in the lower velocity portion of the jet, with a drop to 1×10^4 K at the spatial edges. The authors note that this drop in temperature corresponds to the rise in n_e on one side of the jet. The ionisation fraction is around 0.5 at high red-shifted velocities but around 0.3 in the rest of the cross-section. This profile corresponds only partially to shock models (Hartigan et al., 1994), as these would predict a low-velocity peak in temperature along with the peak in x_e at high velocities.

Based on these previous studies, the overall picture of the Th 28 jet suggests very high electron densities close to the source, followed by a rapid drop in both n_e and n_H along the jet axes, which is a typical profile for stellar jets. The jet lobes themselves are clearly asymmetric, with the blue-shifted jet being hotter, more ionised and less dense, while the red-shifted jet is slightly cooler, less ionised and denser. In addition, there are some indications of spatial asymmetries *across* the jet cross-section. The MUSE data therefore affords the opportunity to simultaneously investigate these asymmetries, both between the two jet lobes and within each side of the jet, as well as providing the kinematic information to look for signs of velocity asymmetries in the jets along the launching axis.

5.3 BE Diagnostics

This project makes use of the technique detailed by Bacciotti & Eislöffel (1999) for carrying out optical FEL diagnostics. This technique is relevant to regions of low-excitation conditions without nearby strong sources of photoionisation, such that the gas is collisionally excited and emits FELs.

The method assumes that the sulphur in this region is singly ionised, due to its low ionisation potential (IP), and that the ionisation of oxygen and nitrogen is governed by charge exchange with hydrogen, e.g. in the case of oxygen:

$$O^0 + H^+ \rightarrow O^+ + H^0 \tag{5.2}$$

This process has a very large cross-section as the the ionisation potentials (IPs) for O and H are very close, and thus it becomes important where there is high H^0 density but low radiation density. Because H is far more abundant then O, this process may dominate the ionisation balance of O but not H. If the temperature is high relative to the IP difference between the species ($T_e \sim 1 \times 10^4$ K, typical in jets), an equilibrium is reached in which their ratios depend primarily on their statistical weights and the ionisation fraction of O is 'locked' to that of H. A similar case applies for N which also has an IP close to that of H and so these conditions can also apply. Because O and N have a much shorter recombination time than that of H, their ionisation can be assumed to be in equilibrium with that of H at any time.

The BE method also assumes that that O, S, and N are singly ionised in accordance with the fact that low-excitation jet conditions apply, i.e., no lines of [S III], [O III], [N III] are detected (Dougados, 2008). The emitting gas is considered to be at a single temperature (homogeneous excitation conditions), although the temperature can vary in space. No assumptions are made about heating mechanisms.

The BE method makes use of the prominent jet-tracing lines[O I]λ6300 and 6363, [N II]λ6548 and 6583, and [S II]λ6717 and 6731. The [S II] lines can be used to determine n_e as described in Section 5.1.1, and given this value, the two key ratios [S II]λ(6716+6731)/[O I]λ(6300+6363) and [O I]λ(6300+6363)/[N II]λ(6548+6583) can be described as functions primarily dependent on T_e and x_e. Using the equations of statistical equilibrium for the level populations of involved species, these functions can be calculated on a grid of possible values of x_e and T_e (Bacciotti & Eislöffel, 1999). This forms well defined surfaces in the parameter space (of x_e, T_e, and the line intensity ratios). The observed values of the ratios then define contour levels on each corresponding surface which can be projected on the x_e, T_e plane; the points at which these contours cross defines the values of these variables for which the model gives the observed ratios. Figure 5.2 shows an example which takes into account the measurement, so that the diagram gives rise to the crossing of three stripes. The intersection of these stripes in such a diagram thus provides an estimation of x_e and T_e, and hence the approximate hydrogen density n_H (derived as $n_H = n_e/x_e$).

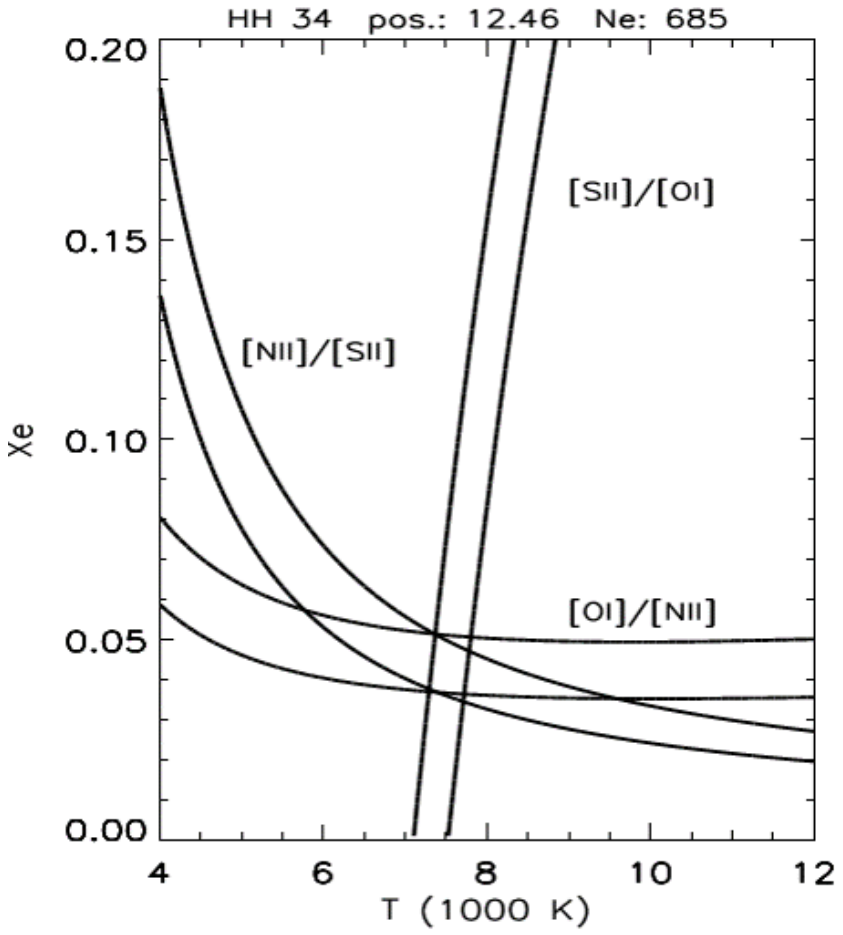

FIGURE 5.2: A sample of diagnostic curves of key emission line ratios for the BE method in x_e and T_e space, reproduced from Bacciotti & Eislöffel (1999).

Typical results for jets show a partially ionised jet with $0.01 < x_e < 0.6$, with little variation along the jet outflow, consistent with slow recombination rates of H. This causes 'freezing' of the ionisation which is probably produced close to the source. The derived total densities n_H are typically in the region of 10^3 - 10^5 cm^{-3}, with denser jets generally exhibiting lower ionisation.

The method does not account for photoionisation of O and N that may be produced, for example, by strong ultraviolet sources. Typical HH jet sources do not produce sufficient high-energy photons for photoionisation of the jet. However, this assumption may not hold in the terminal bow shock of a jet where there is high ionisation, or in cases where the jet is irradiated by another source such as a nearby OB star (see for example the jets HH 444 and HH 1158 (Andrews et al., 2004; Riaz & Whelan, 2015). Suitable conditions have been met if the derived x_e is below 0.8.

The assumption of locally homogeneous excitation conditions in the sampled spatial

region may also not hold in the cooling zone behind a shock front. These regions have strong spatial gradients in n_H, x_e, and temperature over scales of a few au in length, which are too small to be resolved in typical observations. The combination of line fluxes from different regions may therefore bias the integrated line ratios; on the other hand, the optical lines used in this method originate at similar distances from the shock front probing intermediate T_e and x_e, and so this effect should be minimised in shocks with $v_{shock} < 50$ km s^{-1} and pre-shock densities $< 10^4$ cm^{-3}.

The technique does not itself account for reddening of the line fluxes, which would affect the relevant ratios between them. However, an advantage of the BE method is that it makes use of lines close in wavelength (in a range < 450 Å) and therefore the effect of reddening is minimised. It is therefore a useful technique to estimate physical diagnostics in jets where the extinction is not well-constrained. Bacciotti & Eislöffel (1999) estimate the impact of reddening on the obtained values and conclude that at a reasonable value of $A_v = 3$ mag, the introduced uncertainty on x_e and T_e is only 10-15%, and so the impact is likely to be small especially in jets with less extinction. Similarly an uncertainty of approximately 15% is associated with the commonly adopted uncertainties for the assumed local abundances relative to H (Podio et al., 2006).

The main uncertainties associated with this method then are in the observational uncertainties, e.g. measurements of line fluxes and extinction, as well as its dependence on the adopted abundances and atomic parameters. A key limitation is that the density can only be reliably estimated below the critical density of the [S II] lines ($\sim 2.5 \times 10^4$ cm^{-3}). However, this and the other assumed conditions are generally applicable within stellar jets which are known to emit FELs. This technique is therefore a valuable tool to estimate physical diagnostics of jets in the optical band, and well suited to analysing large datasets.

5.3.1 Diagnostic Code

To analyze the MUSE dataset we make use of a code which applies the BE method, comparing the input line fluxes with those predicted from a grid of values of n_e, x_e and T_e (see further discussion in Podio et al. (2006); Melnikov et al. (2008)). In this study we use an updated version of the code (provided by F. Bacciotti) which calculates the surfaces for [S II]λ6716/[S II]λ6731, [O I]/[N II] and [S II]/[O I] at the same time. It then determines the values of n_e, x_e, and T_e that simultaneously match the model with the observations, based on where the observed contours cross on the three surfaces. In comparison, in the version of the technique used in previous papers n_e was calculated independently from the [S II]λ6716/[S II]λ6731 ratio, neglecting temperature variations

and fixing this at the determined value before x_e and T_e were derived from the other two surfaces. This new approach has the advantage of including the effect of T_e variations in the estimate of n_e and provides a more realistic estimate. A more accurate estimate of n_e in turn has the effect of improving the diagnostic determination of all the parameters in regions of high ionisation and excitation. The code also makes use of abundances and collision strengths which are updated from the previous BE analysis of Th 28 (Bacciotti & Eislöffel (1999), discussed in the next section). In particular we assume solar photospheric abundances of S, N and O from Asplund et al. (2005) which are lower than the values taken in the previous analysis.

5.3.2 Previous Results

The previous analysis of Th 28 using the BE method made use of spectra obtained in February 1987 with the ESO/MPI Boller & Chivens spectrograph. The instrument had a spectral resolution of 1.6 Å px^{-1} and a spatial resolution of 1."76. The analysis was limited to the red-shifted jet due to contamination of the inner blue-shifted jet with emission from the central region, while the more distant HH objects in this lobe could not be detected in [O I] and [S II].

Figure 5.3 shows the results of this analysis. The electron density n_e decreases along the jet beam from 2500 cm^{-3} to 800 cm^{-3}, with a steep gradient similar to that reported by Krautter (1986). The ionisation fraction x_e is quite high along the jet with scattered values around $\sim 0.5 \pm 0.1$, except at the position closest to the source (offset ~ 2") where it is 0.07. Total density n_H depends on x_e and n_e and hence this also declines from 3.3 $\times 10^4$ cm^{-3} to 1500 cm^{-3}. The average temperature T_e declines from 2.5 $\times 10^4$ to 1.5 $\times 10^4$ K. The overall picture is therefore that of a sharp decline in density with a slower decline in temperature but strong ionisation along the jet.

In the bow shock HHW, n_e also declines (from the back of the HH object towards the front or 'upstream') dropping steadily from 1200 cm^{-3} to 170 cm^{-3}, while x_e decreases from 0.4 to 0.04. Total density n_H decreases slowly from 3000-2500 cm^{-3}, while the temperature rises from 1.3-1.7 $\times 10^4$ K.

The authors note that these results show somewhat atypical properties for a HH jet, including the higher [O I] than [S II] flux in the first 4."5 of the jet beam. Reliable recombination curves and mass-loss and momentum estimates could not be estimated either in the jet or the HH object. We note also that the high values of x_e observed suggest some difficulty in applying this diagnostic method to the Th 28 jet, as ionisation fractions $0.5-0.6$ indicate that the assumption of [N II] ionisation being solely controlled by charge exchange is no longer valid and photoionisation may also be a factor.

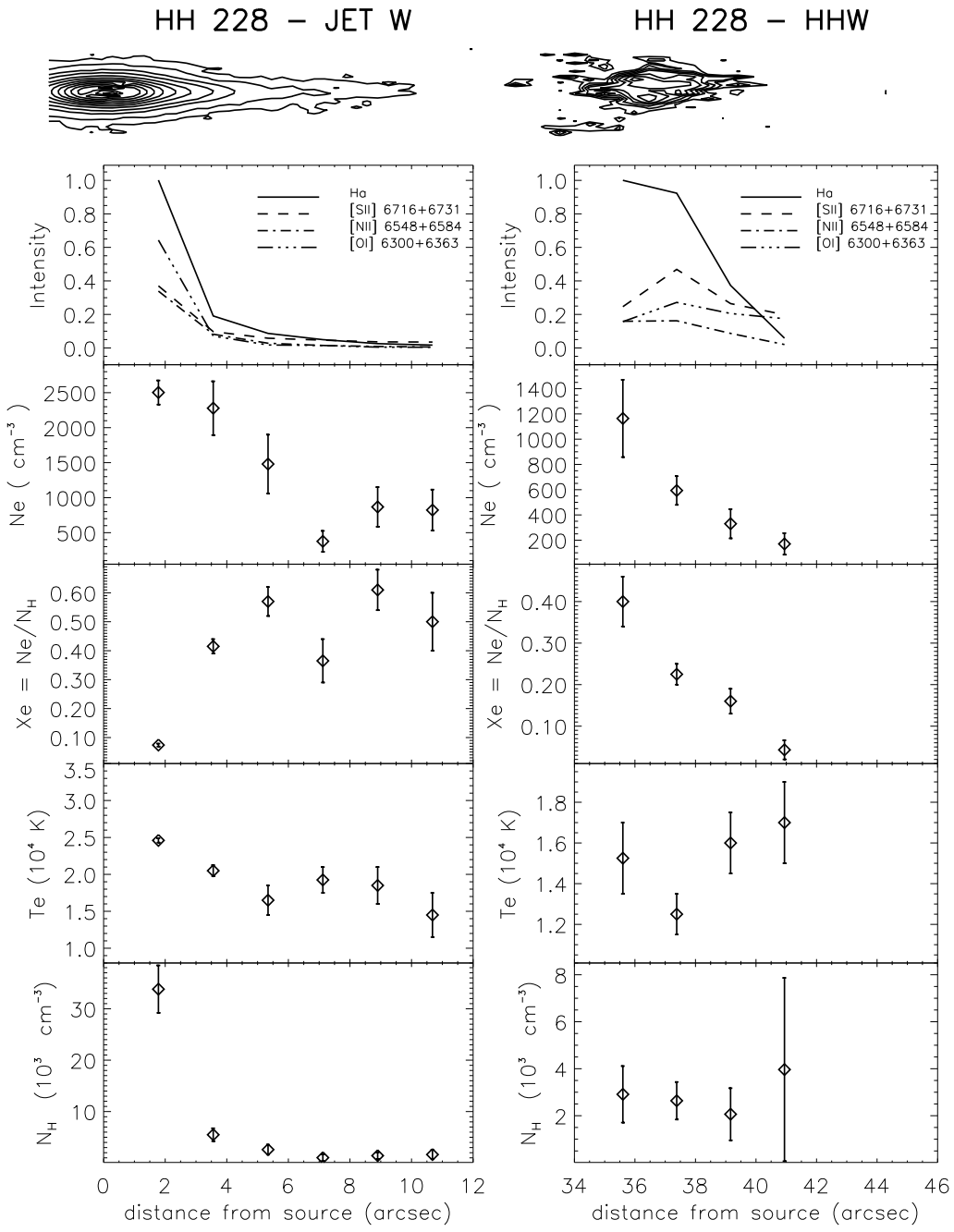

FIGURE 5.3: Figure from Bacciotti & Eislöffel (1999) showing the diagnostic parameters along the red-shifted jet and HHW. The top panel shows contour plots of the respective regions, while the second row of panels shows the flux across each region normalised to the peak in Hα. Figure kindly provided by F. Bacciotti.

5.3.3 New BE Results

Here we apply the BE method to the 2014 MUSE data and compare the results with those obtained by Bacciotti & Eislöffel (1999). This will allow us to explore any changes in the jet properties between 1987 and 2014. The results from the MUSE data were obtained by binning the flux in each emission line over a 1" × 1" box at several points along the jet, and then integrating over a Gaussian fit to the resulting line profile. As in the results from Bacciotti & Eislöffel (1999), the spectral resolution of MUSE did not allow us to isolate any individual velocity components in the emission lines. We then applied the updated BE (*muse3D*) code to the fluxes obtained. The results for the red-shifted jet are shown in Figure 5.4. Similar to the previous results, we see a decline in n_e along the jet from 5300 cm^{-3} to 300 cm^{-3}, with x_e rising sharply from 0.28 at the first position to a value of 0.5 around 2-3" and then increasing slowly to a steady value of about 0.6 - 0.65. The density n_H thus decreases from 1.9 × 10^4 cm^{-3} to 300 cm^{-3} with a slight bump at the position of the bright knot HHW_2. The temperature decreases slightly from ∼2.1 × 10^4 K at the first position to a fairly constant value around 1.8 × 10^4 K along the jet, with a small peak at HHW_2.

The results for HHW are shown in Figure 5.5. The trend across the bow shock is broadly similar to the results of Bacciotti & Eislöffel (1999), with a steady decrease in n_e from 250 cm^{-3} to 100 cm^{-3}. The ionisation fraction x_e also decreases from 0.75 to 0.5-0.6 with a slight dip just ahead of the flux peak and n_H declines from 340 cm^{-3} to 100 cm^{-3}. Similarly there is a small drop in T_e from ∼2 × 10^4 K to 1.8 × 10^4 K. There is an increase in n_e, n_H and T_e in front of the bow shock, but we note this is a region where the flux of our FELs is dropping and where the BE method may be less applicable.

Uncertainties for our derived values are primarily determined by the uncertainty in the line fluxes. We initially estimated this using the 1-σ variation of the local continuum region for each line, multiplied by the line width (Nisini et al., 2002). However, due to the high S/N of the lines in the red-shifted jet, this resulted in a small uncertainty $< 1\%$, which is negligible in comparison to the typical estimated flux calibration error of 5% for MUSE (Weilbacher et al., 2015). We therefore take this as the uncertainty of the fluxes. Corresponding uncertainties of n_e, x_e, T_e and n_H were obtained by varying the input fluxes to the code by ±5%, leading to typical uncertainties of 40% for the n_e estimates and 25% for the other parameters.

The overall results for both regions are summarized in Table 5.4. Comparing the results between the two epochs we find generally comparable parameters for the red-shifted jet with similar trends in n_e, x_e and n_H as well as similar values of T. The 2014

Region	Year	n_e (cm^{-3})	T_e ($\times 10^4$ K)	x_e	n_H (cm^{-3})
Red-shifted jet	1987	2500-800	2.5-1.5	0.07-0.6	3.3×10^4 - 1500
	2014	5300-300	2.1-1.8	0.28-0.65	1.9×10^4 - 500
HHW	1987	1200-170	1.3-1.7	0.4-0.04	3000-2500
	2014	225-100	2.0-1.8	0.75-0.5	350-200

TABLE 5.4: Table of diagnostic parameters using the BE method, with 1987 values from Bacciotti & Eislöffel (1999).

Region	Year	n_e (cm^{-3})	T_e ($\times 10^4$ K)	x_e	n_H (cm^{-3})
Red-shifted jet	1987	2500-800	2.5-1.5	0.07-0.6	3.3×10^4 - 1500
	2014	6000-300	2.2-1.8	0.16-0.65	3.8×10^4 - 400

TABLE 5.5: Table of diagnostic parameters using the BE method, with 1987 values from Bacciotti & Eislöffel (1999). 2014 values are obtained from fluxes binned to match a spatial resolution of 1."8.

data shows higher densities close to the source and lower values further along the jet, i.e. a steeper decline in both n_e and n_H compared to the 1987 data. The temperature values are a little higher overall with a flatter profile along the jet. The HHW values show a much more substantial difference between epochs. Although the overall trend across the bow shock is similar in density, x_e and T, we find much lower densities and significantly higher values of temperature and x_e than in the 1987 data.

Some of the discrepancies may be due simply to the difference in spatial resolution between the observations. To illustrate this, Figure 5.6 shows the values obtained for the red-shifted jet if we bin across a spatial box of 1."8 $\times$ 1."8. We now see similar variation in the profile of T_e along the jet, with a dip at 3-4" followed by a slow rise and a bump at 8" (the position of the bright terminal knot HHW_2). The results are compared in Table 5.5. However if we apply the same resolution to HHW, the main effect is to smooth out the values on either side of the central bow shock region (see Figure 5.7). The spatial resolution therefore cannot account for the change in density, temperature and ionisation in HHW over time, although HH objects are expected to show variation in their conditions.

The differences between the two sets of results may then reflect some changes in the conditions of the jet over time, but also the increased accuracy of the updated BE method using the new diagnostic code, as discussed in Section 5.3.1.

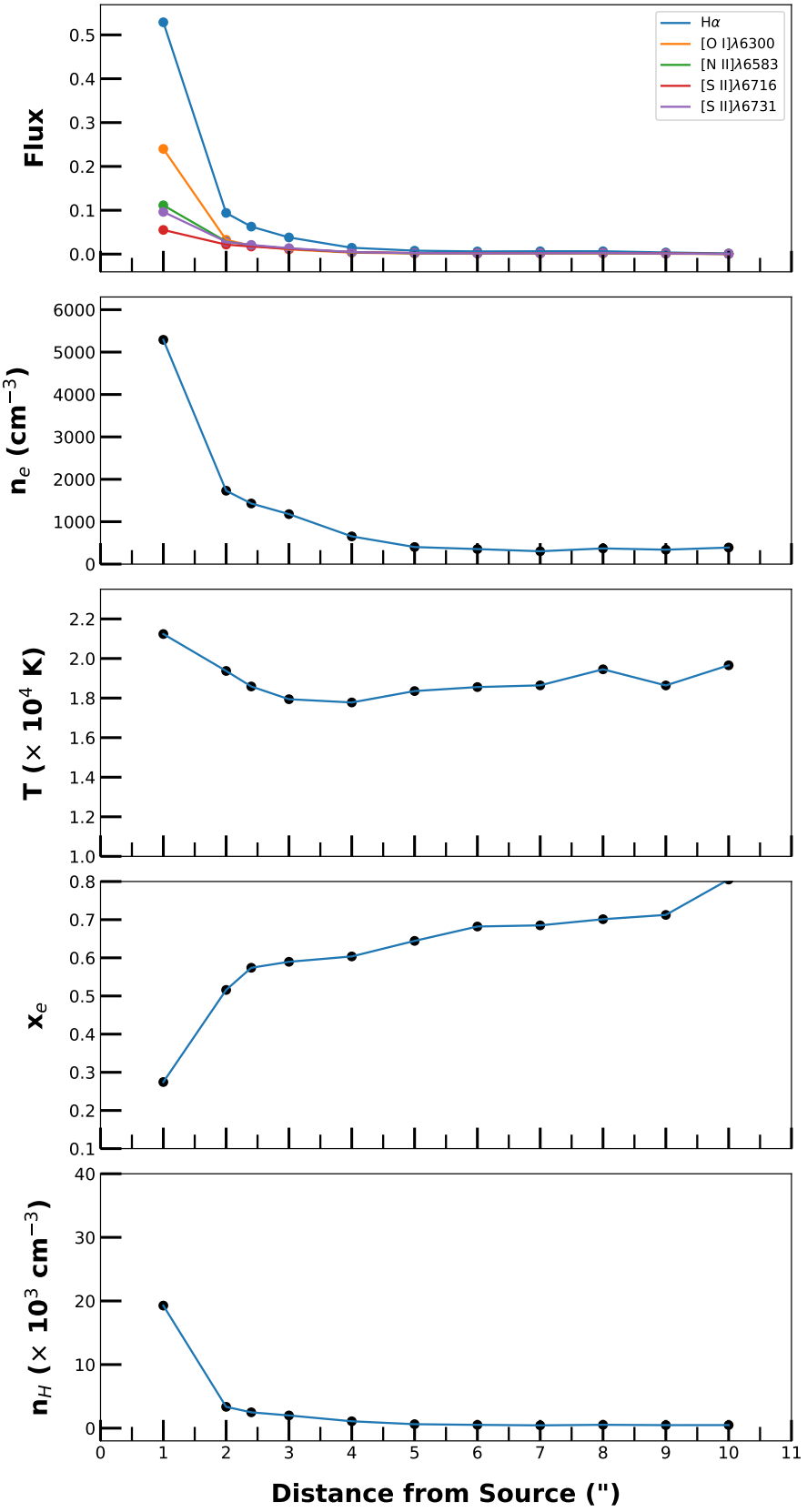

FIGURE 5.4: Diagnostic parameters along the red-shifted jet obtained with the current BE code. Top are the flux values for the relevant FELs as well as Hα. To match the format of the Bacciotti & Eislöffel (1999) figure the fluxes are normalized to the Hα peak value.

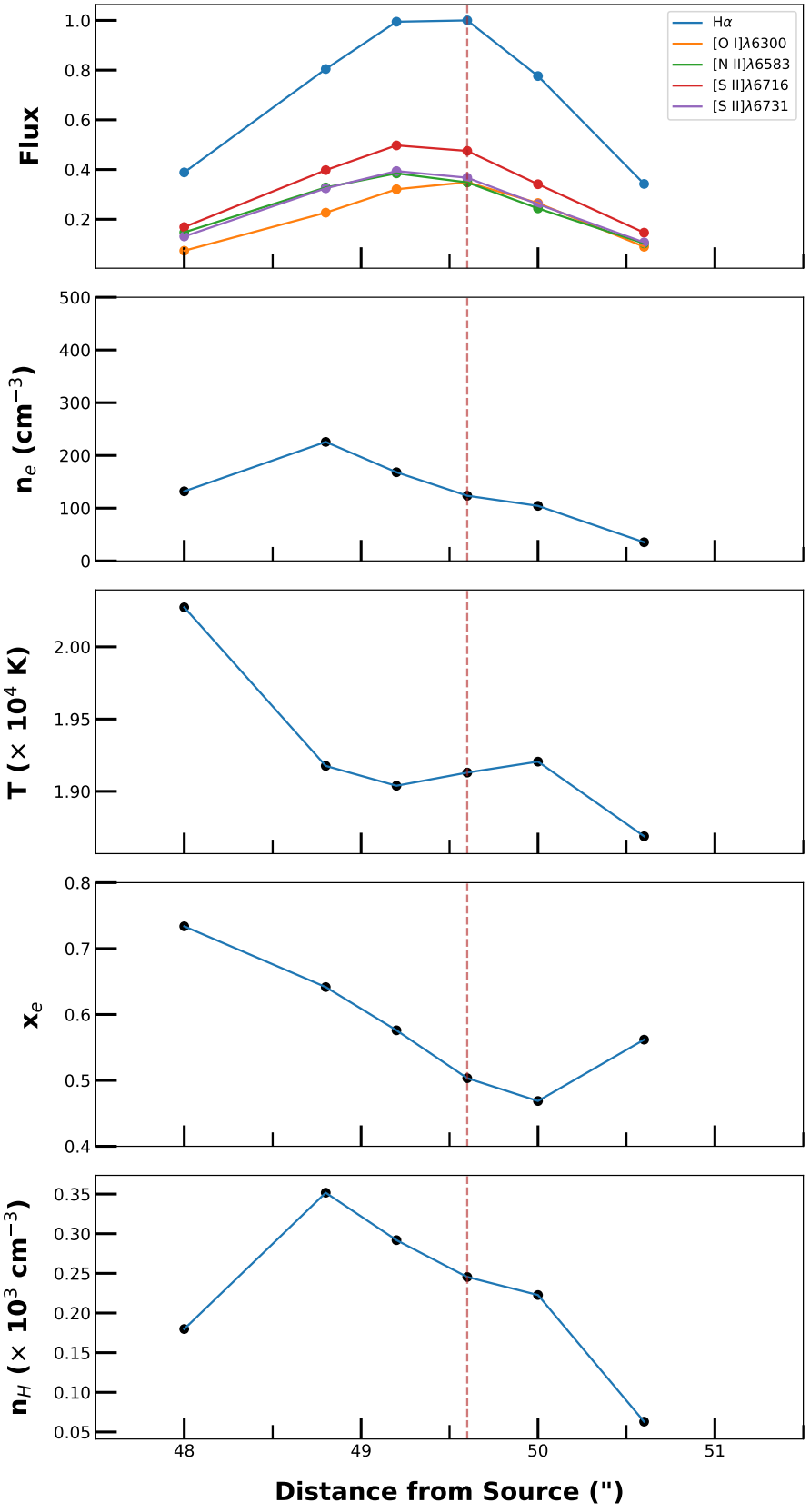

FIGURE 5.5: As in Figure 5.4, but for the bow shock HHW.

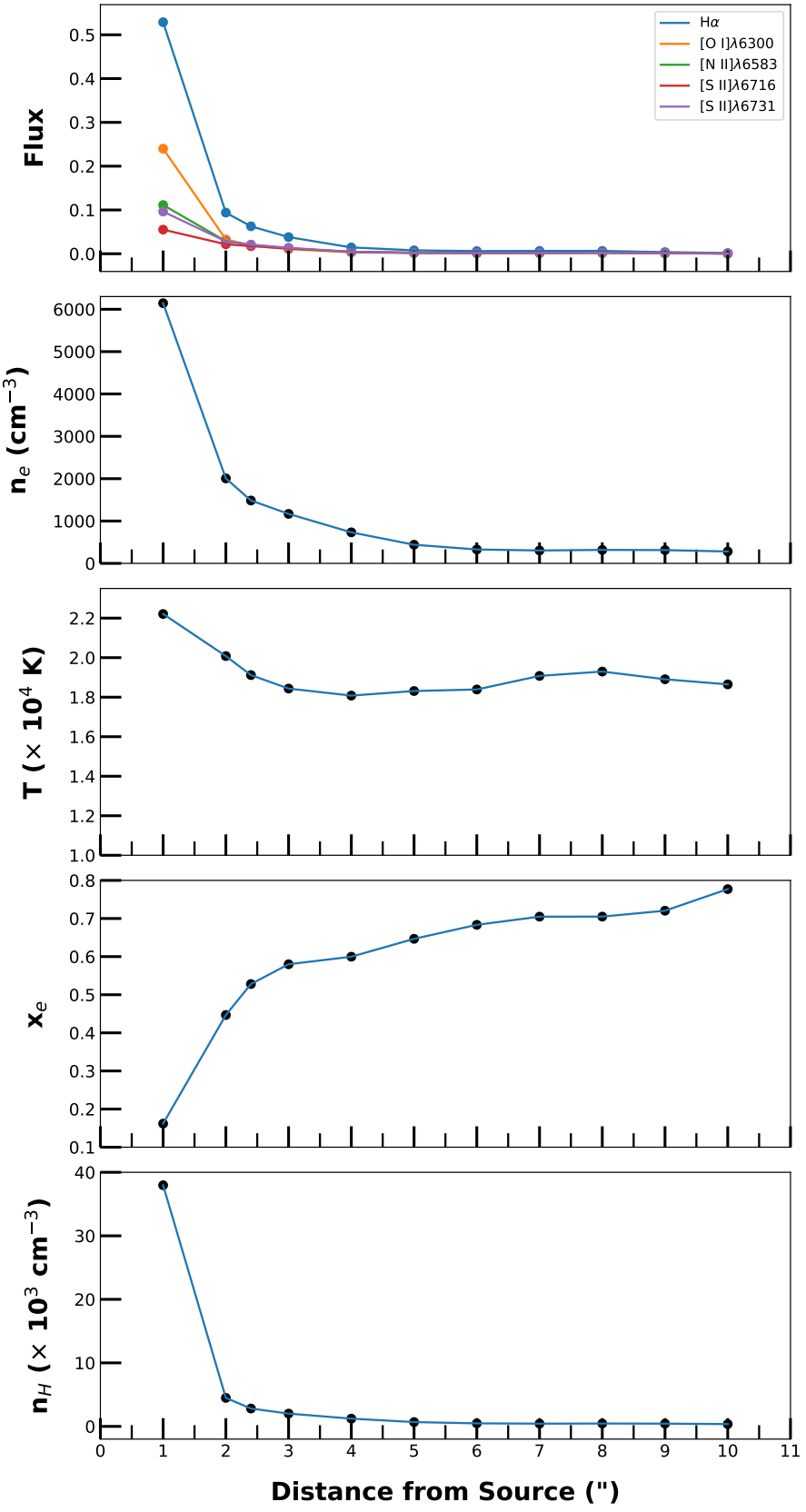

FIGURE 5.6: Diagnostic values for the red-shifted jet as in Figure 5.4, but with the input line fluxes binned over a box of 1."8 × 1."8 to match the resolution of the Bacciotti & Eislöffel (1999) results.

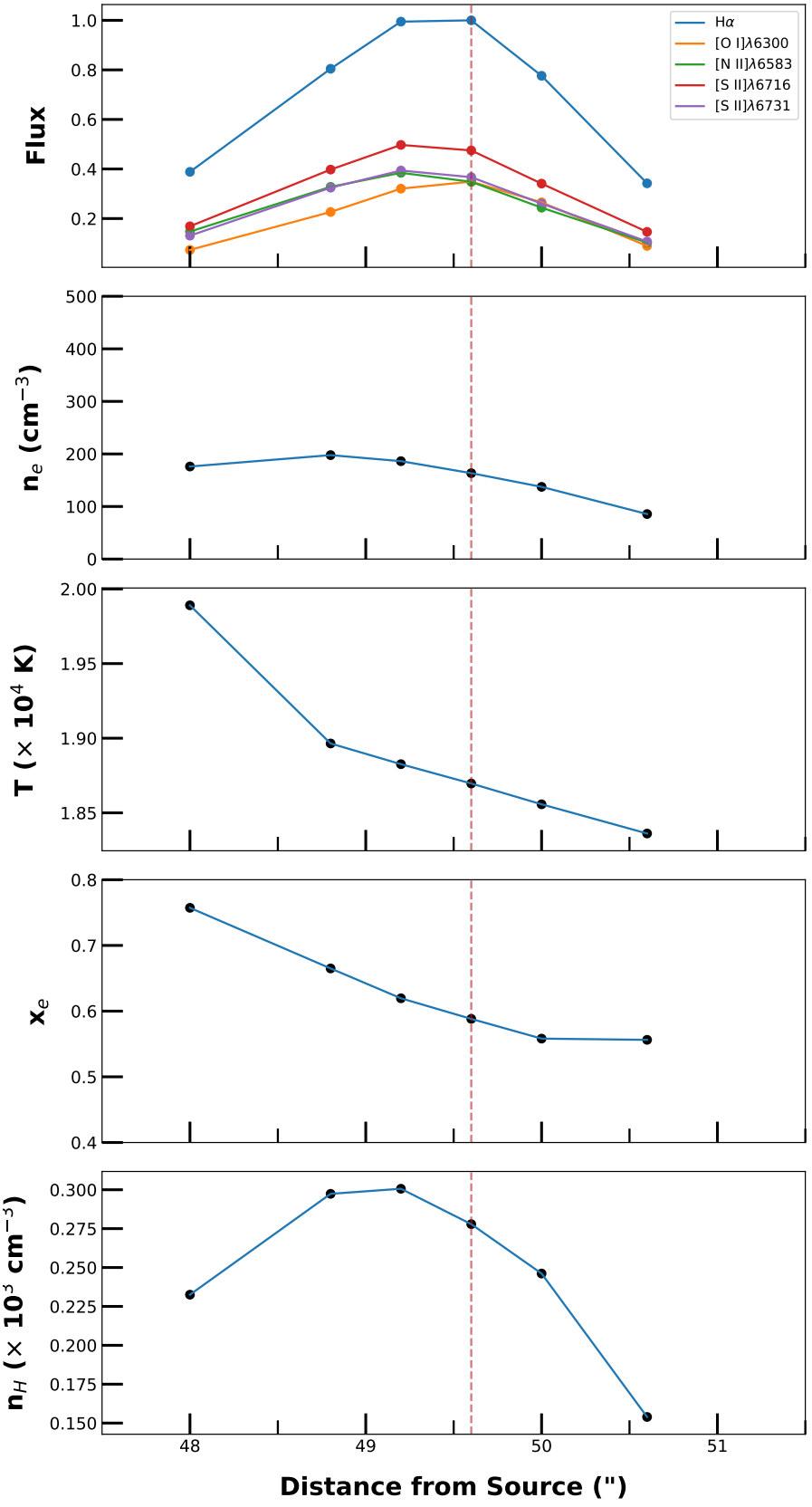

FIGURE 5.7: As in Figure 5.6, but for the bow shock HHW.

5.4 Extinction

A key attribute of the BE method is that it makes use of emission lines close in wavelength and thus minimizes the need to account for extinction. However, both the MUSE and available X-Shooter spectra of Th 28 show a wide array of optical and IR emission lines which can be used to extend our diagnostic study, for example lines of [Fe II] and [Ca II]. Additionally, we can estimate the mass accretion rate using emission lines across the MUSE spectrum. We therefore wish to make use of a much wider range of lines, including ratios which may differ in wavelength by >1000 Å. Thus it is useful to estimate and correct for reddening effects which vary in the different regions of the Th 28 jet, both for this study and as groundwork for future diagnostics, for example combining UV, optical and IR lines of Fe (Giannini et al., 2013).

There are several methods to estimate extinction using standard extinction curves. One possibility is to make use of the [Fe II]λ1.64/1.32 μm ratio, using the IR band of available 2015 X-Shooter observations of Th 28. However, the [Fe II] lines are only of use in regions of very high density (i.e. close to the source), and inspection of the X-Shooter data indicated little or no emission in 1.32 μm.

An alternative method was therefore employed using the Balmer decrement between emission in Hα and Hβ. This is a standard method for estimating extinction which has the advantages of both emission lines being within the range of the MUSE spectra, and both being emitted throughout both jet lobes and in the bow shock HHW.

The theoretical ratio of Hα/Hβ varies slightly with local density and temperature, however the primary factor to consider is its relationship to local shock velocities. As shown by Hartigan et al. (1994), in regions with high shock velocities (hence strong ionization) the expected ratio should approach the intrinsic recombination value ∼2.9, but in shocks with lower v_{shock} the lower ionization results in fewer free electrons and thus an enhancement of the lower-excitation lines such as Hα in relation to those with higher excitation energies such as Hβ; this causes the value of the Hα/Hβ ratio to be increased in low-velocity shocks before the effect of extinction.

5.4.1 Th 28

Previous estimates of extinction for Th 28 vary widely between 0.32 and 2.9 (Hughes et al., 1994; Sartori et al., 2003; Evans et al., 2009; Mortier et al., 2011). Louvet et al. (2016) suggest that given a 1.5 $M_\odot$ protostar of ≤3.5 Myr the expected luminosity would be ∼1.9 $L_\odot$ versus the 0.03 $L_\odot$ observed (Mortier et al., 2011); on this basis A_v = 4.5 mag would be required to cause this attenuation. Although this might be achievable

given the near edge-on disc, Liu et al. (2014) estimate that an A_v of 2.5 mag would imply a true X-ray luminosity that is unrealistically bright for a T Tauri star; on the other hand they also find this extinction consistent with the absorption column density and thus adopt $A_v = 2.5$ mag as an upper limit to the visual absorption. This is close to other estimates which give A_v = 2.5-2.9 mag (Evans et al., 2009; Mortier et al., 2011).

Since Th 28 is observed primarily in scattered light, this introduces an additional uncertainty as to whether the extinction at the source position can be estimated accurately. However, our primary interest is in the extinction along the jet rather than the source. For these estimates we adopt RV = 5.5 as the typical value used to estimate extinction in the Lupus clouds (Evans et al., 2009; Mortier et al., 2011). It should be noted that if the typical galactic value RV = 3.1 is adopted, any estimated extinction will be substantially reduced.

5.4.2 Dereddening

To estimate the extinction curve, the *RedCorr()* method of the *pyneb* Python package was used (Luridiana et al., 2015). Given the Balmer decrement and reference ratio (i.e. the expected value at 0 extinction) this function estimates the extinction with a fit to one of several standard extinction curves, and can also return the corresponding dereddening correction at a given wavelength relative to another. We use the extinction law described by Fitzpatrick & Massa (1990) as this is suitable for the optical regime.

As Hβ is outside the wavelength range of the re-reduced MUSE cubes (as discussed in Chapter 2), this and Hα were sampled from the originally reduced cube in order to ensure consistency in the reduction procedure. This also ensured that line fluxes would be sampled from identical spatial positions along the jets and in HHW. Both of the extracted emission lines were continuum subtracted and the cubes rotated using the standard procedure described in Chapter 2. The channel maps were then binned across the full velocity range of the two jets and divided to obtain a map of the Balmer decrement/ratio, shown in Figure 5.8 (top).

As the two jet lobes are known to have markedly different velocities and hence shock properties, we refer to the models of (Hartigan et al., 1994) to estimate the theoretical ratios for different regions of the jet. The presence of [O III]λ5007 emission in the blue-shifted jet and in HHW indicates $v_{shock} >$ 80-90 km s^{-1}, and the expected decrement should therefore be close to 2.9. The red-shifted jet has a significantly lower velocity and hence we assume correspondingly lower $v_{shock} \sim$ 40-50 km s^{-1}. This would imply an expected decrement $\sim$ 3.5. Finally, for the on-source position we assume a theoretical value of 2.74, given the high estimated densities and temperature $\sim 2 \times 10^4$ K found

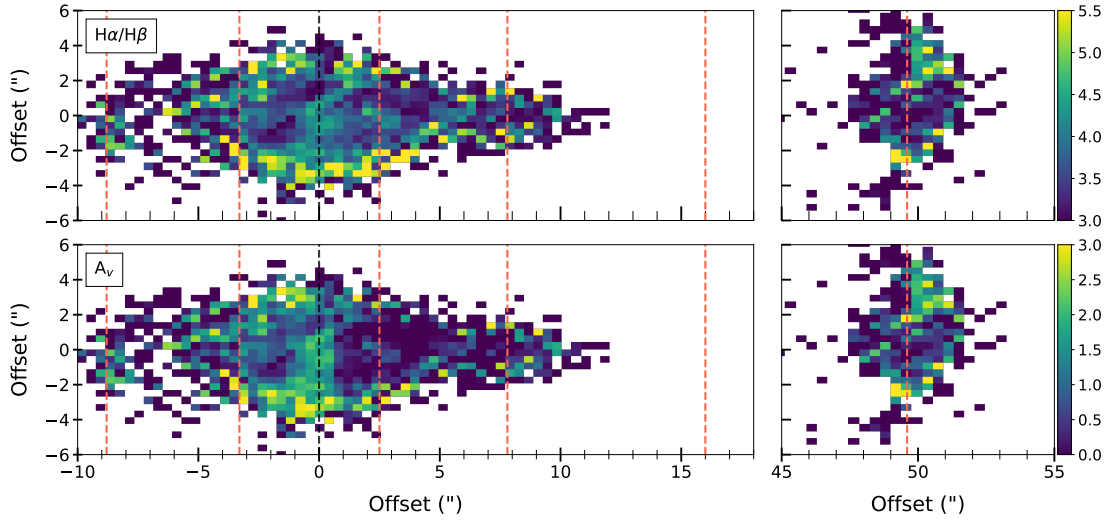

FIGURE 5.8: Top: Balmer decrement map of the Th 28 inner jet region (left) and bow shock HHW (right). Bottom: the corresponding A_v maps for each region.

in Section 5.3.3 and the corresponding value of the line ratio under Case B (optically thick) conditions (Osterbrock, 1989).

To examine the extinction in each region, the Hα and Hβ line fluxes were binned over 1" x 1" spatial boxes at several points along the jet axis, and fitted with Gaussian models to obtain the integrated line fluxes. Figure 5.9 shows the profile of the resulting Balmer decrement sampled along the centre of the jet axis in the top panel, while the lower panel shows the corresponding extinctions assuming RV = 5.5. We estimate an overall extinction for the star and jet between 1 - 2.5 mag. Based on the 5% uncertainty estimated for the flux in each line (see Section 5.3.3) this gives an approximate uncertainty of 7% for the ratio Hα/Hβ; by varying the input ratios to the RedCorr() routine by this value we estimate an uncertainty of $\pm$ 0.3 mag for the extinction in all regions of the jet.

Based on these profiles, we subdivide the required corrections into four regions: 1), the blue-shifted jet with relatively high extinction 1.5-2.0 mag; 2), the on-source region around the star and disc which makes a clear peak $\sim$2.4 mag; 3), the red-shifted jet which shows significantly less extinction at 0.5-1.0 mag, although some variation can be seen roughly corresponding to the known knot positions; and 4), HHW, which shows comparable extinction to the blue-shifted jet with A_v = 1.4 mag. The highest extinction is found at the source position as we would expect, and we find A_v= 2.1-2.4 mag for the source, in line with previous estimates. The high extinction of the blue-shifted jet relative to the red-shifted lobe is consistent with previous observations and may partially account for the relative faintness of this side of the jet. The average extinction values for the various jet regions are summarised in Table 5.6.

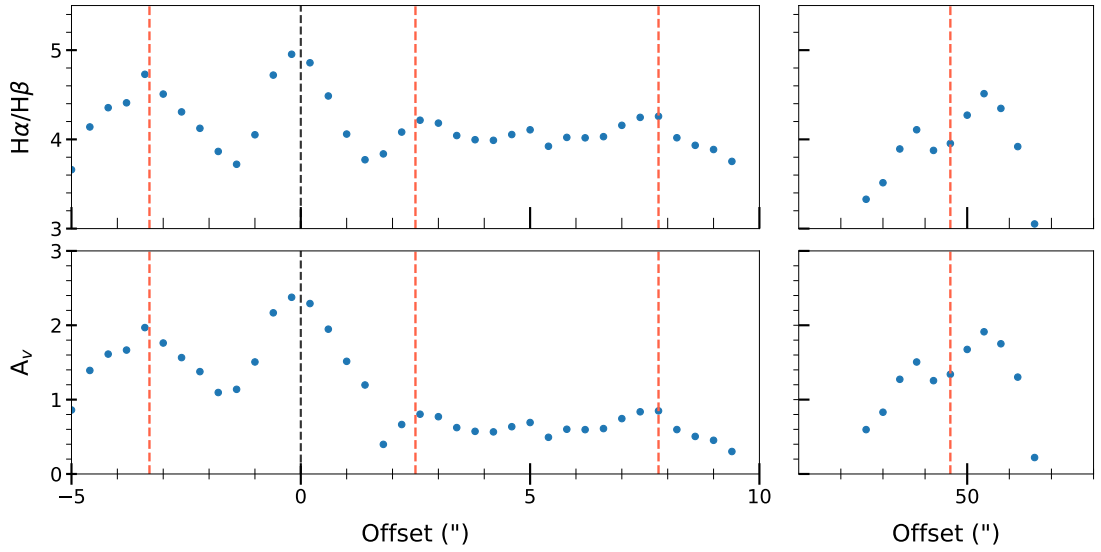

FIGURE 5.9: Top: profile of the Balmer decrement sampled along the jet axis for the inner jet region (left) and bow shock HHW (right). Bottom: corresponding A_v profiles calculated using the average decrement for each region of the jet as given in Table 5.6.

Region	Offset (")	T_e (K)	n_e (cm^{-3})	v_{shock} (km s^{-1})	Hα/Hβ Int.	Hα/Hβ Obs.	A_v (mag)
Blue-shifted jet	> -1.5	-	-	90	3.0	4.2	1.5
On-source	-1.5 - +1.5	2×10^4	$> 10^4$	0	2.74	4.3	2.1
Red-shifted jet	+1.5-8.5	2×10^4	∼400	40-50	3.5	4.0	0.6
HHW	+48.0-51.0	2×10^4	∼200	90	2.9	4.0	1.4

TABLE 5.6: Table of estimated Balmer decrements and A_v values for the regions of the Th 28 jet.

Following these estimates, a Python routine *quick_deredden()* was written to apply the corresponding corrections to line ratio maps; this routine uses the RedCorr() function to deredden a MUSE image or map in one wavelength with varying extinction factors in the different spatial regions. Given for example a channel map, a set of regions defined by distance to the source, and the corresponding average Balmer decrement and reference values in each region, it generates a reference image and thus corresponding correction map. This gives the intensity correction factor in each region relative to a second or 'reference' wavelength. The routine then multiplies the image by this map to obtain a dereddened image which can be used in estimating the line ratio. The function will also return the extinction map corresponding to an input Balmer decrement map, and the extinction map for Th 28 is shown in Figure 5.8 (lower panels). This method will be used to deredden the emission lines used in the ratio maps for the next section.

Line	λ (Å)	Upper level	Lower level	F_{line} (10^{-17} erg s^{-1} cm^{-2})	ΔF_{line} -
[S II]	6716.44	$^3D_{3/2}$	$^4S_{3/2}$	127.2	6.4
	6731.816	$^2D_{5/2}$	$^4S_{3/2}$	152.5	7.6
[O I]	5577.34	$^1S_0$	$^1D_2$	5.3	0.3
	6300.304	$^1D_2$	$^3P_2$	126.6	6.3
	6363.776	$^1D_2$	$^3P_1$	44.2	2.2
[N II]	5754.59	$^1S_0$	$^1D_2$	4.0	0.2
	6548.05	$^1D_2$	$^3P_1$	50.4	2.5
	6583.45	$^1D_2$	$^3P_2$	145.5	7.3
[N I]	5197.902[a]	$^2D_{3/2}$	$^4S_{3/2}$	15.7	0.8
	5200.257	$^2D_{5/2}$	$^4S_{3/2}$	-	-
[Fe II]	7155.1742	$^2G_{9/2}$	$^4F_{9/2}$	21.6	1.1
	8616.9498	$^4P_{5/2}$	$^4F_{9/2}$	21.1	1.1
[Ca II]	7291.47	$^2D_{5/2}$	$^2S_{1/2}$	22.6	1.1
Ca II	8542.09	$^2P_{3/2}$	$^2D_{5/2}$	11.8	0.6

TABLE 5.7: Key emission lines for the diagnostic ratio maps in Section 5.5, with sample line fluxes integrated over a 1" × 1" region at the position of the red-shifted knot M4. (a) The [N I]λ5198,5200 Å lines are blended in the MUSE spectra and so their total combined flux is reported.

5.5 Ratio Maps

The MUSE spectra of the jets show numerous emission lines which are of interest to us as tracers of different physical conditions within the jet, specifically when we examine the ratios of specific line intensities as discussed in Section 5.1.1. In this section we make use of the 3D MUSE data to map some of these ratios across the jet in both channel maps and in position-velocity space. A list of the relevant lines is given in Table 5.7, with sample fluxes from the knot M4 in the red-shifted jet.

5.5.1 Density

To estimate the electron density we make use of four line ratios of [S II], [O I], [Fe II] and [Ca II]. As discussed in Section 5.1.1, the [S II]λ6716/6731 ratio is proportional to

n_e between about 50 cm^{-3} and 2 $\times$ 10^4 cm^{-3} (where T_e <2 x 10^4 K) and is used to determine n_e in the BE method. Additionally, we examine the ratio [O I]λ(6300+6363)/[S II]λ(6716+6731) (hereafter the [O I]/[S II] ratio). This is primarily sensitive to density, although the [O I]λ6300 line also has a weak positive dependence on temperature not present in the [S II] lines (this is because the collision strength of [O I] is a function of temperature) (Hartigan & Morse, 2007). It is of interest to us because [O I]λ6300 has a critical density of $\sim$ 10^6 cm^{-3}, significantly higher than that of [S II]. This means that the [O I] doublet becomes stronger relative to [S II] in high-density regions (i.e. close to the star) and should increase sharply where the [S II] doublet begins to saturate.

To explore the higher-density regions of the jet, we can also look at ratios of [Fe II] and [Ca II] which have even higher critical densities (Nisini et al., 2005; Podio et al., 2006). The ratio [Fe II]λ7155/8617 (the [Fe II] ratio) traces regions of $n_e \sim 10^6$ - 10^7 cm^{-3}, with theoretical curves for this relationship calculated by Bautista & Pradhan (1998). The [Ca II]λ8542/7291 ratio is almost independent of temperature and traces regions where $n_e > 10^6$ cm^{-3}, making it ideal to check for very high densities (Nisini et al., 2005).

The ratio channel maps were obtained from the rotated, continuum-subtracted datacubes by summing each of the key emission lines over the central velocity bins (+/- 150 km s^{-1}) and dereddening each of them using the method and extinction estimates described in Section 5.4. Position-velocity maps along the jet axis, as well as transverse PV maps across the jet beam, were also obtained for each line as in Chapter 3 and similarly dereddened using the appropriate extinction estimates in each region. For each image or PV map the background flux was estimated and the mean subtracted; a threshold of 3-σ of the background was then applied so that any pixel with flux below this level was excluded from the ratio maps. For ratios involving one or more lines which fall outside the range of the re-reduced datacubes (e.g. the [Fe II] ratio), all of the images were extracted from the older version of the reduced MUSE datacube to ensure consistency in the pipeline and flux calibrations.

Figure 5.10 shows the spatial ratio maps corresponding to n_e in order of increasing critical density. From the top panel down, the maps thus show regions of progressively higher density. Figure 5.11 shows a profile of this map taken from a cut along the jet axis. As expected, the [S II] ratio ($n_e < 2.5 \times 10^4$ cm^{-3}) traces most regions of the jet, but approaches the high-density limit within 1" of the source and in the blue-shifted lobe, showing a roughly flat profile in this region. This ratio also very weakly detects the low-density knot M1 at -14."2 (not shown). In the red-shifted jet the ratio approaches the low-density limit at distances >4", beyond the knot M4. This is expected given the low n_e values ($\sim$ 400 cm^{-3}) derived for this region from the BE method.

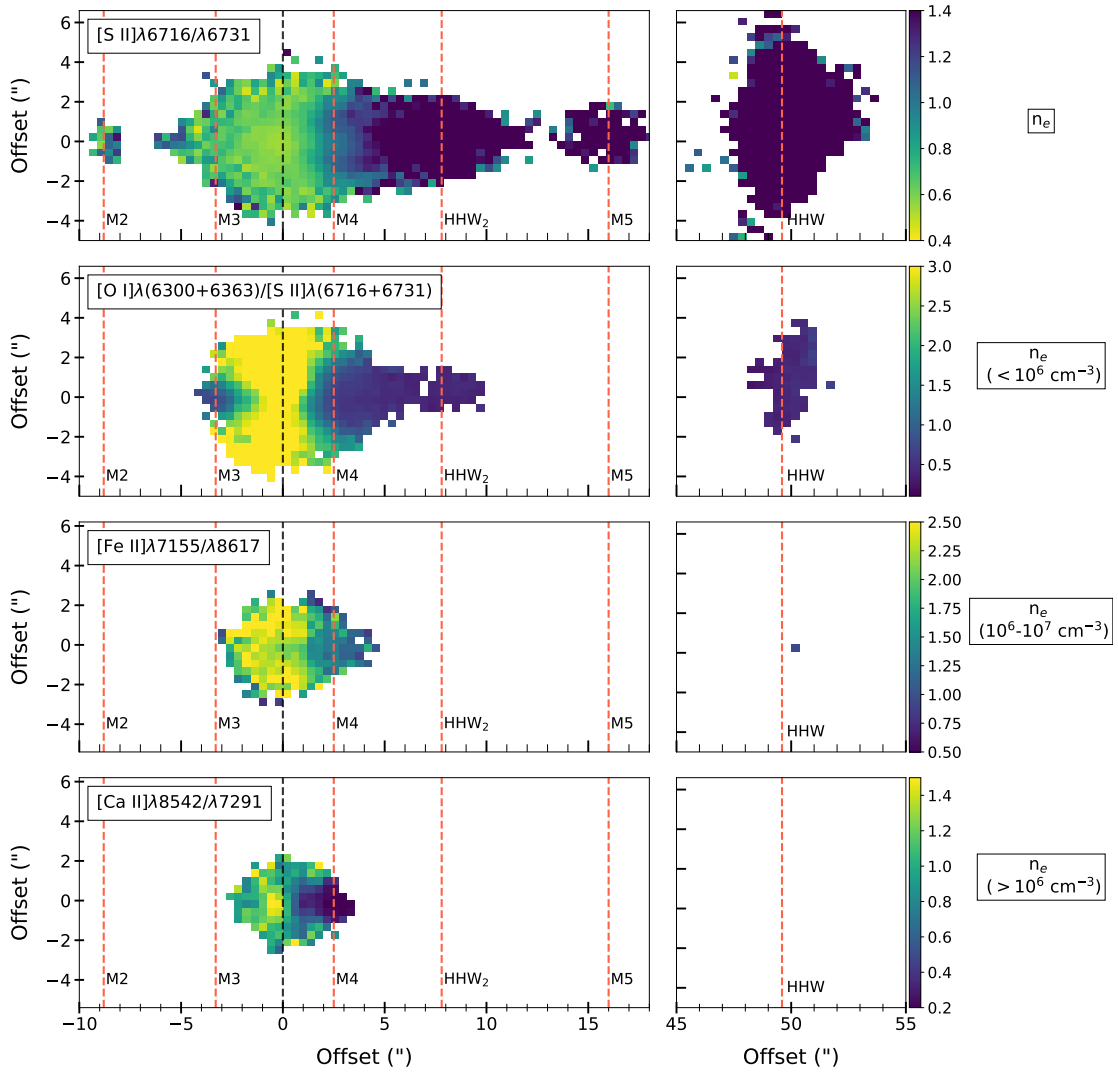

FIGURE 5.10: Spatial ratio maps of the Th 28 jet correlating to the distribution of n_e; left panels show the inner jet region while panels on the right show the bow shock HHW. Note that white (0) regions show those where at least one of the relevant lines has flux less than 3-σ of the background level. The colour bars are arranged so that the brighter (yellow) regions correspond to regions of increasing n_e.
Orange dashed lines show the labelled knot positions with the black vertical line marking the source position.

The higher density tracers show more detail close to the source; it can be seen from the profile cuts especially that in the red-shifted jet[O I]/[S II] increases sharply within $\sim <$ 2" of the source, where the [S II] ratio approaches saturation. Interestingly, this ratio is also high for 1-2" of the blue-shifted jet, starting in a broad region across the jet base and dropping sharply close to the jet axis while still being high at the sides of the jet. The higher ratio in the inner blue-shifted jet is consistent with higher n_e in this lobe, as reflected in the [S II] ratio and in previous diagnostic studies, but it is unclear how well this reflects the blue-shifted jet rather than scattered [O I] emission from the red-shifted jet. The [Fe II] and [Ca II] ratios, in the bottom panels, trace the highest

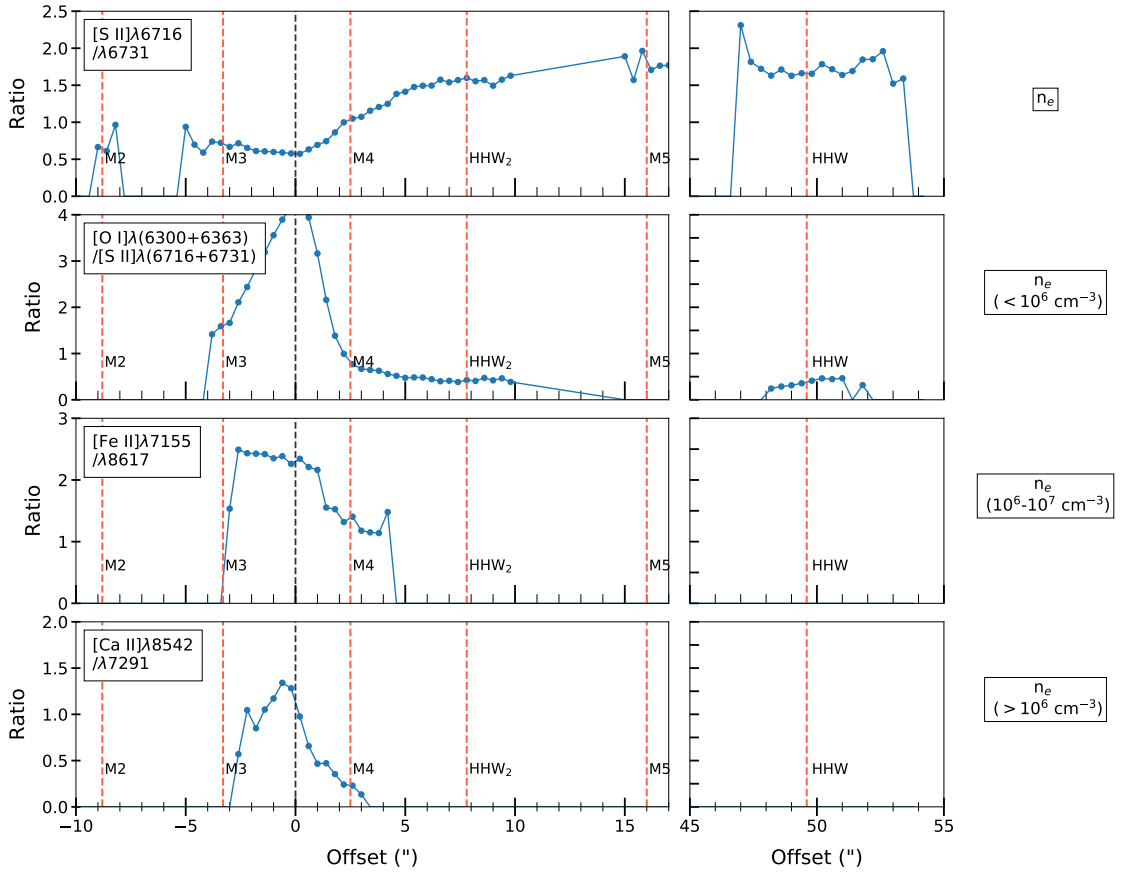

FIGURE 5.11: Profile of the ratio values shown in Fig. 5.10, with cuts taken along the jet axis. Left panels show the inner jet region while panels on the right show the bow shock HHW. Vertical lines mark the source and knot positions as in Fig. 5.10.

density regions, with $n_e \sim 10^6$ cm^{-3}; in particular, the [Ca II] ratio exceeds 0.1 within about ±2" of the source, indicating regions of $n_e > 10^6$ cm^{-3} here.

The PV maps are shown in Figure 5.12 (with corresponding profile cuts in Figure 5.13), showing the distribution of n_e with respect to velocity. Again [S II] and [O I]/[S II] show higher n_e in the blue-shifted lobe and the profiles show small peaks at the knot positions. Here we observe red-shifted regions in the blue-shifted jet with high electron densities but note that scattered emission from the red-shifted jet may affect the line ratios in this region, as the velocity resolution of MUSE does not allow the red- and blue-shifted jet components to be well distinguished. This may help to account for a surprising contradiction: the PV maps of the [S II] ratio show saturation of the ratio in the high-velocity red-shifted channels (as well as in the red-shifted emission of the blue-shifted jet) suggesting higher n_e in these channels, whereas each of the other ratio maps indicates the opposite pattern, with highest n_e in the low-velocity channels of both jets. The [O I]/[S II] and [Ca II] ratios do show some high values in the red-shifted channels on the blue-shifted jet within 1" of the source; in the case of the former this may be

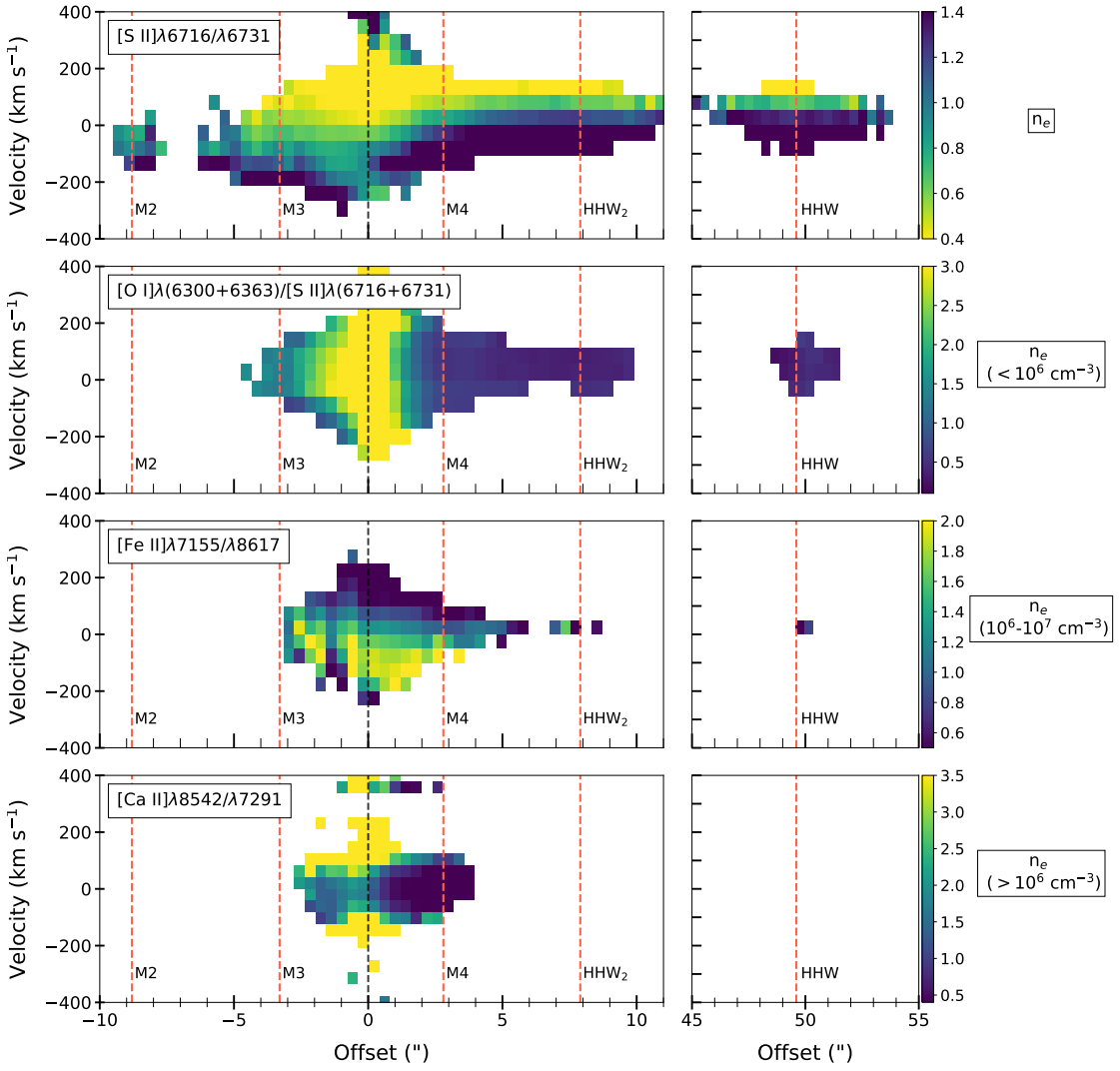

FIGURE 5.12: Position-velocity ratio maps of the Th 28 jet correlating to the distribution of n_e; left panels show the inner jet region while panels on the right show the bow shock HHW. White (0) regions show positions where at least one of the relevant lines has flux less than 3-σ of the background level. Vertical lines mark the source and knot positions and colour bars are arranged as in Fig. 5.10.

due to scattered [O I] emission, while the [Ca II] ratio may be vulnerable to dispersion effects as will be discussed below.

The transverse PV maps for the blue- and red-shifted jets are shown in Figures 5.14 and 5.15, respectively. Similarly to the PV maps these show asymmetries in the electron density associated with different velocities. In the blue-shifted jet, the bow shock M2 (at -8."8 from the source) is only detected in [S II] with a low inferred density as we would expect. Closer to the source, the knot M3 (-3."3 offset) shows higher densities at low velocities in the first two ratios. This is consistent with the expectation of a higher-density low-velocity component for the jet structure, although as seen with the results of Liu et al. (2014), without an estimate of the corresponding ionisation fraction

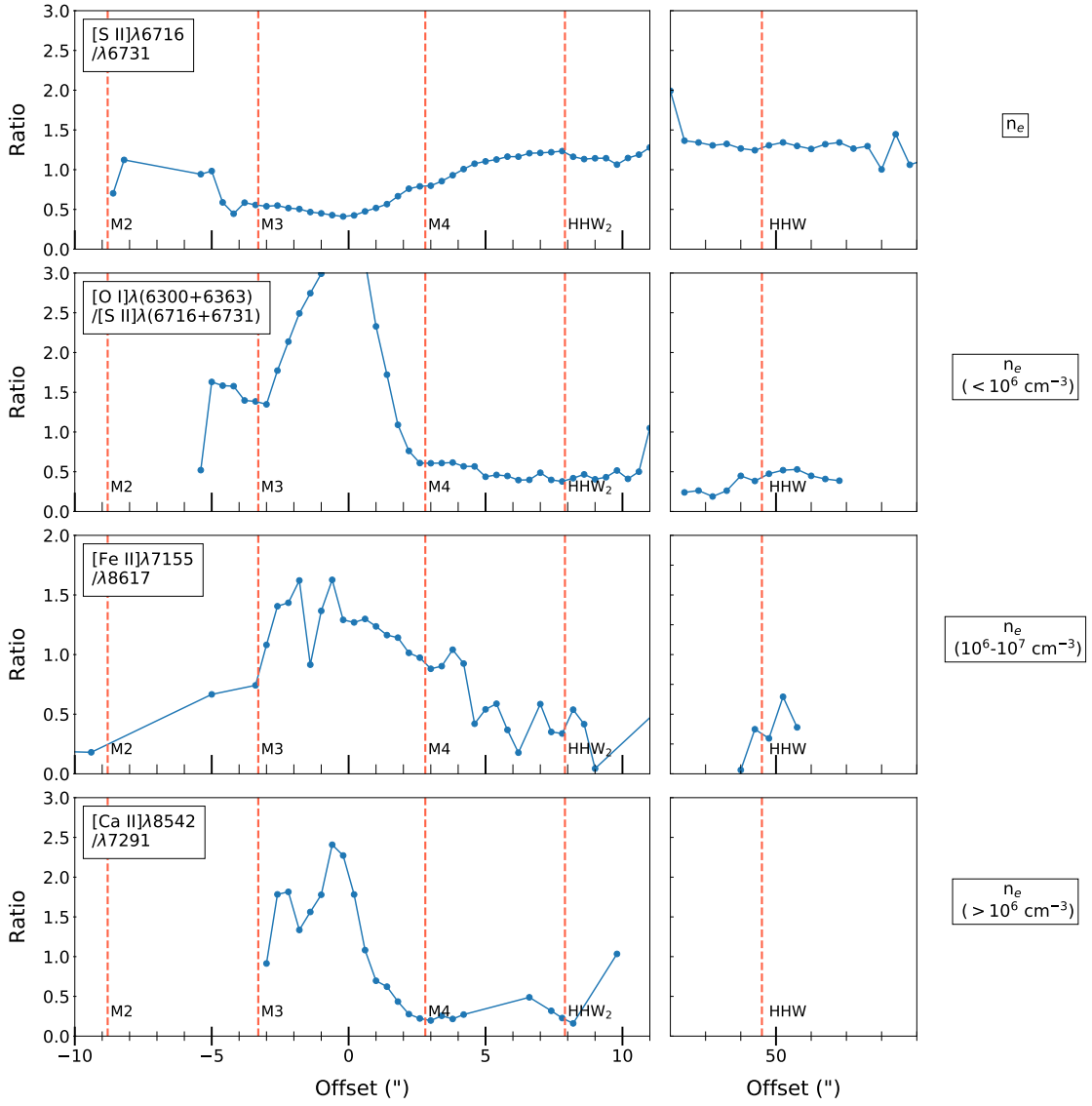

FIGURE 5.13: Profile of the ratio values shown in Fig. 5.12, with cuts taken along the jet axis. Left panels show the inner jet region while panels on the right show the bow shock HHW. Vertical lines mark the source and knot positions as in Fig. 5.10.

in each region it could also be the case that higher n_e values reflect higher ionisation rather than higher total density.

As expected, we only see the Fe and Ca ratios at the slice centered at the source position. [Fe II] shows higher n_e at blue-shifted velocities while Ca shows the highest densities at high velocities (both blue and red shifted). For these ratios in particular, high values at the edges of the PV diagrams may reflect the effect of differing dispersion across the spectral pixels, as the line spectra are not resampled in velocity to account for this. While this is less likely to impact ratios of the [S II] and [O I] lines which are all close in wavelength, the [Fe II] and [Ca II] ratios compare lines with wavelength differences > 1000 Å and thus differences in velocity resolution of ~ 10 km s^{-1}. Future

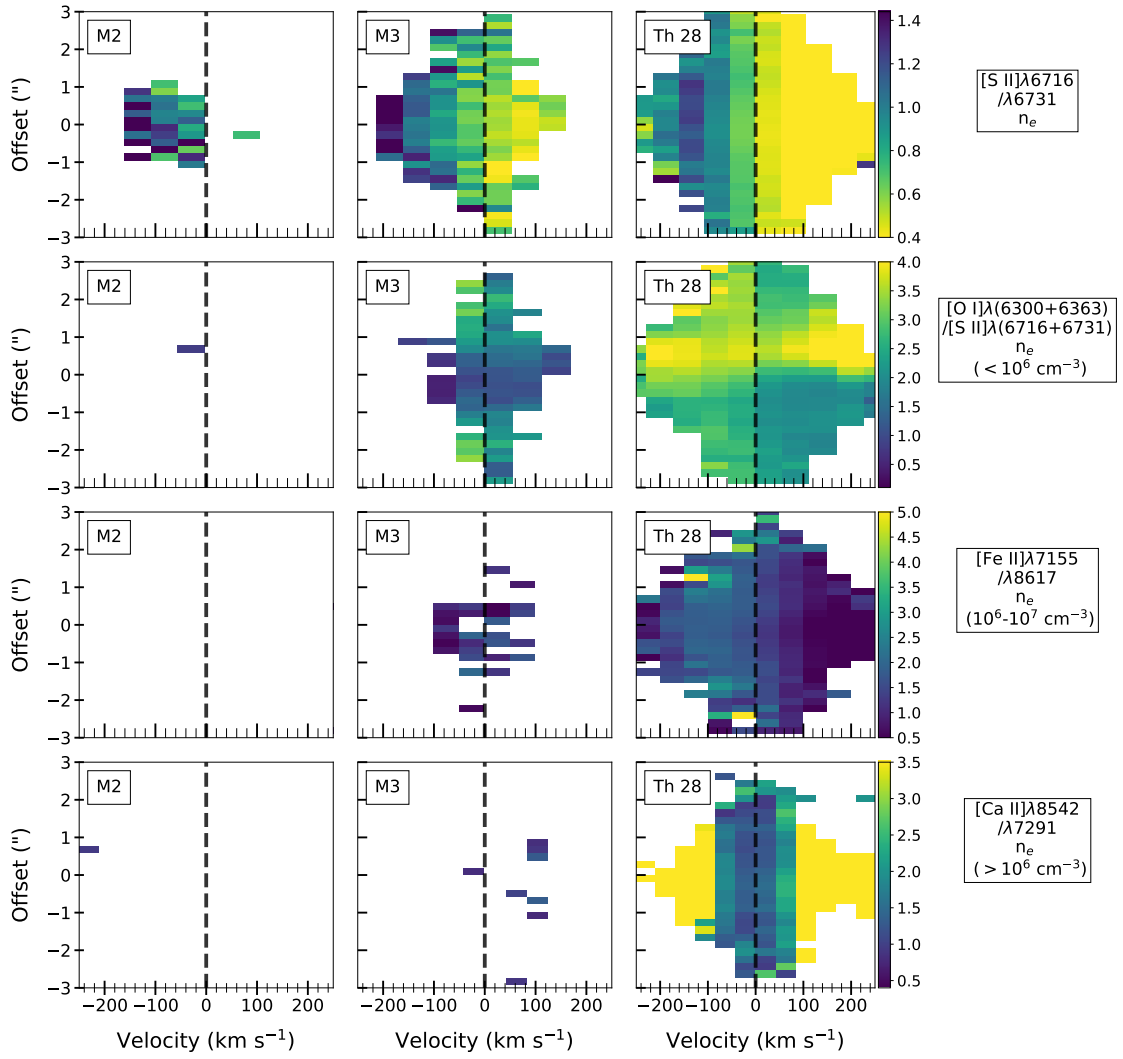

FIGURE 5.14: Transverse PV ratio maps showing the distribution of n_e in cuts across the blue-shifted knots and source position of the Th 28 jet. The dashed vertical line marks the 0 km s^{-1} position. White (0) regions and colour bars are arranged as in Fig. 5.10.

refinement of this work should correct for the differential velocity sampling of the lines used in each ratio. We also note that our transverse maps do not show the *spatial* n_e asymmetry reported by Coffey et al. (2008); however, as their data were obtained close to the jet base (0."3) with much higher spatial resolution, we cannot make a direct comparison with these results.

5.5.2 Excitation

Two line ratios which can be readily correlated with temperature are [N II]λ(6548+6583)/5755 and [O I]λ(6300 +6363)/5577 (hereafter the [NII] ratio and the [O I] ratio). As discussed in detail in Osterbrock & Ferland (2006) and examined further later in this

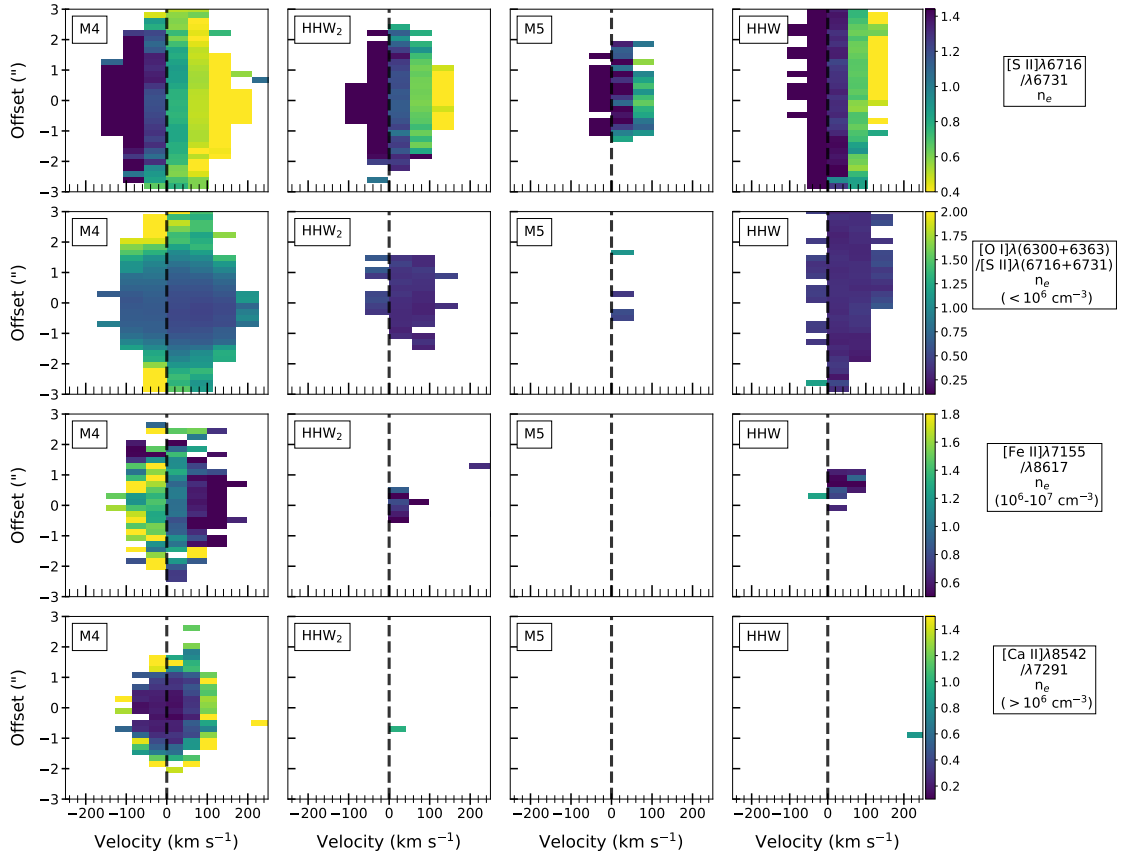

FIGURE 5.15: As in Fig. 5.14 but for the red-shifted knots.

section, both of these ratios are inversely correlated with the temperature, with almost identical curves. We show maps for both ratios here. Additionally, as mentioned the [S II]λ(6716+6731)/[O I] (6300+6363) ratio (the inverse of the [O I]/[S II] ratio) is sensitive to temperature and ionisation fraction in regions below the [S II] critical density (and is one of the diagnostic ratios used to determine these parameters in the BE method); we therefore also show this map to highlight ionisation in the lower-density regions of the jet (Hartigan et al., 1994; Podio et al., 2011).

To explore the ionisation along the jet we can first use [N II]λ6583/[S II]λ(6716+6731) (the [N II]/[S II] ratio) which is primarily dependent on x_e; however it also has a weak positive dependence on n_e and T_e and therefore traces high-excitation regions, increasing where the gas is hotter, denser and more ionised, i.e. in shock regions (Hartigan & Morse, 2007). The ratio [N II]λ(6548+6583)/[O I]λ(6300+6363) (the [N II]/[O I] ratio) also traces x_e and T_e (and is also used in the BE method). Finally, the [N II]λ6583/[N I]λ5200 ratio provides an additional check on x_e as discussed by Hartigan & Morse (2007). If the ionization fraction is constant along the jet, this ratio should increase steadily toward the source (due to the greater critical density of [N II]λ6583 relative to [N I]λ(5199+5201) and increased reddening; however given the drop in x_e close to the

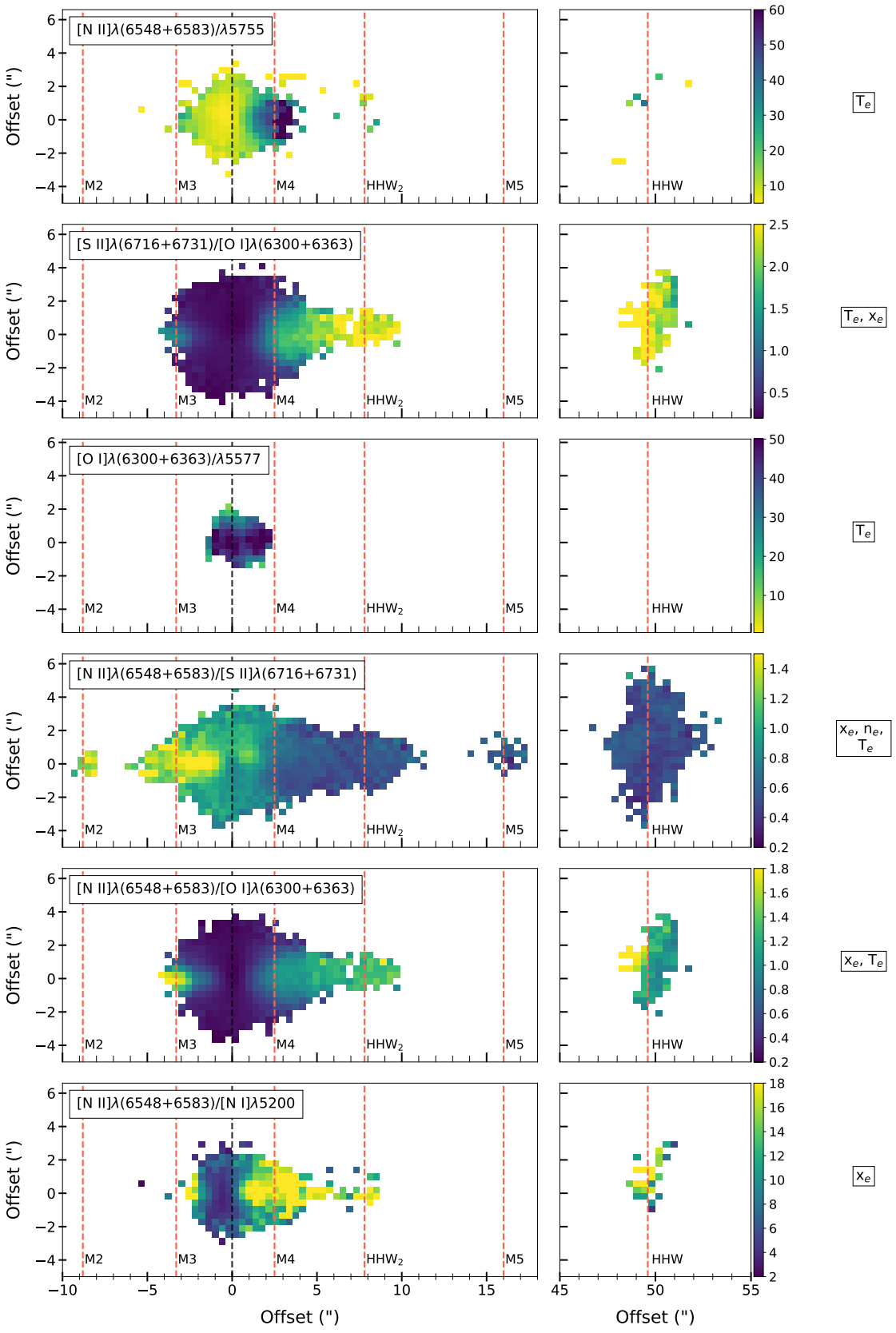

FIGURE 5.16: Spatial ratio maps of the Th 28 jet correlating to the distribution of x_e and Te; left panels show the inner jet region while panels on the right show the bow shock HHW. The colour bars are arranged so that the brighter (yellow) regions correspond to increases in the relevant parameters (x_e and T_e). White (0) regions, and vertical lines as in Fig. 5.10.

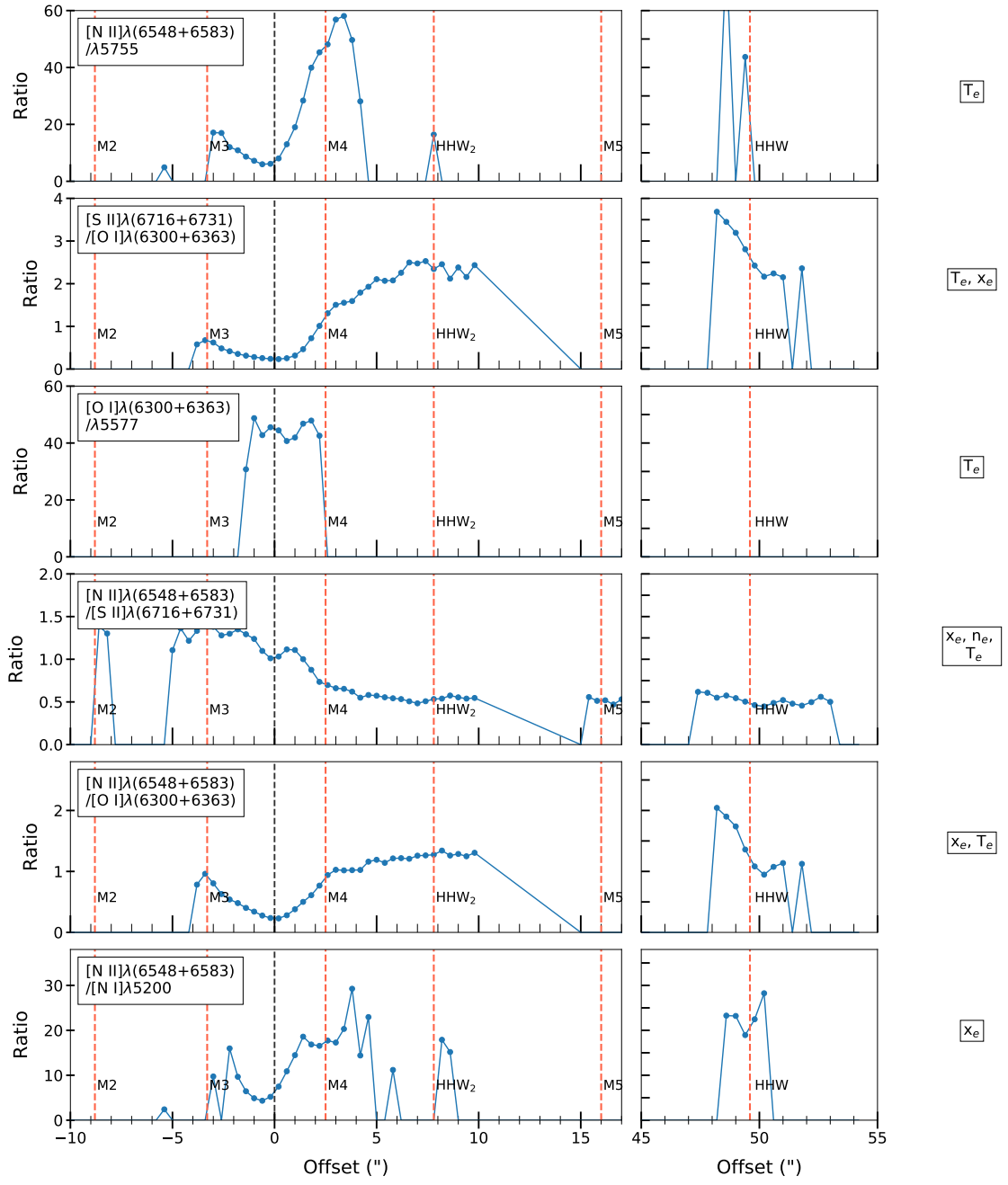

FIGURE 5.17: Profile along the jet axis of the ratio values shown in Fig. 5.16. Vertical lines mark the source and knot positions as in Fig. 5.10.

source shown by the results of the BE method, we expect to see this ratio decrease here instead.

Ratio maps for the line ratios tracing excitation were obtained using the same procedure as in the preceding section. The spatial maps are shown in Figure 5.16: the upper three rows show ratios which are primarily correlated with temperature while the lower 3 rows give ratios tracing x_e; however many of these ratios trace more than one parameter and so this is a rough distinction.

The asymmetry in ionisation between the jet lobes is seen most clearly in the [N II]/[S II] ratio, which traces both lobes well including the bow shock HHW. The blue-shifted jet is more ionised from about 1" of the source, with the centre of the jet and the bow shocks showing highest ionisation. In the red-shifted jet we see x_e and T_e increase before the position of the first knot M4 and remain fairly constant along the jet axis to about +10" (the knot M5 visible at +16" in the [N II]/[S II] ratio shows similar ionisation to the rest of the jet lobe). HHW is visible in several of the ratios and shows similar properties to the red-shifted lobe overall with a slight increase in x_e toward the back of the shock.

The profiles shown in Figure 5.17 illustrate the same trends of generally higher ionisation in the blue-shifted lobe, with both jets showing increase in x_e around the position of the first knots. Interestingly, these maps suggest a higher temperature in the red-shifted jet, though this may partly be due to the main temperature-tracing emission lines not being well detected in the blue-shifted jet. Due to the faintness of this jet lobe the ratios of [O I] and [N II] are not traced beyond about 2-3" from the source in this lobe. Similarly the [N II]/[O I] ratio which mainly traces x_e is only measured within <3 of the source in the blue-shifted lobe. Again, ratios of [O I] in the blue-shifted jet should be considered with the caveat of contamination by scattered red-shifted emission.

The PV maps shown in Figure 5.18 paint a similar picture. Temperature and ionisation rise sharply in the red-shifted jet at about the position of the first knot M4, although the [O I] and [N II] temperature ratios are only measured close to the source. The values of these ratios are similar overall as expected from their similar dependence on T_e. The profile cuts along the jet axis, shown in Figure 5.19, show excitation increasing in the blue-shifted jet as well. Small peaks in T_e and x_e are traced by the [S II]/[O I] and [N II]/[O I] ratios respectively, corresponding to the positions of the knot M3. We also note an apparent rise in ionisation in the high-velocity wings of the blue-shifted lobe close to the source as shown by the [N II]/[S II] ratio, although this is not observed in any of the other ratios.

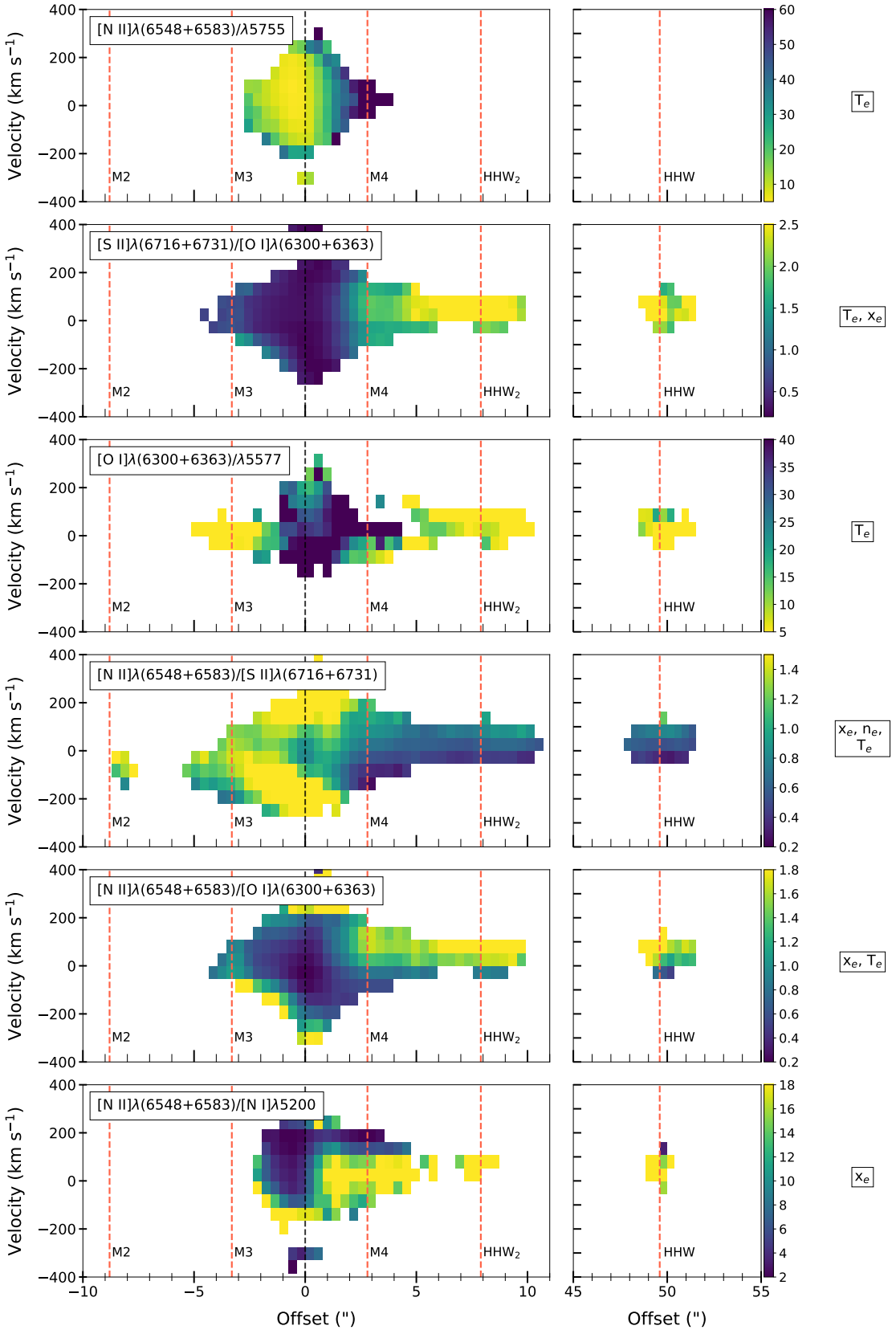

FIGURE 5.18: Position-velocity ratio maps of the Th 28 jet correlating to the distribution of x_e and T_e; left panels show the inner jet region while panels on the right show the bow shock HHW. White (0) regions, colour bars and vertical lines as in Fig. 5.16.

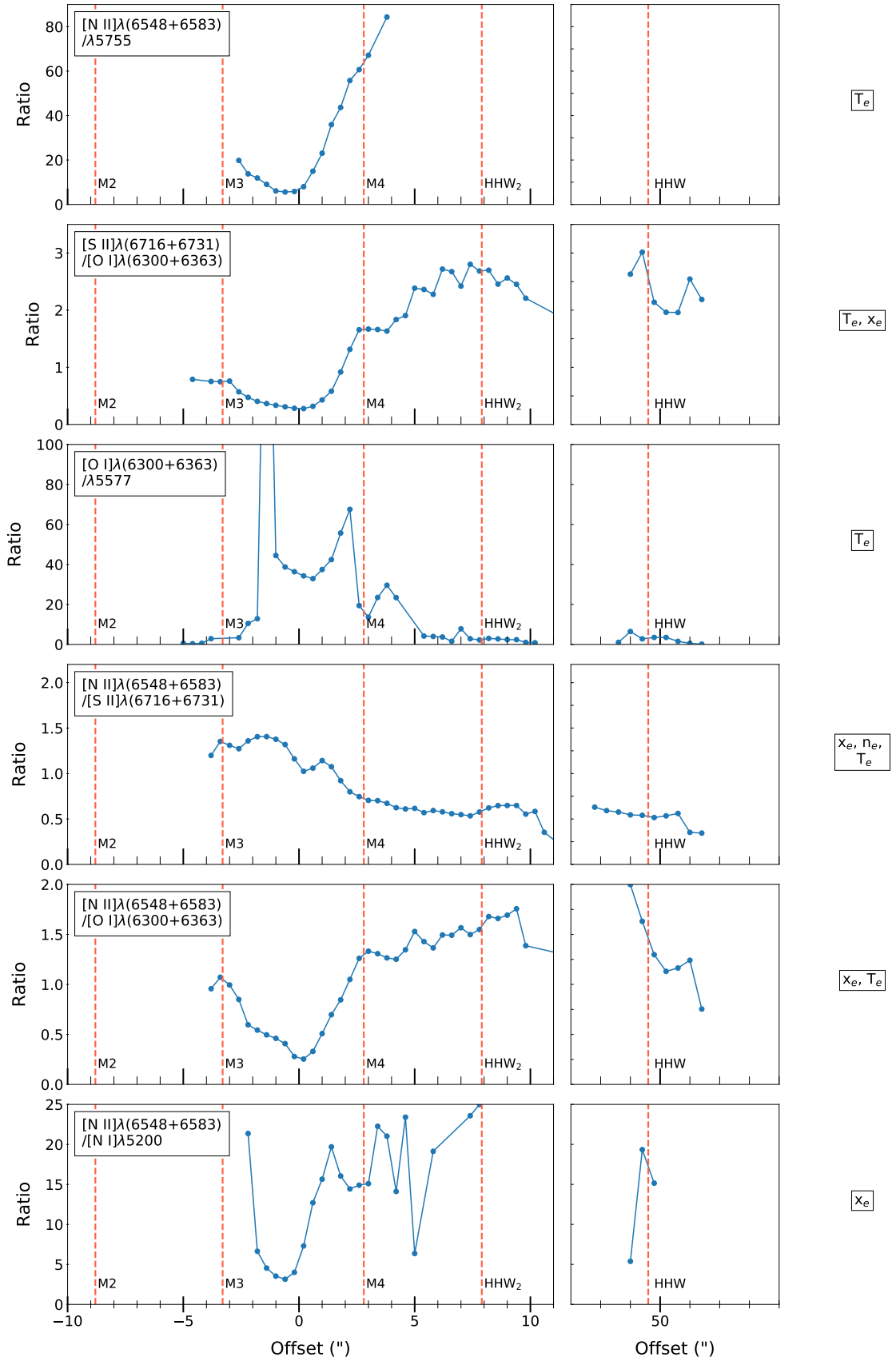

FIGURE 5.19: Profile of the ratio values shown in Fig. 5.18, with cuts taken along the jet axis. Left panels show the inner jet region while panels on the right show the bow shock HHW. Vertical lines as in Fig. 5.10.

Transverse maps for the blue- and red-shifted jets are shown in Figures 5.20 and 5.21, respectively. The faintest knots, M1 in the blue- and M5 in the red-shifted jet, are not well-detected in any line ratios, while M3 and HHW_2 are detected in only a few. Overall the knots M3, M4 and HHW_2 (and to a lesser extent the bow shock HHW) show higher temperatures and ionisations toward the spatial centre of the jet and typically at higher velocities, consistent with what we would expect from the 'onion layer' model of jet structure. This is particularly clear in ratios involving [N II] (the bottom three rows) which should favor the fast inner jet component.

Slices taken at the source position (Figure 5.20, right column) show a more complex picture, likely due to multiple jet components being detected here. The lower three rows show ratios tracing x_e, which again show higher ionisation fractions at higher velocities. We also note a spatial asymmetry in the [S II]/[O I] ratio (second row) and also in the [N II]/[O I] x_e-tracing ratio (fifth row) in which the red-shifted region on the lower half of the jet appears to have higher temperature and ionisation though the reason is unclear. We may again draw a comparison with the spatial asymmetry in temperature detected across the red-shifted jet axis by Coffey et al. (2008), although in those observations the asymmetry occurred at all velocities, whereas the one observed here occurs only in the red-shifted side.

5.5.2.1 Temperature Determination with [N II]

As briefly discussed, the [N II]λ(6548+6583)/5755 ratio is inversely related to temperature, with a small dependence on n_e. The full relationship is derived in Osterbrock & Ferland (2006) and shown to be:

$$[NII]\frac{(6548+6583)}{5755} = \frac{8.23\exp 2.5\times\ 10^4/T}{1+4.4\times\ 10^{-5}n_e/T^{1/2}} \tag{5.3}$$

Figure 5.22 shows this relationship for several representative values of n_e. We can therefore compare the values of the ratio estimated along the red-shifted jet with the corresponding curve, taking the values of n_e determined at the same positions using the BE method (Section 5.3.3). The [N II] line fluxes were sampled between the source position and +4", binning the spectra over 1" x 1" boxes and fitting a Gaussian function to determine the total flux.

The resulting temperature profile is plotted in Figure 5.23. Beyond 3" the [N II]λ5755 line becomes too faint to accurately fit. The results show a steady decrease in temperature along the jet axis, from 2.1 $\times$ 10^4 K to 1.25 $\times$ 10^4 K. This is somewhat in contrast to the BE results which also show a drop in temperature in this region, but

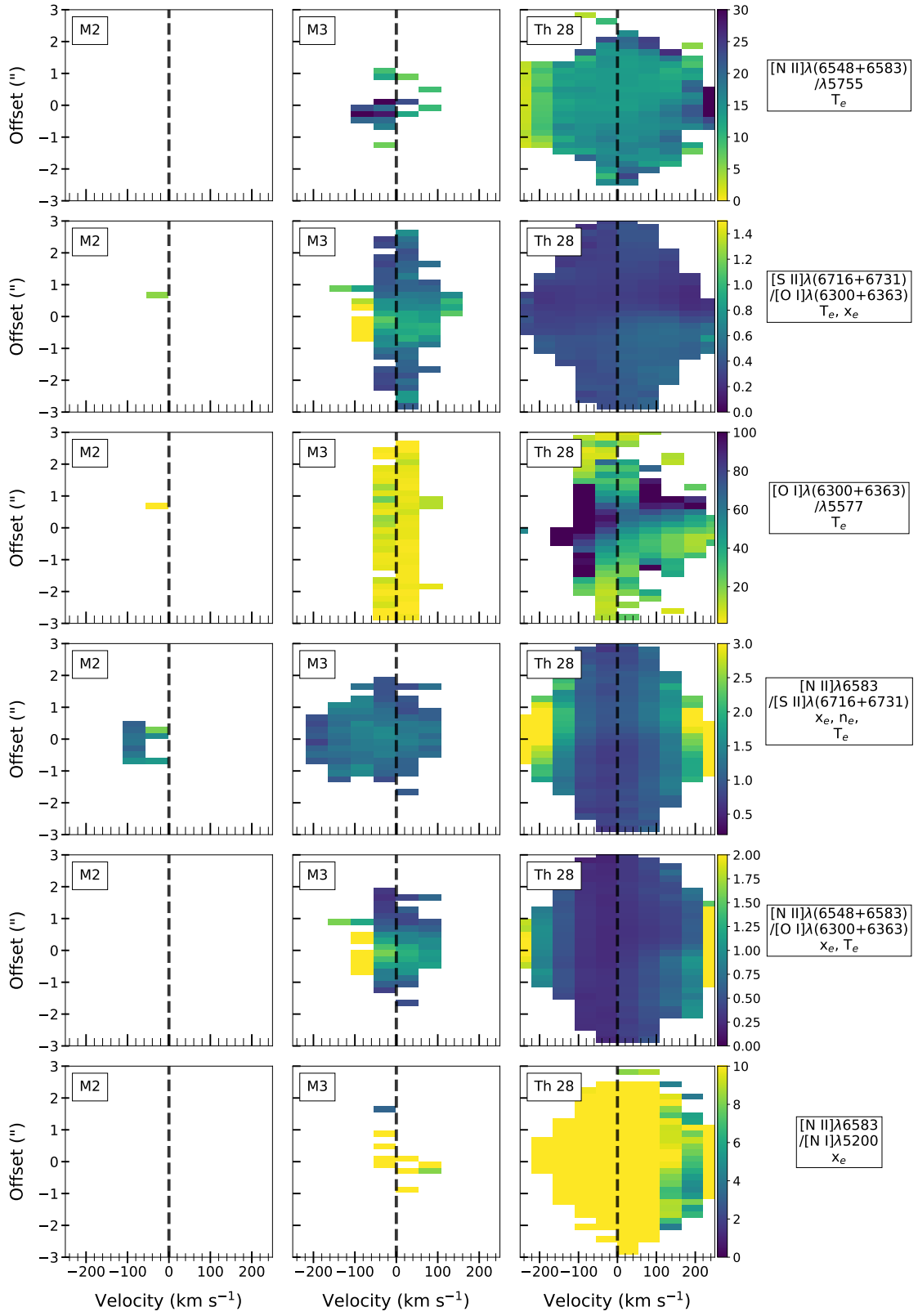

FIGURE 5.20: Transverse PV ratio maps showing the distribution of x_e and T_e in cuts across the blue-shifted knots and source position of the Th 28 jet. The dashed vertical line marks the 0 km s^{-1} position. White (0) regions and colour bars are as in Fig. 5.16.

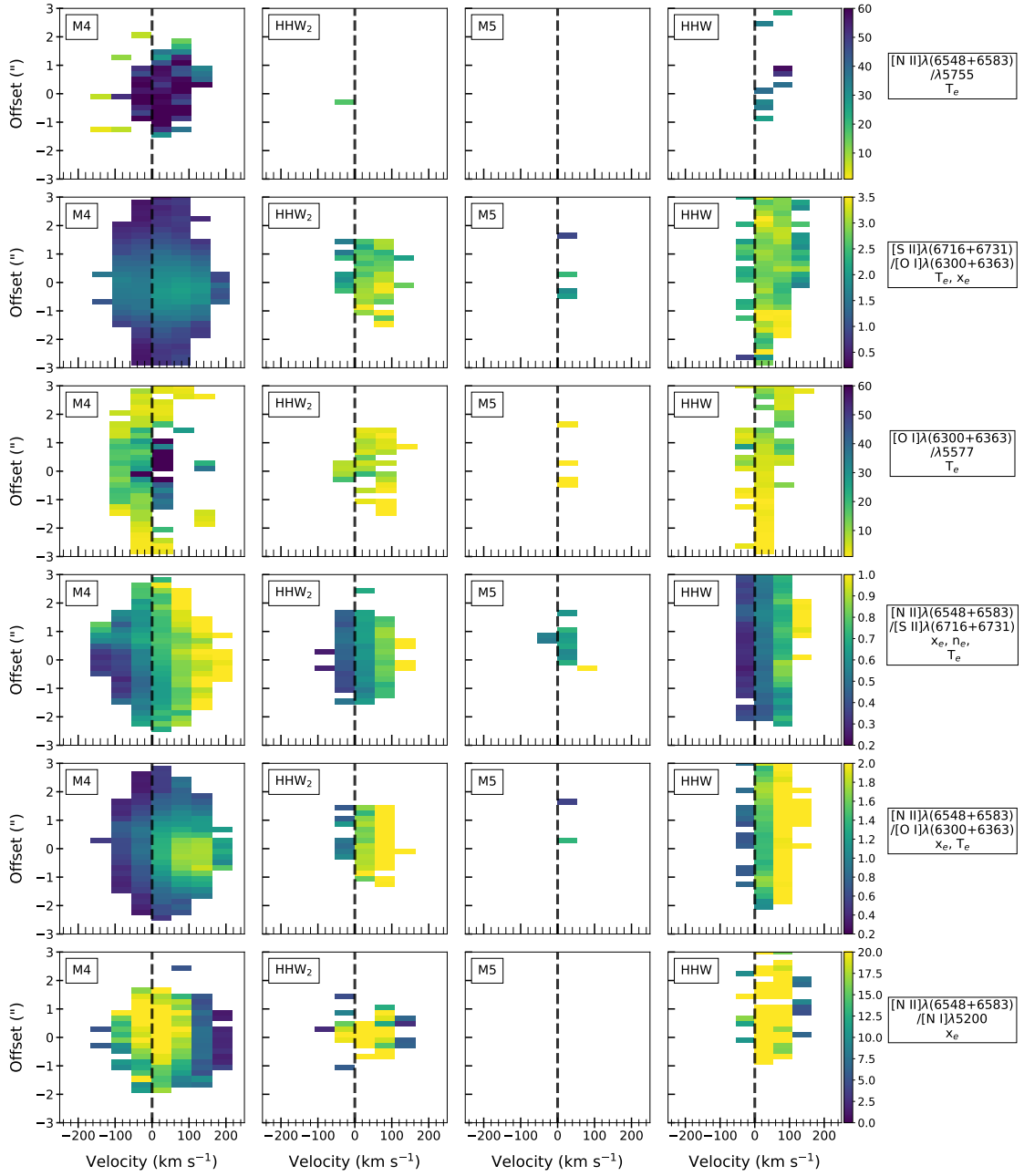

FIGURE 5.21: As in Fig. 5.20 but for the red-shifted knots.

only from about 2.1 $\times$ 10^4 K to 1.8 $\times$ 10^4 K. This difference may primarily reflect the faintness of the [N II]λ5755 at greater distances from the source, as the two methods agree well on temperature values within 1" of the source.

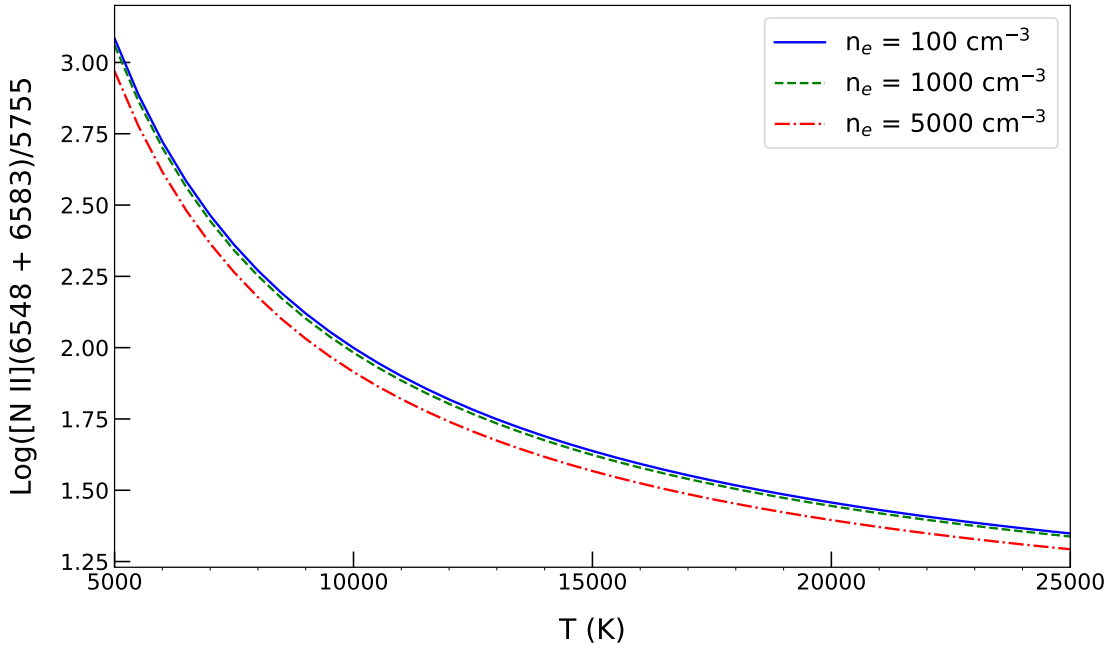

FIGURE 5.22: The intensity ratio of [N II]λ(6548+6583)/5755 as a function of temperature, for several values of n_e.

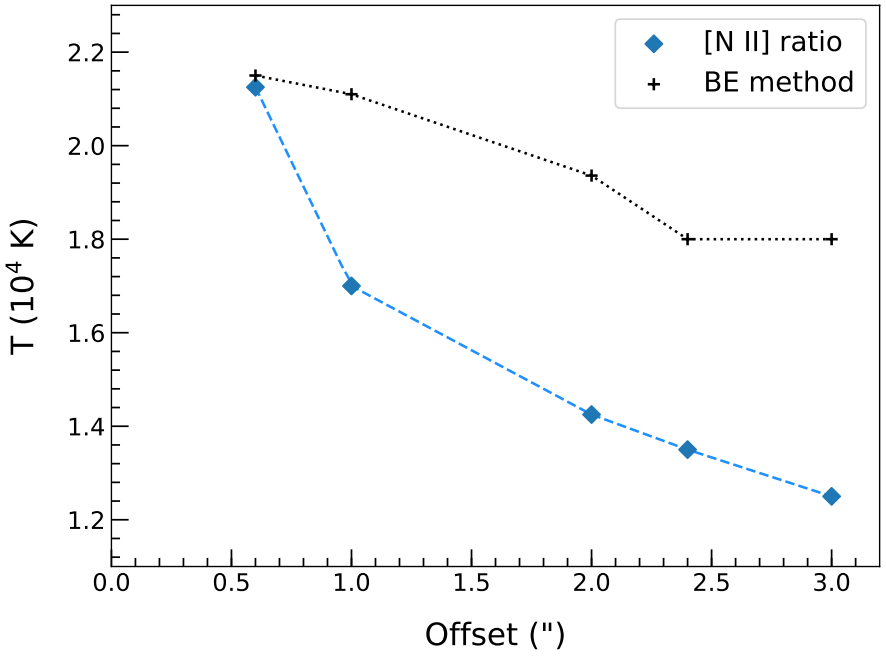

FIGURE 5.23: Estimated temperatures for the values of the [N II]λ(6548+6583)/5755 line ratio at several positions along the red-shifted jet, given the corresponding estimated of n_e from Section 5.3.3.The temperature values obtained in the same section using the BE method are plotted for comparison.

5.6 Refractory Species and Depletion

5.6.1 Theory

The amount of depletion in a given region is determined by competing processes of accretion (dominating in dense regions) and erosion (dominating in low density regions subject to shocks, i.e. jet environments). The main processes involved in dust erosion are sputtering, i.e. high-energy grain-ion collisions, and dust destruction in grain-grain collisions. Of these, sputtering is most significant for dust re-processing, since it has a selective effect for different species (for example, Mg and Cr are more easily eroded by sputtering than Fe and Ni) and thus alters the composition of the dust (Jones, 2000). The overall depletion of Fe and Ca are measured using ratios of their FELs with those of non refractory species emitted in the same jet region. The observed ratios can be compared with their predicted values at solar abundances (and for given estimates of T, n_e and x_e) to determine the depletion.

Measurements of depletion are therefore important to constrain shock properties in jets, including velocity and excitation. Only partial depletion is expected in typical low-velocity shocks ($\sim$40-50 km s^{-1}), while only high shock velocities > 100 km s^{-1} allow for total destruction of grains (Jones, 2000).

The measured depletions of gas-phase Fe and Ca in jets can vary strongly from 20-90%, although in cases where these are measured at significant distances from the source, Agra-Amboage et al. (2011) notes that significant shock processing may have occurred. Observing depletion in the inner jet regions as well as the processing of dust along the jet are therefore important to better understand the original dust content. This in turn is of interest given that some studies show higher depletion in lower velocity components of the jet (Podio et al., 2009; Agra-Amboage et al., 2011). This could suggest that this slower material is less shock processed, or that it originates from regions of the disk further from the source, i.e. beyond the dust sublimation radius close to the star. Understanding the origins and processes affecting dust in the jet is thus also relevant to constraining models of jet launching.

Key ratios for measuring the depletion of Fe are [Fe II]λ8617/[S II]λ(6716+6731) and [Fe II]λ8617/[O I]λ6300. The [S II] and [O I] lines have similar spatial distributions to [Fe II], however results obtained from these ratios may be inconsistent and care should be taken to consider whether the S and O lines arise from the same excitation regions as the Fe emission (Nisini et al., 2005). This is less of a concern for another ratio, [Ca II]λ(7291+7234)/ [S II]λ(6716+6731) as their excitation conditions are more comparable.

Additionally, we can examine the selective depletion of refractory species. As mentioned, different species have different erosion patterns which depend on the shock properties. Their relative abundances can therefore also probe shock properties as well as the composition and structure of dust grains, and the reprocessing of dust in the jet. We detect the relevant emission lines for two useful line ratios in this regard, [Cr II]λ8000/[Fe II]λ8617 and [Ni II]λ7378/[Fe II]λ8617. Of these, the excitation conditions of [Ni II] are particularly well correlated with [Fe II]; they have similarly high critical densities, very similar excitation energies, and are close in wavelength, which minimizes uncertainties introduced by corrections for reddening (Bautista et al., 1996). As they are known to coexist, any change in their ratio correlates well to a change in their relative abundance.

In this section, we estimate ratios of each of these emission lines along the Th 28 jet and present ratio maps of their distribution. Although we do not estimate abundances in this work, we will use these results to take an initial look at the presence and distribution of key line ratios in preparation for further study of the dust processing signatures in the Th 28 jet.

5.6.2 Results

The resulting ratio maps are shown in Figure 5.24, with profile cuts along the jet shown in Figure 5.25. As noted, without a full calculation of the inferred abundances we can make limited inferences from these, however we discuss the results briefly. The estimated values of all ratios are generally comparable to those measured by Nisini et al. (2005) for the HH1 jet, which suggests that the values obtained are reasonable.

First the [Fe II]/[S II] ratio is detected well to 2."5 in the blue- and 4" in the red-shifted jet, including the position of the first knot M4. The ratio peaks at a value of 0.2 at the source position and drops off along the axis of both jet lobes, though less strongly in the blue-shifted jet (to 0.15) than in the red-shifted jet (0.05). This is generally consistent with the [Fe II] line tracing high-density regions and with the higher values of n_e obtained in the blue-shifted jet; on the other hand the blue-shifted jet exhibits shocks with high velocities (> 90 km s^{-1}) and could therefore be expected to show lower depletion relative to the red-shifted jet.

We make particular note of the [Ca II]/[S II] ratio as one of the Ca lines, [Ca II]λ7324, is strongly blended with the [O II] doublet at 7330 Å in the MUSE spectra. The map shown therefore includes points only where estimation of the Ca line could be obtained by fitting Gaussian functions to the three lines and subtracting the fitted [O II] lines. This has the effect of limiting the region where the ratio can be estimated

(particularly close to the source where the [O II] lines are brightest), and again these results would require further analysis to determine abundances and depletion values.

However, this map shows two interesting features for future investigation. First, the extent of the [Ca II] lines along the jet allow this ratio to be estimated as far as the knot HHW_2 in the red-shifted jet; second, the ratio peaks at 1" from the source in the red-shifted jet, seen most clearly in the profile in Figure 5.24. This feature could be an effect of [Ca II]λ7324 being too blended to detect at the source position (and in the blue-shifted jet); on the other hand this peak at 1" may also be faintly seen in the [Fe II]/[O I] profile. Since these [Ca II] lines are also detected in the 2015 X-Shooter spectra of Th 28, which have a slightly better velocity resolution, this presents the possibility of attempting to extract the Ca line from that data and more fully investigate the Ca depletion along the jet.

Finally, looking at the selective depletion ratios, the [Cr II]/[Fe II] ratio is detected to 2" in both jets, with a consistent value of $\sim$0.1. The [Ni II]/[Fe II] extends to 2" in the blue and around 3" in the red, and appears to be slightly higher in the blue-shifted jet than in the red-shifted lobe, with values of 0.6-7 versus 0.5, respectively.

5.7 Mass Accretion and Outflow

The jet efficiency, or the ratio of the mass outflow rate in the jet to the mass accretion rate onto the star (i.e., $\dot{M}_{out}/\dot{M}_{acc}$), is an important parameter for constraining models of jet launching. We therefore want to obtain accurate estimates of the mass accretion and outflow rate close to the star. Additionally, mass flux estimates along the jet are important to understand the outward transport of linear and angular momentum by the jet and the impact of outflows on the surrounding environment.

There are several methods to estimate the accretion rate $\dot{M}_{acc}$ of a star using tracers in different wavelength regions. It can be traced by the luminosity of continuum excesses in IR or UV which are proportional to accretion; however, excess IR emission can also come from stellar light reprocessed in disc, and is therefore an imprecise tracer especially in sources with low $\dot{M}_{acc}$. An alternative, particularly at optical wavelengths, is to use the luminosity of emission lines emitted in the boundary layer which are correlated with other measures of mass accretion rate.

This method will be discussed in more detail below; however from all methods the typical estimates for $\dot{M}_{acc}$ in CTTSs are approximately 10^{-7} $M_\odot$ yr^{-1} (Hartigan et al., 1995) with some variation between 10^{-8}-10^{-6} $M_\odot$ yr^{-1} (Bertout et al., 1988; Hartigan et al., 1991, 1995). Methods of estimating the mass outflow rate will be discussed in

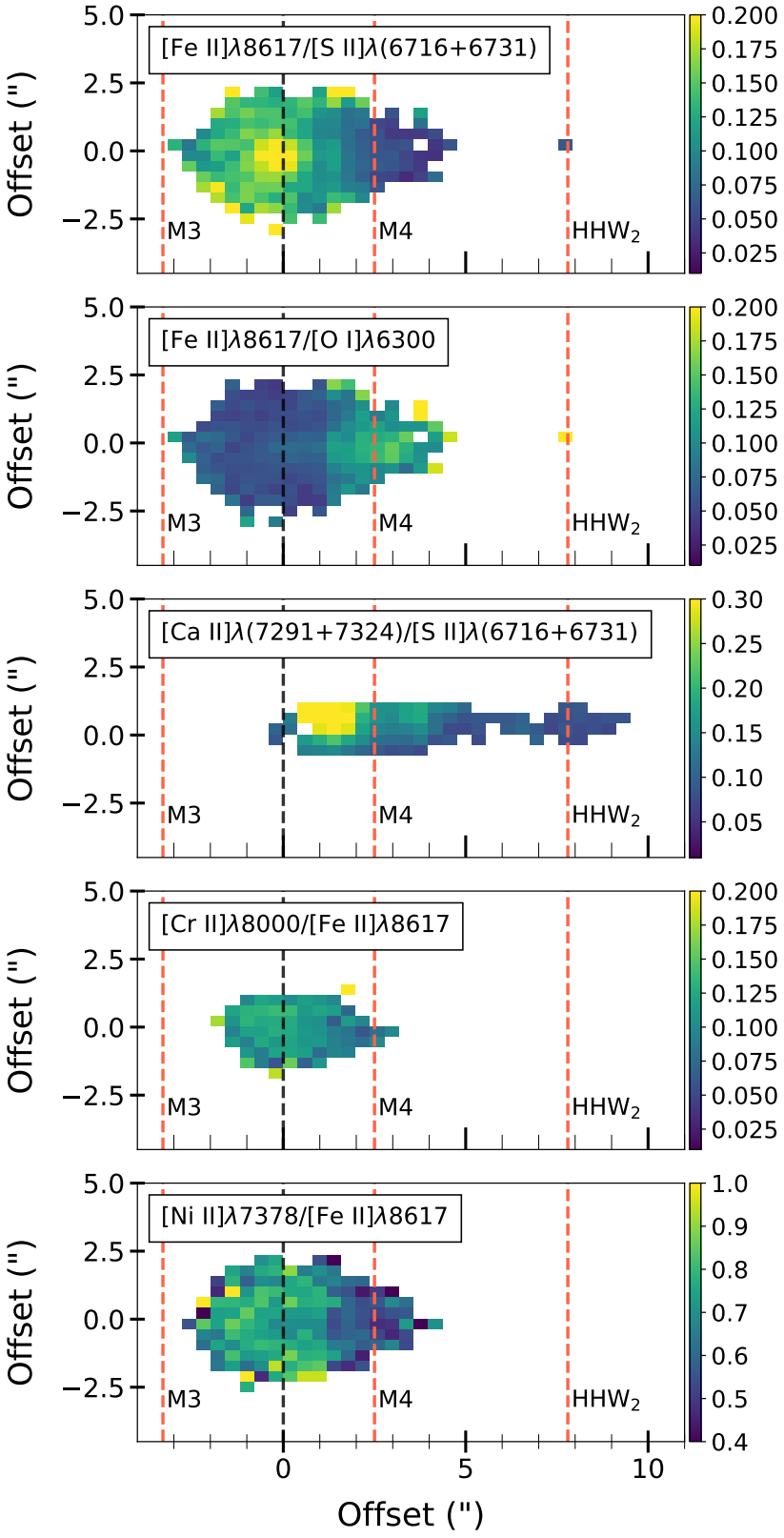

FIGURE 5.24: Spatial ratio maps of refractory species in the inner regions of the Th 28 jet. As in preceding figures, white (0) regions show those where at least one of the relevant lines has flux less than 3-σ of the background level; orange dashed lines show the labelled knot positions with the black vertical line marking the source position.

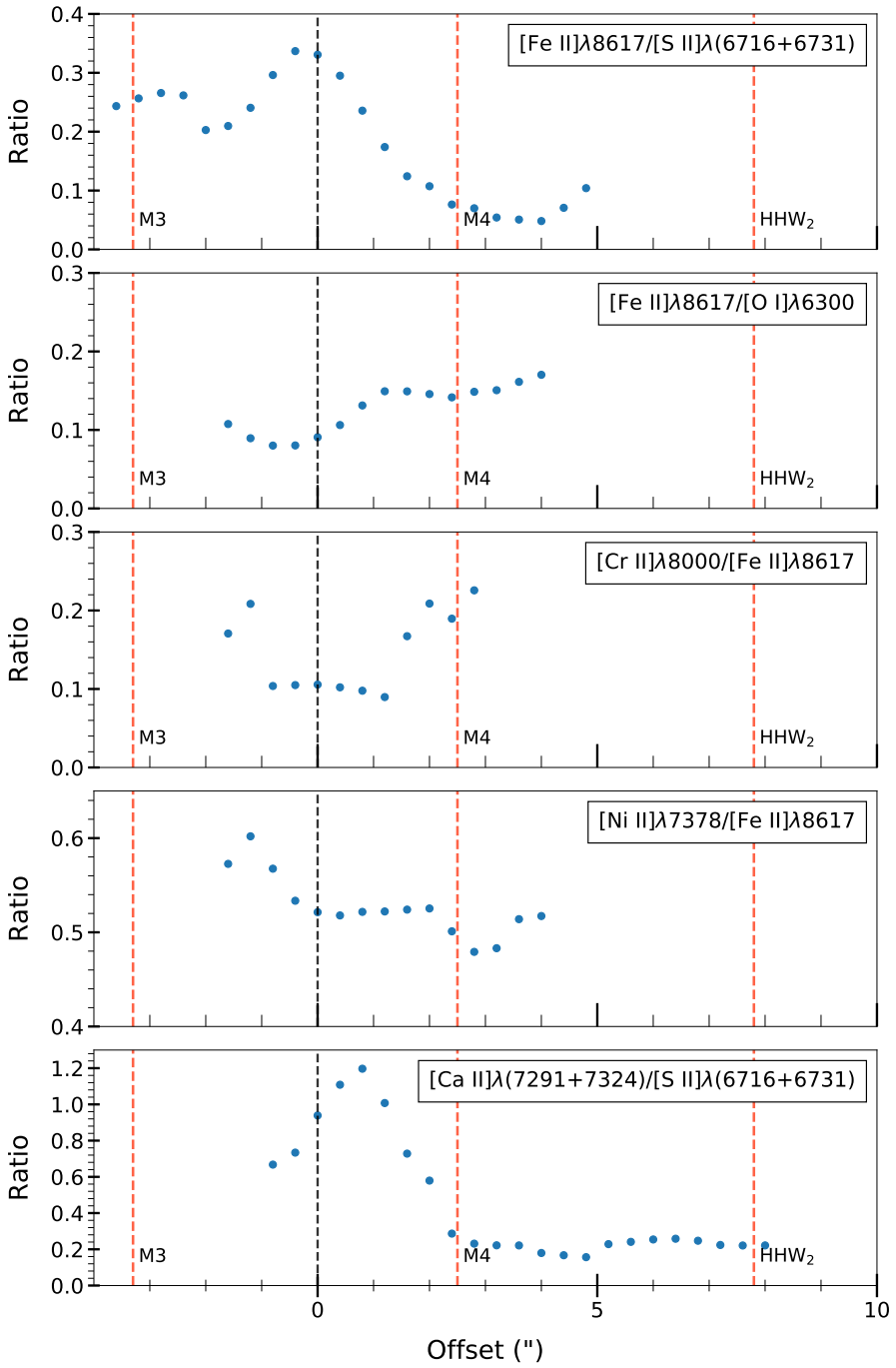

FIGURE 5.25: Profile of the ratios shown in Fig. 5.24, taken from integrated flux values sampled along the jet axis. Vertical lines mark the source and knot positions as in Fig. 5.24.

Section 5.7.3, but typical outflow estimates are approximately 10^{-9} - 10^{-8} $M_\odot$ yr^{-1}, yielding typical efficiencies of 0.01-0.1.

5.7.1 Previous Estimates in Th 28

The accretion rate for Th 28 was previously estimated by Comerón & Fernández (2010) using the luminosity of the permitted line Ca II λ8662 (method described in Section 5.7.3.2 with the coefficients given in Mohanty et al. (2005). They assume a T_{eff} for the star of 4100-4600 K based on M_* = 0.6-0.9 $M_\odot$ and age 1-2 Myr. Based on these assumptions they determined $\dot{M}_{acc}$ = 4.2-6.3 $\times$ 10^{-8} $M_\odot$ yr^{-1} (for ages of 2-1 Myr respectively). This estimate falls within the range of expected values for the expected $M_*/\dot{M}_{acc}$ ratio (Mohanty et al., 2005). It should be noted that this work assumes a somewhat higher mass of M_* = 1.6 $M_\odot$, and that the assumption of T_{eff} and hence bolometric luminosity also affects the assumed value of R_*.

The outflow rate has been estimated by Coffey et al. (2008, 2010) using both optical line diagnostics and Fe line luminosity. The optical diagnostics made use of the [S II] doublet to estimate the total jet density and hence mass outflow through a cross-section close to the jet base. They estimate $\dot{M}_{out}$ = 1.2 $\times$ 10^{-8} $M_\odot$ yr^{-1} in the red-shifted jet alone. They treat this as as an average value rather than an upper or lower limit, as close to the star there should be relative homogeneity and high densities; this means that less-dense parts of the jet which are underrepresented in the estimate of $\dot{M}_{out}$ are compensated for by the jet regions where the [S II] doublet saturates (and hence underestimates the density). Interestingly, they also find an asymmetry in the H density between one side of the jet axis and another, leading to an estimate of $\dot{M}_{out}$ which is twice as large on one side of the jet relative to the other. Using the average density n_H in the upper and lower halves they estimate values of $\dot{M}_{out}$ = 0.4 $\times$ 10^{-8} $M_\odot$ yr^{-1} and 0.9 $\times$ 10^{-8} $M_\odot$ yr^{-1} for the two halves of the jet. The latter region includes pixels where the [S II] doublet ratio is saturated and hence may represent a lower limit to $\dot{M}_{out}$.

A further estimate for $\dot{M}_{out}$ in both lobes of the jet comes from the luminosity of [Fe II]λ1.64 μm (Coffey et al., 2010), assuming the iron is completely ionised with A_v = 0 and T_e = 1 $\times$ 10^4 K. This study yields estimates of $\dot{M}_{out}$ = 2 $\times$ 10^{-9} $M_\odot$ yr^{-1} in the red-shifted jet and 1 $\times$ 10^{-9} $M_\odot$ yr^{-1} for the blue-shifted jet. This asymmetry stems from the lower apparent flux in the blue-shifted jet, which is not compensated for by the higher jet velocity in this lobe. This may be due to the asymmetric extinction in the two lobes which is not accounted for in these results. The authors note that these estimates represent a lower limit on $\dot{M}_{out}$, both due to the lack of correction for extinction and due to having no estimate of the Fe depletion in the jet with respect to solar abundance.

This estimate also shows an order of magnitude difference to the results obtained using the density estimates from optical line ratios, which is typical in comparing the results of these methods. Additionally, the optical line fluxes are 2 orders of magnitude brighter than the IR [Fe II] lines, but it is unclear if this is intrinsic or due to a depletion of Fe.

Taking the first estimate of $\dot{M}_{out}$ from the jet density and comparing it with the estimated $\dot{M}_{acc}$ yields an estimated efficiency of 0.2. This is strikingly high especially when considering that this represents only the red-shifted jet outflow, implying a total (two-sided) efficiency of ~ 0.4. On the other hand, using the estimates for $\dot{M}_{out}$ in both jets from the Fe II luminosity gives a more typical value of 0.05. Both estimates however are subject to substantial uncertainties of a factor of a few due to measurement uncertainties in line fluxes and estimated densities; additional uncertainty stems from the known variability of outflow and accretion rates.

5.7.2 Estimating the Th 28 Accretion Rate

To estimate $\dot{M}_{acc}$ in Th 28 we estimate the accretion luminosity L_{acc} indirectly, by making use of permitted lines known to be well correlated with the mass accretion. These empirically-determined relationships for each emission line allow $\dot{M}_{acc}$ to be estimated from the line luminosity L_{line}.

However, the edge-on disc of Th 28 presents a challenge in this regard, as a clear stellar spectrum is not observed. Instead, the observed line fluxes are significantly reduced due to the obscuring dust. Two main components should be considered, reddening, or wavelength-dependent extinction, and 'grey scattering'. The former is discussed in more detail in Section 5.4, and can be corrected for using the estimated A_v found therein. 'Grey scattering', in contrast, is wavelength independent. It can be approximated as an obscuration factor which suppresses L_{acc} and L_* by the same amount. As such it has no effect on the relationship of L_{acc} to L_{line}, and once estimated can be corrected for in a straightforward way. Fom Alcalá et al. (2014):

$$\dot{M}_{acc}\ (corrected) = (obscuration factor)^{1.5} \dot{M}_{acc} \tag{5.4}$$

The obscuration factor for Th 28 has not been previously estimated, but is expected to be substantial due to the edge-on disc and the under-luminosity of the source. However, we can make an estimate of the obscuration using the [O I]λ6300 line. This line is emitted from the jet, so that it arises above the dust plane and is, in theory, not subject to obscuration, but is also correlated with the accretion rate (Herczeg & Hillenbrand,

2008; Riaz et al., 2015). We therefore estimate $\dot{M}_{acc}$ using [O I]λ6300 and compare it with values obtained from the permitted lines to obtain an estimate of the obscuration.

Table 5.8 gives the full list of accretion tracers identified in the MUSE spectrum. For each one a continuum-subtracted spectrum was extracted in 1" x 1" box centred on the source position in each cube. A Gaussian fit was made to the line and the flux integrated to estimate L_{line}. We derive L_{acc} from the relationship:

$$logL_{acc} = AlogL_{line} = B \tag{5.5}$$

with coefficients A and B given in Table 5.8. These are determined empirically from correlation of line fluxes with accretion luminosity L_{acc}. The accretion rate is then given by:

$$\dot{M}_{acc} = \frac{1.25 L_{acc} R_*}{G M_*} \tag{5.6}$$

We estimate R_* from the bolometric luminosity:

$$L_{bol} = 4\pi R_*^2 \sigma T_{eff}^4 \tag{5.7}$$

As mentioned, we take $M_* = 1.6$ $M_\odot$. Extinction-corrected values of $T_{eff} = 3100$ K and L_{bol} =0.22 $L_\odot$ were obtained from Dunham et al. (2015a) (associated paper Dunham et al. (2015b)) and are derived from integration of the Th 28 SED. Based on these values we find $R_* \sim 1.63$ $R_\odot$.

By comparison with $\dot{M}_{acc}$ derived from the [O I]λ6300 line we estimate an average obscuration factor of approximately 71. We can compare this value with the case of ESO-Hα, a jet with a similarly edge-on disk, but in which the accretion tracers are noted to be extremely suppressed (Whelan et al., 2014). The obscuration factor estimated for this source is 150, suggesting that Th 28 is significantly less obscured in comparison. We note however that although the [O I] line is less obscured by the disc, there may still be some obscuration at this level and so this obscuration value may represent an underestimate. The results are summarized in Table 5.8, with corrected $\dot{M}_{acc}$ values given for the permitted lines. Figure 5.26 shows the log $\dot{M}_{acc}$ for the different lines with the permitted lines shown before and after correction for obscuration.

From the [O I] line we find $\dot{M}_{acc} = 9.8 \times 10^{-8}$ $M_\odot$ yr^{-1}. Combining this with the corrected values of $\dot{M}_{acc}$ using our obscuration factor, we obtain an an average $\dot{M}_{acc} = 1.15 \times 10^{-7}$ $M_\odot$ yr^{-1}. We will use the averaged value in comparisons with the mass

outflow rate, in order to take account of the variability in the $\dot{M}_{acc}$ estimates using the full range of emission lines (see Whelan et al. (2014)). This value is consistent with typical accretion rates for CTTS sources. It is somewhat higher than the 6.3×10^{-8} $M_\odot$ yr^{-1} estimated by Comerón & Fernández (2010), however our estimate for $\dot{M}_{acc}$ derived from Ca II λ8662, the line they used, yields 7×10^{-8} $M_\odot$ yr^{-1}. As discussed in Section 5.3.3, we estimate an uncertainty of 5% on the total line fluxes (dominated by the flux calibration uncertainty of MUSE due to the high S/N of lines close to the source). Propagation of this uncertainty with the uncertainties of the coefficients A and B as given in Table 5.8 gives an average uncertainty of 25% on the estimates of $\dot{M}_{acc}$.

The Ca lines overall give the lowest estimates of $\dot{M}_{acc}$ in our sample, although all fall within 1-σ of the mean $\dot{M}_{acc}$. Given the uncertainties due to extinction, flux uncertainty, assumed stellar mass and distance, and accretion variability, our estimates agree well with the previous measurement. The similarity in these estimates is interesting, as the Comerón & Fernández (2010) value is derived using estimates of the intrinsic properties of the source to estimate the total line flux, rather than a comparison to the [O I]λ6300 line. This suggests that our method provides a good estimate of the obscuration factor affecting Th 28, and that the [O I] line is minimally subject to obscuration from the disc. The results from the MUSE spectra have the additional advantage that making use of a broad range of emission lines provides a more reliable estimate of $\dot{M}_{acc}$; additionally, the consistency of the accretion estimates from these lines, and the lack of a pronounced trend in $\dot{M}_{acc}$ with wavelength (see Figure 5.26) further suggests that our estimate of the extinction at the source position is reasonable.

As a further comparison, a future extension of this work will be to make use of the X-Shooter spectrum of Th 28 to extend the analysis to accretion tracing lines in the UV wavelength range, as well as to fit the UV continuum excess and hence an alternative estimate of L_{acc}(see for example Manara et al. (2021)). Similarly an alternative estimate of the obscuration factor may be obtained by placing the source on the Hertzsprung-Russel (HR) diagram and comparison with the expected position for its estimated mass and age.

5.7.3 Mass Outflow

Several methods can be used to estimate $\dot{M}_{out}$, the rate of mass outflow through the jet. The methods used here are 1), estimating the density of the atomic jet and hence the mass flux through the cross-sectional area of the jet, and 2), using the luminosity of the FELs in the jet to estimate the mass moving through a given spatial region (the luminosity method). The range of optical emission lines available through the MUSE

Line	λ	A	B	L_{line} (10^{-5} $L_\odot$)	ΔL_{line} -	L_{acc} (10^{-3} $L_\odot$)	ΔL_{line} -	$\dot{M}_{acc}$ (10^{-8} $M_\odot$ yr^{-1})	Δ $\dot{M}_{acc}$ -	Obsc.
Hβ	4861.33	1.11 $\pm$ 0.05	2.31 $\pm$ 0.23	10.8	0.54	8.10	1.98	19.5	4.8	45
He I λ5876	5875.9	1.13 $\pm$ 0.06	3.51 $\pm$ 0.30	1.19	0.06	8.78	2.21	21.1	5.3	42
Na I λ5890	5889.95	0.93 $\pm$ 0.06	2.56 $\pm$ 0.32	0.53	0.03	4.49	1.19	10.8	2.9	66
Na I λ5896	5895.92	0.90 $\pm$ 0.06	2.56 $\pm$ 0.37	0.42	0.02	5.29	1.42	12.7	3.4	59
[O I] 6300	6300.304	1.33 $\pm$ 0.14	5.37 $\pm$ 0.62	17.8	0.9	2.42×10^3	5.80×10^2	9.84	2.4	-
Hα	6562.8	1.12 $\pm$ 0.07	1.50 $\pm$ 0.26	37.6	1.9	4.62	1.11	11.1	2.7	65
He I λ6678	6678.2	1.16 $\pm$ 0.08	4.12 $\pm$ 0.45	0.22	0.01	3.68	0.94	8.86	2.3	76
He I λ7065	7065.2	1.14 $\pm$ 0.07	4.16 $\pm$ 0.39	0.29	0.02	7.06	1.81	17.0	4.35	49
O I λ8446	8446.36	1.06 $\pm$ 0.18	3.09 $\pm$ 0.90	0.41	0.02	2.42	0.6	5.83	1.5	100
Ca II λ8498	8498.0	0.95 $\pm$ 0.07	2.18 $\pm$ 0.38	1.12	0.06	3.00	0.78	7.23	1.9	87
Ca II 8542	8542.09	0.95 $\pm$ 0.08	2.13 $\pm$ 0.42	1.30	0.07	3.09	0.8	7.43	1.9	85
Ca II λ8662	8662.14	0.95 $\pm$ 0.09	2.20 $\pm$ 0.43	1.04	0.05	2.92	0.76	7.03	1.8	88

TABLE 5.8: Accretion luminosities, uncorrected mass accretion rates and relevant coefficients for the accretion tracers used in Section 5.7.2, including obscuration factors estimated for each permitted line (last column). The coefficients A and B are those obtained by Alcalá et al. (2014), except in the case of the [O I]λ6300 line where updated values from Nisini et al. (2018) are used.

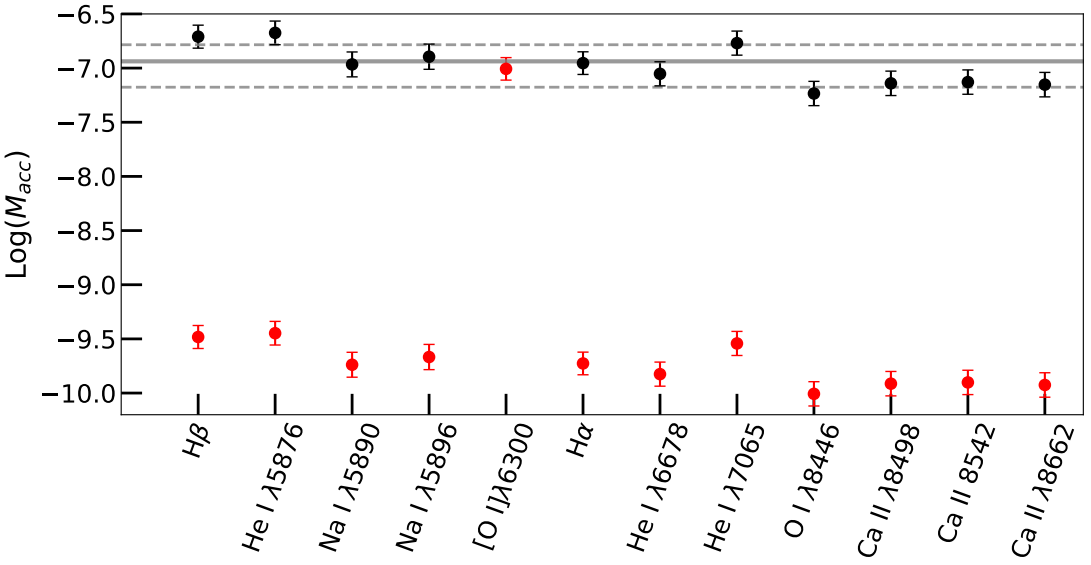

FIGURE 5.26: Mass accretion rates calculated from emission line tracers. Points in red show the calculated rates before correction for obscuration; points in black show the corrected accretion estimates, which are now closer to the accretion rate estimated using [O I]λ6300. The grey solid line shows the average accretion rate calculated from the corrected values and [O I]λ6300. The grey dashed lines mark the +/- 1-σ variation from the mean.

data make it possible to use both of these methods and we discuss them further in this section.

5.7.3.1 Method 1: Jet Density and Cross-section

Method 1 uses the estimate of the total density in the jet n_H, obtained using the BE method as described in Section 5.3.3. We further estimate the jet radius r at the same positions as half of the intrinsic jet FWHM. Corresponding to the sampling of the line spectra used in the BE diagnostics, we use the jet width estimated from Gaussian fitting of the jet cross-section at a 1" section centred at the knot positions in [S II] (as described in Chapter 3). This is however an assumption and may underestimate the jet radius if the emission is strongly peaked at the jet axis; we discuss the implications of this assumption later in this section.

The mass outflow rate is then given by

$$\dot{M} = \mu m_H n_H \times \pi r^2 v_j \tag{5.8}$$

Here $\mu = 1.25$, the average atomic mass, m_H the mass of the hydrogen atom, and v_j is the jet velocity as derived in Chapter 3. The width of the red-shifted jet ranges

from 0."9-1."2 at the knot positions, or 144-192 au at 160 pc; v_j = 270 km s^{-1}, and n_H from 2.4 × 10^3 cm^{-3} to 500 cm^{-3} between the knots.

The results are shown for the knot positions in Table 5.9, with the full set of measurements along the jet plotted in Figure 5.27. We obtain an average $\dot{M}_{out}$ of 7.5 × 10^{-9} $M_\odot$ yr^{-1} along the red-shifted jet knots. As the blue-shifted jet exhibits no [O I]λ6300 emission, the ionisation and hence total density could not be estimated using the BE method and we do not include results for this lobe.

This method is not affected by uncertainties in the reddening, however we consider uncertainties in the jet velocity, width, and the measured density. Due to the small inclination angle of the jet, the measurement of the velocity is dominated by the proper motions. These are well-constrained in the red-shifted lobe and so we take an uncertainty of +/- 0."05 or approximately 30 km s^{-1}, corresponding to an 11% uncertainty. We take a 10% uncertainty on the jet radius and 40% uncertainty on the jet density (see Section 5.3.3). Using error propagation this corresponds to an overall uncertainty of 40% on the estimated values of $\dot{M}_{out}$.

Additionally, it should be noted that this method assumes the cross-section volume is uniformly filled with gas at the estimated density, i.e. it has a filling factor = 1. This assumption may not hold as the jet travels farther from the source, but the regions of lower density included in the cross-section should be partly compensated for by regions of higher density than the [S II] doublet can trace.

5.7.3.2 Method 2: Forbidden Line Luminosity

The second method makes use of the proportional relationship between the luminosity of optically thin FELs and the mass of the emitting gas. This method is also described in detail in Hartigan et al. (1995). Briefly, $\dot{M}_{out}$ can be calculated as:

$$\dot{M} = \mu m_H \times (n_H V) \times v_t / l_t \tag{5.9}$$

where v_t is the tangential velocity measured from proper motions, and l_t the length of the sampled knot on the plane of the sky. The number of atoms in the emitting volume (i.e. the amount of emitting gas) n_H V is given by:

$$n_H V = L_{line} \times (h\nu A_i f_i \frac{X_i}{X} \frac{[X]}{[H]})^{-1} \tag{5.10}$$

where for a given transition, L_{line} is the emission line luminosity, A_i is the radiative rate of the transition, and f_i the fractional population of the upper level. X_i/X is the ionization fraction of the species and [X]/[H] its abundance with respect to hydrogen. For a given emission line this relationship can be simplified assuming solar abundances, so for [O I]λ6300 from Hartigan et al. (1995):

$$\mu m_H \times n_H V = 9.61 \times\ 10^{-6}\ \left(1 + \frac{n_{cr}}{n_e}\right)\left(\frac{L_{[OI]\lambda6300}}{L_\odot}\right) M_\odot \tag{5.11}$$

and

$$\dot{M} = 2.27\times\ 10^{-10}\left(1 + \frac{n_{cr}}{n_e}\right)\left(\frac{L_{[OI]\lambda6300}}{10^{-4}\ L_\odot}\right)\left(\frac{v_t}{150\ km\ s^{-1}}\right)\left(\frac{l_t}{2\times\ 10^{15}\ cm}\right)^{-1}\ M_\odot\ yr^{-1} \tag{5.12}$$

Agra-Amboage et al. (2009) gives an updated version of this equation which adopts a factor to account for ionisation so that:

$$\mu m_H \times n_H V = 9.61 \times\ 10^{-6}\ \left(\frac{1}{1-x_e}\right)\left(1 + \frac{n_{cr}}{n_e}\right)\left(\frac{L_{[OI]\lambda6300}}{L_\odot}\right) M_\odot \tag{5.13}$$

We give results for the latter method making use of the ionization factors estimated using the BE method. Hartigan et al. (1995) obtains an analogous equation for [S II]λ6731 assuming sulphur is all in S+ and in the high density limit, which has been modified by Bacciotti et al. (2011) to be applicable to values of n_e below the critical density:

$$\dot{M}_{out} = 4.51 \times\ 10^{9}\left(1 + \frac{n_{cr}}{n_e}\right)\left(\frac{L_{[SI]\lambda6731}}{L_\odot}\right)\left(\frac{v_t\ (km\ s^{-1})}{l_t\ (cm)}\right) M_\odot\ yr^{-1} \tag{5.14}$$

The estimates from both [S II] and [O I] are expected to be comparable, however [S II] luminosities are typically lower due to the lower abundance of S in comparison to O.

$\dot{M}_{out}$ was estimated using extinction-corrected fluxes of [O I]λ6300 and [S II]λ6731 sampled from 1" x 1" apertures centred at several positions along the red-shifted jet. The approximate length l_t is then 1" or 160 au. The tangential velocity is $v_t = 265$ km s^{-1} from the jet proper motions, with values of n_e determined from the BE results, as well as the ionisation which is ~ 0.6 in this lobe. Additionally, the presence of [S II]

doublet emission in the blue-shifted lobe allows n_e and $\dot{M}_{out}$ to be estimated in this jet using the [S II]λ6731 luminosity. Here $v_t = 360$ km s^{-1} from proper motions.

The results are tabulated in Table 5.9, with the full measurements shown in Figures 5.27 and 5.28 for the red- and blue-shifted lobes respectively. We find an average $\dot{M}_{out}$ of 8.8×10^{-9} $M_\odot$ yr^{-1} in the red-shifted jet from [O I] luminosity. With [S II] luminosity we find 6.6×10^{-9} $M_\odot$ yr^{-1} in the red-shifted jet and 0.2×10^{-9} $M_\odot$ yr^{-1} in the blue-shifted jet. This indicates a very large asymmetry between the lobes which is discussed further below.

This method implicitly takes into account the filling factor of the jet within the sampled aperture. However, uncertainties may arise due to the assumed distance, extinction, and the measured n_e and x_e derived from the BE method - the latter value has a strong impact on the value of $\dot{M}_{out}$ derived from the [O I] line in specific. The dominant consideration however is the uncertainty on the line fluxes, not only as this determines the estimated line luminosity but also affects the estimates of n_e and x_e derived from the optical line ratios. Propagating the uncertainty of 5% in the relevant line fluxes as well as the uncertainty in n_e, we obtain uncertainties of 50% and 25% for $\dot{M}_{out}$ derived from the [O I]λ6300 and [S II]λ6731 line luminosities, respectively.

5.7.4 Discussion

How do these estimates of $\dot{M}_{out}$ compare to previous results for Th 28? In the red-shifted jet, the average values of 6.5 - 8.8 $\times$ 10^{-9} $M_\odot$ yr^{-1} compare reasonably well to the estimate of 1.2 $\times$ 10^{-8} $M_\odot$ yr^{-1} by Coffey et al. (2008), and looking at the knot closest to the source, M4, we find even better agreement with values of 0.92 - 1.26 $\times$ 10^{-8} $M_\odot$ yr^{-1}. As shown in Table 5.10, when combined with our estimate of $\dot{M}_{acc}$ = 1.15 $\times$ 10^{-7} $M_\odot$ yr^{-1}, the averaged values give efficiencies of 0.06-0.08 (increasing to $\sim$ 0.1 if we take $\dot{M}_{out}$ from the first knot only).

Typically values of $\dot{M}_{out}$ derived from Method 1 are expected to be larger than values obtained via line luminosity; however that is not the case here and the estimates obtained using both methods are similar along the jet. Additionally the mass flux from Method 1 is expected to be roughly constant along the jet axis with the drop in n_H compensated by the increasing jet radius; however this is also not the case and the mass flux from this method decreases similar to the values determined from the luminosity. This may be due to sideways losses of mass channelled outward by the internal working surfaces of the jet, leading to a drop in density along the jet as observed in the from the BE method results in Section 5.3.3. It is also possible that if the gas recombines and cools, this may increase the proportion of neutral gas which is not traced by the

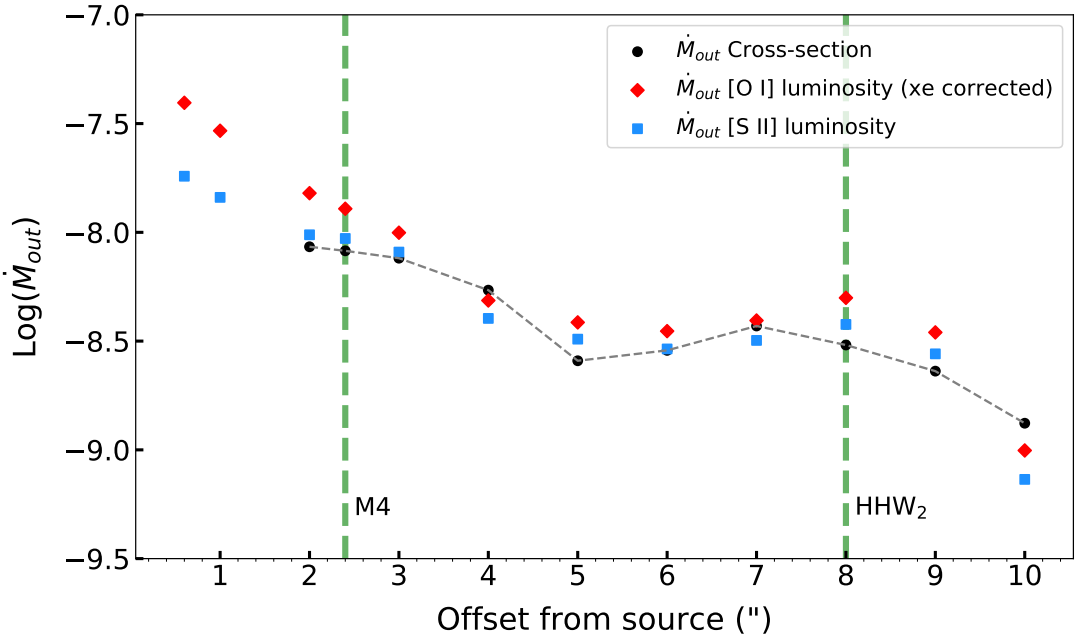

FIGURE 5.27: Mass outflow rates estimated along the red-shifted jet using the three methods described in Section 5.7.3. The apparent drop in the mass outflow rate along the jet axis may be due to sideways losses of material due to the internal working surfaces of the jet.

emission lines; however, the same results do not see a significant drop in temperature along the jet axis.

In the blue-shifted jet, we can only draw a comparison using the [S II] luminosity, but this corresponds well with the other measures of $\dot{M}_{out}$ in the red-shifted lobe. However, the averaged $\dot{M}_{out}$ across the knot positions is just 0.2×10^{-8} $M_\odot$ yr^{-1}, which gives a far lower ratio to the mass flux in the red-shifted lobe than the 1:2 ratio estimated by Coffey et al. (2010). This is in spite of the fluxes used being corrected for differential extinction, which was not the case in the previous study. The blue-shifted lobe is nevertheless much fainter; it is also much less collimated and characterised by bow shocks, as discussed in Chapter 3. This can lead to a drop in apparent mass flux if the jet width increases beyond the sampling aperture, or if there is significant loss in mass due to large bow shocks (Podio et al., 2006).

If we attempt to compare the two jet lobes as close to the base as possible to reduce the impact of bow shocks, and sample the [S II] luminosity at +/- 1" from the source, then indeed we find nearly identical values of $\dot{M}_{out}$ at $\sim 1.4 \times 10^{-8}$ $M_\odot$ yr^{-1}. However, inspection of the spectra shows that this is because at this distance, the emission from the blue-shifted lobe is dominated by the scattered red-shifted emission, so that at both positions we are essentially estimating the flux from the red-shifted lobe.

	$\dot{M}_{out}$ ($\times 10^{-9}$ $M_\odot$ yr^{-1})					
	Red-shifted Jet			Blue-shifted Jet		
Method	M4	HHW_2	Avg.	M3	M2	Avg.
Cross-section	8.2	3.0	5.6			
$L_{[OI]\lambda6300}$	12.8	5.0	8.9			
$L_{[SII]\lambda6731}$	9.4	3.8	6.6	0.34	0.05	0.2

TABLE 5.9: Outflow rates for the red and blue-shifted jet lobes.

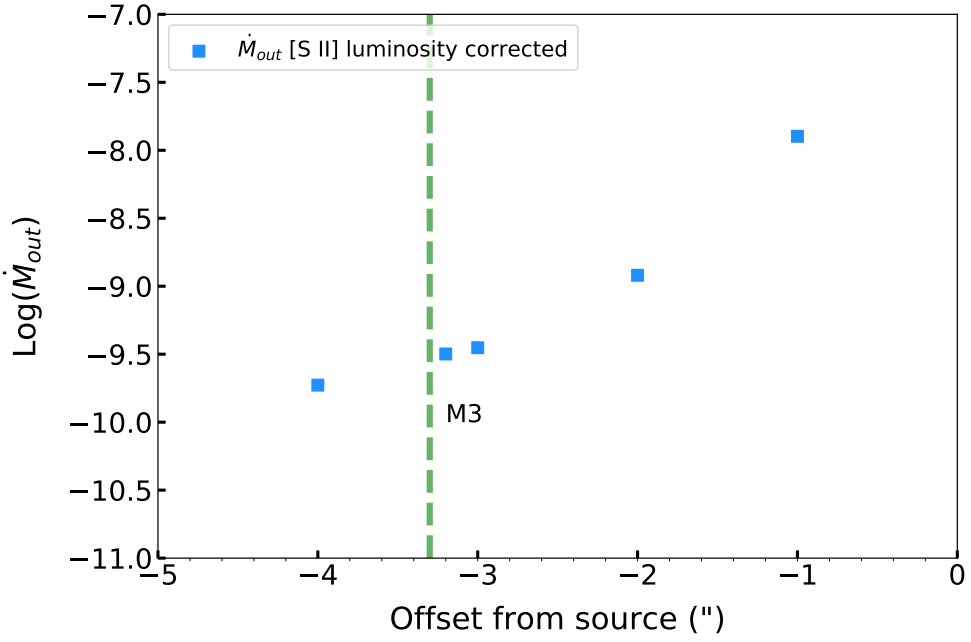

FIGURE 5.28: Mass outflow rates estimated along the blue-shifted jet using [S II]λ6731 luminosity (see Section 5.7.3.2).

The ratio of $\dot{M}_{out}$ derived from the line luminosity to that derived from the jet density can also provide a valuable check on our estimates of the jet radius. As the filling factor of the jet should be at most 1, $\dot{M}_{out}$ should be approximately the same derived using both methods; imposing this constraint we can determine the effective radius of the jet (i.e. the radius required to produce the line luminosities observed. The calculated ratio is plotted in Figure 5.29. Overall this is roughly constant along the jet between about 1.1 to 1.6 particularly in the [O I] measurements. We derive the effective radius first from the [S II]λ6731 luminosity since the jet width is estimated in the same line, and find that the effective radius (and hence width) of the jet is at most 5-10 % higher than the estimates derived in Section 3.2. Making the same estimate with the [O I]λ6300 line luminosity yields an effective jet radius approximately 15 % higher than estimates from the Gaussian fitting.

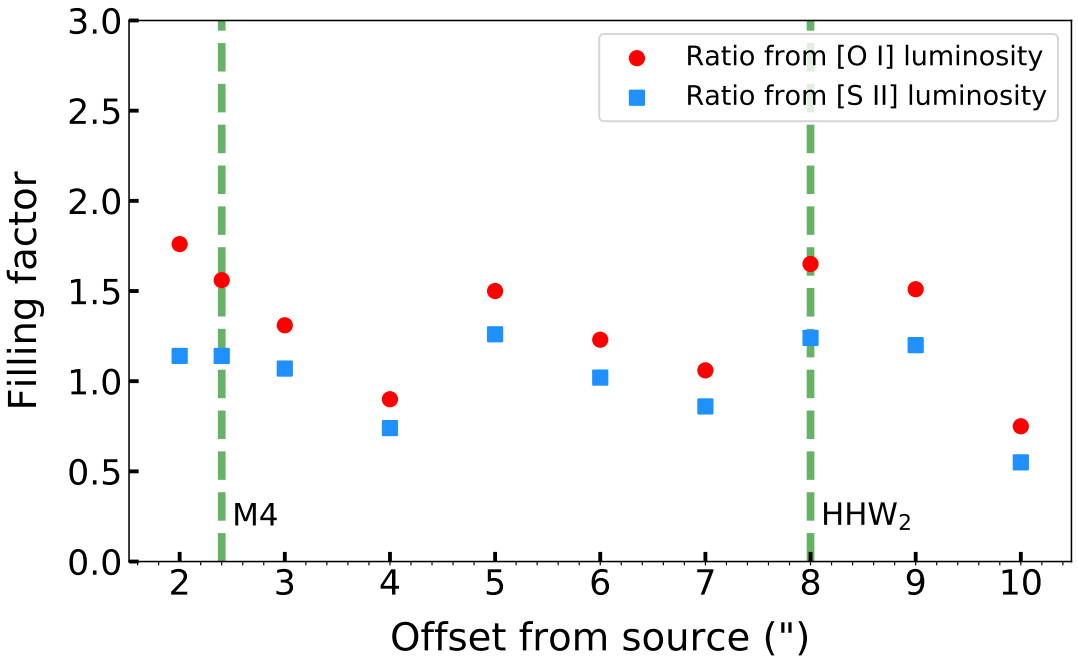

FIGURE 5.29: Filling factor estimated along the red-shifted jet.

	Red-shifted Jet		Blue-shifted Jet	
Method	$\dot{M}_{out}$ ($\times$ 10^{-9} $M_\odot$ yr^{-1})	$\dot{M}_{out}/\dot{M}_{acc}$	$\dot{M}_{out}$ ($\times$ 10^{-9} $M_\odot$ yr^{-1})	$\dot{M}_{out}/\dot{M}_{acc}$
Cross-section	5.6	0.049		
$L_{[OI]\lambda6300}$	8.9	0.077		
$L_{[SII]\lambda6731}$	6.6	0.057	0.2	0.002

TABLE 5.10: Jet efficiencies estimated for the red- and blue-shifted jet lobes.

5.8 Summary

- In this chapter we review previous diagnostic results for the physical conditions in the Th 28 jet, including previous applications of the BE diagnostic method for deriving n_e, x_e, T_e and n_H from optical emission lines.

- We carry out a diagnostic study with an updated form of the BE diagnostic code for points sampled along the red-shifted jet axis and compare the results with the previous values obtained for this jet in Bacciotti & Eislöffel (1999). Our results show similar trends along the jet in n_e, x_e, T_e and n_H to the previous investigation, with similar estimates for the jet temperature and slightly higher ionisation fractions compared to the previous results.

- We make use of the Balmer lines Hα and Hβ to estimate the average extinction in the Th 28 jet. We find A_v of 2.5 mag at the source position, with 2.1 mag in the blue-shifted jet lobe and 0.6 mag in the red-shifted jet lobe. Uncertainties of $\pm$ 0.3 mag are estimated on the A_v values found in each region.

- We obtain spatial and PV maps for optical line ratios which trace the density and excitation conditions within the jet, and find that the blue-shifted jet shows higher n_e as well as x_e compared with the red-shifted jet lobe. We also examine line ratios of [Ca II], [Fe II], [Cr II] and [Ni II] to map the relative depletion of refractory species along the jet axis.

- The mass accretion rate of Th 28 is estimated using emission lines at the source position, with an average value obtained of $\dot{M}_{acc} = 1.15 \times 10^{-7}$ $M_\odot$ yr^{-1}. A comparison of $\dot{M}_{acc}$ estimated from permitted lines with the unobscured [O I]λ6300 line gives an estimated obscuration factor of 71.

- The mass outflow rate in the red-shifted jet is estimated using both the estimated jet density and cross-sectional area, and the luminosity of the [O I]λ6300 and [S II]λ6731 lines, yielding average values of $\dot{M}_{out}$ = 6-9 $\times 10^{-9}$ $M_\odot$ yr^{-1}, decreasing with distance along the jet. Combined with the estimated value of $\dot{M}_{acc}$ this gives efficiencies of 0.08-0.08 in the red-shifted jet lobe. The mass flux in the blue-shifted jet lobe can only be estimated from the [S II]λ6731 luminosity; due to the low luminosity of the line we find $\dot{M}_{out} = 0.2 \times 10^{-9}$ $M_\odot$ yr^{-1}.

Chapter 6

Conclusions and Future Work

Protostellar jets and outflows are an important window into processes of star formation, the evolution of protoplanetary disks, and the feedback between newly forming stars and their surrounding clouds. Optical and NIR studies allow us to capture many of the main emission lines tracing atomic jets and shocks, and to carry out detailed diagnostics relating to the internal physical conditions of the jet as well as the shocks formed where it interacts with the surrounding medium.

IFS instruments have proven a key tool in studying jets due to their ability to provide a 3D view of jets, simultaneously encompassing both spatial details along the extended jet region and spectral information concerning multiple emission lines and velocity components of the jet. This has been further enhanced in recent years, both by technological advances enabling IFS instruments with broader spatial and spectral ranges, and the advancement of AO techniques to the optical regime. Together these have enabled high spatial resolution IFS observations along larger portions of extended jets, allowing the details of different jet regions to be examined in multiple emission lines at once.

The MUSE instrument exemplifies these advancements with its broad spatial and spectral range and AO-enhanced spatial resolution. The major goals of this project were therefore twofold. Firstly, to make use of MUSE WFM observations to investigate the asymmetric jet of the CTTS Th 28 close to the source, taking advantage of the system geometry (with the jet in the plane of the sky) and the large FOV of MUSE to simultaneously characterize the morphology, kinematics and physical conditions of both jet lobes. Second, we aimed to use this study as a stepping stone to explore the potential of MUSE for jet studies and to develop Python tools which facilitate analysis of jet observations. In this final section we review the overall findings of this work and the avenues they suggest for future research.

6.1 Review of the Findings

6.1.1 The Morphology and Kinematics of Th 28

The first part of this work (Chapter 3) concerned the overall morphology of the jet, in particular the inner jet region within about 20" of the source in each lobe. As highlighted in Table 3.1, we identify the jet in a broad array of emission lines, of which a full spectro-image catalogue is given in Appendix A.1. Of particular note are the [O III]λ5007 emission in the blue-shifted jet, indicating high excitation and fast shocks ($>$ 90 km s^{-1}), as well as He I emission primarily in the red-shifted jet lobe.

Lines of refractory species including Fe^+ and Ca^+ are also observed in the jets, some of which extend as far as 8" in the red-shifted lobe. This highlights the value of the large FOV and the spatial information, since the [O III] line in particular has previously not been associated with the jet in Th 28. Similarly we are able to identify numerous emission lines in the bow shock HHW which is within the FOV (illustrated in Figure 3.3).

The large FOV furthermore allows the morphology of both jet lobes to be elucidated. Their asymmetry in collimation and brightness has been noted in previous studies; here we can show that the blue-shifted jet exhibits bow shock structures with swept-back wings within 10" of the source, which combined with the faintness of this lobe may contribute to its apparently low collimation and large opening angles estimated (including in this study), relative to the red-shifted counter-jet.

We identify three new knots in each lobe, making six in total, as well as measuring the position of the previously identified HHW_2. Combining this with available X-Shooter data we are able to estimate proper motions for the two innermost knots and show that these are asymmetric close to the source; we further obtain radial velocities for all of our identified knots and show that these are consistent with previous estimates for HHW and HHW_2 as well as the more distant HH objects in the outflow. From the proper motions, we also show that the ages of the knots on each side of the source suggest the knots are ejected in pairs at similar times in each lobe.

The MUSE datacube equally allows us to prepare a catalogue of the observed emission lines as PV maps; this is provided in full in Appendix A.5. We can thus investigate the velocity components of the jet in all emission lines and spatial regions; although there is limited kinematic information to be obtained in the Th 28 jet due to its inclination, this also highlights the radial velocity asymmetry between the jet lobes, as well as the significant component of scattered emission from the bright red-shifted jet which is seen close to the source on the eastern side (i.e. the same side as the blue-shifted jet).

6.1.2 Precession In the Jet

The major result of our morphology investigation was the detection of a small-scale 'wiggling' in the jet centroids, first observed in the brighter red-shifted jet and verified by comparison of the signature in multiple emission lines and velocity channels. This is best observed in the [N II]λ6583 emission which traces preferentially the fast inner flow of the jet.

Further investigation (Chapter 4) shows that this wiggling is a precession signature with a distinct point-symmetry between the two jet lobes. The deprojected jet can be fitted with a precessing jet model based on that given in Anglada et al. (2007), which accounts for the difference in jet velocities between the two lobes. The fitted model gives a precession period of 7.9 years and precession angle 0.6°, corresponding to length scales of 2."8 and 3."5 in the red- and blue-shifted lobes, respectively.

We show that this precession could be caused by an unresolved BD companion within a broken disk with mass $\leq$ 70 M_{Jup} and separation $\leq$ 0.3 au, with an orbital period of 45 days. Allowing for reasonable uncertainties in distance to the jet and estimated jet velocities does not significantly impact this result. We will discuss the implications of this result further in Section 6.2.

6.1.3 Diagnostic Study of Th 28

The last section of this thesis (Chapter 5) turns our attention to the diagnostic potential of the MUSE data. The array of catalogued emission lines in the jet allows us to examine numerous emission line ratios which trace the density and excitation properties within the jet as well as the bow shock HHW. For the first part of this diagnostic study we made use of the BE technique, a well-tested method for ascertaining the n_e, x_e, T_e and n_H in typical jet regions.

We applied an updated version of the BE code to spectra extracted along the red-shifted jet axis as well as the axis of HHW, as a test of the code and a first estimate of the jet properties. In the red-shifted jet we find n_e = 8000-300 cm^{-3}, x_e = 0.1-0.65, $T_e \sim 2 \times 10^4$ K and $n_H = 5 \times 10^4$ cm^{-3} to 300 cm^{-3}. In HHW we find $n_e \sim 200$ cm^{-3}, $x_e \sim 0.6$, $T_e \sim 2 \times 10^4$ K and $n_H \sim 300$ cm^{-3}. Compared with previous results obtained for this jet using the BE method (Bacciotti & Eislöffel, 1999) the red-shifted jet parameters are quite similar, but a sharp drop in density and increase in estimated temperature and x_e for HHW. This difference cannot be well attributed to the higher spatial resolution of the MUSE data. It is likely to reflect improvements in the code

used to analyse the line ratios, as well as possible changes in the conditions of the jet over time.

A second approach to analysing the jet conditions is to map the line ratios along the jet in both channel maps and position-velocity space. We carried this out for a number of diagnostic ratios, as a preliminary step to applying the BE code to produce similar maps of the jet density and excitation. In contrast to the BE code, these ratio maps currently only allow *relative* variations of n_e, x_e and T_e to be shown in a given map. We can similarly explore the relative depletion of the refractory elements Ca, Fe and Ni by making use of ratios involving these lines.

The main finding from these maps is an agreement with previous studies suggesting higher n_e and higher excitation (x_e, T_e) in the blue-shifted jet relative to the red-shifted jet. Our transverse PV maps of the line ratios do not reflect the spatial asymmetry in density found by Coffey et al. (2008) in the red-shifted jet; however this is likely due to the much higher spatial resolution of their data. Curiously, the [S II]λ6716/[S II]λ6731 line ratio suggests a higher n_e in higher velocity channels of the red-shifted jet, the opposite pattern to that suggested by the other ratio maps tracing n_e. Further investigation is needed to understand this effect and to obtain numerical estimates of the jet density, ionisation and temperature from these line ratios, as well as to estimate the absolute values of the refractory species depletion.

The array of emission lines detected close to the source also included a number of accretion tracers, both permitted lines and the FEL [O I]λ6300. Estimating the mass accretion rate $\dot{M}_{acc}$ in Th 28 has historically proved challenging due to the poorly constrained extinction and the obscuration by the edge-on disk. We used the measured Balmer decrement in both jet lobes as well as at the source position to estimate the extinction in each of these regions. In the source region we find $A_v = 2.1 \pm 0.3$; we therefore used this estimate to deredden our line fluxes. We estimated $\dot{M}_{acc}$ using the luminosity of the relatively unobscured line [O I]λ6300, using the relationship given by Nisini et al. (2018). We then compared this with the values of $\dot{M}_{acc}$ obtained using the other line fluxes to obtain an estimate of the obscuration factor ~ 70, with the average estimate of $\dot{M}_{acc}$ found to be 1.15×10^{-7} $M_\odot$ yr^{-1}, comparable with typical accretion rates for CTTSs.

We can further combine this estimate of $\dot{M}_{acc}$ with estimates of the mass outflow rate $\dot{M}_{out}$ in each jet lobe. In the red-shifted jet we estimate this using first the estimated density and cross-sectional radius of the jet along its axis, and then using the line luminosities of [O I]λ6300 and [S II]λ6731. From these methods we obtain $\dot{M}_{out}$ = 6-9 $\times 10^{-9}$ $M_\odot$ yr^{-1}, indicating a jet efficiency of 0.05-0.08. This is significantly lower than the 0.2 one-sided efficiency obtained by Coffey et al. (2010), and more in line with typical

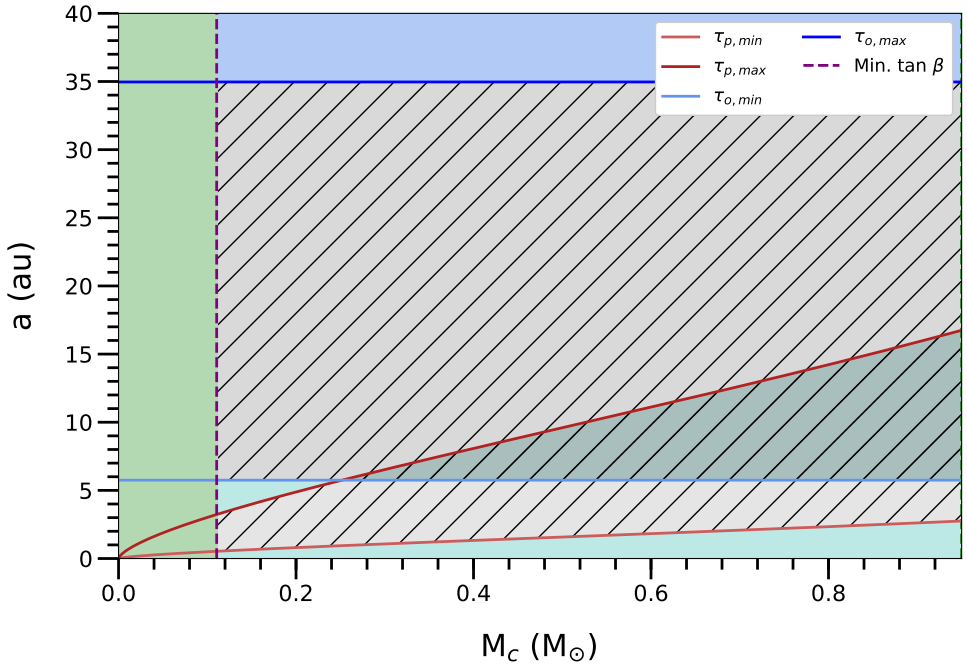

FIGURE 6.1: Constraints on a possible companion in HD 163296, based on measured jet velocities and observations by Kirwan et al. (in prep.)[1]. Parameter space of the possible companion ranges that are expected to produce a detectable wiggling in the HD 163296 jet axis. The grey hatched regions indicate parameter regions excluded by our observations (where a companion would be likely to cause a wiggling due to either orbital motion or precession, corresponding to the upper and lower hatched regions, respectively). The region shaded in green (left) contains companion objects which would produce a wiggle opening angle too small to detect in our observations; the regions shaded in blue (top) and light blue (bottom) give companions with wiggling period too long or short, respectively, to be observed in these data.

jet efficiencies of ~ 0.1. The blue-shifted jet, of course, poses more difficulty, due to the lack of [O I]λ6300 emission or density estimates (as this lobe could not be included in the BE method analysis). We therefore use only the [S II]λ6731 luminosity and obtain $\dot{M}_{out}$ of 0.2×10^{-9} $M_\odot$ yr^{-1}, implying an efficiency of 0.002. This is far lower than the estimate for the red-shifted lobe, suggesting a much greater asymmetry in mass outflow than the 1:2 ratio found by Coffey et al. (2010). This may be simply a result of the faintness in the blue-shifted jet, but shows that constraining the asymmetry in the mass-loading of these jet lobes is still challenging. Much work remains to comprehensively analyse the wealth of diagnostic information contained in the MUSE data, as will be discussed below.

6.2 Precessing Jets: A Window on Planet Formation?

The most striking result of this study is the detection of a small-scale precession in the Th 28 jet, with a period of 8 years and a half-opening angle of 0.6°. This may be an alternative cause of the rotation signatures previously detected in this jet, and suggests a BD companion at ≤ 0.3 au. In tandem with recent detections of similar small-scale wiggling (on lengths of a few arcseconds) in DO Tau and HH 211 (Lee et al., 2009, 2010; Erkal et al., 2021), this raises the possibility of using jet wiggling detected close to the source to detect companion objects in the inner protoplanetary disk, especially in sources such as Th 28 where the inner disk and star are obscured.

Conversely, we can consider whether similar reasoning can be used to constrain possible inner disk companions in jets where no wiggling is detected. As an example we can consider HD 163296, a 1.9 $M_\odot$ Herbig Ae star which has been the focus of numerous studies seeking to constrain possible companions within the disk (Grady et al., 2000; Isella et al., 2016; Teague et al., 2018; Pinte et al., 2018). The bipolar jet from this star has been observed with MUSE WFM, and examination of the jet centroids indicates no sign of systematic wiggling within 20 arcseconds and with an opening angle greater than 0.2° (Kirwan et al., in prep.). Based on this finding we may construct a counterpart plot to Figure 4.17. for HD 163296, showing the companion masses and separations which would be expected to cause a detectable wiggling in this data, in either the orbital motion or precession cases. This plot is shown in Figure 6.1[1]. We note here that the presence of a detectable precession would depend on the companion orbiting at a significant inclination to the disk; as this is not necessarily so, the bounds derived for this case do not exclude a *non*-inclined companion in that region.

An additional caveat is that in these observations, the jet is not traced to the source within 5" due to instrument saturation; since we know from the case of Th 28 that the precession signature can be rapidly distorted after about 1000 au (6" at the distance of Th 28), this analysis does not exclude the possibility of wiggling close to the source that is distorted or disrupted by the shocks in the jet. However a search for measurable jet wiggling may present an additional test for the presence of close companions, especially where it can be shown that the expected companion parameters are likely to have this effect.

Several questions remain open, however. The first is simply whether the precession signature in Th 28 can be shown to be consistent over time and further sub-arcsecond

[1]This plot is provided as part of the author's contribution to Kirwan et al. (in prep.) but this work is not included in this thesis.

resolution observations are needed to clearly show that the ∼2" length wiggling is independent of any unresolved shocks in the micro-jet regions. Another important question is highlighted by Erkal et al. (2021) in the case of DO Tau. They propose that a disk warp (Lai, 2003) rather than a companion might be the source of the detected precession, and note that the expected period in such a scenario is < 10 years. This condition would also apply to Th 28, and distinguishing the disk warp scenario from an inner disk companion would be difficult without high-resolution observations of the inner disk. Additionally, observing a wider sample of precessing jets close to the source at different inclinations might allow us to determine whether precession can be linked to either or both scenarios. If jet precession is caused by a disk warp, this may itself be a useful probe of the inner disk which is otherwise difficult to image. We might ask further if such indications of warping can provide insight into asymmetries within the jet launching regions of the disk, as an indication of differing conditions on each side of the disk.

An additional open question concerns the significance of the apparent curving in the large-scale HH flow associated with Th 28. We conclude in Chapter 4 that this is most likely due to interactions with the surrounding environment and unlikely to be connected with the precession close to the source. This is consistent with both our observations and simulations of precession jets (Masciadri & Raga, 2002) which show the precession signature is quickly altered by the effects of drag and shocks. It therefore seems unlikely that any wiggling would survive to parsec-scale lengths in the Th 28 jet. On the other hand, we can consider the possibility that this could represent a longer-term precession (or orbital motion) in the jet.

This also suggests that caution should be exercised in other cases where an apparent jet precession is determined from large-scale HH patterns, especially if the curvature of the precession is not clearly traced. The significance of wiggling jet trajectories has to be carefully evaluated in each case to disentangle a motion of the jet axis from other effects, and as we have discussed, more information is needed about the possible causes of jet wiggling.

6.3 The Asymmetries of Th 28

The asymmetric nature of Th 28 has previously been observed in morphology, jet velocities and excitation properties. In many ways our MUSE data confirms these properties: we show the asymmetry in the jet radial velocities and proper motions, a possible asymmetry in inclination angle, and indications from FEL emission that the blue-shifted jet

lobe has higher excitation than the red-shifted jet. The data here traces these asymmetric properties from distances of $\sim$ 20" to within 1" of the source, consistent with spectral analyses by Coffey et al. (2010) and Liu et al. (2014).

With the MUSE observations we can observe the morphological asymmetries in much more detail than previously, showing that the lower collimation of the blue-shifted jet may be in part due to the presence of wide bow shocks within 10" of the source. That these asymmetries can be traced so close to the source, before there is likely to be much interaction with the surrounding environment, suggests they may be intrinsic to the jet launching on each side. On the other hand, the higher extinction in the blue-shifted jet might suggest that it is propagating into a denser environment.

Along with these asymmetries, this work also highlights some symmetries in the two jet lobes. For example, we see the apparent synchronicity in knot ejection on each side of the jet, based on their proper motions and positions. Additionally, the precession of the jet axis is detected by a striking point symmetry between the jet centroid positions on each side of the source. Unlike in the case of DO Tau (Erkal et al., 2021), there is not a substantial difference in precession angle suggesting that the jet lobes may differ in their launching radius. The precession in Th 28 can be fitted with a single solution for the precession angle and period, with the major difference between the two lobes being attributable to their differing velocities. The change in direction of the jet axis over time seems to be the same on both sides.

In attempting to compare the two lobes of the Th 28 jet, the major challenge is to understand the blue-shifted jet. Despite the extent of this jet which is spatially within view, it remains elusive due to its faintness, and especially the lack of [O I]λ6300 emission makes it more difficult to assess using the typical optical emission line ratios. Of particular interest would be determing better constraints for the mass outflow in this jet: as discussed above, we obtain far lower $\dot{\mathrm{M}}_{\mathrm{out}}$ in this jet than obtained by previous estimates obtained via IR [Fe II] lines, while the red-shifted jet shows $\dot{\mathrm{M}}_{\mathrm{out}}$ typical for a CTTS. Further study is required to understand the physical conditions in the blue-shifted jet, and the mass loading in this lobe relative to the red-shifted jet.

6.4 Prospects for Future Work

Much work can yet be done with the vast amount of spectral information contained within the MUSE data of Th 28. The next goal of the diagnostic study will be to combine the ratio maps and the updated BE method code in order to create parameter maps of n_e, x_e, T_e and n_H in the red-shifted jet. Using the full range of the MUSE kinematic

information, we can also create longitudinal and transverse PV maps of these parameters to quantitatively estimate the density and excitation parameters in the different spatial and kinematic regions of this jet. This will allow us to look more carefully for potential spatial asymmetries in the jet such as the asymmetry in n_H reported by Coffey et al. (2008).

A second step is then to expand the number of diagnostic lines which we can use to quantify the density and excitation of the two jets, using the line ratios explored in Chapter 5. This will provide an important point of comparison with the values obtained with the BE code, which are applicable primarily to regions below the [S II] critical density limit and cannot be used for the blue-shifted lobe. In conjunction with this, we can attempt to quantify the refractory species depletion in the jet. The dust content of Th 28 is relatively unexplored, but our spectro-images and PV maps show that [Fe II] and [Ca II] lines extend through a significant portion of the red-shifted jet and are even seen in the bow shock HHW. The depletion of Fe especially can impact on the relative values of $\dot{M}_{out}$ obtained from Fe line luminosity when compared with those obtained with optical emission lines on non-refractory species. Depletion estimates would thus help to clarify constraints on the outflow rate and jet efficiency.

The third main goal of the diagnostic investigation is to analyse the bow shock HHW. While not a major focus of the work shown in this thesis, we demonstrate that it shows emission from quite a few emission lines (Figure 3.3) and its diagnostic properties are only briefly touched on in Chapter 5. The [O III] emission seen in this jet indicates a fast $v\_shock > 90$ km s^{-1}, but our analysis with the BE method shows significantly lower ionization and density in HHW compared with previous observations. A more detailed analysis of the shock conditions in this jet can fully exploit the detailed morphology and emission spectrum captured by the MUSE observation.

We can further combine the MUSE diagnostic results with those obtained with the available X-Shooter data, which cover approximately ±4" around the source. This will strengthen the analysis by allowing us to compare the estimated extinction and physical conditions, as well as accretion and outflow rates. Future versions of the BE analysis technique are currently in development which will further extend the code to include line ratios applicable, for example, in regions with densities above the [S II] limit. The Th 28 dataset will therefore be used to test future iterations of the code and compare the results with those currently obtained.

Beyond existing data, higher resolution observations of the Th 28 jet within about 10" of the source on each side could help to trace whether the precession signature can be more clearly detected in the jet morphology. Comparison of the current data with several years between observations (currently it has been 8 years since the MUSE data

was collected) would help to trace whether the precession pattern moves outward as a coherent pattern, as expected if it is due to a true precession of the axis, and rule out the influence of unresolved shocks which might impact the observed point-symmetry of the jet lobes.

On a larger scale, the increasing use of high-resolution IFS observations to study jets is making it more and more feasible to search for such small-scale wiggling close to the jet source. Comparison of detected signatures among a larger sample may help to discern whether they are more likely to be linked to inner-disk companions, or if they are linked by other factors which might favor a warping of the inner disk.

6.5 Jet Studies with MUSE

This project has demonstrated that MUSE is an extremely powerful instrument for characterizing jets, capturing a broad swathe of spatial, kinematic and spectral information in one observation. The broad array of emission lines within its wavelength range allow us to trace morphological features such as shock, collimation, and jet precession which may each be highlighted better in different emission lines, and correlate the appearance of these features at different wavelengths (checking, for example, whether they appear consistently in multiple emission lines).

Furthermore, this wealth of spectral information makes an array of diagnostic line ratios available for investigation, tracing the physical conditions and even dust destruction within the jet across different density regimes and kinematic components. We can also estimate mass accretion and outflow using a variety of emission line signatures contained within the MUSE spectral range. The large FOV makes it possible to trace the evolution of both morphological and kinematic features along the jet, tracking the consistency of proper motions and radial velocities and showing how shocks and environmental interactions can alter the appearance at the jet with distance from the source. Likewise this makes it possible to compare the physical conditions across different regions, for example comparing the extinction of the jet between both lobes simultaneously.

All of this information is valuable to understand the properties of the jet and how it can be linked to the star-disk system from which it originates. Since the start of this work, the MUSE NFM and AO correction modes have come into operation, offering sub-arcsecond spatial resolution which will enable detailed observations of jets within a few 100 au of their source, a critical region to observe in order to trace the jet before it is altered by shocks or drag. The importance of MUSE and other IFS observations is likely to only increase in the future. A goal of this project was to develop Python

tools to facilitate the analysis of these observations, and as discussed in Chapter 2 the *museclasses* package and associated functions were accordingly created and developed to facilitate the analysis in this work.

Since then, the *MUSE Python Data Analysis Framework* (MPDAF) has independently been developed by the MUSE consortium to provide a Python package for MUSE data analysis. This package is not specifically tailored to facilitate jet observations, and so part of the future development of our own package should be to consider how it can be synergized with the MPDAF framework, so as to focus future iterations of our museclasses package on adding efficient and user-friendly functionality for jet research; for example, in interfacing with the diagnostic codes under development for analysis of jet emission line ratios.

6.6 Conclusion

The study of stellar jets has advanced greatly with the advent of IFS techniques to observe jets at optical and IR wavelengths. This work shows how MUSE observations make it possible to investigate jets in exceptional detail, observing features such as precession in the Th 28 jet which have never before been identified and opening up a wealth of optical emission lines for study which trace many different aspects of the asymmetric jet structures and physical conditions. Much work can yet be done to exploit this rich dataset as well as newer MUSE observations of stellar jets, especially with the addition of AO modes to increase the MUSE spatial resolution. The detection of small-scale precession in Th 28 and other stellar jets equally presents intriguing possibilities to trace the structures or even unseen small companions within the inner circumstellar disk. The avenues for future work in these areas appear challenging and exciting in equal measure.

Appendix A

Spectro-Image Catalogue

A.1 Spectro-Images

This section contains a full spectro-image atlas of the rotated, non-deconvolved emission lines detected in the Th 28 micro-jets. Note that continuum subtraction has been carried out. The figures cover an approximate range of - 10" to +15" from the source along the jet axis. The jet spectro-images were binned into three velocity channels: a high-velocity blueshifted bin from -200 to -90 km s^{-1}, a central low-velocity channel at +/- 90 km s^{-1}, and a high-velocity red-shifted channel from +90 to +200 km s^{-1}.

While several of the knots discussed in Chapter 3 fall outside this range, these are visible only in Hα and other emission lines for which more detailed PV maps and spectro-images are given within that chapter. All contours are plotted on a log scale beginning at the 3-σ level, with the exception of the Hα line: this is given with contours beginning at 4-σ to reduce noise in the image. For the same purpose, the images are smoothed by a factor of two.

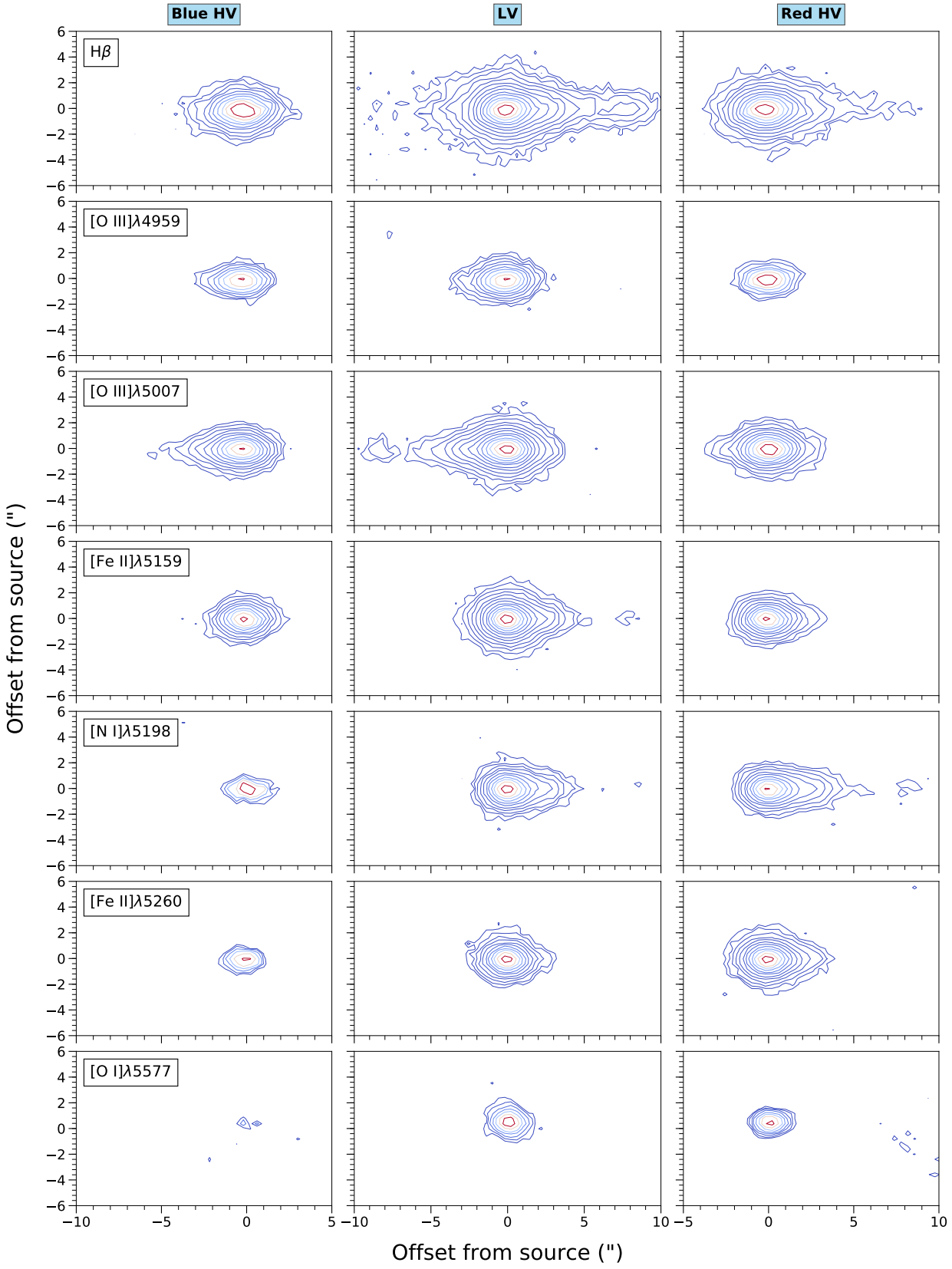

FIGURE A.1: Spectro-images showing the Th 28 jet emission in optical emission lines. Contours begin at the 3-σ level, with adjacent contours increasing as a factor of $\sqrt{3}$. Left, the blue-shifted emission (-200 to -90 km s^{-1}). Centre: the central velocity bin (-90 to +90 km s^{-1}). Right: the red-shifted emission (+90 to +200 km s^{-1})

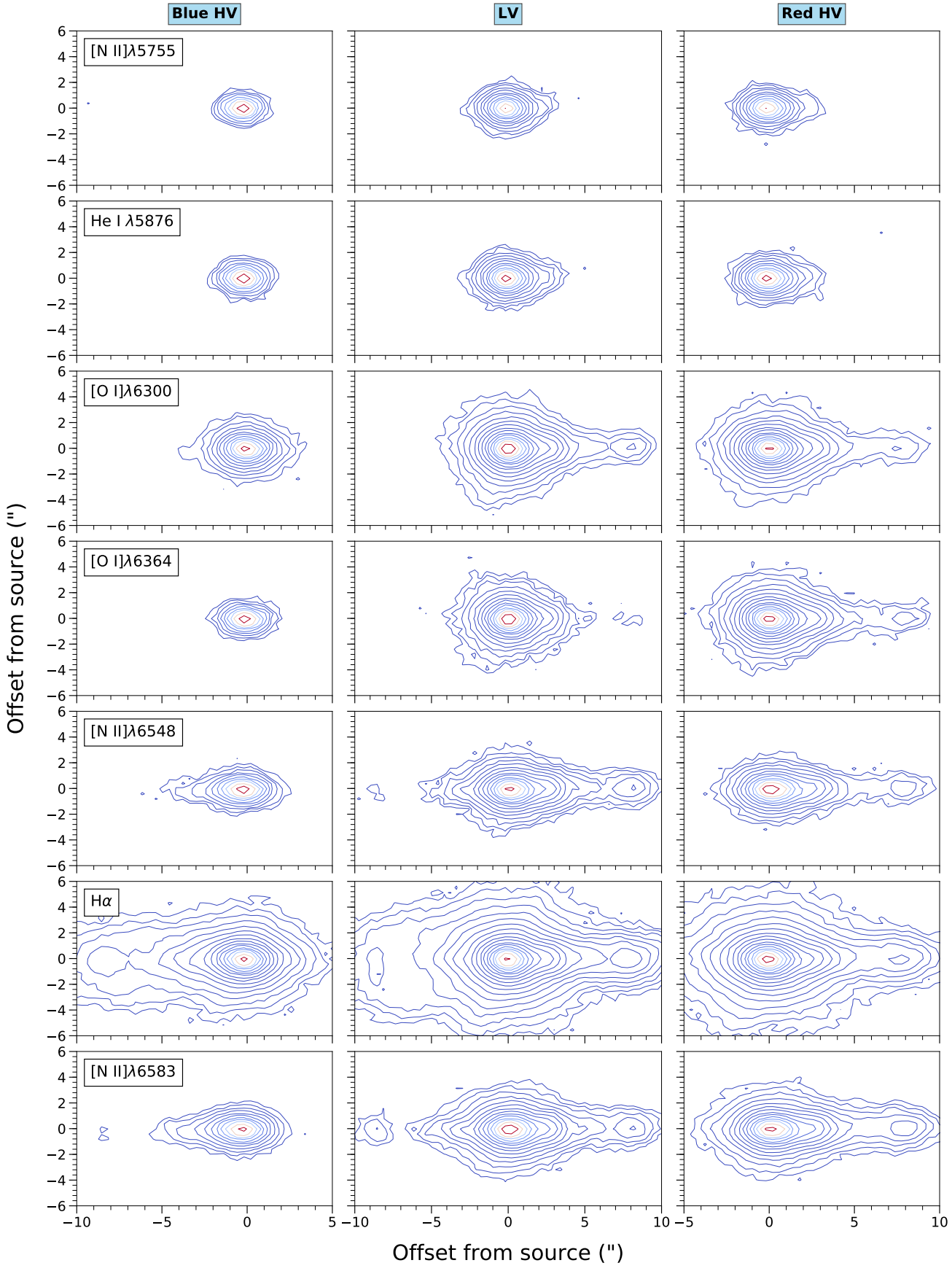

FIGURE A.2: Figure A.1, continued.

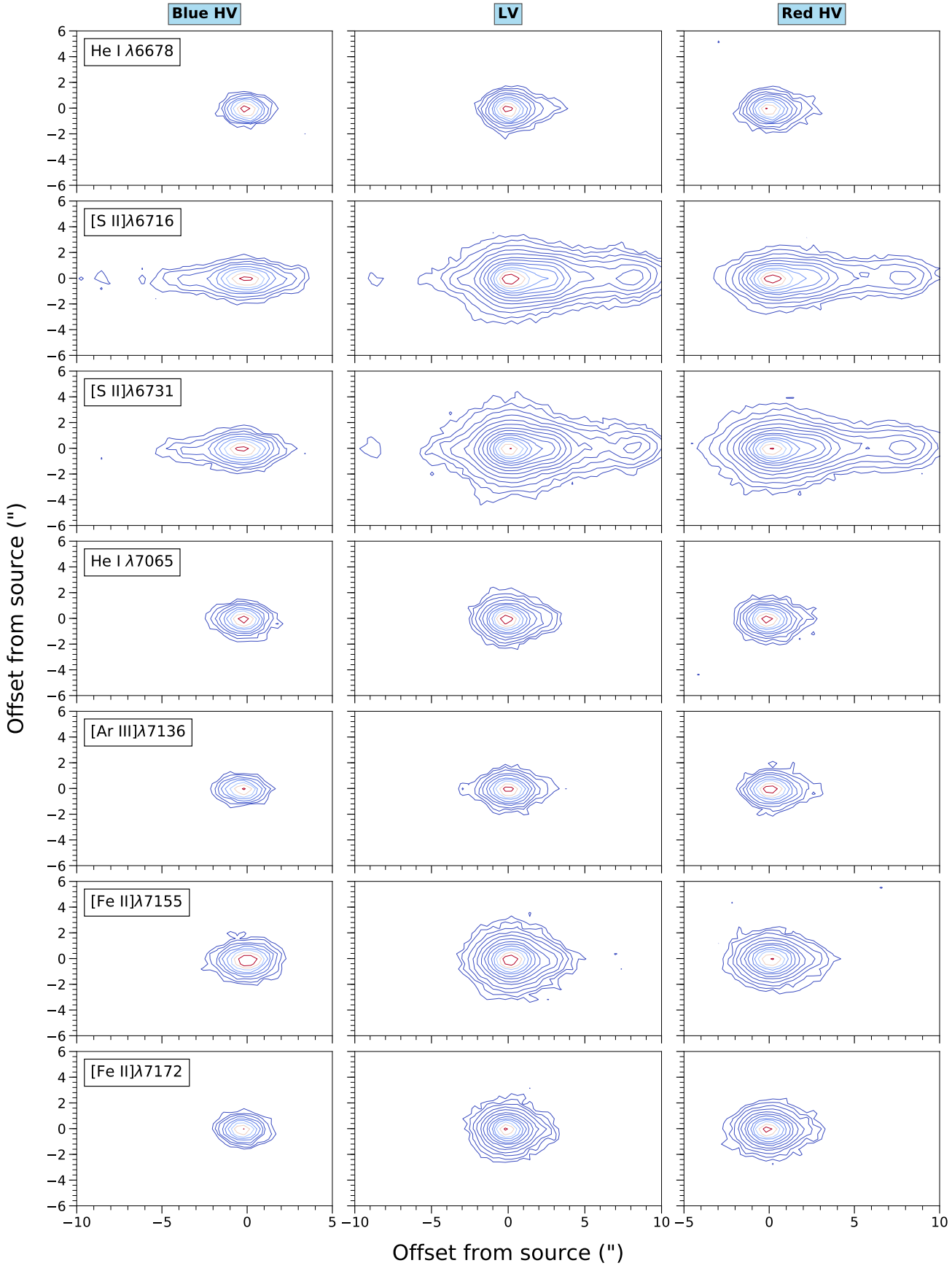

FIGURE A.3: Figure A.1, continued.

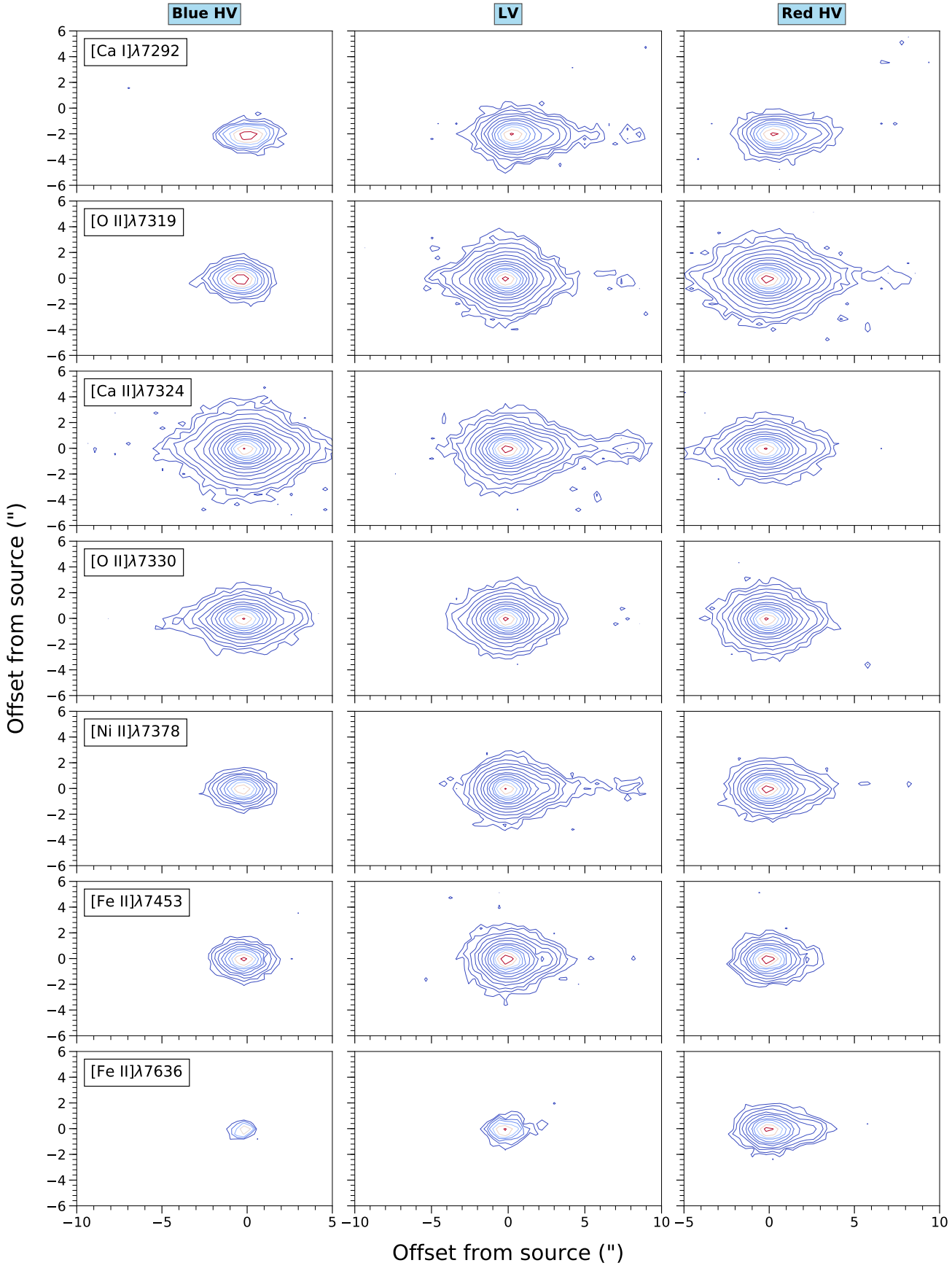

FIGURE A.4: Figure A.1, continued.

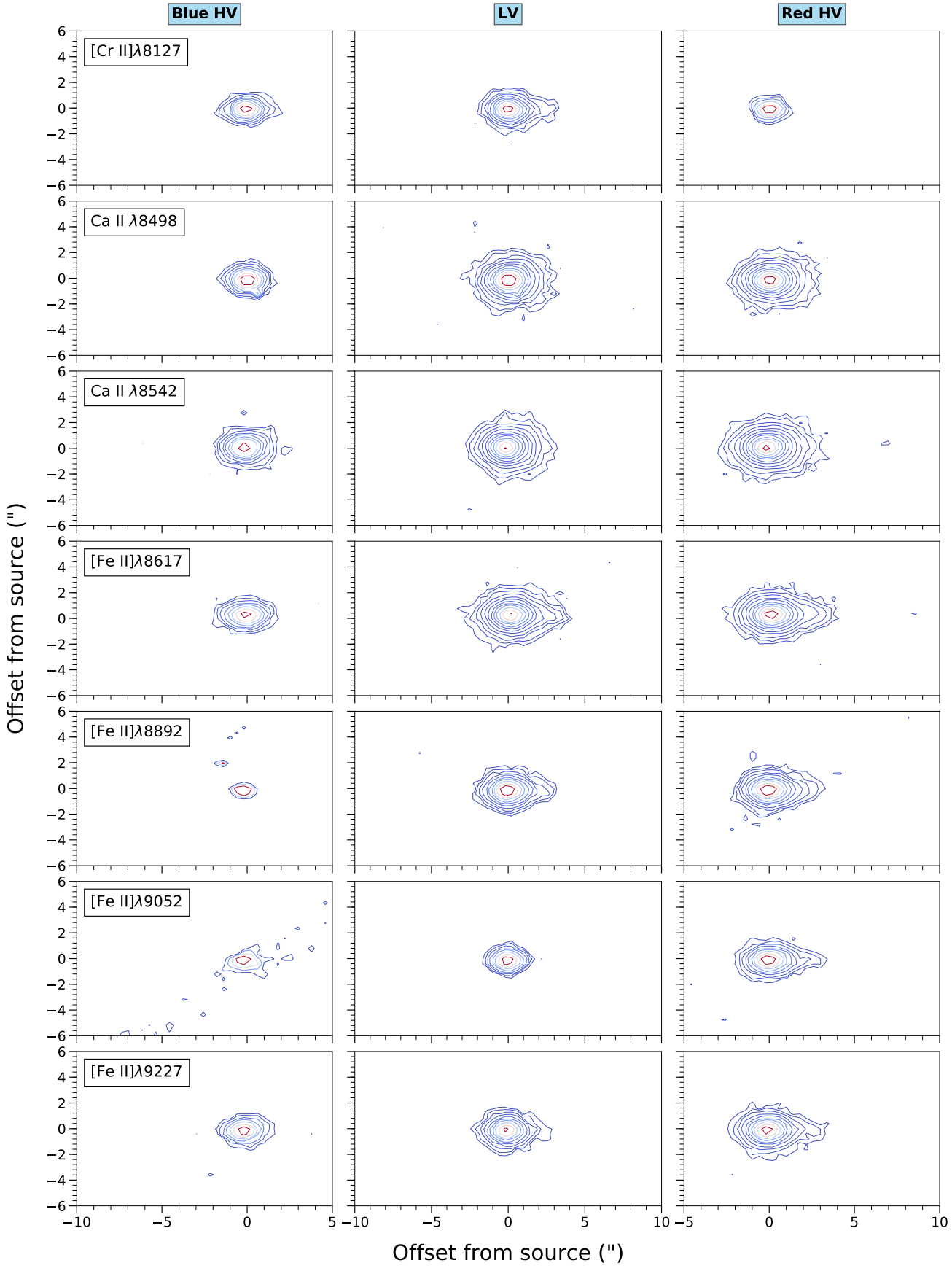

FIGURE A.5: Figure A.1, continued.

A.2 PSF Samples

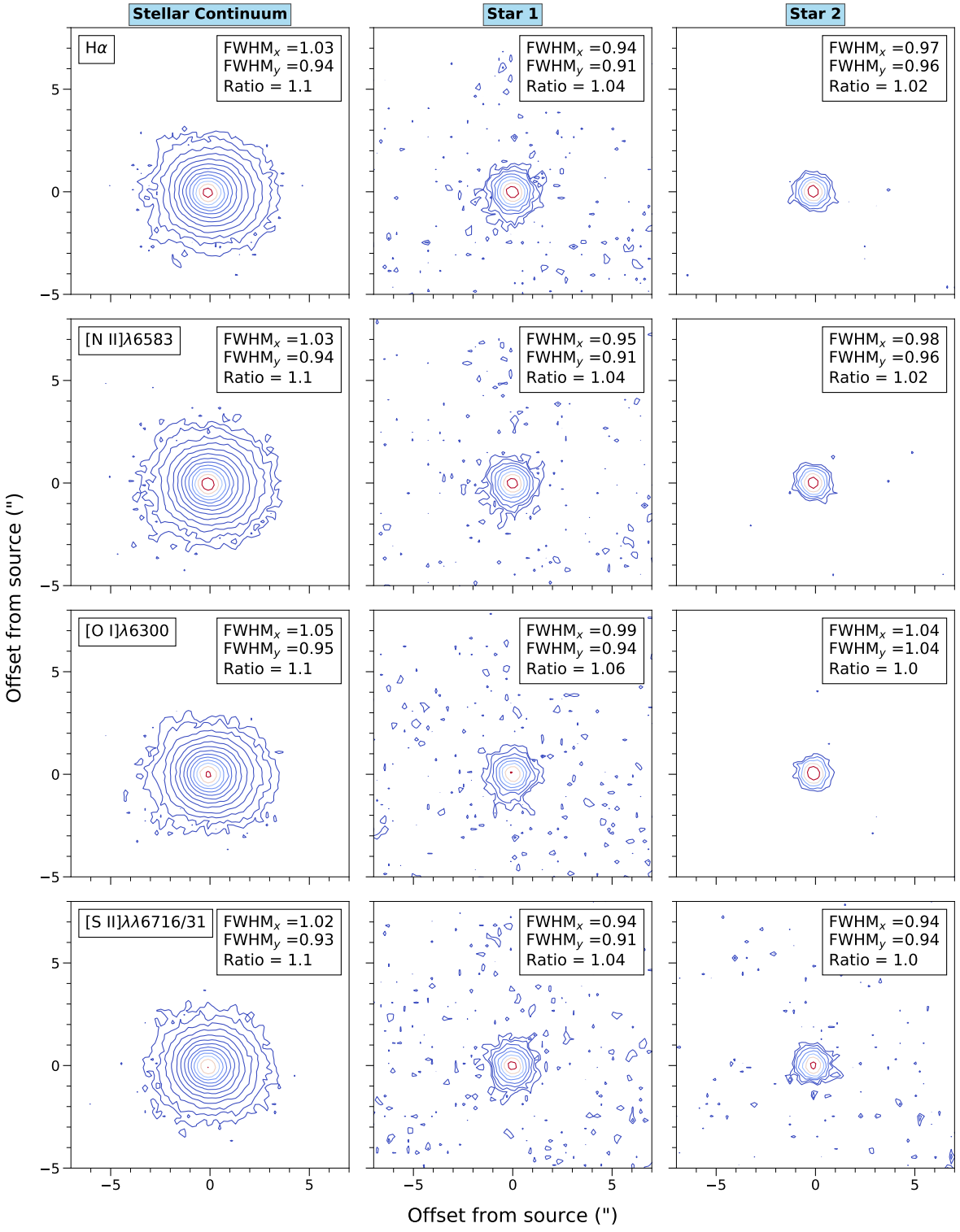

FIGURE A.6: Spectro-images showing samples of the PSF estimated from continuum images of Th 28 (left) and two background stars (center, right).

A.3 Knot Radial Velocities

A.3.1 Undeconvolved Fits

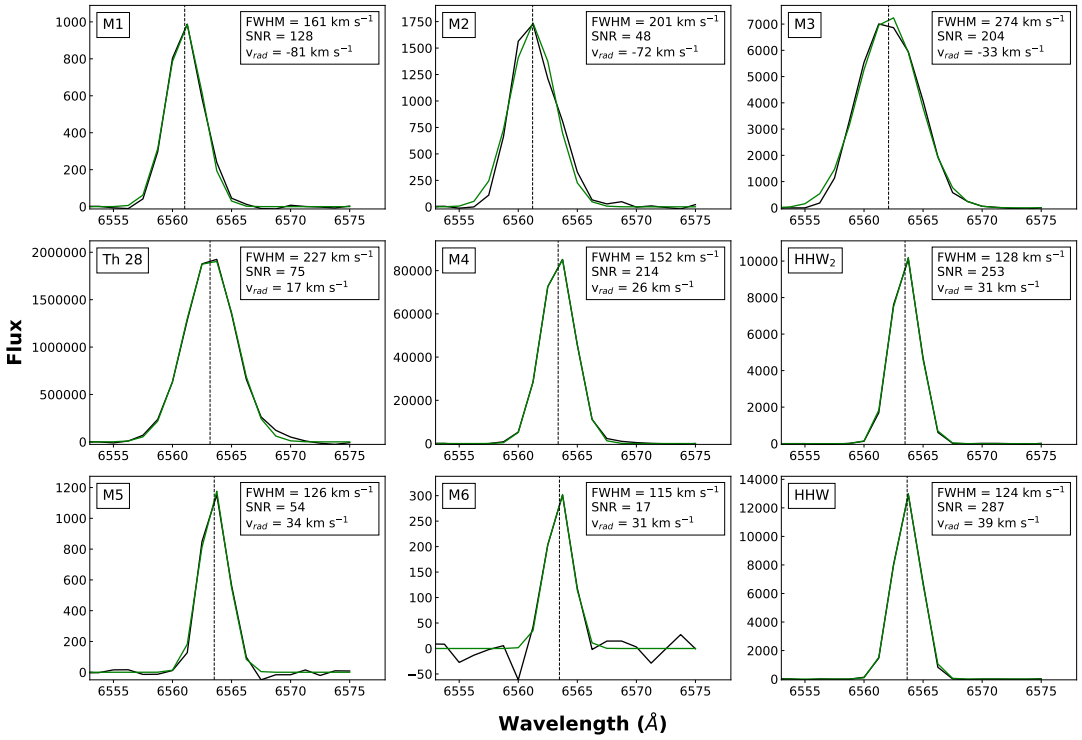

FIGURE A.7: Fits to the peak radial velocities of the knots detected in the Hα micro-jets and source position. Line profiles are binned from a 1" x 1" region centred at the knot position.

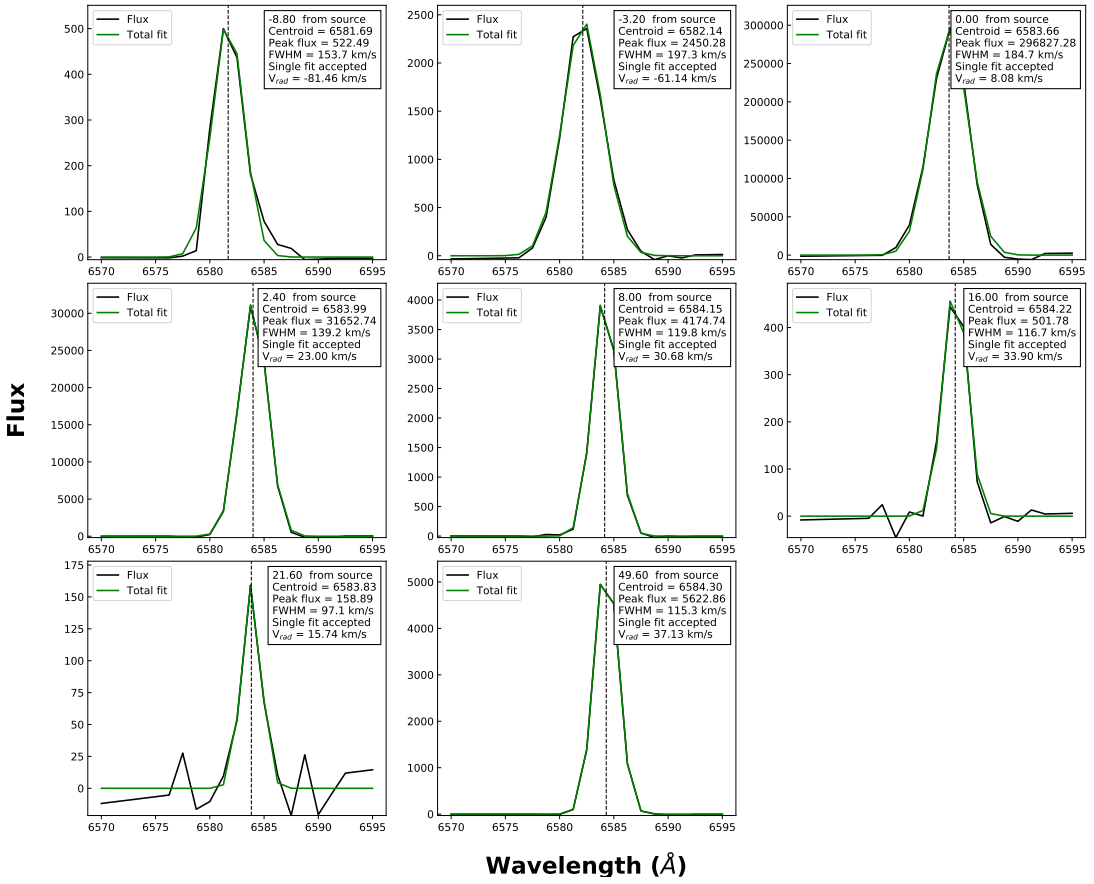

FIGURE A.8: Fits to the peak radial velocities of the knots detected in the [N II]λ6583 micro-jets and source position. Line profiles are binned from a 1" x 1" region centred at the knot position.

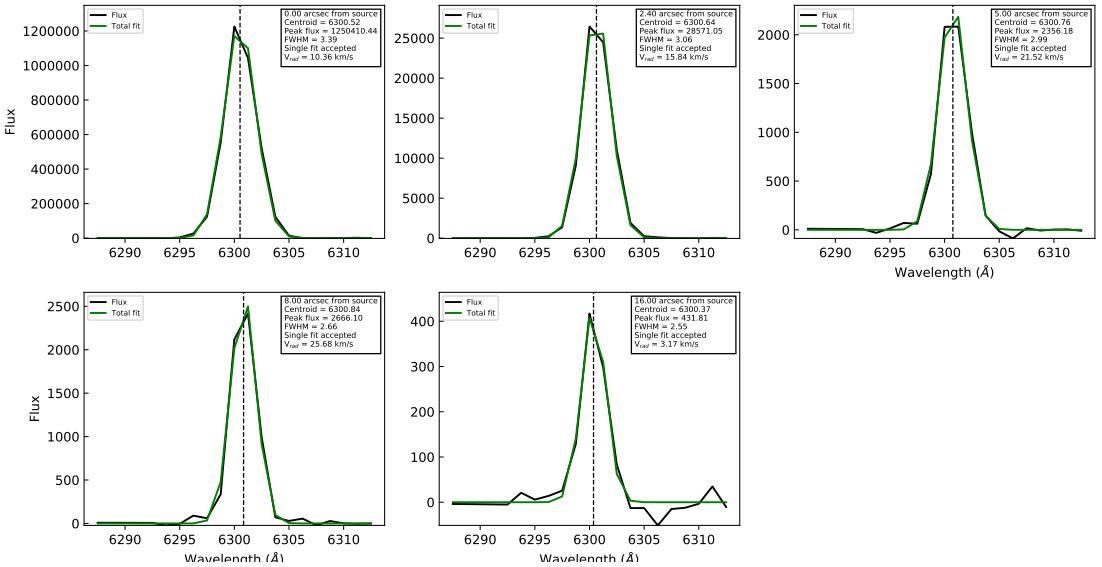

FIGURE A.9: Fits to the peak radial velocities of the knots detected in the [O I]λ6300 micro-jets and source position. Line profiles are binned from a 1" x 1" region centred at the knot position.

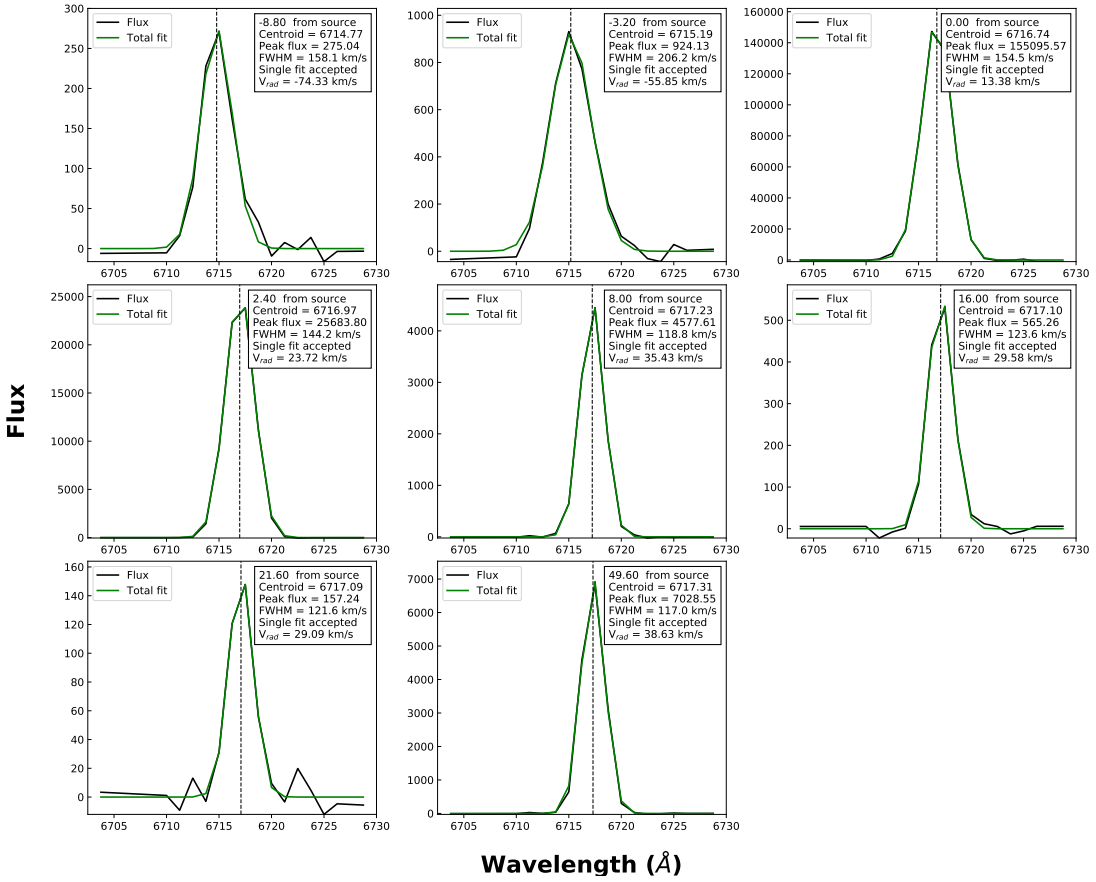

FIGURE A.10: Fits to the peak radial velocities of the knots detected in the[S II]λ6716 micro-jets and source position. Line profiles are binned from a 1" x 1" region centred at the knot position.

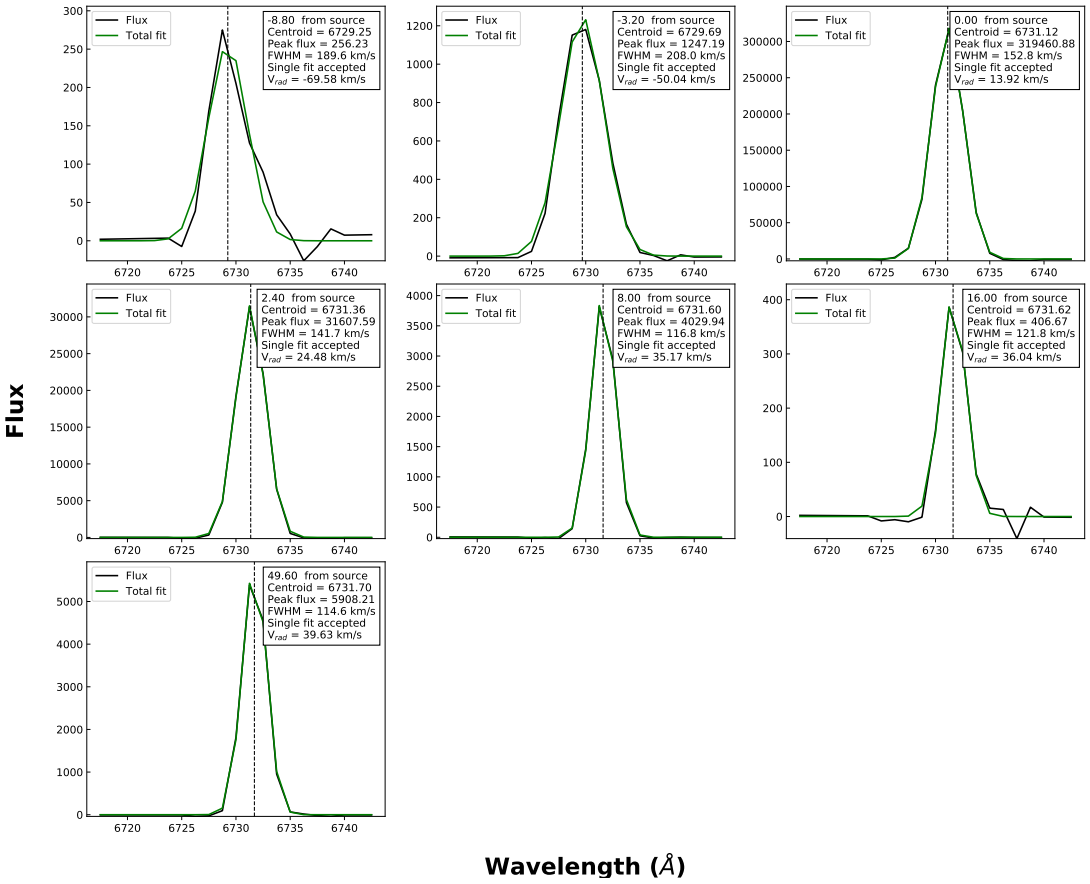

FIGURE A.11: Fits to the peak radial velocities of the knots detected in the [S II]λ6731 micro-jets and source position. Line profiles are binned from a 1" x 1" region centred at the knot position.

A.3.2 Deconvolved Fits

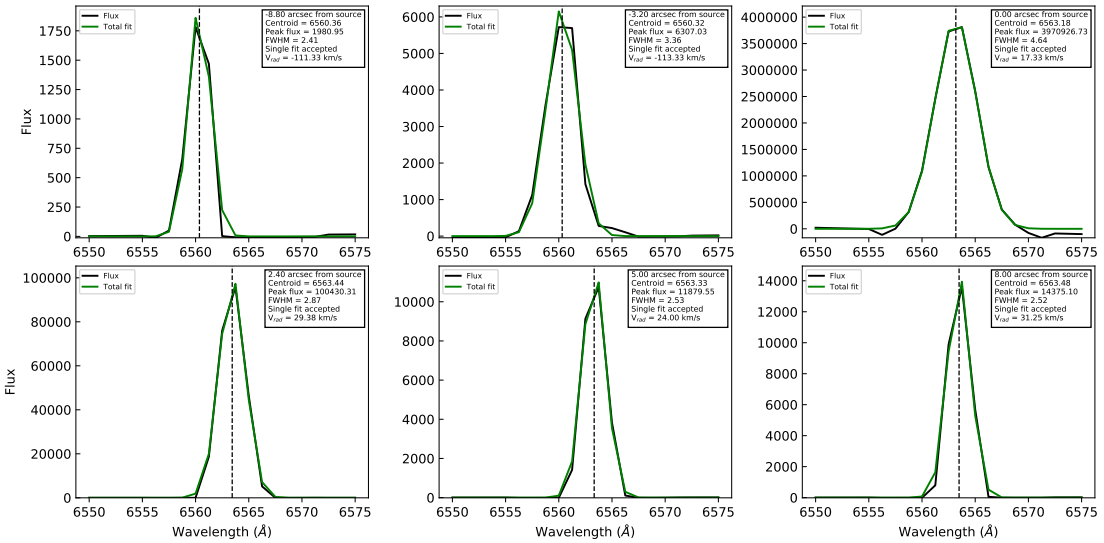

FIGURE A.12: Fits to the peak radial velocities of the knots detected in the deconvolved Hα micro-jets and source position. Line profiles are binned from a 1" x 1" region centred at the knot position.

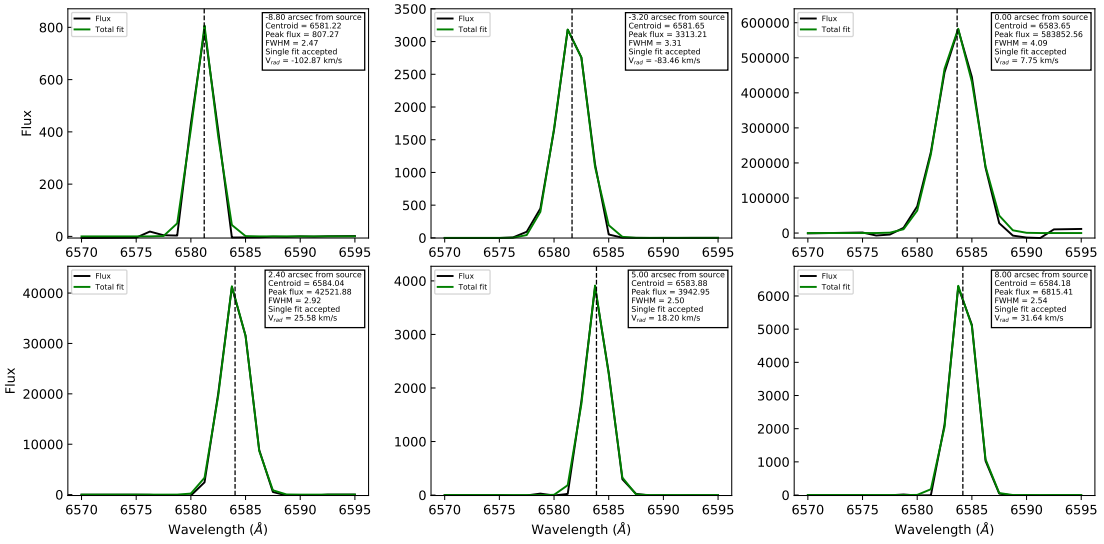

FIGURE A.13: Fits to the peak radial velocities of the knots detected in the deconvolved [N II]λ6583 micro-jets and source position. Line profiles are binned from a 1" x 1" region centred at the knot position.

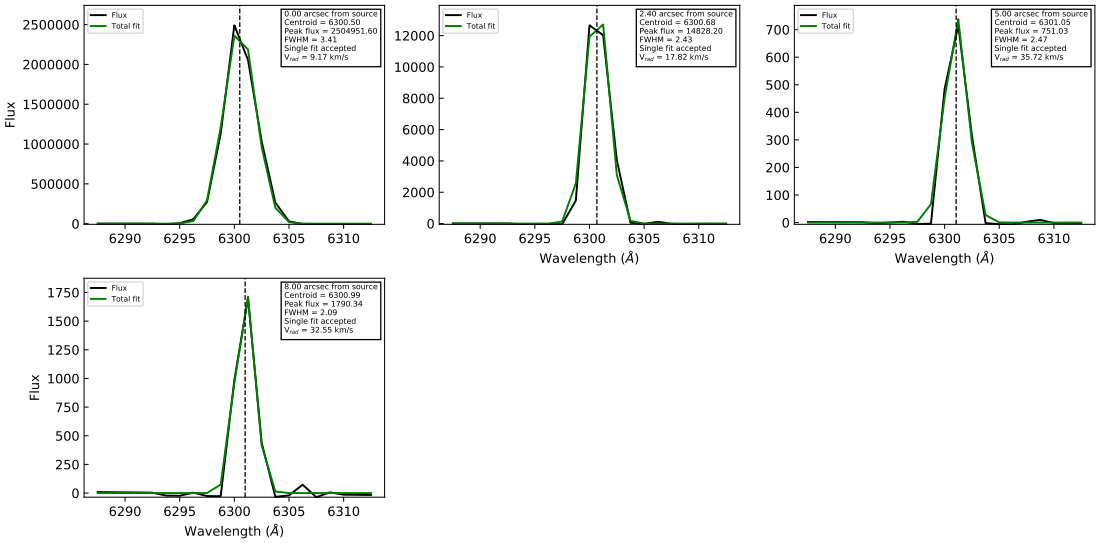

FIGURE A.14: Fits to the peak radial velocities of the knots detected in the deconvolved [O I]λ6300 micro-jets and source position. Line profiles are binned from a 1" x 1" region centred at the knot position.

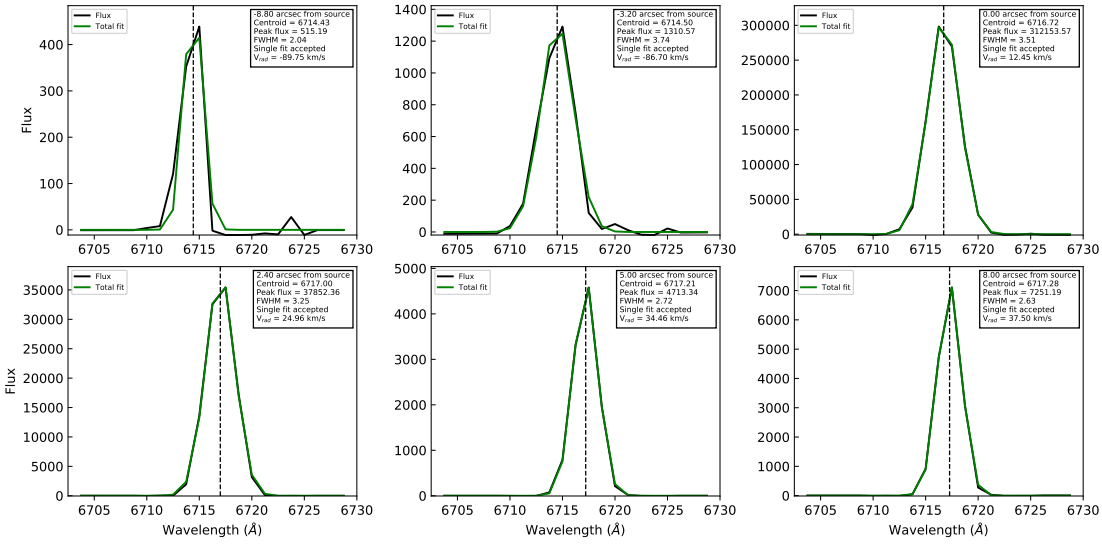

FIGURE A.15: Fits to the peak radial velocities of the knots detected in the deconvolved [S II]λ6716 micro-jets and source position. Line profiles are binned from a 1" x 1" region centred at the knot position.

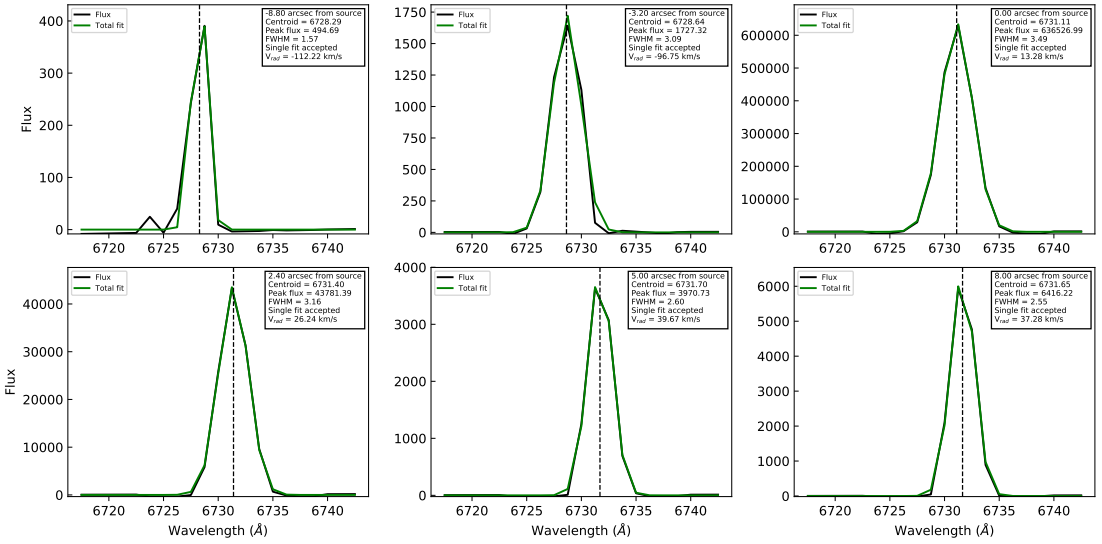

FIGURE A.16: Fits to the peak radial velocities of the knots detected in the deconvolved [S II]λ6731 micro-jets and source position. Line profiles are binned from a 1" x 1" region centred at the knot position.

A.4 Jet Widths

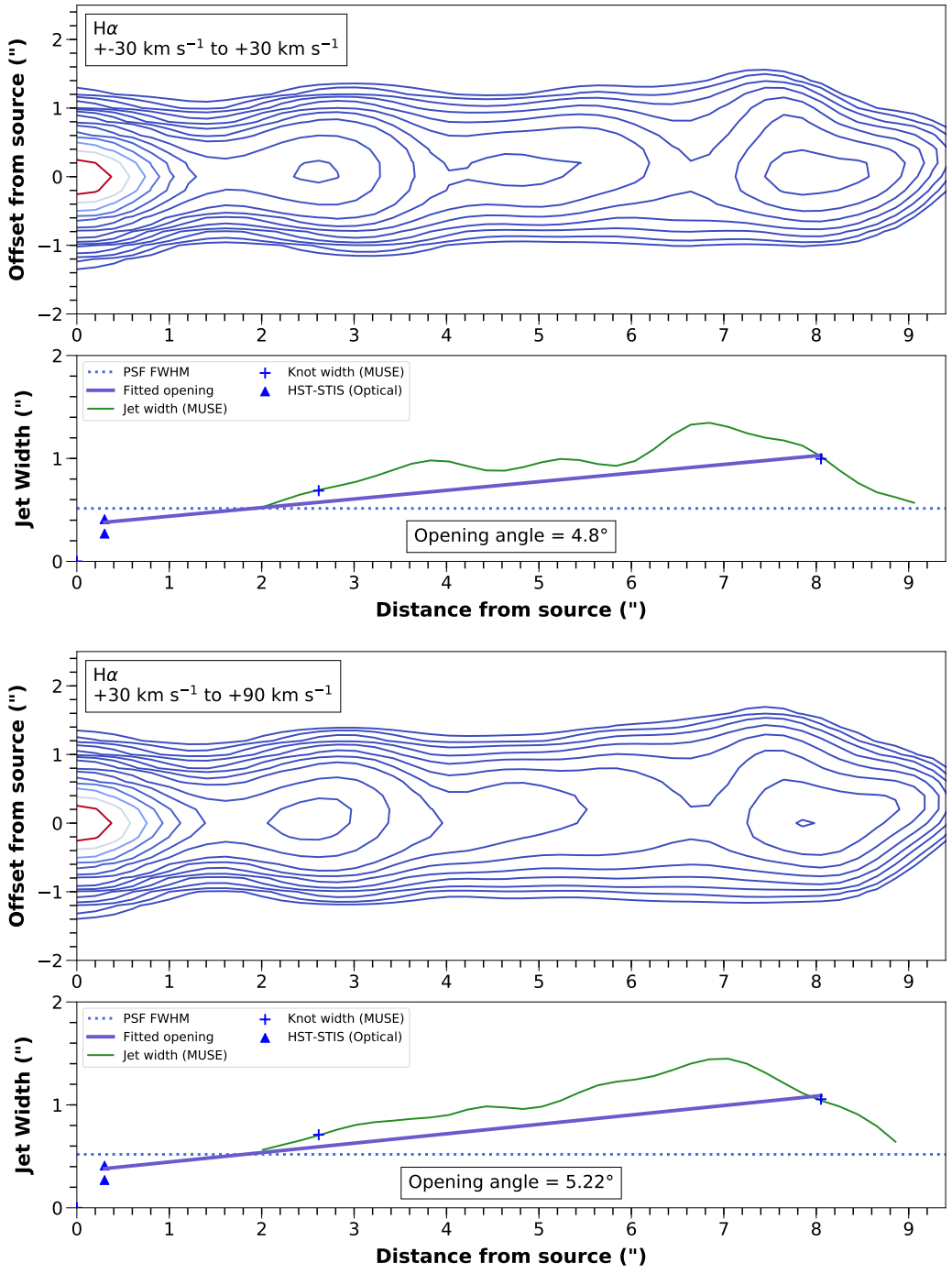

FIGURE A.17: Jet width measured along the red-shifted Hα micro-jet, in the $\pm$ 30 km s^{-1} and +30-90 km s^{-1} channels. The source position is at the origin of each plot. The opening angle is estimated by a fit to the lower bounds of the FWHM measurements, corresponding approximately to observed knot positions.

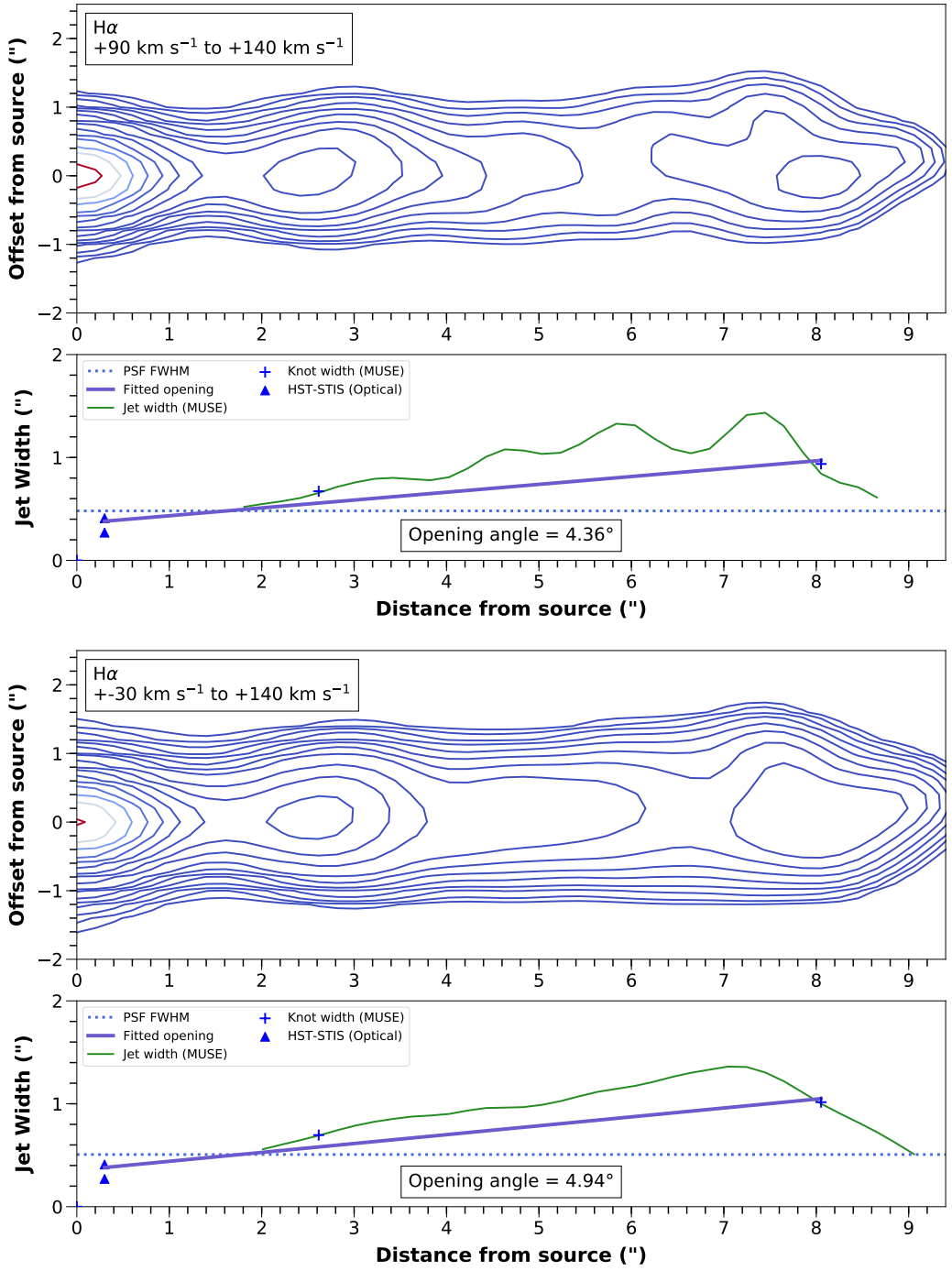

FIGURE A.18: As in A.17, for the +90-140 km s^{-1} and -30 to +140 km s^{-1} channels.

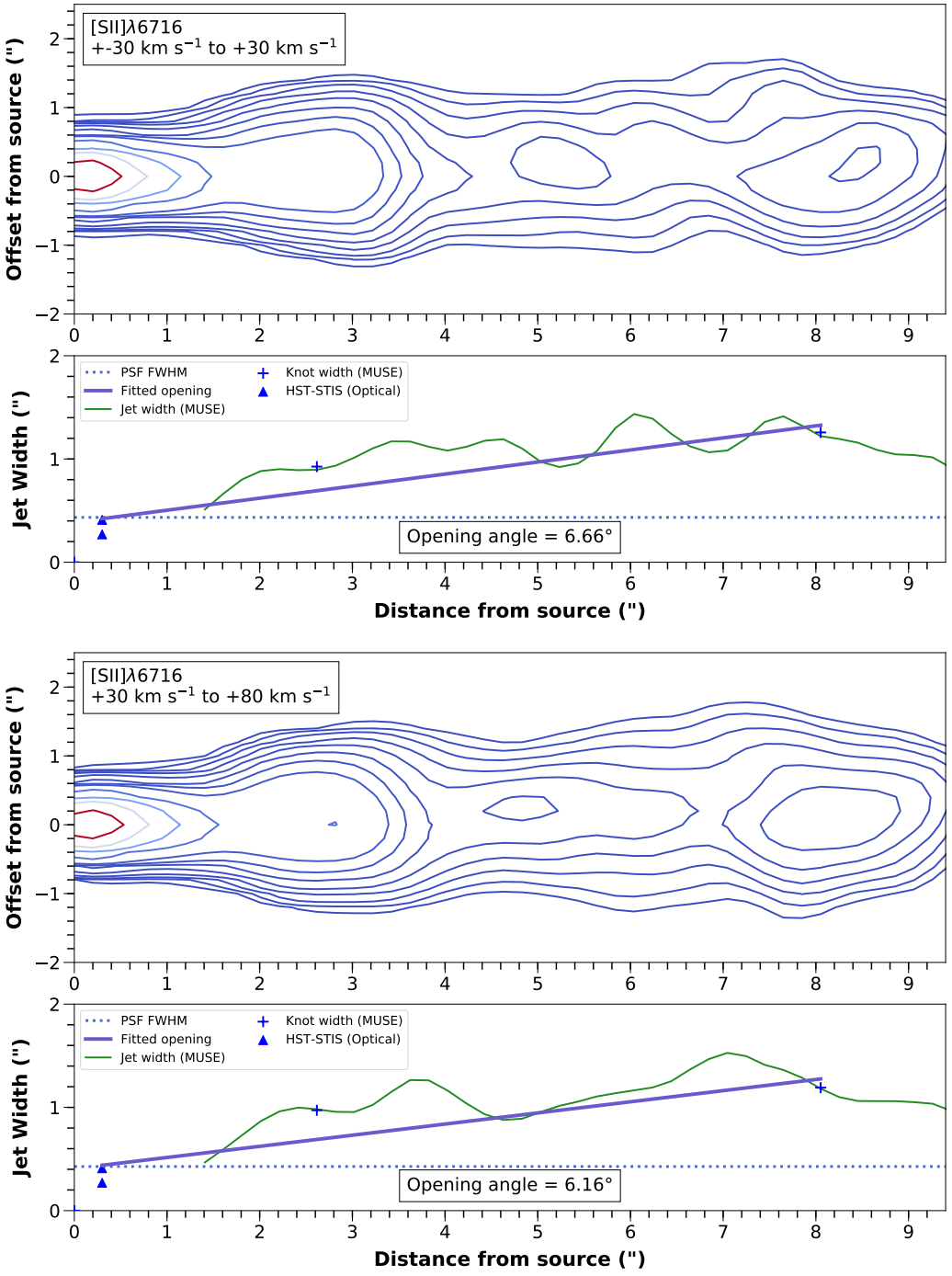

FIGURE A.19: As in A.17, for the [S II]λ6716 line in the ± 30 km s^{-1} and +30-90 km s^{-1} channels.

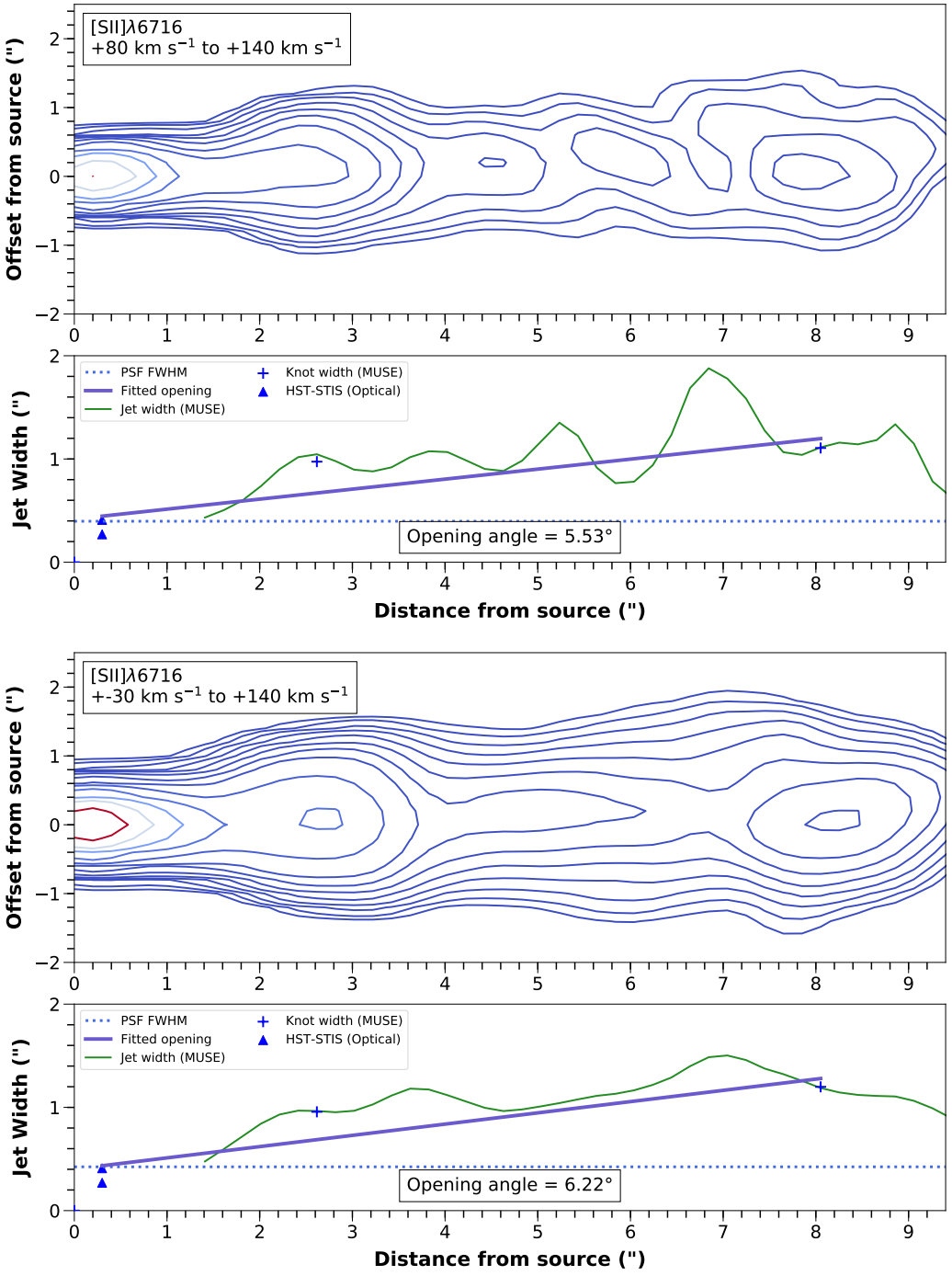

FIGURE A.20: As in A.17, for the [S II]λ6716 line in the +90-140 km s^{-1} and -30 to +140 km s^{-1} channels.

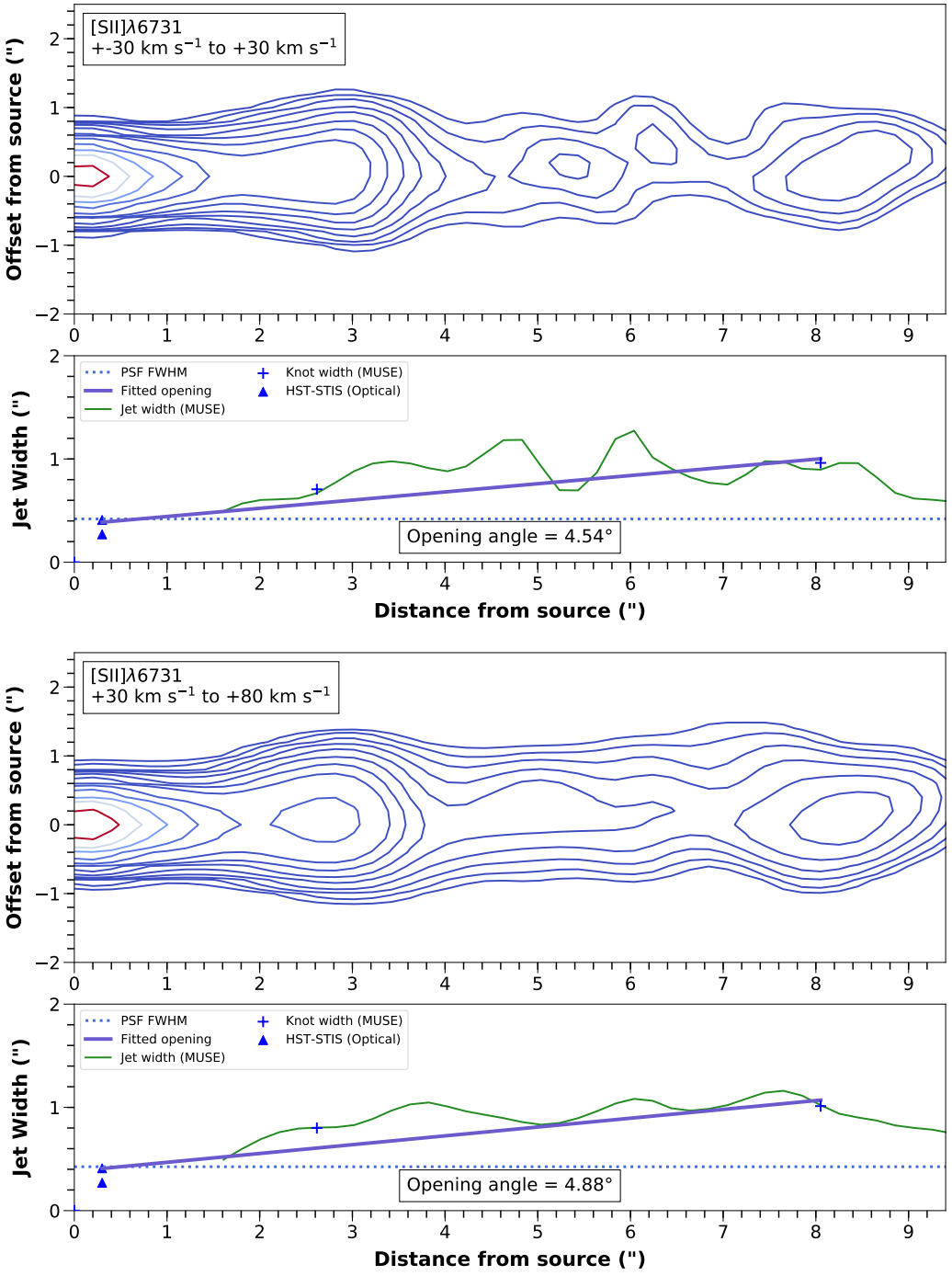

FIGURE A.21: As in A.17, for the [S II]λ6731 line in the ± 30 km s^{-1} and +30-90 km s^{-1} channels.

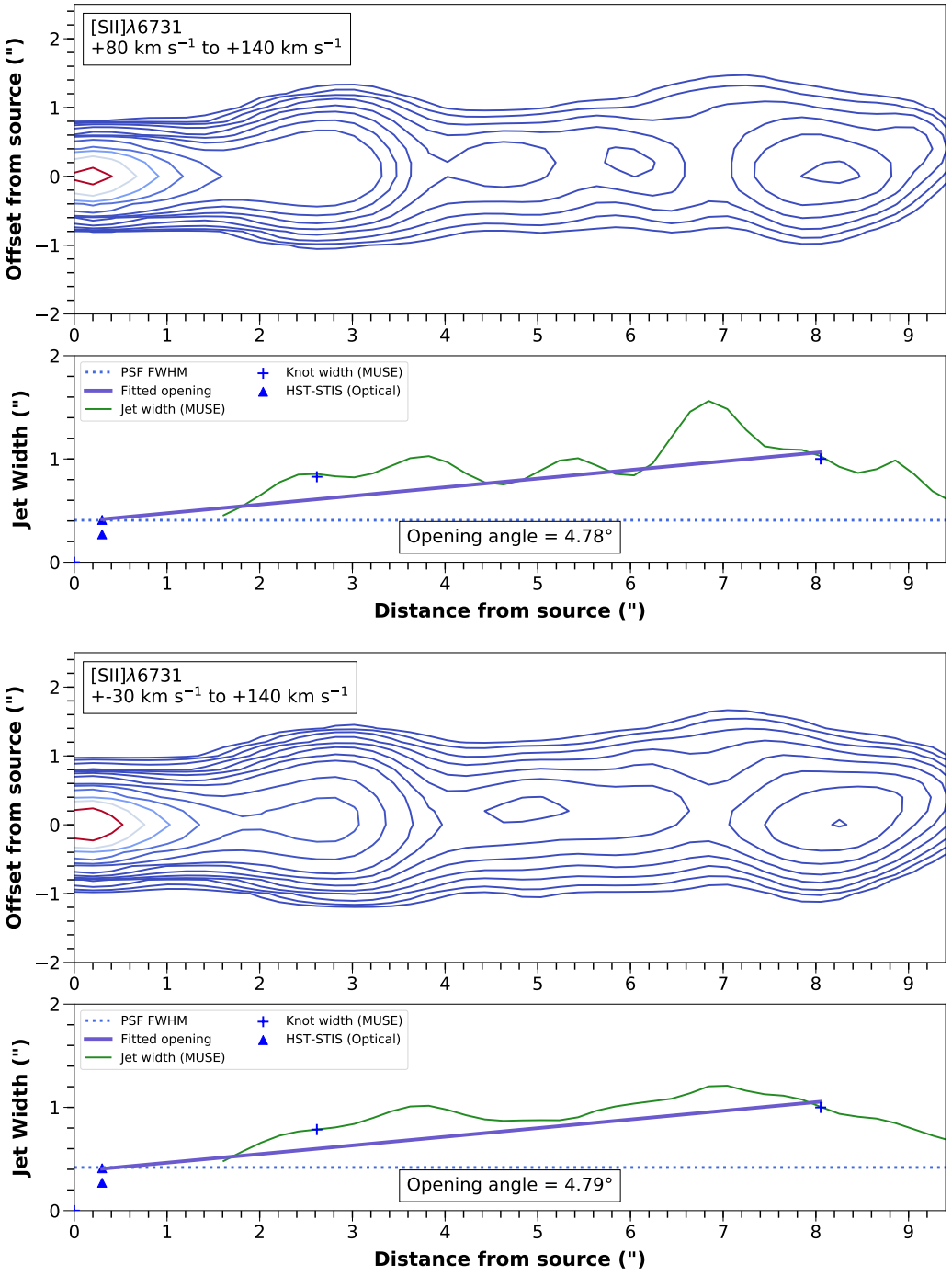

FIGURE A.22: As in A.17, for the [S II]λ6716 line in the +90-140 km s^{-1} and -30 to +140 km s^{-1} channels.

A.5 Position-Velocity Maps

This section contains position-velocity maps of the rotated, non-deconvolved emission lines along the axis of the Th 28 micro-jets. Note that continuum subtraction has been carried out; however residual sky emission lines may be seen in several of the figures especially for emission lines of oxygen. The figures cover an approximate range of +/- 10" of the source.

While several of the knots discussed in Chapter 3 fall outside this range, these are visible only in Hα and other emission lines for which more detailed spectro-images are given within that chapter. All contours are plotted on a log scale beginning at the 4-σ level and increasing as factors of $\sqrt{2}$.

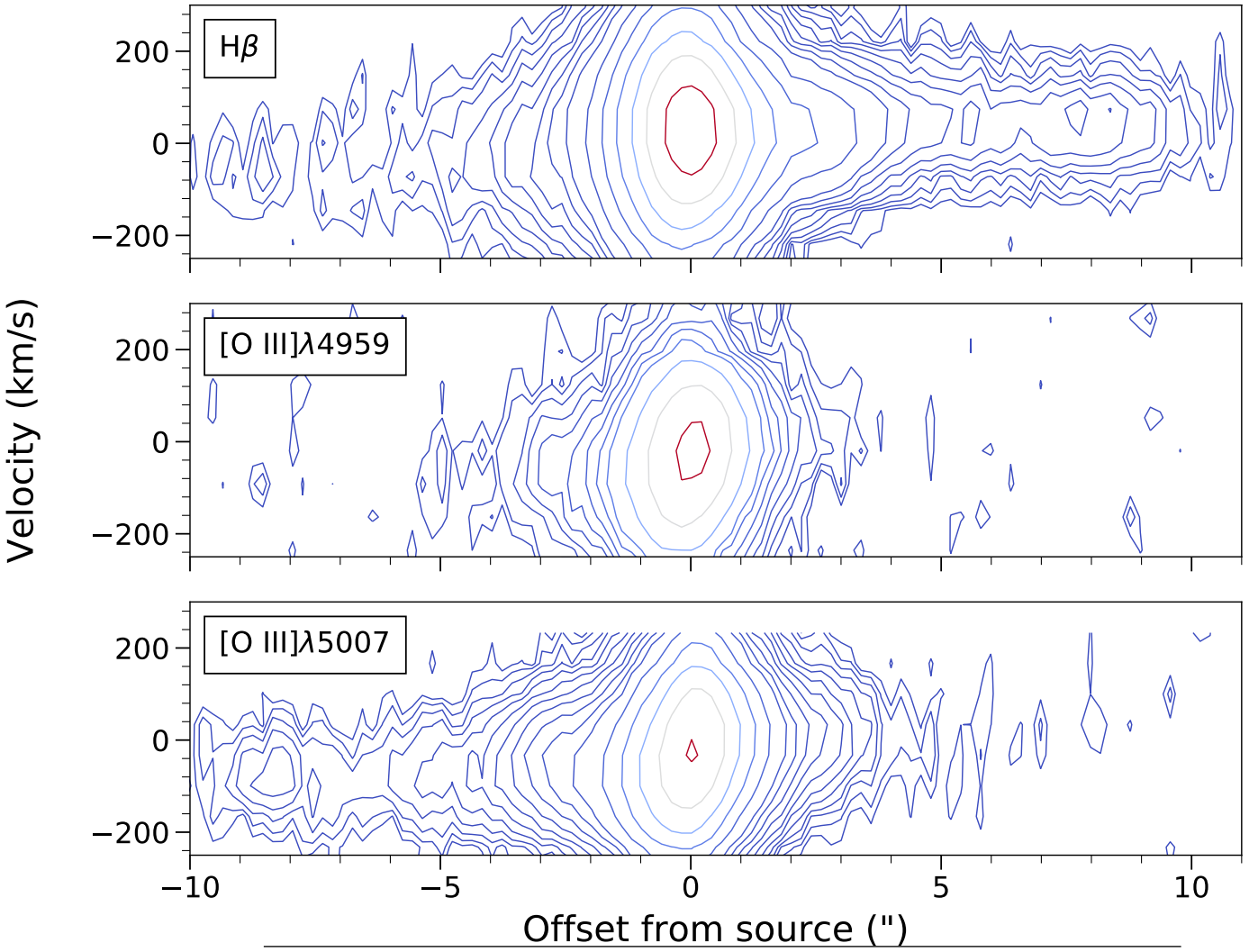

FIGURE A.23: PV maps showing the Th 28 jet emission in optical emission lines. Contours begin at the 3-σ level, with adjacent contours increasing as a factor of $\sqrt{3}$.

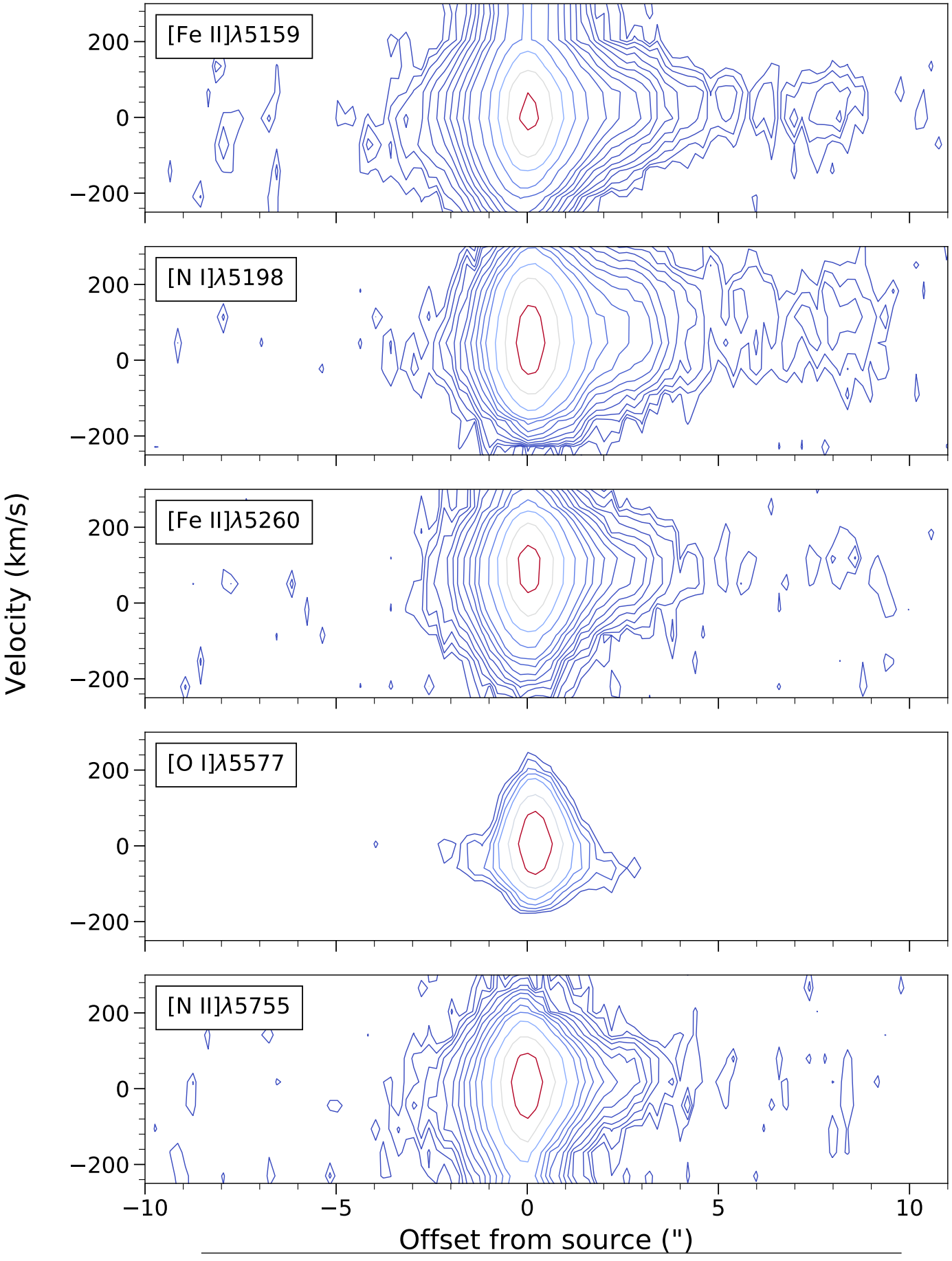

FIGURE A.24: Figure A.23, continued.

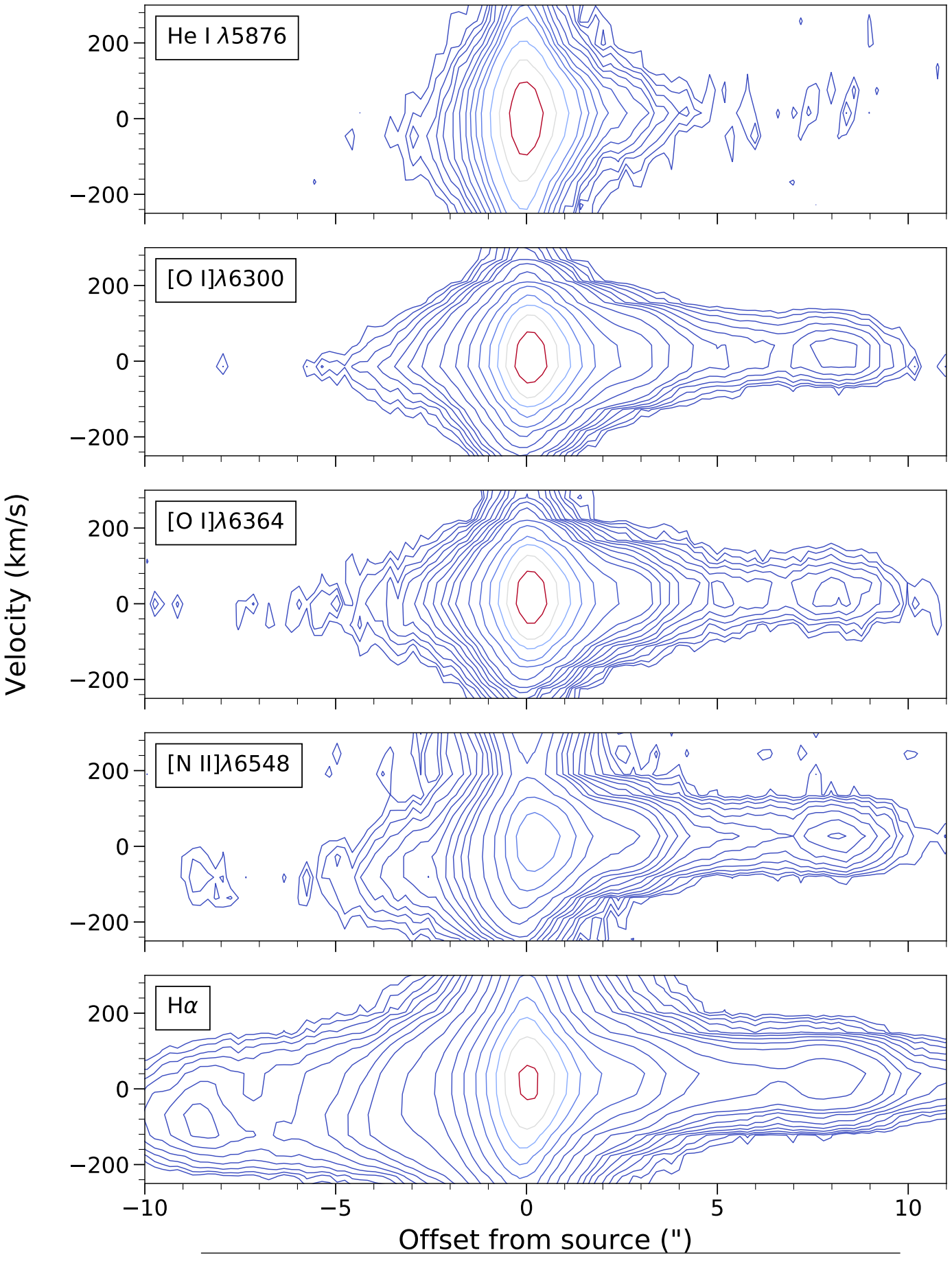

FIGURE A.25: Figure A.23, continued.

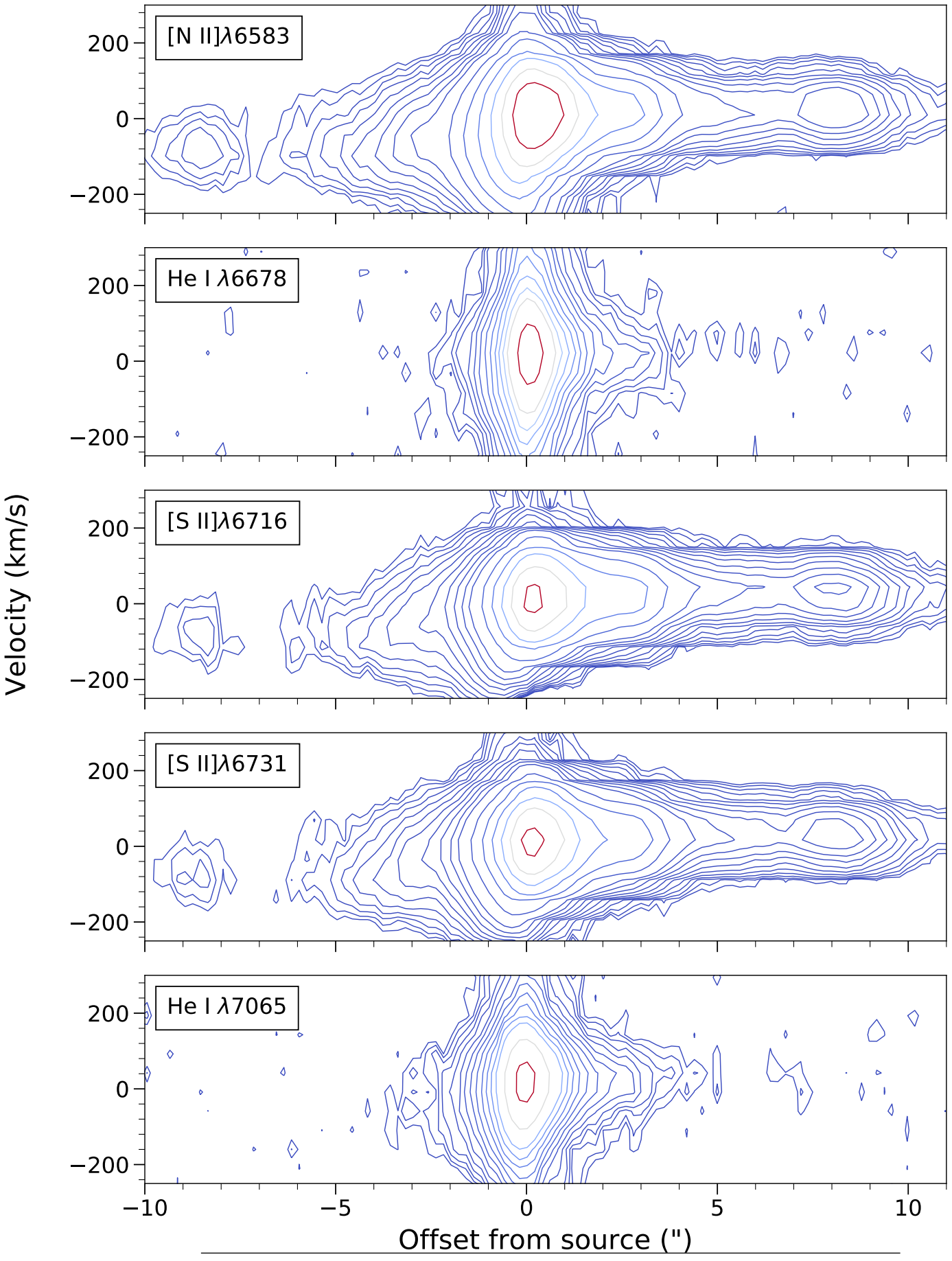

FIGURE A.26: Figure A.23, continued.

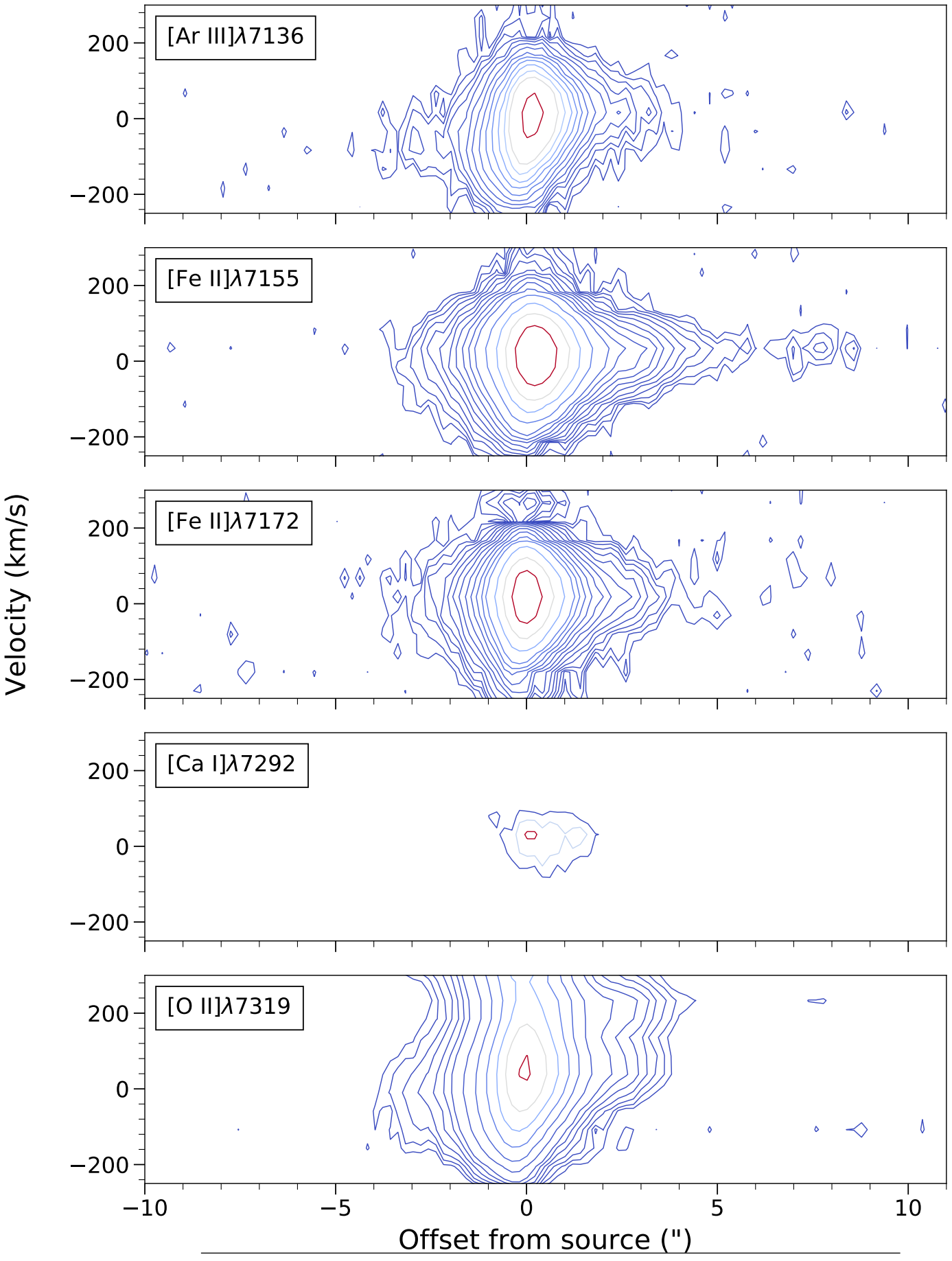

FIGURE A.27: Figure A.23, continued.

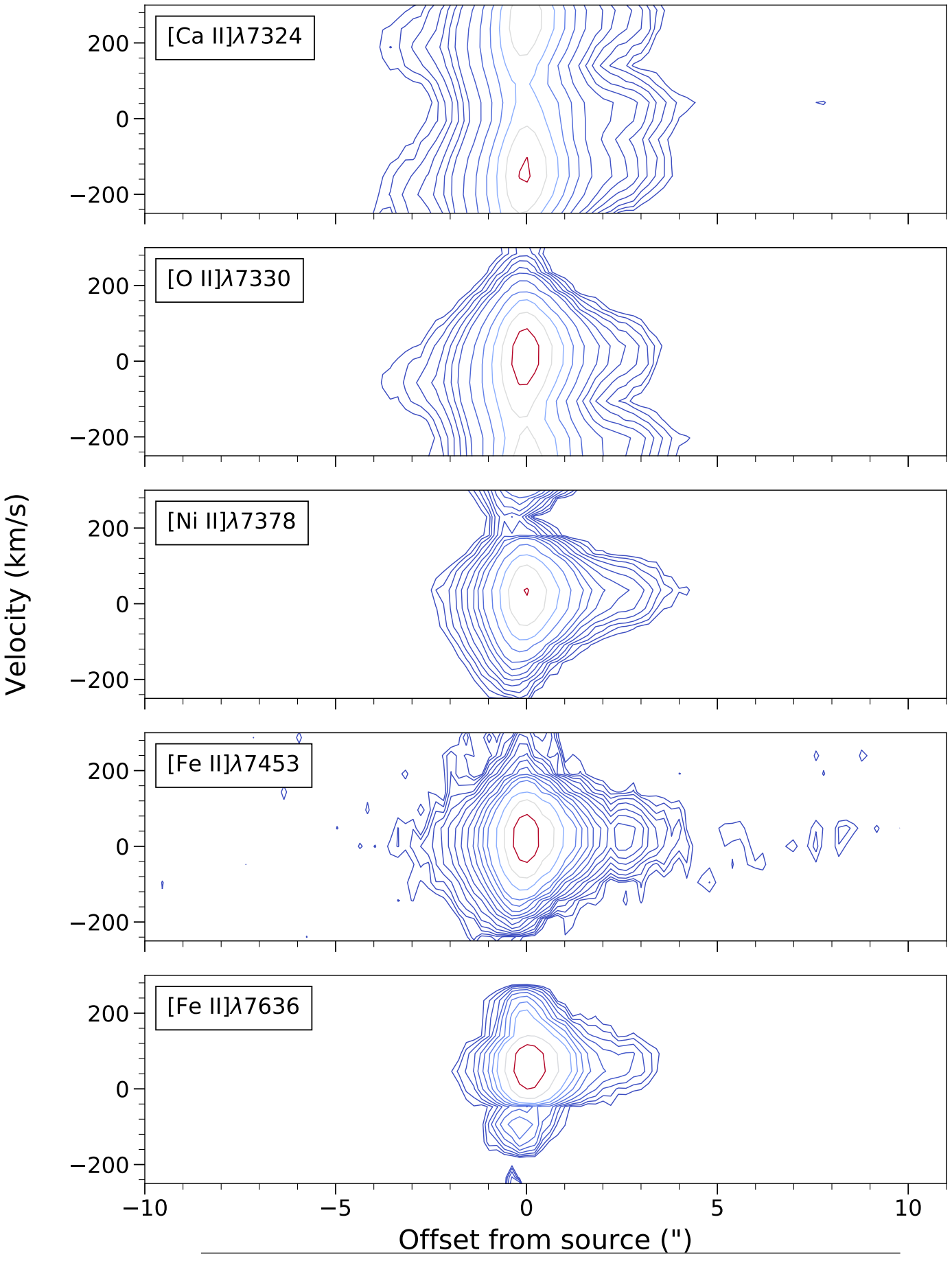

FIGURE A.28: Figure A.23, continued.

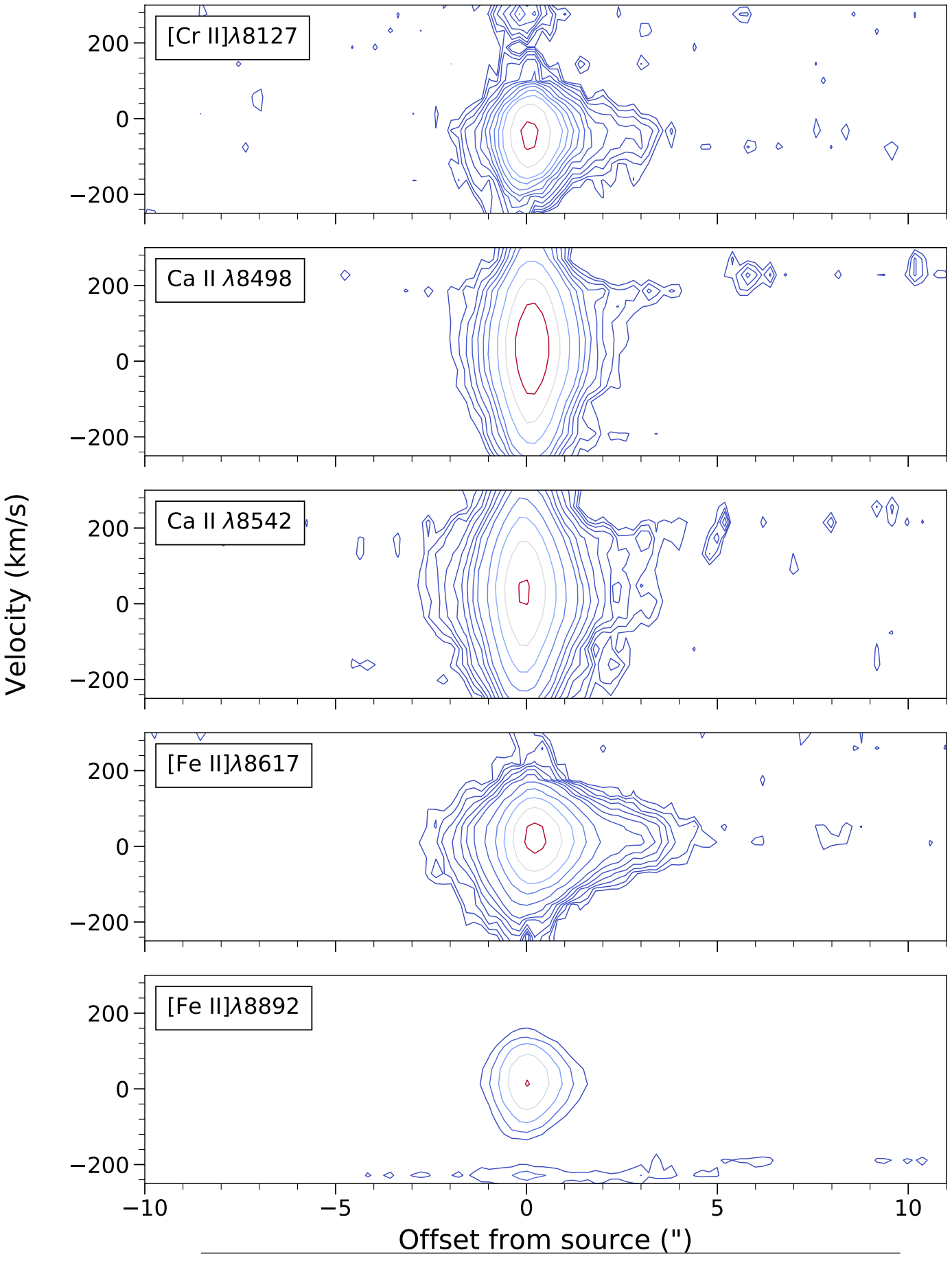

FIGURE A.29: Figure A.23, continued.

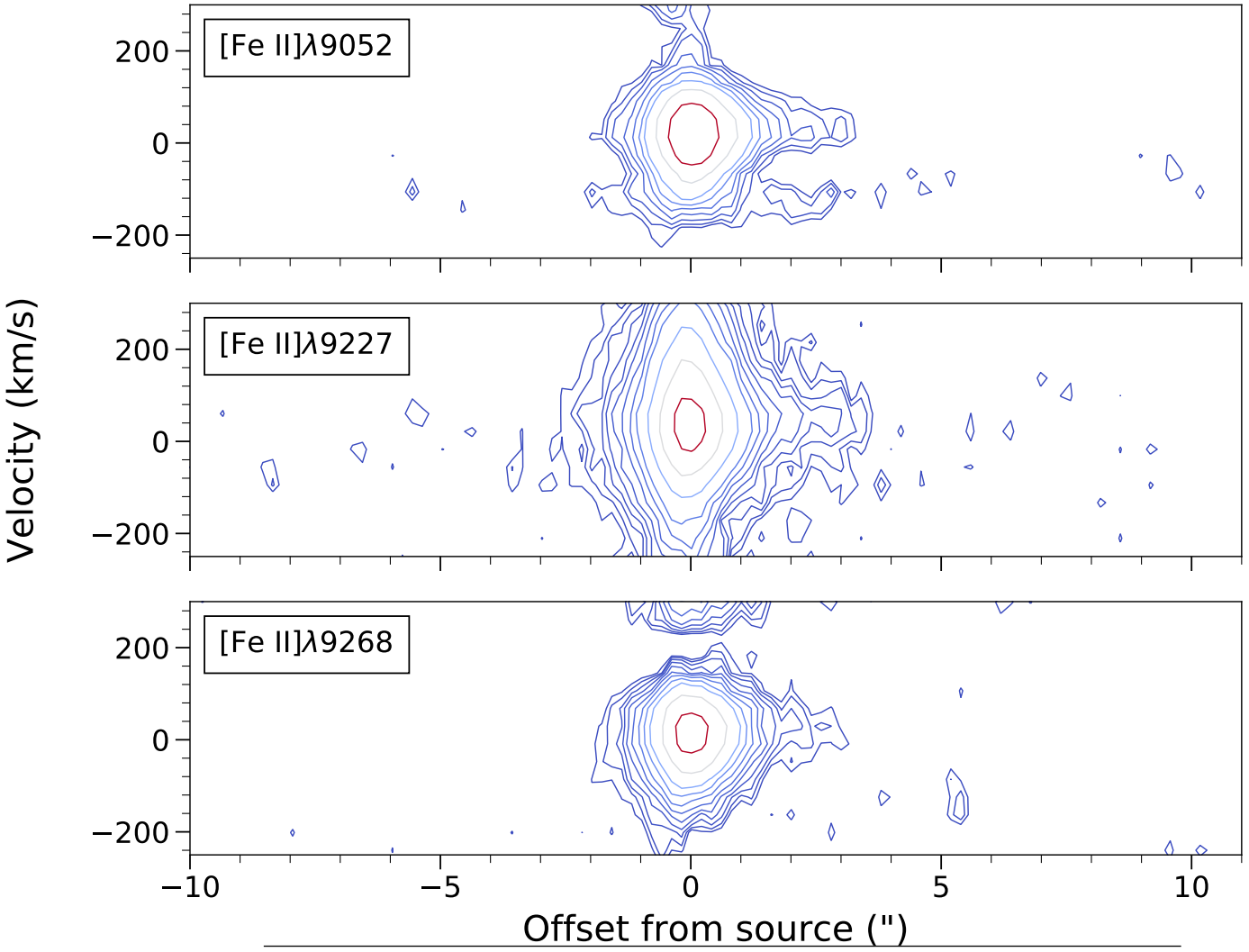

FIGURE A.30: Figure A.23, continued.

Appendix B

Precessing Jets

B.1 Catalogue of Jet Wiggles

This section contains a full list of jets identified in the literature as having a wiggling morphology, with a brief discussion of the main features and details of any inferred binary/companion objects based on measurements of the wiggle properties. The key parameters of all jets detailed here are summarized in Table B.1.

Cep E: This is a wiggling jet from a Class 0 binary source. Both jet lobes are visible, and the jet appears to be driven by bow shocks (Lefloch et al., 2015). Observations in H II show that one lobe exhibits wiggling on a length scale of 23" with a 44 year period. Eislöffel et al. (1996) modelled this as precession due to two 0.5 $M_\odot$ sources at 730 au separation, while Terquem et al. (1999) suggests a separation of 4-20 au assuming a roughly stellar-mass companion. Although both jet lobes are detected, the overall symmetry of the wiggle remains unclear.

V1331 Cyg: A faint but strongly wiggling jet identified by Mundt & Eisloffel (1998). One lobe may show a wiggling with $\lambda \sim 0.71$ pc (deprojected) and a 2300 yr period. Terquem et al. (1999) find this consistent with orbital motion at a separation of 13-66 au assuming a stellar mass companion.

RNO 15-FIR: A potentially wiggling molecular outflow from a Class 0/Class I source which is modeled as orbital motion from a binary source with total mass 12 $M_\odot$ (Davis et al., 1997). Terquem et al. (1999) estimates this outflow to have $\lambda = 0.092$ pc and period 9000 years, with a separation of 33–165 AU between the binary components.

R Aquarii: Unlike the other examples given here, this jet is driven by an evolved source, a white dwarf-red giant binary. The north-eastern lobe has a wiggling outflow

which breaks into a chain of small faint knots, with a helical pattern seen in forbidden lines of N and O, as well as Hα, within 4" or 900 au of the source (Melnikov et al., 2018). The knots along the jet follow the shape of this wiggle (though they are not only located at the peaks). The known binary parameters are used to compare this jet with theoretical wiggle models. However, when using typical assumptions for these models (e.g. $\sigma = 0.33$) Melnikov et al. (2018) find the expected length scales to be much larger than the observed $\lambda = 2$". Whether there is a link between the known binary and the observed jet wiggle is therefore unclear. We note that the jet proper motions of 0.2 "/yr suggest a wiggle period $\sim$ 10 yr. The south-western jet is also observed, but the outflow is relatively distorted and appears to be misaligned from its counterpart with a difference in PA $\sim 20°$. Nichols & Slavin (2009) suggest this less collimated lobe may also represent helical motion with a wider opening angle and subsequent impacting on ambient material.

DG Tau: A well-studied jet with AO images of the jet in [O I] and [S II] show small-scale wiggles with $\lambda = 3$" (Dougados et al., 2000). Masciadri & Raga (2002) measure the wiggle parameters and suggest an orbital motion model with a half-opening angle 3.8°and an estimated 7 year orbital period. From this they derive an orbital velocity of 29.7 km s^{-1} and orbital radius 6.9 au, consistent with a T Tauri star in a binary system.

HH 47: A known binary source with projected separation 120 au. The jet shows a helical morphology which can be divided into four distinct sections of differing lengths, with a small half-opening angle of 2° (Reipurth et al., 2000). Masciadri & Raga (2002) examine the sections separately and find that for an orbital motion model these imply periods of 160-280 yr and an orbital radius of 60-100 au, consistent with the observed separation of the binary components. However, the varying lengths of the jet sections indicates there are most likely other factors affecting the jet shape.

Serpens radio jet: This was suggested as a proto-HH jet by Curiel et al. (1993); and the northwest lobe shows a series of knots tracing a wiggling morphology and the jet is therefore thought to propagate in a cone with half-opening angle $\sim$5°. Raga et al. (2000) use fits to a model of a precessing, variable-velocity jet to estimate a period of 50 years, with measured $\lambda \sim$3."5. Masciadri & Raga (2002) further show the jet shape is compatible with orbital motion of the source, although many of the properties of this jet are not well constrained.

HH 30: A prototypical jet and disk driven by an optically invisible star, the HH 30 outflow extends up to 7' from the source (López et al., 1995, 1996), and the main flow and knots trace a wiggling with $\lambda = 15$" to at least 50". Anglada et al. (2007) note that the whole morphology moves together along the jet axis without changes in the directions

of the knot proper motions, as would be expected if the wiggling was due to their being deflected. They conclude this wiggling is compatible with either orbital motion around a large companion (0.25-1.0 $M_\odot$), or precession due to a massive planet/brown dwarf companion with a separation of ≤ 1 au from the jet source.

IRAS 20126-4104: A high-mass (7 $M_\odot$), very young stellar object with a poorly collimated molecular outflow. The H_2 flow extends for 1 pc (Ayala et al., 1998) and has an S shaped morphology. This indicates precession over an angle of 37° (a much larger angle than most of the other examples) with a period of 12 $\times 10^4$ years (Shepherd et al., 2000; Cesaroni et al., 2005; Su et al., 2007). However, Caratti o Garatti et al. (2008) also find a shorter wiggling in H_2 with an opening angle of 16-21°, λ = 11", and period = 1100 years. They note that if these distinct wiggle patterns represented a combination of orbital and precession components, then this would require the orbital radius of the companion to intersect the accretion disk; it is possible that instead the wiggling is caused by tidal interactions of multiple stellar companions.

DO Tau: A CTTS driving an optical asymmetric jet similar to Th 28. The red-shifted (north-eastern) jet is the source for a number of HH objects. Erkal et al. (2021) show both lobes of the micro-jets exhibit wiggling within about 1.5" with projected $\lambda \sim$ 0."6 (90 au) and half-opening angle $\sim$ 1.3. They compare the jet shape with both orbital and precession models. However, the larger wiggle opening angle in the faster red-shifted jet strongly indicates against the orbital model, in which the wiggle opening angle scales inversely with jet velocity (see Section 4.1.1). A precession model is therefore fitted to the jet with $\beta = 0.5°$ and precession period 9.5 years. In order to obtain a good match to the red-shifted jet, the model required a phase shift and a precession angle approximately twice that in the blue jet be introduced to this lobe. Erkal et al suggest this asymmetry in the wiggle properties may be caused if the two jet lobes originate from separate annuli within a warped disk. They further show that the blue-shifted jet precession may be caused by a massive planetary companion ($\leq$ 12 $M_{\rm Jup}$) within a separation of 0.1-0.15 au.

PV Cep/HH 315: A Herbig PMS star with an optical edge-on jet. The jet knots show an S-symmetry on a length scale $\sim$200" (Gomez et al., 1997) which can be approximately matched with a precession model. The half opening angle of the precession is 22°, with a period 300 years. However, only one cycle of the wiggling is observed in the jet and it is therefore unclear if this represents a periodic precession or a wobbling in the jet axis.

G35.20-074N: An 18 $M_\odot$ YSO binary with a radio jet (Beltrán et al., 2016). A possible S-symmetry is observed in the radio knots. However, the length scale of the wiggle is large, with λ = 0.45-0.6 pc, meaning only a small portion of the wiggle is traced

with the jet. Nonetheless, the jet shape is consistent with precession due to the binary components (with masses of 11 and 6 $M_\odot$).

L1228A/HH 199: This jet source also has a possible s-symmetry seen in knots from the bipolar outflow (Bally et al., 1995). However this is part of a complex outflow region near HH 200 and the origin of the variable outflow axis is unclear; we include this as a possible wiggling jet.

T Tau/HH 355: A HH outflow driven by a well-known T Tauri star which is part of a multiple system. Reipurth et al. (1997) report a point symmetry between the knots in this jet, however there do not appear to be any follow-up studies to see if a wiggle can be detected close to the star. The knots however suggest an opening angle of 26° and a period of 1500-2000 years.

L 1157: A low-mass, Class 0 star (Gueth et al., 1996). The jets exhibit a chain of bow shocks in molecular emission which suggest an S-shaped symmetry with an opening angle of 8°. The precession shows a period of 1640 years with $\lambda \sim$2' (Podio et al., 2016).

IRS 54/YLW 52: A Class 0 source driving a bipolar jet with S-shaped symmetry in H_2 knots (Khanzadyan et al., 2004; Jørgensen et al., 2009; Lopez et al., 2013) which indicates a possible precession with half-opening angle 14° and $\lambda \sim = 2$'.

HH 211: One of the two best examples to date of symmetry detection in a wiggling jet, this is a class 0 source driving a close to edge-on jet ($i = 5° \pm 3°$) which has been observed to 3" resolution in SiO, SO, and CO (Lee et al., 2009, 2010). The SiO and CO observations show a reflection-symmetric wiggling in both jet lobes which is observed out to ∼15" from the source. About 3 wiggle cycles are detected with $\lambda = 5."46$, a half opening angle 0.55°, and a period of 43 ± 23 years. Lee et al. (2009, 2010) finds this points to a very low mass binary where the companion and jet source are both approximately 30 M_{Jup}, with separation of 4.6 au.

HH 111: A second good example of symmetry in a jet, this is a highly collimated jet with lobes extending to 3.5 pc from the source, driven by a possible Class I binary with separation of 15 au (Rodríguez et al., 2008). Interestingly, this jet appears to show two distinct wiggle components. The outer parts of the jet show a point-symmetric deviation from the inner jet of 4° indicating precession on a period of about 23000 years (Reipurth et al., 1997). Within 2' of the source, however, the jet knots exhibit a mirror symmetric wiggle with $\lambda = 216$", half-opening angle = 0.7° and a period of 1800 years (Noriega-Crespo et al., 2011). This is consistent with a binary containing two solar-mass stars at a separation of 186 au. This may mean that HH 111 is an exceptional case where both the orbital motion and precession components due to a binary companion can be

observed, and Noriega-Crespo et al. (2011) note that the ratio $\tau_p/\tau_o = 13$ is consistent with the theoretical predictions discussed in Chapter 4.1.4.

Source	Type	D (pc)	Lobes in which wiggle is detected	Symmetry	λ^a	λ (au)	τ (yr)
Cep E	Class 0 binary	730	One	-	23”	1.68×10^4	400
R Aquarii	WD-RG binary	220	One	-	2”	4.4×10^2	10
V 1131 Cyg	CTTS	550	One	-	0.5 pc	1.03×10^5	2300
RNO 15-FIR	Class 0/I	350	One	-	0.065 pc	4.69×10^6	9000
DG Tau	TTS	140	One	-	3”	4.2×10^2	7
HH 47	PMS binary	450	One	-	-	-	160-280
Serpens		300	One	-	3.”3	9.9×10^2	50
HH 30	Class 0	140	Two	-	15”	2.1×10^3	114
DO Tau	CTTS	140	Two	-	0.”6	8.34×10^1	9.5
IRAS 20126-4104	PMS star	1.7×10^3	Unclear	S-shaped	-	-	>1100
G35.20–0.74N	High-mass YSO	2.2×10^4	Two	S-shaped	-	-	2.35×10^4
HH 211	Class 0	280	Two	Reflection	5-10”	1.4×10^3	43
HH 199		300	Two	S-shaped	∼1’	1.8×10^4	-
T Tau S/HH 355	TTS	140	Two	S-shaped	2-4’	1.68×10^4	1500-2000
PV Cep/HH 315	Herbig PMS	500	Two	S-shaped	200”	1.0×10^5	8000
L 1157	Class 0	250	Two	S-shaped	2’	3.0×10^4	1640
IRS 54	Class I	125	Two	S-shaped	2’	1.5×10^4	4.29×10^4
HH 111	Class I	417	Two	S-shaped	216”	9.01×10^4	1800
-	-	-	-	Reflection	3.5 pc	7.22×10^5	2.3×10^4

Table B.1: Table of jets with wiggles identified in previous literature.

[a]As given in original references.

B.2 Uncertainties on Precession Fits

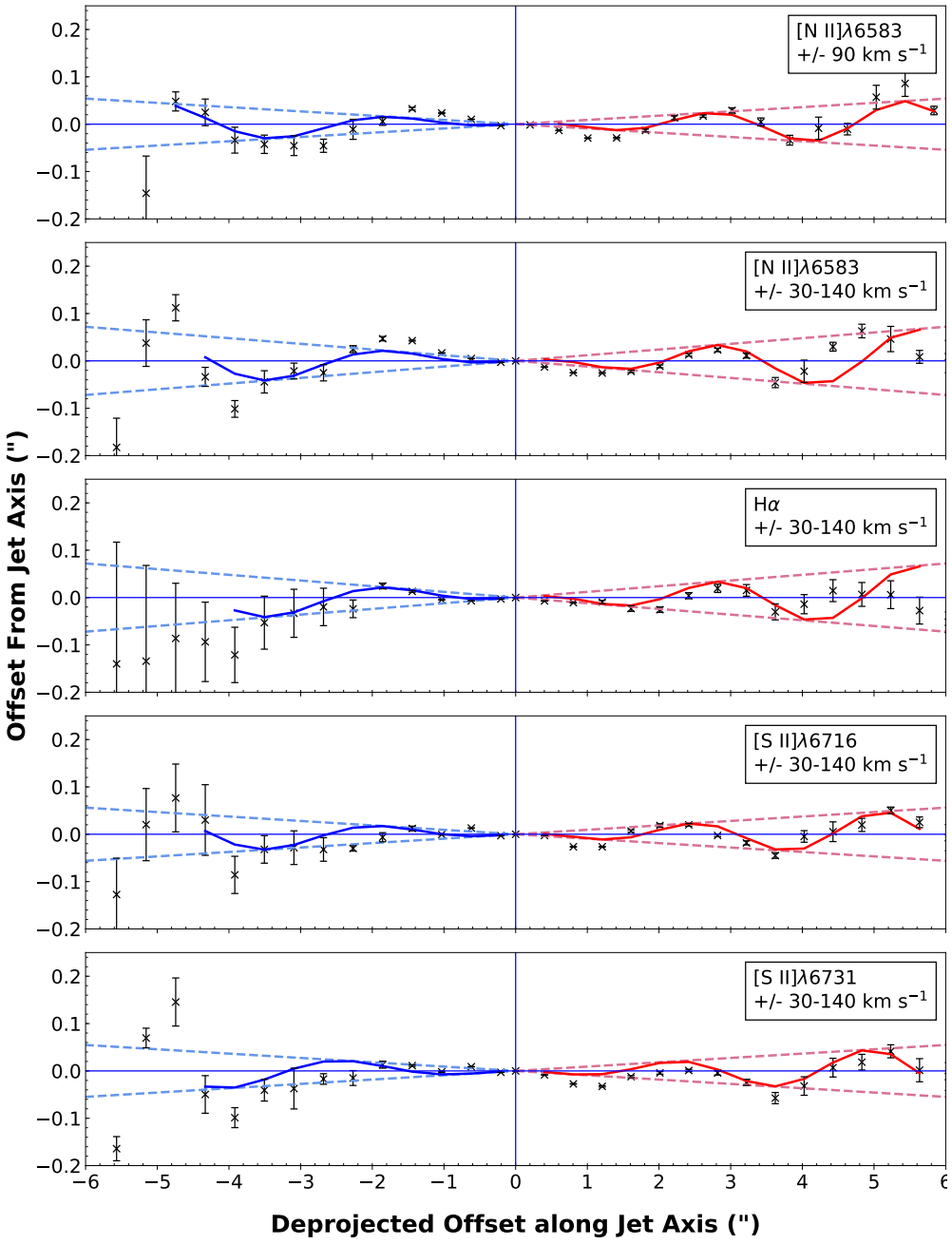

FIGURE B.1: Combined precession models fitted to several emission lines of the jet. Jet velocity is taken as $v_{j,red} = 0.''35$ yr^{-1} (≈ 270 km s^{-1}, as in Chapter 4.2.4) while $v_{j,blue}$ is reduced by $0.''05$ yr^{-1} to $0.''42$ yr^{-1}(≈ 330 km s^{-1}). 0 is at the source position. The models and centroids are shown after subtraction of the linear correction; dashed lines mark the half-opening angle on either side of the jet axis.

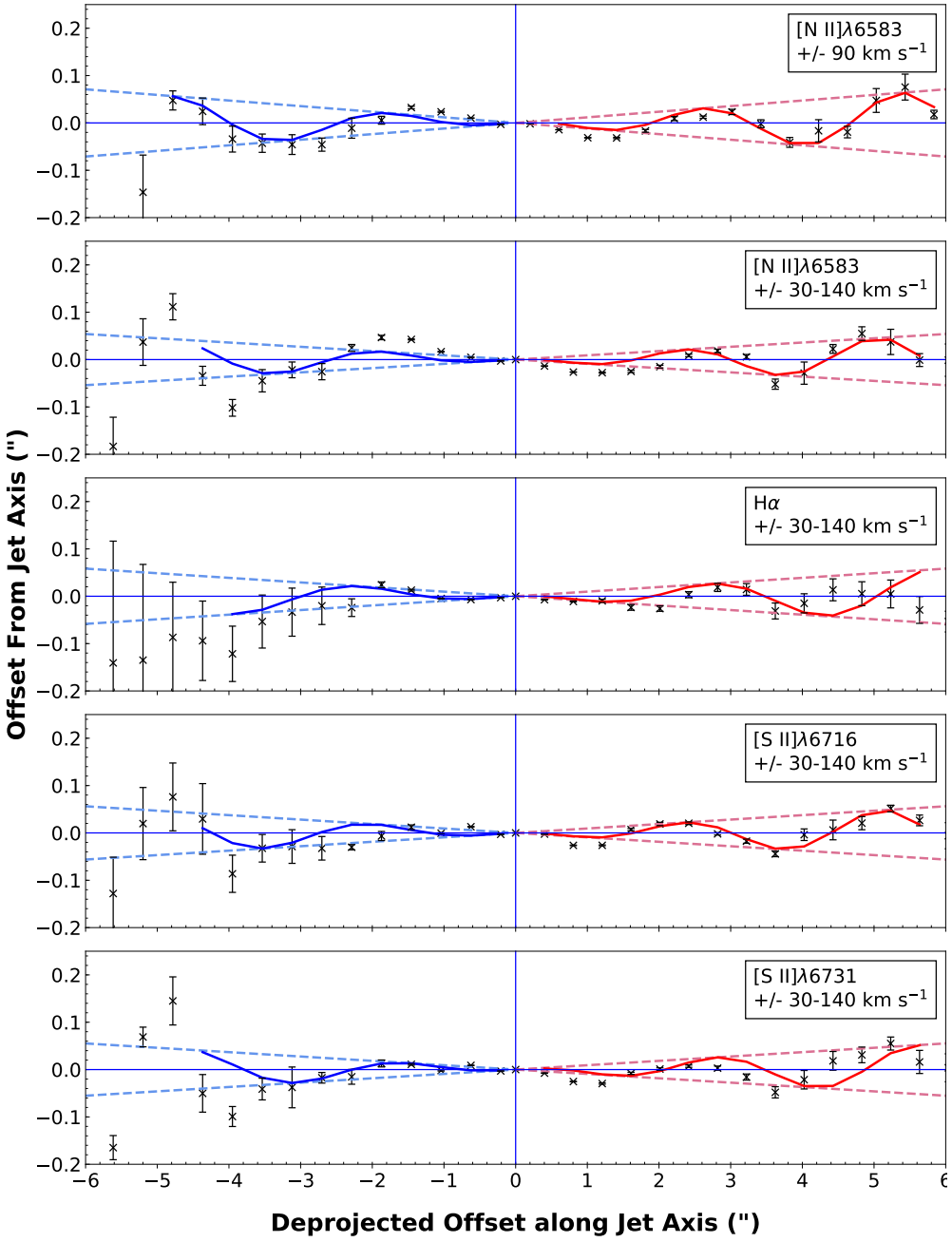

FIGURE B.2: As in Fig. B.1, but with $v_{j,blue}$ reduced by 0."1 yr^{-1} to 0."37 yr^{-1}($\approx$ 300 km s^{-1}).

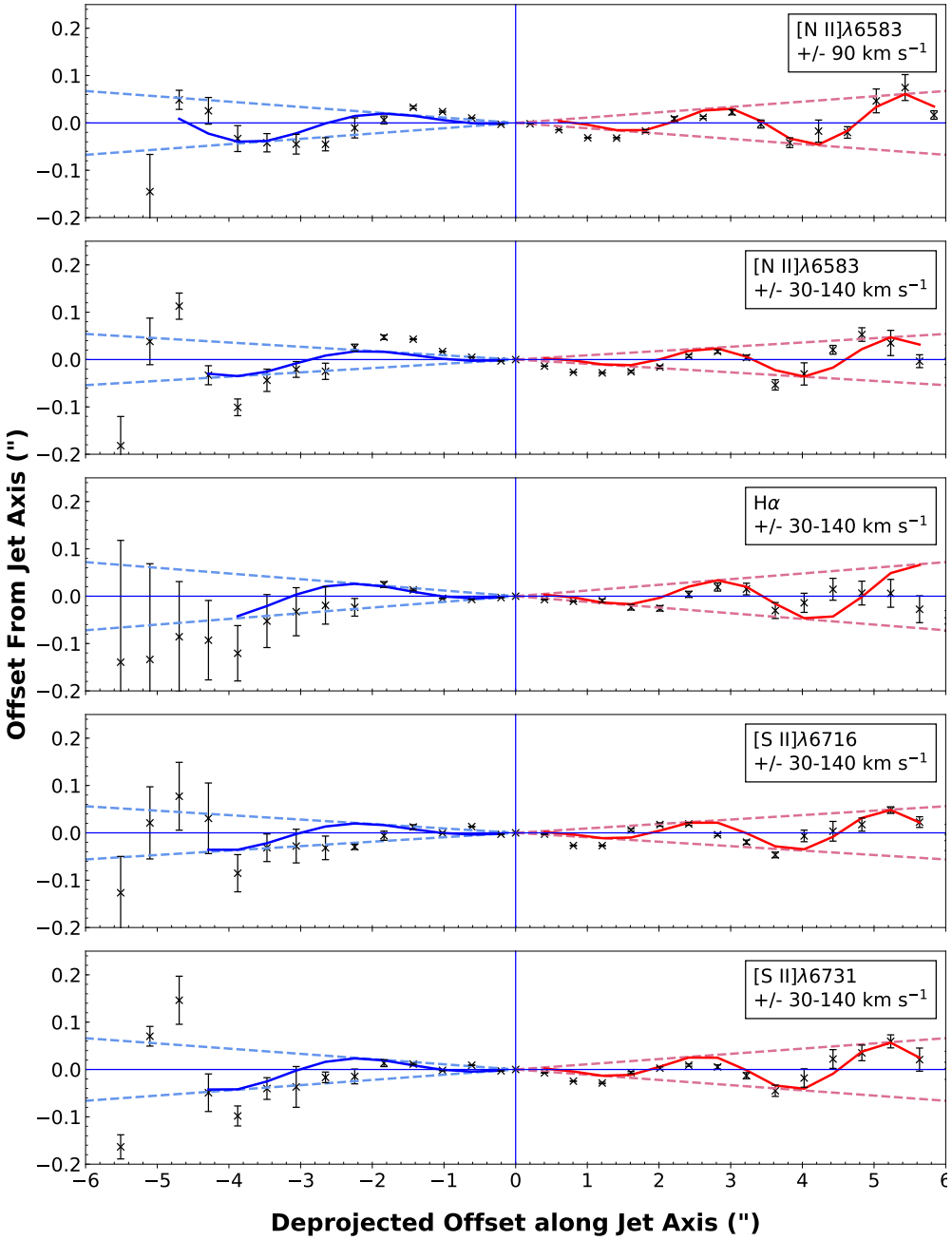

FIGURE B.3: As in Fig. B.1, but with $v_{j,blue}$ increased by 0."05 yr^{-1} to 0."52 yr^{-1}($\approx$ 390 km s^{-1}).

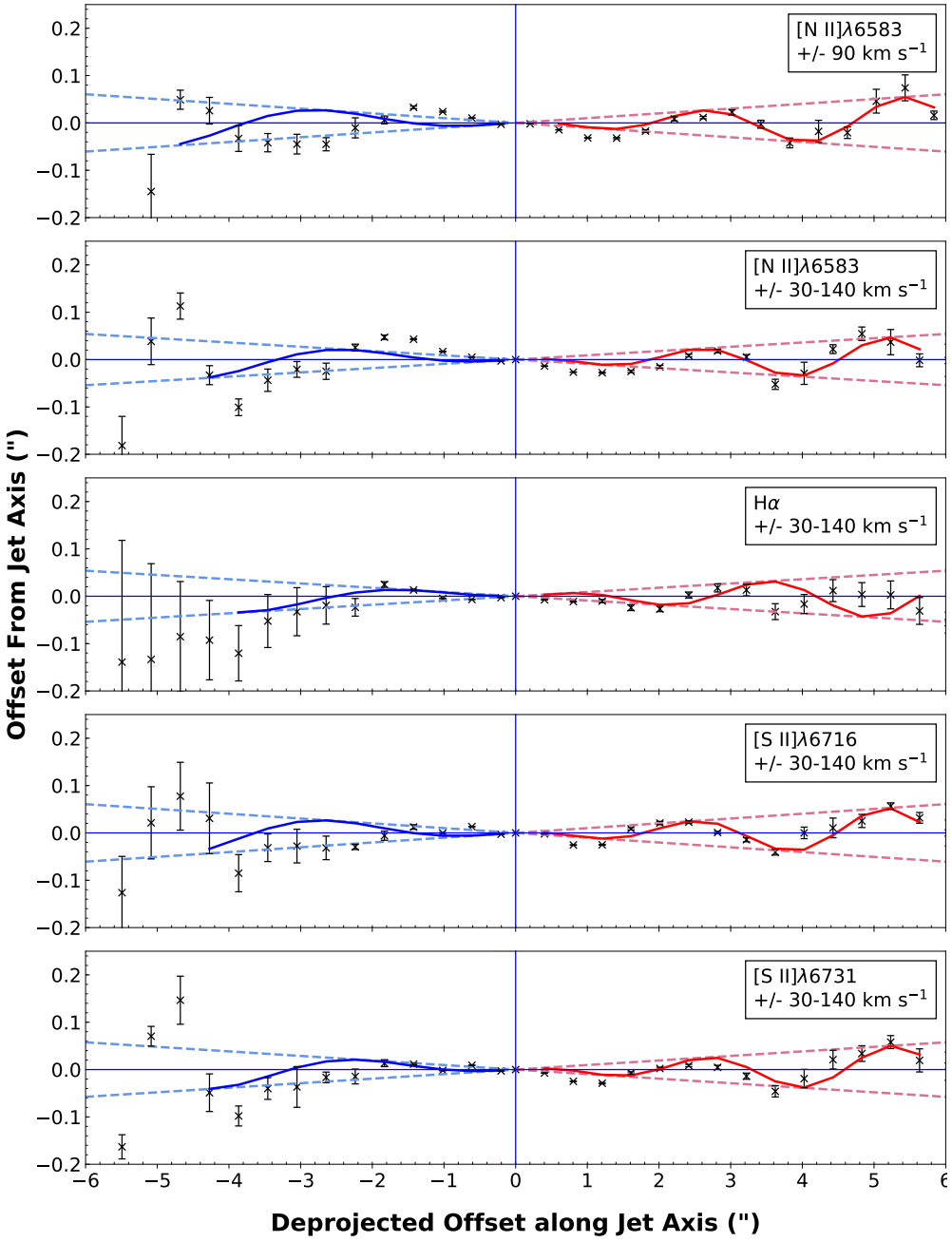

FIGURE B.4: As in Fig. B.1, but with $v_{j,blue}$ increased by 0."1 yr^{-1} to 0."57 yr^{-1}($\approx$ 420 km s^{-1}).

Bibliography

Abergel, A., Ade, P. A., Aghanim, N., et al. 2014, A&A, 571, 1

Agra-Amboage, V., Dougados, C., Cabrit, S., Garcia, P. J., & Ferruit, P. 2009, A&A, 493, 1029

Agra-Amboage, V., Dougados, C., Cabrit, S., & Reunanen, J. 2011, A&A, 532, A59

Alcalá, J. M., Natta, A., Manara, C. F., et al. 2014, A&A, 561, A2

Alencar, S. 2007, in Lect. Notes Phys, Vol. 723, Jets from Young Stars I: Models and Constraints, ed. J. Ferreira, C. Dougados, & E. Whelan (Berlin Heidelberg: Springer), 55–71

Alexander, R., Pascucci, I., Andrews, S., Armitage, P., & Cieza, L. 2014, in Protostars and Planets VI, ed. H. Beuther, R. S. Klessen, C. P. Dullemond, & T. Henning, 475

Allington-Smith, J. 2006, New Astronomy Reviews, 50, 244, integral Field Spectroscopy: Techniques and Data Production

Allington-Smith, J. & Content, R. 1998, PASP, 110, 1216

Almeida, P. V., Gameiro, J. F., Petrov, P. P., et al. 2017, A&A, 600

Anderson, J. M., Li, Z., Krasnopolsky, R., & Blandford, R. D. 2003, ApJ, 590, L107

André, P., Men'shchikov, A., Bontemps, S., et al. 2010, A&A, 518, L102

Andrews, S. M., Reipurth, B., Bally, J., & Heathcote, S. R. 2004, ApJ, 606, 353

Andrews, S. M. & Williams, J. P. 2005, ApJ, 631, 1134

Anglada, G., López, R., Estalella, R., et al. 2007, AJ, 133

Antoniucci, S., Nisini, B., Giannini, T., & Lorenzetti, D. 2008, A&A, 479, 503

Arce, H. G., Borkin, M. A., Goodman, A. A., Pineda, J. E., & Beaumont, C. N. 2011, ApJ, 742, 105

Arce, H. G., Borkin, M. A., Goodman, A. A., Pineda, J. E., & Halle, M. W. 2010, ApJ, 715, 1170

Arce, H. G., Mardones, D., Corder, S. A., et al. 2013, ApJ, 774

Arce, H. G. & Sargent, A. I. 2006, ApJ, 646, 1070

Arce, H. G., Shepherd, D., Gueth, F., et al. 2007, in Protostars and Planets V, ed. B. Reipurth, D. Jewitt, & K. Keil, 245

Ardila, D. R. 2007, in Star-Disk Interaction in Young Stars, ed. J. Bouvier & I. Appenzeller, Vol. 243, 103–114

Artymowicz, P. & Lubow, S. H. 1994, ApJ, 421, 651

Arzoumanian, D., André, P., Didelon, P., et al. 2011, A&A, 529, L6

Asplund, M., Grevesse, N., & Sauval, A. J. 2005, in Astronomical Society of the Pacific Conference Series, Vol. 336, Cosmic Abundances as Records of Stellar Evolution and Nucleosynthesis, ed. I. Barnes, Thomas G. & F. N. Bash, 25

Astropy Collaboration, Price-Whelan, A. M., Sipőcz, B. M., et al. 2018, AJ, 156, 123

Astropy Collaboration, Robitaille, T. P., Tollerud, E. J., et al. 2013, A&A, 558, A33

Ayala, S., Curiel, S., Raga, A. C., Noriega-Crespo, A., & Salas, L. 1998, A&A, 332, 1055

Bacciotti, F. 2009, in Astrophysics and Space Science Proceedings, Vol. 13, Protostellar Jets in Context, 231–240

Bacciotti, F. & Eislöffel, J. 1999, A&A, 342, 717

Bacciotti, F., Mundt, R., Ray, T. P., et al. 2000, ApJ, 537, L49

Bacciotti, F., Ray, T. P., Mundt, R., Eisloffel, J., & Solf, J. 2002, ApJ, 576, 222

Bacciotti, F., Whelan, E. T., Alcalá, J. M., et al. 2011, ApJ, 737, L26

Bacon, R., Accardo, M., Adjali, L., et al. 2010, in Society of Photo-Optical Instrumentation Engineers (SPIE) Conference Series, Vol. 7735, Ground-based and Airborne Instrumentation for Astronomy III, ed. I. S. McLean, S. K. Ramsay, & H. Takami, 773508

Bally, J. 2016, ARA&A, 54

Bally, J., Devine, D., Fesen, R. A., & Lane, A. P. 1995, ApJ, 454, 345

Bally, J., Stark, A. A., Wilson, R. W., & Henkel, C. 1987, ApJS, 65, 13

Bally, J., Walawender, J., & Reipurth, B. 2012, AJ, 144, 143

Banzatti, A., Pascucci, I., Edwards, S., et al. 2019, ApJ, 870, 76

Basri, G. 2007, Proceedings of the International Astronomical Union, 3, 13

Bautista, M. A., Peng, J., & Pradhan, A. K. 1996, ApJ, 460, 372

Bautista, M. A. & Pradhan, A. K. 1998, ApJ, 492, 650

Beck, T. L., Riera, A., Raga, A. C., & Reipurth, B. 2007, AJ, 133, 1221

Beltrán, M. T., Cesaroni, R., Moscadelli, L., et al. 2016, A&A, 593, A49

Benedettini, M., Schisano, E., Pezzuto, S., et al. 2015, MNRAS, 453, 2036

Bertout, C. 1989, ARA&A, 27, 351

Bertout, C., Basri, G., & Bouvier, J. 1988, ApJ, 330, 350

Blair, G. N., Evans, N. J., I., vanden Bout, P. A., & Peters, W. L., I. 1978, ApJ, 219, 896

Blandford, R. D. & Payne, D. G. 1982, MNRAS, 199, 883

Bouvier, J., Bertout, C., Benz, W., & Mayor, M. 1986, A&A, 165, 110

Burrows, C. J., Stapelfeldt, K. R., Watson, A. M., et al. 1996, ApJ, 473, 437

Cabrit, S. 2007, in Star-Disk Interaction in Young Stars, ed. J. Bouvier & I. Appenzeller, Vol. 243, 203–214

Cabrit, S., Pety, J., Pesenti, N., & Dougados, C. 2006, A&A, 452, 897

Cai, M. J., Shang, H., Lin, H.-h., & Shu, F. H. 2008, ApJ, 672, 489

Calvet, N. & Gullbring, E. 1998, ApJ, 509, 802

Camenzind, M. 1990, Reviews in Modern Astronomy, 3, 234

Caratti o Garatti, A. & Eislöffel, J. 2009, in Astrophysics and Space Science Proceedings, Vol. 13, Protostellar Jets in Context, 329–339

Caratti o Garatti, A., Froebrich, D., Eislöffel, J., Giannini, T., & Nisini, B. 2008, A&A, 485, 137

Cerqueira, A. H., Vasconcelos, M. J., Raga, A. C., Feitosa, J., & Plana, H. 2015, AJ, 149, 98

Cerqueira, A. H., Velázquez, P. F., Raga, A. C., Vasconcelos, M. J., & De Colle, F. 2006, A&A, 448, 231

Cesaroni, R., Neri, R., Olmi, L., et al. 2005, A&A, 434, 1039

Cieza, L., Padgett, D. L., Stapelfeldt, K. R., et al. 2007, ApJ, 667, 308

Cieza, L. A., Swift, J. J., Mathews, G. S., & Williams, J. P. 2008, ApJL, 686, L115

Coffey, D., Bacciotti, F., & Podio, L. 2008, ApJ, 689, 1112

Coffey, D., Bacciotti, F., Podio, L., & Nisini, B. 2010, ApJ, 719, 505

Coffey, D., Bacciotti, F., Ray, T., Eislöffel, J., & Woitas, J. 2007, ApJ, 663, 350

Coffey, D., Bacciotti, F., Woitas, J., Ray, T. P., & Eisloffel, J. 2004, Ap&SS, 292, 553

Coffey, D., Rigliaco, E., Bacciotti, F., Ray, T. P., & Eislöffel, J. 2012, ApJ, 749

Combet, C. & Ferreira, J. 2008, A&A, 479, 481

Comerón, F. & Fernández, M. 2004, ApJ, 615, 972

Comerón, F. & Fernández, M. 2010, A&A, 511, L131

Comerón, F. & Fernández, M. 2011, A&A, 528

Comerón, F., Fernández, M., Baraffe, I., Neuhäuser, R., & Kaas, A. A. 2003, A&A, 406, 1001

Curiel, S., Rodriguez, L. F., Moran, J. M., & Cantó, J. 1993, ApJ, 415, 191

Dale, J. E., Ercolano, B., & Bonnell, I. A. 2012, MNRAS, 424, 377

Dame, T. M., Hartmann, D., & Thaddeus, P. 2001, ApJ, 547, 792

Dame, T. M., Ungerechts, H., Cohen, R. S., et al. 1987, ApJ, 322, 706

Davis, C. J., Cervantes, B., Nisini, B., et al. 2011, A&A, 528, A3

Davis, C. J., Eislöffel, J., Ray, T. P., & Jenness, T. 1997, A&A, 324, 1013

Devine, D., Bally, J., Reipurth, B., & Heathcote, S. 1997, AJ, 114, 2095

Dobbs, C. L., Krumholz, M. R., Ballesteros-Paredes, J., et al. 2014, in Protostars and Planets VI, ed. H. Beuther, R. S. Klessen, C. P. Dullemond, & T. Henning, 3

Donati, J.-F., Gregory, S. G., Alencar, S. H. P., et al. 2012, Monthly Notices of the Royal Astronomical Society, 425, 2948

Dopita, M. A., Evans, I., & Schwartz, R. D. 1982, ApJ, 263, L73

Dougados, C. 2008, in Lect. Notes Phys, Vol. 742, Jets from Young Stars II: Clues from High Angular Resolution Observations, ed. F. Bacciotti, E. Whelan, & L. Testi (Berlin Heidelberg: Springer), 105–120

Dougados, C., Cabrit, S., Lavalley, C., & Ménard, F. 2000, A&A, 357, 61

Draine, B. T. & McKee, C. F. 1993, ARA&A, 31, 373

Dunham, M. M., Allen, L. E., Evans, N. J., I., et al. 2015a, VizieR Online Data Catalog, J/ApJS/220/11

Dunham, M. M., Allen, L. E., Evans, Neal J., I., et al. 2015b, ApJS, 220, 11

Edwards, S. 2008, in Lect. Notes Phys, Vol. 742, Jets from Young Stars II: Clues from High Angular Resolution Observations, ed. F. Bacciotti, E. Whelan, & L. Testi (Berlin Heidelberg: Springer), 3–11

Edwards, S., Hartigan, P., Ghandour, L., & Andrulis, C. 1994, AJ, 108, 1056

Eislöffel, J. & Mundt, R. 1992, A&A, 263, 292

Eislöffel, J., Smith, M. D., Davis, C. J., & Ray, T. 1996, AJ, 112, 2086

Ellerbroek, L. E., Podio, L., Dougados, C., et al. 2014, A&A, 563, A87

Erkal, J., Dougados, C., Coffey, D., et al. 2021, A&A

Estalella, R., Opez, R. L. ., Anglada, G., et al. 2012, AJl, 144, 61

Evans, N. J., Dunham, M. M., Jørgensen, J. K., et al. 2009, ApJS, 181, 321

Fang, M., Pascucci, I., Edwards, S., et al. 2018, ApJ, 868, 28

Ferreira, J. 1997, A&A, 319, 340

Ferreira, J. & Casse, F. 2013, MNRAS, 428, 307

Ferreira, J., Dougados, C., & Cabrit, S. 2006, A&A, 453, 785

Ferreira, J., Pelletier, G., & Appl, S. 2000, MNRAS, 312, 387

Fitzpatrick, E. L. & Massa, D. 1990, ApJS, 72, 163

Frank, A., Ray, T., Cabrit, S., et al. 2014, in Protostars and Planets VI, ed. H. Beuther, R. Klessen, C. P. Dullemond, & T. Henning (University of Arizona Press, Tucson), 451–474

Garufi, A., Podio, L., Bacciotti, F., et al. 2019, Astronomy & Astrophysics, 628, A68

Giampapa, M. S., Basri, G. S., Johns, C. M., & Imhoff, C. 1993, ApJS, 89, 321

Giannini, T., Nisini, B., Antoniucci, S., et al. 2013, ApJ, 778

Giannini, T., Nisini, B., Antoniucci, S., et al. 2019, A&A, 631, 1

Gomez, M., Kenyon, S. J., & Whitney, B. A. 1997, AJ, 114, 265

Grady, C. A., Devine, D., Woodgate, B., et al. 2000, ApJ, 544, 895

Graham, J. A. & Heyer, M. H. 1988, PASP, 100, 1529

Greene, T. P., Wilking, B. A., Andre, P., Young, E. T., & Lada, C. J. 1994, ApJ, 434, 614

Gueth, F., Guilloteau, S., & Bachiller, R. 1996, A&A, 307, 891

Hara, A., Tachihara, K., Mizuno, A., et al. 1999, PASJ, 51, 895

Haro, G. 1952, ApJ, 115, 572

Haro, G. 1953, ApJ, 117, 73

Hartigan, P., Edwards, S., & Ghandour, L. 1995, ApJ, 452, 736

Hartigan, P., Holcomb, R., & Frank, A. 2019, ApJ, 876, 147

Hartigan, P., Kenyon, S. J., Hartmann, L., et al. 1991, ApJ, 382, 617

Hartigan, P. & Morse, J. 2007, ApJ, 660, 426

Hartigan, P., Morse, J. A., & Raymond, J. 1994, ApJ, 436, 125

Hartmann, L., Herczeg, G., & Calvet, N. 2016, ARA&A, 54, 135

Hartmann, L., Hewett, R., & Calvet, N. 1994, ApJ, 426, 669

Heathcote, S., Reipurth, B., & Raga, A. C. 1998, AJ, 116, 1940

Herbig, G. H. 1950, ApJ, 111, 11

Herbig, G. H. 1951, ApJ, 113, 697

Herczeg, G. J. & Hillenbrand, L. A. 2008, ApJ, 681, 594

Hester, J. J., Stapelfeldt, K. R., & Scowen, P. A. 1998, AJ, 116, 372

Hill, C. A., Folsom, C. P., Donati, J.-F., et al. 2019, MNRAS, 484, 5810

Hill, T., Motte, F., Didelon, P., et al. 2011, A&A, 533, A94

Hirth, G. A., Mundt, R., Solf, J., & Ray, T. P. 1994, ApJL, 427, L99

Hughes, J., Hartigan, P., Krautter, J., & Kelemen, J. 1994, AJ, 108, 1071

Isella, A., Guidi, G., Testi, L., et al. 2016, Phys. Rev. Lett., 117, 251101

Jensen, E. L. N., Mathieu, R. D., & Fuller, G. A. 1996, ApJ, 458, 312

Jhan, K.-S. & Lee, C.-F. 2021, ApJ, 909, 11

Johns, C. M. & Basri, G. 1995, ApJ, 449, 341

Johns-Krull, C. M., Valenti, J. A., & Koresko, C. 1999, ApJ, 516, 900

Jones, A. P. 2000, J. Geophys. Res. Space Phys., 105, 10257

Jørgensen, J. K., van Dishoeck, E. F., Visser, R., et al. 2009, A&A, 507, 861

Khanzadyan, T., Gredel, R., Smith, M. D., & Stanke, T. 2004, A&A, 426, 171

Kirk, H., Myers, P. C., Bourke, T. L., et al. 2013, ApJ, 766, 115

Kirwan, A., Murphy, A., Schneider, P. C., et al. in prep., A&A, submitted

Königl, A. 1991, ApJ, 370, L39

Krautter, J. 1986, A&A, 161, 195

Kutner, M. L., Tucker, K. D., Chin, G., & Thaddeus, P. 1977, ApJ, 215, 521

Kwan, J. & Tademaru, E. 1988, ApJ, 332, L41

Lada, C. J. 1976, ApJS, 32, 603

Lada, C. J. 1987, in Star Forming Regions, ed. M. Peimbert & J. Jugaku, Vol. 115, 1

Lada, C. J. & Wilking, B. A. 1984, ApJ, 287, 610

Lai, D. 1999, ApJ, 524, 1030

Lai, D. 2003, ApJ, 591, L119

Lavalley, C., Cabrit, S., Dougados, C., Ferruit, P., & Bacon, R. 1997, A&A, 327, 671

Lavalley-Fouquet, C., Cabrit, S., & Dougados, C. 2000, A&A, 356, 41

Lee, C.-F., Hasegawa, T. I., Hirano, N., et al. 2010, ApJ, 713, 731

Lee, C. F., Hirano, N., Palau, A., et al. 2009, ApJl, 699, 1584

Lefloch, B., Gusdorf, A., Codella, C., et al. 2015, A&A, 581, A4

Liu, C., Shang, H., Walter, F., & Herczeg, G. 2014, ApJ, 786:99, 1

Liu, C.-F., Shang, H., Herczeg, G. J., & Walter, F. M. 2021, ApJ, 909, 196

Livio, M. 2009, in Astrophysics and Space Science Proceedings, Vol. 13, Protostellar Jets in Context, 3–9

López, R., Raga, A., Riera, A., Anglada, G., & Estalella, R. 1995, MNRAS, 274, L19

López, R., Riera, A., Raga, A. C., et al. 1996, MNRAS, 282, 470

Lopez, R. G., Garatti, A. C. o., Weigelt, G., Nisini, B., & Antoniucci, S. 2013, A&A, 552, 2

Louvet, F., Dougados, C., Cabrit, S., et al. 2016, A&A, A88, 596

Lubow, S. H. & Ogilvie, G. I. 2000, ApJ, 538, 326

Luhman, K. L., Joergens, V., Lada, C., et al. 2007, in Protostars and Planets V, ed. B. Reipurth, D. Jewitt, & K. Keil (University of Arizona Press, Tucson), 443–457

Luridiana, V., Morisset, C., & Shaw, R. A. 2015, A&A, 573, A42

Manara, C. F., Frasca, A., Venuti, L., et al. 2021, A&A, 650, A196

Masciadri, E. & Raga, A. C. 2002, ApJ, 568, 733

Matt, S. & Pudritz, R. E. 2005, ApJ, 632, L135

Matt, S. P., MacGregor, K. B., Pinsonneault, M. H., & Greene, T. P. 2012, ApJ, 754, L26

Maurri, L., Bacciotti, F., Podio, L., et al. 2014, A&A, 565, A110

McGroarty, F. & Ray, T. P. 2004, A&A, 420, 975

McKee, C. F. & Ostriker, E. C. 2007, ARA&A, 45, 565

Meliani, Z., Casse, F., & Sauty, C. 2006, A&A, 460, 1

Melnikov, S., Stute, M., & Eislöffel, J. 2018, Astronomy & Astrophysics, 612, A77

Melnikov, S., Woitas, J., Eislöffel, J., et al. 2008, A&A, 483, 199

Micono, M., Massaglia, S., Bodo, G., Rossi, P., & Ferrari, A. 1998, A&A, 333, 989

Mirabel, I. F. & Rodríguez, L. F. 1999, ARA&A, 37, 409

Mohanty, S., Basri, G., & Jayawardhana, R. 2005, Astron. Nachr., 326, 891

Molinari, S., Bally, J., Glover, S., et al. 2014, in Protostars and Planets VI, ed. H. Beuther, R. S. Klessen, C. P. Dullemond, & T. Henning, 125

Mortier, A., Oliveira, I., & van Dishoeck, E. F. 2011, MNRAS, 418, 1194

Mundt, R. & Eisloffel, J. 1998, AJ, 116, 860

Mundt, R. & Fried, J. W. 1983, ApJ, 274, L83

Mundt, R., Ray, T. P., & Raga, A. C. 1991, A&A, 252, 740

Myers, P. C. 2009, ApJ, 700, 1609

Nakajima, Y., Nagata, T., Sato, S., et al. 2003, AJ, 125, 1407

Nichols, J. & Slavin, J. D. 2009, ApJ, 699, 902

Nicholson, B. A., Hussain, G. A. J., Donati, J.-F., et al. 2018, MNRAS, 480, 1754

Nisini, B. 2009, in Astrophysics and Space Science Proceedings, Vol. 13, Protostellar Jets in Context, 215–224

Nisini, B., A. Caratti o Garatti, Giannini, T., & Lorenzetti, D. 2002, A&A, 393, 1035

Nisini, B., Antoniucci, S., Alcalá, J. M., et al. 2018, A&A, 609, A87

Nisini, B., Bacciotti, F., Giannini, T., et al. 2005, A&A, 441, 159

Nisini, B., Giannini, T., Antoniucci, S., et al. 2016, A&A, 595, A76

Noriega-Crespo, A., Raga, A. C., Lora, V., Stapelfeldt, K. R., & Carey, S. J. 2011, ApJL, 732, 16

Ogura, K. 1995, ApJ, 450

Osterbrock, D. E. 1989, Astrophysics of gaseous nebulae and active galactic nuclei (University Science Books)

Osterbrock, D. E. & Ferland, G. J. 2006, Astrophysics of gaseous nebulae and active galactic nuclei (University Science Books)

Paczynski, B. 1977, ApJ, 216, 822

Papaloizou, J. C. B. & Pringle, J. E. 1977, MNRAS, 181, 441

Pinte, C., Price, D. J., Ménard, F., et al. 2018, ApJ, 860, L13

Podio, L., Bacciotti, F., Nisini, B., et al. 2006, A&A, 456, 189

Podio, L., Codella, C., Gueth, F., et al. 2015, A&A, 581, A85

Podio, L., Codella, C., Gueth, F., et al. 2016, A&A, 593, L4

Podio, L., Eislöffel, J., Melnikov, S., Hodapp, K. W., & Bacciotti, F. 2011, A&A, 527, A13

Podio, L., Medves, S., Bacciotti, F., Eislöffel, J., & Ray, T. 2009, in Astrophysics and Space Science Proceedings, Vol. 13, Protostellar Jets in Context, 305–310

Porter, J. M., Oudmaijer, R. D., & Baines, D. 2004, A&A, 428, 327

Pudritz, R. E. & Norman, C. A. 1983, ApJ, 274, 677

Pudritz, R. E., Ouyed, R., Fendt, C., & Brandenburg, A. 2007, in Protostars and Planets V, ed. B. Reipurth, D. Jewitt, & K. Keil, 277

Pyo, T.-S., Hayashi, M., Kobayashi, N., Terada, H., & Tokunaga, A. T. 2009, ApJ, 694, 654

Quillen, A. C. 2001, ApJ, 563, 313

Raga, A. & Noriega-Crespo, A. 1998, AJ, 116, 2943

Raga, A. C., Binette, L., & Canto, J. 1990, ApJ, 360, 612

Raga, A. C., Curiel, S., Rodríguez, L. F., & Cantó, J. 2000, A&A, 364, 763

Raga, A. C., Mundt, R., & Ray, T. P. 1991, A&A, 252, 733

Raga, A. C., Velázquez, P. F., Cantó, J., & Masciadri, E. 2002, A&A, 395, 647

Ray, T., Dougados, C., Bacciotti, F., Eisloeffel, J., & Chrysostomou, A. 2006, in Protostars and Planets V, ed. K. Reipurth, B., Jewitt, D., Keil (University of Arizona Press, Tucson), 231–244

Ray, T. & Ferreira, J. 2021, New Astronomy Reviews, 93, 101615

Reipurth, B. & Bally, J. 2001, ARA&A, 39, 403

Reipurth, B., Bally, J., & Devine, D. 1997, AJ, 114, 2708

Reipurth, B., Yu, K. C., Heathcote, S., Bally, J., & Rodríguez, L. F. 2000, AJ, 120, 1449

Riaz, B., Thompson, M., Whelan, E. T., & Lodieu, N. 2015, MNRAS, 446, 2550

Riaz, B. & Whelan, E. T. 2015, ApJ, 815, L31

Rodríguez, L. F., Torrelles, J. M., Anglada, G., & Reipurth, B. 2008, AJ, 136, 1852

Sartori, M. J., Lépine, J. R. D., & Dias, W. S. 2003, A&A, 404, 913

Sauty, C., Cayatte, V., Lima, J. J. G., Matsakos, T., & Tsinganos, K. 2012, ApJL, 759, L1

Sauty, C., Tsinganos, K., & Trussoni, E. 1999, A&A, 348, 327

Schneider, N., Csengeri, T., Bontemps, S., et al. 2010, A&A, 520, A49

Schwartz, R. D. 1977, ApJS, 35, 161

Schwartz, R. D., Cohen, M., Jones, B. F., et al. 1993, AJ, 106, 740

Shang, H., Li, Z. Y., & Hirano, N. 2007, in Protostars and Planets V, ed. B. Reipurth, D. Jewitt, & K. Keil, 261

Sheikhnezami, S. & Fendt, C. 2015, ApJ, 814, 113

Sheikhnezami, S. & Fendt, C. 2018, ApJ, 861, 11

Shepherd, D. S., Yu, K. C., Bally, J., & Testi, L. 2000, ApJ, 535, 833

Shu, F., Najita, J., Ostriker, E., et al. 1994, ApJ, 429, 781

Shu, F. H., Najita, J. R., Shang, H., & Li, Z. Y. 2000, in Protostars and Planets IV, ed. V. Mannings, A. P. Boss, & S. S. Russell, 789–814

Simon, M. N., Pascucci, I., Edwards, S., et al. 2016, ApJ, 831, 169

Stute, M., Gracia, J., Tsinganos, K., & Vlahakis, N. 2012, A&A, 538, A116

Su, Y., Liu, S., Chen, H., Zhang, Q., & Cesaroni, R. 2007, ApJ, 671, 571

Symington, N. H., Harries, T. J., Kurosawa, R., & Naylor, T. 2005, MNRAS, 358, 977

Tachihara, K., Rengel, M., Nakajima, Y., et al. 2007, ApJ, 659, 1382

Teague, R., Bae, J., Bergin, E. A., Birnstiel, T., & Foreman-Mackey, D. 2018, ApJ, 860, L12

Teixeira, P. S., Lada, C. J., & Alves, J. F. 2005, ApJ, 629, 276

Teixeira, P. S., Scholz, A., & Alves, J. 2020, A&A, 642, A86

Terquem, C., Eislöffel, J., Papaloizou, J. C. B., & Nelson, R. P. 1999, ApJl, 512(2), L131

Testi, L., Natta, A., Manara, C. F., et al. 2022, arXiv e-prints, arXiv:2201.04079

Tsinganos, K. 2007, in Lect. Notes Phys, Vol. 723, Jets from Young Stars I: Models and Constraints, ed. J. Ferreira, C. Dougados, & E. Whelan (Berlin Heidelberg: Springer), 117–157

Vernet, J., Dekker, H., D'Odorico, S., et al. 2011, A&A, 536, A105

Wang, H. & Henning, T. 2009, AJ, 138, 1072

Weilbacher, P. M., Monreal-Ibero, A., Kollatschny, W., et al. 2015, A&A, 582, A114

Weilbacher, P. M., Palsa, R., Streicher, O., et al. 2020, A&A, 641, A28

Whelan, E. 2014, Astron. Nachr., 335, 537

Whelan, E. T., Bonito, R., Antoniucci, S., et al. 2014, A&A, 565, A80

Whelan, E. T., Pascucci, I., Gorti, U., et al. 2021, ApJ, 913, 43

Whelan, E. T., Riaz, B., & Rouzé, B. 2018, A&A, 610, 9

Woitas, J., Bacciotti, F., Ray, T. P., et al. 2005, A&A, 432, 149

Zanni, C. & Ferreira, J. 2013, A&A, 550

Zhu, Z. 2019, MNRAS, 483, 4221

Zweibel, E. G., Hole, K. T., & Mathieu, R. D. 2006, ApJ, 649, 879